Publication Year	2016
Acceptance in OA	2020-05-27T13:13:17Z
Title	Planck 2015 results. XIII. Cosmological parameters
Authors	Planck Collaboration, Ade, P. A. R., Aghanim, N., Arnaud, M., Ashdown, M., Aumont, J., Baccigalupi, C., Banday, A. J., Barreiro, R. B., Bartlett, J. G., Bartolo, N., Wehus, I. K., White, M., White, S. D. M., Wilkinson, A., Yvon, D., Bucher, M., ZACCHEI, Andrea, Zonca, A., BURIGANA, CARLO, Huang, Z., PAOLETTI, DANIELA, Butler, R. C., Calabrese, E., Cardoso, J. -F., Catalano, A., Challinor, A., Chamballu, A., Chary, R. -R., Chiang, H. C., Chluba, J., Christensen, P. R., Partridge, B., Huffenberger, K. M., Church, S., Clements, D. L., Colombi, S., Colombo, L. P. L., Combet, C., Coulais, A., Crill, B. P., Curto, A., CUTTAIA, FRANCESCO, Pasian, F., Danese, L., Battaner, E., Davies, R. D., Davis, R. J., de Bernardis, P., De Rosa, A., de Zotti, G., Delabrouille, J., Désert, F. -X., Di Valentino, E., Patanchon, G., Dickinson, C., Diego, J. M., Hurier, G., Dolag, K., Dole, H., Donzelli, S., Doré, O., Douspis, M., Ducout, A., Dunkley, J., Pearson, T. J., Dupac, X., Efstathiou, G., Elsner, F., Jaffe, A. H., Enßlin, T. A., Eriksen, H. K., Farhang, M., Fergusson, J., FINELLI, FABIO, Forni, O., Perdereau, O., FRAILIS, Marco, Fraisse, A. A., FRANCESCHI, ENRICO, Frejsel, A., Jaffe, T. R., GALEOTTA, Samuele, Galli, S., Ganga, K., Gauthier, C., Gerbino, M., Perotto, L., Ghosh, T., Giard, M., Giraud-Héraud, Y., Giusarma, E., Gjerløw, E., Jones, W. C., González-Nuevo, J., Górski, K. M., Gratton, S., Gregorio, A., Perrotta, F., GRUPPUSO, ALESSANDRO, Gudmundsson, J. E., Hamann, J., Hansen, F. K., Hanson, D., Harrison, D. L., Juvela, M., Helou, G., Henrot-Versillé, S., Keihänen, E., Pettorino, V., Keskitalo, R., Kisner, T. S., Kneissl, R., Knoche, J., Battye, R., Knox, L., Kunz, M., Kurki-Suonio, H., Lagache, G., Lähteenmäki, A., Bock, J. J., Lamarre, J. -M., Lasenby, A., Lattanzi, M., Lawrence, C. R., Leahy, J. P., Benabed, K., Leonardi, R., Lesgourgues, J., Levrier, F., Lewis, A., Hernández-Monteagudo, C., Liguori, M., Lilje, P. B., Linden-Vørnle, M., López-Caniego, M., Lubin, P. M., Macías-Pérez, J. F., Benoît, A., Maggio, G., Maino, D., Mandolesi, N., Piacentini, F., Mangilli, A., Marchini, A., MARIS, Michele, Martin, P. G., Martinelli, M., Martínez-González, E., Masi, S., Benoit-Lévy, A., Matarrese, S., McGehee, P., Piat, M., Meinhold, P. R., Melchiorri, A., Melin, J. -B., Mendes, L., Mennella, A., Migliaccio, M., Millea, M., Mitra, S., Bernard, J. -P., Miville-Deschênes, M. -A., Pierpaoli, E., Moneti, A., Montier, L., MORGANTE, GIANLUCA, Mortlock, D., Moss, A., Munshi, D., Murphy, J. A., Naselsky, P., Nati, F., Bersanelli, M., Pietrobon, D., Natoli, P., Netterfield, C. B., Nørgaard-Nielsen, H. U., Noviello, F., Novikov, D., Novikov, I., Oxborrow, C. A., Paci, F., Pagano, L., Pajot, F., Plaszczynski, S., Bielewicz, P., Paladini, R., Pointecouteau, E., Polenta, G., Popa, L., Pratt, G. W., Prézeau, G., Herranz, D., Bonaldi, A., Prunet, S., Puget, J. -L., Rachen, J. P., Reach, W. T., Rebolo, R., Reinecke, M., Remazeilles, M., Renault, C., Renzi, A., Hildebrandt, S. R., Ristorcelli, I., Bonavera, L., Rocha, G., Rosset, C., ROSSETTI, MARIACHIARA, Roudier, G., Rouillé

Planck 2015 results

Planck 2015 results

XIII. Cosmological parameters

Planck Collaboration: P. A. R. Ade[105], N. Aghanim[71], M. Arnaud[87], M. Ashdown[83,7], J. Aumont[71], C. Baccigalupi[103], A. J. Banday[117,12], R. B. Barreiro[78], J. G. Bartlett[1,80], N. Bartolo[38,79], E. Battaner[120,121], R. Battye[81], K. Benabed[72,116], A. Benoît[69], A. Benoit-Lévy[29,72,116], J.-P. Bernard[117,12], M. Bersanelli[41,58], P. Bielewicz[97,12,103], J. J. Bock[80,14], A. Bonaldi[81], L. Bonavera[78], J. R. Bond[11], J. Borrill[17,109], F. R. Bouchet[72,107], F. Boulanger[71], M. Bucher[1], C. Burigana[57,39,59], R. C. Butler[57], E. Calabrese[112], J.-F. Cardoso[88,1,72], A. Catalano[89,86], A. Challinor[75,83,15], A. Chamballu[87,19,71], R.-R. Chary[68], H. C. Chiang[33,8], J. Chluba[28,83], P. R. Christensen[98,44], S. Church[111], D. L. Clements[67], S. Colombi[72,116], L. P. L. Colombo[27,80], C. Combet[89], A. Coulais[86], B. P. Crill[80,14], A. Curto[78,7,83], F. Cuttaia[57], L. Danese[103], R. D. Davies[81], R. J. Davis[81], P. de Bernardis[40], A. de Rosa[57], G. de Zotti[54,103], J. Delabrouille[1], F.-X. Désert[64], E. Di Valentino[72,107], C. Dickinson[81], J. M. Diego[78], K. Dolag[119,94], H. Dole[71,70], S. Donzelli[58], O. Doré[80,14], M. Douspis[71], A. Ducout[72,67], J. Dunkley[112], X. Dupac[47], G. Efstathiou[75,83,★], F. Elsner[29,72,116], T. A. Enßlin[94], H. K. Eriksen[76], M. Farhang[11,102], J. Fergusson[15], F. Finelli[57,59], O. Forni[117,12], M. Frailis[56], A. A. Fraisse[33], E. Franceschi[57], A. Frejsel[98], S. Galeotta[56], S. Galli[82], K. Ganga[1], C. Gauthier[1,93], M. Gerbino[114,100,40], T. Ghosh[71], M. Giard[117,12], Y. Giraud-Héraud[1], E. Giusarma[40], E. Gjerløw[76], J. González-Nuevo[23,78], K. M. Górski[80,123], S. Gratton[83,75], A. Gregorio[42,56,63], A. Gruppuso[57], J. E. Gudmundsson[114,100,33], J. Hamann[115,113], F. K. Hansen[76], D. Hanson[95,80,11], D. L. Harrison[75,83], G. Helou[14], S. Henrot-Versillé[85], C. Hernández-Monteagudo[16,94], D. Herranz[78], S. R. Hildebrandt[80,14], E. Hivon[72,116], M. Hobson[7], W. A. Holmes[80], A. Hornstrup[20], W. Hovest[94], Z. Huang[11], K. M. Huffenberger[31], G. Hurier[71], A. H. Jaffe[67], T. R. Jaffe[117,12], W. C. Jones[33], M. Juvela[32], E. Keihänen[32], R. Keskitalo[17], T. S. Kisner[91], R. Kneissl[46,9], J. Knoche[94], L. Knox[35], M. Kunz[21,71,3], H. Kurki-Suonio[32,52], G. Lagache[5,71], A. Lähteenmäki[2,52], J.-M. Lamarre[86], A. Lasenby[7,83], M. Lattanzi[39,60], C. R. Lawrence[80], J. P. Leahy[81], R. Leonardi[10], J. Lesgourgues[73,115], F. Levrier[86], A. Lewis[30], M. Liguori[38,79], P. B. Lilje[76], M. Linden-Vørnle[20], M. López-Caniego[47,78], P. M. Lubin[36], J. F. Macías-Pérez[89], G. Maggio[56], D. Maino[41,58], N. Mandolesi[57,39], A. Mangilli[71,85], A. Marchini[61], M. Maris[56], P. G. Martin[11], M. Martinelli[122], E. Martínez-González[78], S. Masi[40], S. Matarrese[38,79,49], P. McGehee[68], P. R. Meinhold[36], A. Melchiorri[40,61], J.-B. Melin[19], L. Mendes[47], A. Mennella[41,58], M. Migliaccio[75,83], M. Millea[35], S. Mitra[66,80], M.-A. Miville-Deschênes[71,11], A. Moneti[72], L. Montier[117,12], G. Morgante[57], D. Mortlock[67], A. Moss[106], D. Munshi[105], J. A. Murphy[96], P. Naselsky[99,45], F. Nati[33], P. Natoli[39,4,60], C. B. Netterfield[24], H. U. Nørgaard-Nielsen[20], F. Noviello[81], D. Novikov[92], I. Novikov[98,92], C. A. Oxborrow[20], F. Paci[103], L. Pagano[40,61], F. Pajot[71], R. Paladini[68], D. Paoletti[57,59], B. Partridge[51], F. Pasian[56], G. Patanchon[1], T. J. Pearson[14,68], O. Perdereau[85], L. Perotto[89], F. Perrotta[103], V. Pettorino[50], F. Piacentini[40], M. Piat[1], E. Pierpaoli[27], D. Pietrobon[80], S. Plaszczynski[85], E. Pointecouteau[117,12], G. Polenta[4,55], L. Popa[74], G. W. Pratt[87], G. Prézeau[14,80], S. Prunet[72,116], J.-L. Puget[71], J. P. Rachen[25,94], W. T. Reach[118], R. Rebolo[77,18,22], M. Reinecke[94], M. Remazeilles[81,71,1], C. Renault[89], A. Renzi[43,62], I. Ristorcelli[117,12], G. Rocha[80,14], C. Rosset[1], M. Rossetti[41,58], G. Roudier[1,86,80], B. Rouillé d'Orfeuil[85], M. Rowan-Robinson[67], J. A. Rubiño-Martín[77,22], B. Rusholme[68], N. Said[40], V. Salvatelli[40,6], L. Salvati[40], M. Sandri[57], D. Santos[89], M. Savelainen[32,52], G. Savini[101], D. Scott[26], M. D. Seiffert[80,14], P. Serra[71], E. P. S. Shellard[15], L. D. Spencer[105], M. Spinelli[85], V. Stolyarov[7,110,84], R. Stompor[1], R. Sudiwala[105], R. Sunyaev[94,108], D. Sutton[75,83], A.-S. Suur-Uski[32,52], J.-F. Sygnet[72], J. A. Tauber[48], L. Terenzi[104,57], L. Toffolatti[23,78,57], M. Tomasi[41,58], M. Tristram[85], T. Trombetti[57,39], M. Tucci[21], J. Tuovinen[13], M. Türler[65], G. Umana[53], L. Valenziano[57], J. Valiviita[32,52], F. Van Tent[90], P. Vielva[78], F. Villa[57], L. A. Wade[80], B. D. Wandelt[72,116,37], I. K. Wehus[80,76], M. White[34], S. D. M. White[94], A. Wilkinson[81], D. Yvon[19], A. Zacchei[56], and A. Zonca[36]

(Affiliations can be found after the references)

ABSTRACT

This paper presents cosmological results based on full-mission *Planck* observations of temperature and polarization anisotropies of the cosmic microwave background (CMB) radiation. Our results are in very good agreement with the 2013 analysis of the *Planck* nominal-mission temperature data, but with increased precision. The temperature and polarization power spectra are consistent with the standard spatially-flat 6-parameter ΛCDM cosmology with a power-law spectrum of adiabatic scalar perturbations (denoted "base ΛCDM" in this paper). From the *Planck* temperature data combined with *Planck* lensing, for this cosmology we find a Hubble constant, $H_0 = (67.8 \pm 0.9)$ km s^{-1}Mpc^{-1}, a matter density parameter $\Omega_m = 0.308 \pm 0.012$, and a tilted scalar spectral index with $n_s = 0.968 \pm 0.006$, consistent with the 2013 analysis. Note that in this abstract we quote 68% confidence limits on measured parameters and 95% upper limits on other parameters. We present the first results of polarization measurements with the Low Frequency Instrument at large angular scales. Combined with the *Planck* temperature and lensing data, these measurements give a reionization optical depth of $\tau = 0.066 \pm 0.016$, corresponding to a reionization redshift of $z_{re} = 8.8^{+1.7}_{-1.4}$. These results are consistent with those from WMAP polarization measurements cleaned for dust emission using 353-GHz polarization maps from the High Frequency Instrument. We find no evidence for any departure from base ΛCDM in the neutrino sector of the theory; for example, combining *Planck* observations with other astrophysical data we find $N_{eff} = 3.15 \pm 0.23$ for the effective number of relativistic degrees of freedom, consistent with the value $N_{eff} = 3.046$ of the Standard Model of particle physics. The sum of neutrino masses is constrained to $\sum m_\nu < 0.23$ eV. The spatial curvature of our Universe is found to be very close to zero, with $|\Omega_K| < 0.005$. Adding a tensor component as a single-parameter extension to base ΛCDM we find an upper limit on the tensor-to-scalar ratio of $r_{0.002} < 0.11$, consistent with the *Planck* 2013 results and consistent with the *B*-mode polarization constraints from a joint analysis of BICEP2, Keck Array, and *Planck* (BKP) data. Adding the BKP *B*-mode data to our analysis leads to a tighter constraint of $r_{0.002} < 0.09$ and disfavours inflationary models with a $V(\phi) \propto \phi^2$ potential. The addition of *Planck* polarization data leads to strong constraints on deviations from a purely adiabatic spectrum of fluctuations. We find no evidence for any contribution from isocurvature perturbations or from cosmic defects. Combining *Planck* data with other astrophysical data, including Type Ia supernovae, the equation of state of dark energy is constrained to $w = -1.006 \pm 0.045$, consistent with the expected

---

★ Corresponding author: G. Efstathiou, e-mail: gpe@ast.cam.ac.uk

value for a cosmological constant. The standard big bang nucleosynthesis predictions for the helium and deuterium abundances for the best-fit *Planck* base ΛCDM cosmology are in excellent agreement with observations. We also constraints on annihilating dark matter and on possible deviations from the standard recombination history. In neither case do we find no evidence for new physics. The *Planck* results for base ΛCDM are in good agreement with baryon acoustic oscillation data and with the JLA sample of Type Ia supernovae. However, as in the 2013 analysis, the amplitude of the fluctuation spectrum is found to be higher than inferred from some analyses of rich cluster counts and weak gravitational lensing. We show that these tensions cannot easily be resolved with simple modifications of the base ΛCDM cosmology. Apart from these tensions, the base ΛCDM cosmology provides an excellent description of the *Planck* CMB observations and many other astrophysical data sets.

Key words cosmology: observations – cosmology: theory – cosmic background radiation – cosmological parameters

1. Introduction

The cosmic microwave background (CMB) radiation offers an extremely powerful way of testing the origin of fluctuations and of constraining the matter content, geometry, and late-time evolution of the Universe. Following the discovery of anisotropies in the CMB by the COBE satellite (Smoot et al. 1992), ground-based, sub-orbital experiments and notably the *Wilkinson* Microwave Anisotropy Probe (WMAP) satellite (Bennett et al. 2003, 2013) have mapped the CMB anisotropies with increasingly high precision, providing a wealth of new information on cosmology.

Planck[1] is the third-generation space mission, following COBE and WMAP, dedicated to measurements of the CMB anisotropies. The first cosmological results from *Planck* were reported in a series of papers (for an overview see Planck Collaboration I 2014, and references therein) together with a public release of the first 15.5 months of temperature data (which we will refer to as the nominal mission data). Constraints on cosmological parameters from *Planck* were reported in Planck Collaboration XVI (2014)[2]. The *Planck* 2013 analysis showed that the temperature power spectrum from *Planck* was remarkably consistent with a spatially flat ΛCDM cosmology specified by six parameters, which we will refer to as the base ΛCDM model. However, the cosmological parameters of this model were found to be in tension, typically at the $2-3\sigma$ level, with some other astronomical measurements, most notably direct estimates of the Hubble constant (Riess et al. 2011), the matter density determined from distant supernovae (Conley et al. 2011; Rest et al. 2014), and estimates of the amplitude of the fluctuation spectrum from weak gravitational lensing (Heymans et al. 2013; Mandelbaum et al. 2013) and the abundance of rich clusters of galaxies (Planck Collaboration XX 2014; Benson et al. 2013; Hasselfield et al. 2013b). As reported in the revised version of PCP13, and discussed further in Sect. 5, some of these tensions have been resolved with the acquisition of more astrophysical data, while other new tensions have emerged.

The primary goal of this paper is to present the results from the full *Planck* mission, including a first analysis of the *Planck* polarization data. In addition, this paper introduces some refinements in data analysis and addresses the effects of small instrumental systematics discovered (or better understood) since PCP13 appeared.

The *Planck* 2013 data were not entirely free of systematic effects. The *Planck* instruments and analysis chains are complex and our understanding of systematics has improved since PCP13. The most important of these was the incomplete removal of line-like features in the power spectrum of the time-ordered data, caused by interference of the 4-K cooler electronics with the bolometer readout electronics. This resulted in correlated systematics across detectors, leading to a small "dip" in the power spectra at multipoles $\ell \approx 1800$ at 217 GHz, which is most noticeable in the first sky survey. Various tests were presented in PCP13 that suggested that this systematic caused only small shifts to cosmological parameters. Further analyses, based on the full mission data from the HFI (29 months, 4.8 sky surveys) are consistent with this conclusion (see Sect. 3). In addition, we discovered a minor error in the beam transfer functions applied to the 2013 217-GHz spectra, which had negligible impact on the scientific results. Another feature of the *Planck* data, not fully understood at the time of the 2013 data release, was a 2.6% calibration offset (in power) between *Planck* and WMAP (reported in PCP13, see also Planck Collaboration XXXI 2014). As discussed in Appendix A of PCP13, the 2013 *Planck* and WMAP power spectra agree to high precision if this multiplicative factor is taken into account and it has no significant impact on cosmological parameters apart from a rescaling of the amplitude of the primordial fluctuation spectrum. The reasons for the 2013 calibration offsets are now largely understood and in the 2015 release the calibrations of both *Planck* instruments and WMAP are consistent to within about 0.3% in power (see Planck Collaboration I 2016, for further details). In addition, the *Planck* beams have been characterized more accurately in the 2015 data release and there have been minor modifications to the low-level data processing.

The layout of this paper is as follows. Section 2 summarizes a number of small changes to the parameter estimation methodology since PCP13. The full mission temperature and polarization power spectra are presented in Sect. 3. The first subsection (Sect. 3.1) discusses the changes in the cosmological parameters of the base ΛCDM cosmology compared to those presented in 2013. Section 3.2 presents an assessment of the impact of foreground cleaning (using the 545-GHz maps) on the cosmological parameters of the base ΛCDM model. The power spectra and associated likelihoods are presented in Sect. 3.3. This subsection also discusses the internal consistency of the *Planck* TT, TE, and EE spectra. The agreement of TE and EE with the TT spectra provides an important additional test of the accuracy of our foreground corrections to the TT spectra at high multipoles.

PCP13 used the WMAP polarization likelihood at low multipoles to constrain the reionization optical depth parameter τ. The 2015 analysis replaces the WMAP likelihood with polarization data from the *Planck* Low Frequency Instrument (LFI, Planck Collaboration II 2016). The impact of this change on τ is discussed in Sect. 3.4, which also presents an alternative (and competitive) constraint on τ based on combining the *Planck* TT spectrum with the power spectrum of the lensing potential

measured by *Planck*. We also compare the LFI polarization constraints with the WMAP polarization data cleaned with the *Planck* HFI 353-GHz maps.

Section 4 compares the *Planck* power spectra with the power spectra from high-resolution ground-based CMB data from the Atacama Cosmology Telescope (ACT, Das et al. 2014) and the South Pole Telescope (SPT, George et al. 2015). This section applies a Gibbs sampling technique to sample over foreground and other "nuisance" parameters to recover the underlying CMB power spectrum at high multipoles (Dunkley et al. 2013; Calabrese et al. 2013). Unlike PCP13, in which we combined the likelihoods of the high-resolution experiments with the *Planck* temperature likelihood, in this paper we use the high-resolution experiments mainly to check the consistency of the "damping tail" in the *Planck* power spectrum at multipoles ≳ 2000.

Section 5 introduces additional data, including the *Planck* lensing likelihood (described in detail in Planck Collaboration XV 2016) and other astrophysical data sets. As in PCP13, we are highly selective in the astrophysical data sets that we combine with *Planck*. As mentioned above, the main purpose of this paper is to describe what the *Planck* data have to say about cosmology. It is not our purpose to present an exhaustive discussion of what happens when the *Planck* data are combined with a wide range of astrophysical data. This can be done by others, using the publicly released *Planck* likelihood. Nevertheless, some cosmological parameter combinations are highly degenerate using CMB power spectrum measurements alone, the most severe being the "geometrical degeneracy" that opens up when spatial curvature is allowed to vary. Baryon acoustic oscillation (BAO) measurements are a particularly important astrophysical data set. Since BAO surveys involve a simple geometrical measurement, these data are less prone to systematic errors than most other astrophysical data. As in PCP13, BAO measurements are used as a primary astrophysical data set in combination with *Planck* to break parameter degeneracies. It is worth mentioning explicitly our approach to interpreting tensions between *Planck* and other astrophysical data sets. Tensions may be indicators of new physics beyond that assumed in the base ΛCDM model. However, they may also be caused by systematic errors in the data. Our primary goal is to report *whether the Planck data support any evidence for new physics*. If evidence for new physics is driven primarily by astrophysical data, but not by *Planck*, then the emphasis must necessarily shift to establishing whether the astrophysical data are free of systematics. This type of assessment is beyond the scope of this paper, but sets a course for future research.

Extensions to the base ΛCDM cosmology are discussed in Sect. 6, which explores a large grid of possibilities. In addition to these models, we also explore constraints on big bang nucleosynthesis, dark matter annihilation, cosmic defects, and departures from the standard recombination history. As in PCP13, we find no convincing evidence for a departure from the base ΛCDM model. As far as we can tell, a simple inflationary model with a slightly tilted, purely adiabatic, scalar fluctuation spectrum fits the *Planck* data and most other precision astrophysical data. There are some "anomalies" in this picture, including the poor fit to the CMB temperature fluctuation spectrum at low multipoles, as reported by WMAP (Bennett et al. 2003) and in PCP13, suggestions of departures from statistical isotropy at low multipoles (as reviewed in Planck Collaboration XXIII 2014; Planck Collaboration XVI 2016), and hints of a discrepancy with the amplitude of the matter fluctuation spectrum at low redshifts (see Sect. 5.5). However, none of these anomalies are of decisive statistical significance at this stage.

One of the most interesting developments since the appearance of PCP13 was the detection by the BICEP2 team of a *B*-mode polarization anisotropy (BICEP2 Collaboration 2014), apparently in conflict with the 95% upper limit on the tensor-to-scalar ratio, $r_{0.002} < 0.11$[3], reported in PCP13. Clearly, the detection of *B*-mode signal from primordial gravitational waves would have profound consequences for cosmology and inflationary theory. However, a number of studies, in particular an analysis of *Planck* 353-GHz polarization data, suggested that polarized dust emission might contribute a significant part of the BICEP2 signal (Planck Collaboration Int. XXX 2016; Mortonson & Seljak 2014; Flauger et al. 2014). The situation is now clearer following the joint analysis of BICEP2, Keck Array, and *Planck* data (BICEP2/Keck Array and Planck Collaborations 2015, hereafter BKP); this increases the signal-to-noise ratio on polarized dust emission primarily by directly cross-correlating the BICEP2 and Keck Array data at 150 GHz with the *Planck* polarization data at 353 GHz. The results of BKP give a 95% upper limit on the tensor-to-scalar ratio of $r_{0.05} < 0.12$, with no statistically significant evidence for a primordial gravitational wave signal. Section 6.2 presents a brief discussion of this result and how it fits in with the indirect constraints on *r* derived from the *Planck* 2015 data.

Our conclusions are summarized in Sect. 7.

2. Model, parameters, and methodology

The notation, definitions and methodology used in this paper largely follow those described in PCP13, and so will not be repeated here. For completeness, we list some derived parameters of interest in Sect. 2.2. We have made a small number of modifications to the methodology, as described in Sect. 2.1. We have also made some minor changes to the model of unresolved foregrounds and nuisance parameters used in the high-ℓ likelihood. These are described in detail in Planck Collaboration XI (2016), but to make this paper more self-contained, these changes are summarized in Sect. 2.3.

2.1. Theoretical model

We adopt the same general methodology as described in PCP13, with small modifications. Our main results are now based on the lensed CMB power spectra computed with the updated January 2015 version of the camb[4] Boltzmann code (Lewis et al. 2000), and parameter constraints are based on the January 2015 version of CosmoMC (Lewis & Bridle 2002; Lewis 2013). Changes in our physical modelling are as follows.

- For each model in which the fraction of baryonic mass in helium Y_P is *not* varied independently of other parameters, it is now set from the big bang nucleosynthesis (BBN) prediction by interpolation from a recent fitting formula based on results from the PArthENoPE BBN code (Pisanti et al. 2008). We now use a fixed fiducial neutron decay constant of $\tau_n = 880.3$ s, and also account for the small difference between the mass-fraction ratio Y_P and the nucleon-based fraction Y_P^{BBN}.

---

[3] The subscript on *r* refers to the pivot scale in Mpc^{-1} used to define the tensor-to-scalar ratio. For *Planck* we usually quote $r_{0.002}$, since a pivot scale of 0.002 Mpc^{-1} is close to the scale at which there is some sensitivity to tensor modes in the large-angle temperature power spectrum. For a scalar spectrum with no running and a scalar spectral index of $n_s = 0.965$, $r_{0.05} \approx 1.12 r_{0.002}$ for small *r*. For $r \approx 0.1$, assuming the inflationary consistency relation, we have instead $r_{0.05} \approx 1.08 r_{0.002}$.
[4] http://camb.info

These modifications result in changes of about 1% to the inferred value of Y_P compared to PCP13, giving best-fit values $Y_P \approx 0.2453$ ($Y_P^{BBN} \approx 0.2467$) in ΛCDM. See Sect. 6.5 for a detailed discussion of the impact of uncertainties arising from variations of τ_n and nuclear reaction rates; however, these uncertainties have minimal impact on our main results. Section 6.5 also corrects a small error arising from how the difference between $N_{eff} = 3.046$ and $N_{eff} = 3$ was handled in the BBN fitting formula.

- We have corrected a missing source term in the dark energy modelling for $w \neq -1$. The correction of this error has very little impact on our science results, since it is only important for values of w far from -1.
- To model the small-scale matter power spectrum, we use the `halofit` approach (Smith et al. 2003), with the updates of Takahashi et al. (2012), as in PCP13, but with revised fitting parameters for massive neutrino models[5]. We also now include the `halofit` corrections when calculating the lensed CMB power spectra.

As in PCP13 we adopt a Bayesian framework for testing theoretical models. Tests using the "profile likelihood" method, described in Planck Collaboration Int. XVI (2014), show excellent agreement for the mean values of the cosmological parameters and their errors, for both the base ΛCDM model and its N_{eff} extension. Tests have also been carried out using the `class` Boltzmann code (Lesgourgues 2011) and the `Monte Python` MCMC code (Audren et al. 2013) in place of `camb` and `CosmoMC`, respectively. Again, for flat models we find excellent agreement with the baseline choices used in this paper.

2.2. Derived parameters

Our base parameters are defined as in PCP13, and we also calculate the same derived parameters. In addition we now compute:

- the helium nucleon fraction defined by $Y_P^{BBN} \equiv 4n_{He}/n_b$;
- where standard BBN is assumed, the mid-value deuterium ratio predicted by BBN, $y_{DP} \equiv 10^5 n_D/n_H$, using a fit from the `PArthENoPE` BBN code (Pisanti et al. 2008);
- the comoving wavenumber of the perturbation mode that entered the Hubble radius at matter-radiation equality z_{eq}, where this redshift is calculated approximating all neutrinos as relativistic at that time, i.e., $k_{eq} \equiv a(z_{eq})H(z_{eq})$;
- the comoving angular diameter distance to last scattering, $D_A(z_*)$;
- the angular scale of the sound horizon at matter-radiation equality, $\theta_{s,eq} \equiv r_s(z_{eq})/D_A(z_*)$, where r_s is the sound horizon and z_* is the redshift of last scattering;
- the amplitude of the CMB power spectrum $\mathcal{D}_\ell \equiv \ell(\ell + 1)C_\ell/2\pi$ in μK^2, for $\ell = 40, 220, 810, 1520,$ and 2000;
- the primordial spectral index of the curvature perturbations at wavenumber $k = 0.002\,\text{Mpc}^{-1}$, $n_{s,0.002}$ (as in PCP13, our default pivot scale is $k = 0.05\,\text{Mpc}^{-1}$, so that $n_s \equiv n_{s,0.05}$);
- parameter combinations close to those probed by galaxy and CMB lensing (and other external data), specifically $\sigma_8\Omega_m^{0.5}$ and $\sigma_8\Omega_m^{0.25}$;
- various quantities reported by BAO and redshift-space distortion measurements, as described in Sects. 5.2 and 5.5.1.

---

[5] Results for neutrino models with galaxy and CMB lensing alone use the `camb` Jan 2015 version of `halofit` to avoid problems at large Ω_m; other results use the previous (April 2014) `halofit` version.

2.3. Changes to the foreground model

Unresolved foregrounds contribute to the temperature power spectrum and must be modelled to extract accurate cosmological parameters. PPL13 and PCP13 used a parametric approach to modelling foregrounds, similar to the approach adopted in the analysis of the SPT and ACT experiments (Reichardt et al. 2012; Dunkley et al. 2013). The unresolved foregrounds are described by a set of power spectrum templates together with nuisance parameters, which are sampled via MCMC along with the cosmological parameters[6]. The components of the extragalactic foreground model consist of:

- the shot noise from Poisson fluctuations in the number density of point sources;
- the power due to clustering of point sources (loosely referred to as the CIB component);
- a thermal Sunyaev-Zeldovich (tSZ) component;
- a kinetic Sunyaev-Zeldovich (kSZ) component;
- the cross-correlation between tSZ and CIB.

In addition, the likelihood includes a number of other nuisance parameters, such as relative calibrations between frequencies, and beam eigenmode amplitudes. We use the same templates for the tSZ, kSZ, and tSZ/CIB cross-correlation as in the 2013 papers. However, we have made a number of changes to the CIB modelling and the priors adopted for the SZ effects, which we now describe in detail.

2.3.1. CIB

In the 2013 papers, the CIB anisotropies were modelled as a power law:

$$\mathcal{D}_\ell^{\nu_1 \times \nu_2} = A_{\nu_1 \times \nu_2}^{CIB} \left(\frac{\ell}{3000} \right)^{\gamma^{CIB}}. \qquad (1)$$

Planck data alone provide a constraint on $A_{217 \times 217}^{CIB}$ and very weak constraints on the CIB amplitudes at lower frequencies. PCP13 reported typical values of $A_{217 \times 217}^{CIB} = (29 \pm 6)\,\mu K^2$ and $\gamma^{CIB} = 0.40 \pm 0.15$, fitted over the range $500 \leq \ell \leq 2500$. The addition of the ACT and SPT data ("highL") led to solutions with steeper values of γ_{CIB}, closer to 0.8, suggesting that the CIB component was not well fit by a power law.

Planck results on the CIB, using H I as a tracer of Galactic dust, are discussed in detail in Planck Collaboration XXX (2014). In that paper, a model with 1-halo and 2-halo contributions was developed that provides an accurate description of the *Planck* and IRAS CIB spectra from 217 GHz through to 3000 GHz. At high multipoles, $\ell \gtrsim 3000$, the halo-model spectra are reasonably well approximated by power laws, with a slope $\gamma_{CIB} \approx 0.8$ (though see Sect. 4). At multipoles in the range $500 \lesssim \ell \lesssim 2000$, corresponding to the transition from the 2-halo term dominating the clustering power to the 1-halo term dominating, the Planck Collaboration XXX (2014) templates have a shallower slope, consistent with the results of PCP13. The amplitudes of these templates at $\ell = 3000$ are

$$A_{217 \times 217}^{CIB} = 63.6\,\mu K^2, \qquad A_{143 \times 217}^{CIB} = 19.1,\mu K^2,$$
$$A_{143 \times 143}^{CIB} = 5.9\,\mu K^2, \qquad A_{100 \times 100}^{CIB} = 1.4\,\mu K^2. \qquad (2)$$

---

[6] Our treatment of Galactic dust emission also differs from that used in PPL13 and PCP13. Here we describe changes to the extragalactic model and our treatment of errors in the *Planck* absolute calibration, deferring a discussion of Galactic dust modelling in temperature and polarization to Sect. 3.

Note that in PCP13, the CIB amplitude of the 143×217 spectrum was characterized by a correlation coefficient

$$A_{143 \times 217}^{\mathrm{CIB}} = r_{143 \times 217}^{\mathrm{CIB}} \sqrt{A_{217 \times 217}^{\mathrm{CIB}} A_{143 \times 143}^{\mathrm{CIB}}}. \qquad (3)$$

The combined *Planck*+highL solutions in PCP13 always give a high correlation coefficient with a 95% lower limit of $r_{143 \times 217}^{\mathrm{CIB}} \gtrsim 0.85$, consistent with the model of Eq. (2), which has $r_{143 \times 217}^{\mathrm{CIB}} \approx 1$. In the 2015 analysis, we use the Planck Collaboration XXX (2014) templates, fixing the relative amplitudes at 100×100, 143×143, and 143×217 to the amplitude of the 217×217 spectrum. Thus, the CIB model used in this paper is specified by only one amplitude, $A_{217 \times 217}^{\mathrm{CIB}}$, which is assigned a uniform prior in the range 0–$200\,\mu\mathrm{K}^2$.

In PCP13 we solved for the CIB amplitudes *at the CMB effective frequencies* of 217 and 143 GHz, and so we included colour corrections in the amplitudes $A_{217 \times 217}^{\mathrm{CIB}}$ and $A_{143 \times 143}^{\mathrm{CIB}}$ (there was no CIB component in the 100×100 spectrum). In the 2015 *Planck* analysis, we do not include a colour term since we define $A_{217 \times 217}^{\mathrm{CIB}}$ to be the *actual* CIB amplitude measured in the *Planck* 217-GHz band. This is higher by a factor of about 1.33 compared to the amplitude at the CMB effective frequency of the *Planck* 217-GHz band. This should be borne in mind by readers comparing 2015 and 2013 CIB amplitudes measured by *Planck*.

2.3.2. Thermal and kinetic SZ amplitudes

In the 2013 papers we assumed template shapes for the thermal (tSZ) and kinetic (kSZ) spectra characterized by two amplitudes, A^{tSZ} and A^{kSZ}, defined in equations (26) and (27) of PCP13. These amplitudes were assigned uniform priors in the range 0–$10\,(\mu\mathrm{K})^2$. We used the Trac et al. (2011) kSZ template spectrum and the $\epsilon = 0.5$ tSZ template from Efstathiou & Migliaccio (2012). We adopt the same templates for the 2015 *Planck* analysis, since, for example, the tSZ template is actually a good match to the results from the recent numerical simulations of McCarthy et al. (2014). In addition, we previously included a template from Addison et al. (2012) to model the cross-correlation between the CIB and tSZ emission from clusters of galaxies. The amplitude of this template was characterized by a dimensionless correlation coefficient, $\xi^{\mathrm{tSZ} \times \mathrm{CIB}}$, which was assigned a uniform prior in the range 0–1. The three parameters A^{tSZ}, A^{kSZ}, and $\xi^{\mathrm{tSZ} \times \mathrm{CIB}}$, are not well constrained by *Planck* alone. Even when combined with ACT and SPT, the three parameters are highly correlated with each other. Marginalizing over $\xi^{\mathrm{tSZ} \times \mathrm{CIB}}$, Reichardt et al. (2012) find that SPT spectra constrain the linear combination

$$A^{\mathrm{kSZ}} + 1.55\,A^{\mathrm{tSZ}} = (9.2 \pm 1.3)\,\mu\mathrm{K}^2. \qquad (4)$$

The slight differences in the coefficients compared to the formula given in Reichardt et al. (2012) come from the different effective frequencies used to define the *Planck* amplitudes A^{kSZ} and A^{tSZ}. An investigation of the 2013 *Planck*+highL solutions show a similar degeneracy direction, which is almost independent of cosmology, even for extensions to the base ΛCDM model:

$$A^{\mathrm{SZ}} = A^{\mathrm{kSZ}} + 1.6\,A^{\mathrm{tSZ}} = (9.4 \pm 1.4)\,\mu\mathrm{K}^2 \qquad (5)$$

for *Planck*+WP+highL, which is very close to the degeneracy direction (Eq. (4)) measured by SPT. In the 2015 *Planck* analysis, we impose a conservative Gaussian prior for A^{SZ}, as defined in Eq. (5), with a mean of $9.5\,\mu\mathrm{K}^2$ and a dispersion $3\,\mu\mathrm{K}^2$ (i.e., somewhat broader than the dispersion measured by Reichardt et al. 2012). The purpose of imposing this prior on A^{SZ}

is to prevent the parameters A^{kSZ} and A^{tSZ} from wandering into unphysical regions of parameter space when using *Planck* data alone. We retain the uniform prior of [0,1] for $\xi^{\mathrm{tSZ} \times \mathrm{CIB}}$. As this paper was being written, results from the complete $2540\,\mathrm{deg}^2$ SPT-SZ survey area appeared (George et al. 2015). These are consistent with Eq. (5) and in addition constrain the correlation parameter to low values, $\xi^{\mathrm{tSZ} \times \mathrm{CIB}} = 0.113_{-0.054}^{+0.057}$. The looser priors on these parameters adopted in this paper are, however, sufficient to eliminate any significant sensitivity of cosmological parameters derived from *Planck* to the modelling of the SZ components.

2.3.3. Absolute *Planck* calibration

In PCP13, we treated the calibrations of the 100 and 217-GHz channels relative to 143 GHz as nuisance parameters. This was an approximate way of dealing with small differences in relative calibrations between different detectors at high multipoles, caused by bolometer time-transfer function corrections and intermediate and far sidelobes of the *Planck* beams. In other words, we approximated these effects as a purely multiplicative correction to the power spectra over the multipole range $\ell = 50$–2500. The absolute calibration of the 2013 *Planck* power spectra was therefore fixed, by construction, to the absolute calibration of the 143-5 bolometer. Any error in the absolute calibration of this reference bolometer was not propagated into errors on cosmological parameters. For the 2015 *Planck* likelihoods we use an identical relative calibration scheme between 100, 143, and 217 GHz, but we now include an absolute calibration parameter y_{p}, at the map level, for the 143-GHz reference frequency. We adopt a Gaussian prior on y_{p} centred on unity with a (conservative) dispersion of 0.25%. This overall calibration uncertainty is then propagated through to cosmological parameters such as A_{s} and σ_8. A discussion of the consistency of the absolute calibrations across the nine *Planck* frequency bands is given in Planck Collaboration I (2016).

3. Constraints on the parameters of the base ΛCDM cosmology from *Planck*

3.1. Changes in the base ΛCDM parameters compared to the 2013 data release

The principal conclusion of PCP13 was the excellent agreement of the base ΛCDM model with the temperature power spectra measured by *Planck*. In this subsection, we compare the parameters of the base ΛCDM model reported in PCP13 with those measured from the full-mission 2015 data. Here we restrict the comparison to the high multipole temperature (TT) likelihood (plus low-ℓ polarization), postponing a discussion of the TE and EE likelihood blocks to Sect. 3.2. The main differences between the 2013 and 2015 analyses are as follows.

(1) There have been a number of changes to the low-level *Planck* data processing, as discussed in Planck Collaboration II (2016) and Planck Collaboration VII (2016). These include: changes to the filtering applied to remove "4-K" cooler lines from the time-ordered data (TOD); changes to the deglitching algorithm used to correct the TOD for cosmic ray hits; improved absolute calibration based on the spacecraft orbital dipole and more accurate models of the beams, accounting for the intermediate and far sidelobes. These revisions largely eliminate the calibration difference between *Planck*-2013 and WMAP reported in PCP13 and Planck Collaboration XXXI (2014), leading to upward shifts of the HFI and LFI *Planck* power spectra

Table 1. Parameters of the base ΛCDM cosmology (as defined in PCP13) determined from the publicly released nominal-mission `CamSpec` DetSet likelihood [2013N(DS)] and the 2013 full-mission `CamSpec` DetSet and cross-yearly (Y1×Y2) likelihoods with the extended sky coverage [2013F(DS) and 2013F(CY)].

[1] Parameter	[2] 2013N(DS)	[3] 2013F(DS)	[4] 2013F(CY)	[5] 2015F(CHM)	[6] 2015F(CHM) (Plik)	([2]–[6])/$\sigma_{[6]}$	([5]–[6])/$\sigma_{[5]}$
$100\theta_{MC}$	1.04131 ± 0.00063	1.04126 ± 0.00047	1.04121 ± 0.00048	1.04094 ± 0.00048	1.04086 ± 0.00048	0.71	0.17
$\Omega_b h^2$	0.02205 ± 0.00028	0.02234 ± 0.00023	0.02230 ± 0.00023	0.02225 ± 0.00023	0.02222 ± 0.00023	−0.61	0.13
$\Omega_c h^2$	0.1199 ± 0.0027	0.1189 ± 0.0022	0.1188 ± 0.0022	0.1194 ± 0.0022	0.1199 ± 0.0022	0.00	−0.23
H_0	67.3 ± 1.2	67.8 ± 1.0	67.8 ± 1.0	67.48 ± 0.98	67.26 ± 0.98	0.03	0.22
n_s	0.9603 ± 0.0073	0.9665 ± 0.0062	0.9655 ± 0.0062	0.9682 ± 0.0062	0.9652 ± 0.0062	−0.67	0.48
Ω_m	0.315 ± 0.017	0.308 ± 0.013	0.308 ± 0.013	0.313 ± 0.013	0.316 ± 0.014	−0.06	−0.23
σ_8	0.829 ± 0.012	0.831 ± 0.011	0.828 ± 0.012	0.829 ± 0.015	0.830 ± 0.015	−0.08	−0.07
τ	0.089 ± 0.013	0.096 ± 0.013	0.094 ± 0.013	0.079 ± 0.019	0.078 ± 0.019	0.85	0.05
$10^9 A_s e^{-2\tau}$	1.836 ± 0.013	1.833 ± 0.011	1.831 ± 0.011	1.875 ± 0.014	1.881 ± 0.014	−3.46	−0.42

Notes. These three likelihoods are combined with the WMAP polarization likelihood to constrain τ. The column labelled 2015F(CHM) lists parameters for a `CamSpec` cross-half-mission likelihood constructed from the 2015 maps using similar sky coverage to the 2013F(CY) likelihood (but greater sky coverage at 217 GHz and different point source masks, as discussed in the text). The column labelled 2015F(CHM) (`Plik`) lists parameters for the `Plik` cross-half-mission likelihood that uses identical sky coverage to the `CamSpec` likelihood. The 2015 temperature likelihoods are combined with the *Planck* lowP likelihood to constrain τ. The last two columns list the deviations of the `Plik` parameters from those of the nominal-mission and the `CamSpec` 2015(CHM) likelihoods. To help refer to specific columns, we have numbered the first six explicitly. The high-ℓ likelihoods used here include only TT spectra. H_0 is given in the usual units of km s^{-1} Mpc^{-1}.

of approximately 2.0% and 1.7%, respectively. In addition, the mapmaking used for 2015 data processing utilizes "polarization destriping" for the polarized HFI detectors (Planck Collaboration VIII 2016).

(2) The 2013 papers used WMAP polarization measurements (Bennett et al. 2013) at multipoles $\ell \leq 23$ to constrain the optical depth parameter τ; this likelihood was denoted "WP" in the 2013 papers. In the 2015 analysis, the WMAP polarization likelihood is replaced by a *Planck* polarization likelihood constructed from low-resolution maps of Q and U polarization measured by LFI at 70 GHz, foreground cleaned using the LFI 30-GHz and HFI 353-GHz maps as polarized synchrotron and dust templates, respectively, as described in Planck Collaboration XI (2016). After a comprehensive analysis of survey-to-survey null tests, we found possible low-level residual systematics in Surveys 2 and 4, likely related to the unfavourable alignment of the CMB dipole in those two surveys (for details see Planck Collaboration II 2016). We therefore conservatively use only six of the eight LFI 70-GHz full-sky surveys, excluding Surveys 2 and 4, The foreground-cleaned LFI 70-GHz polarization maps are used over 46% of the sky, together with the temperature map from the `Commander` component-separation algorithm over 94% of the sky (see Planck Collaboration IX 2016, for further details), to form a low-ℓ *Planck* temperature+polarization pixel-based likelihood that extends up to multipole $\ell = 29$. Use of the polarization information in this likelihood is denoted as "lowP" in this paper The optical depth inferred from the lowP likelihood combined with the *Planck TT* likelihood is typically $\tau \approx 0.07$, and is about 1σ lower than the typical values of $\tau \approx 0.09$ inferred from the WMAP polarization likelihood (see Sect. 3.4) used in the 2013 papers. As discussed in Sect. 3.4 (and in more detail in Planck Collaboration XI 2016) the LFI 70-GHz and WMAP polarization maps are consistent when both are cleaned with the HFI 353-GHz polarization maps[7].

(3) In the 2013 papers, the *Planck* temperature likelihood was a hybrid: over the multipole range $\ell =2-49$, the likelihood was based on the `Commander` algorithm applied to 87% of the sky computed using a Blackwell-Rao estimator for the likelihood at higher multipoles ($\ell =50$–2500) was constructed from cross-spectra over the frequency range 100−217 GHz using the `CamSpec` software (Planck Collaboration XV 2014), which is based on the methodology developed in Efstathiou (2004, 2006). At each of the *Planck* HFI frequencies, the sky is observed by a number of detectors. For example, at 217 GHz the sky is observed by four unpolarized spider-web bolometers (SWBs) and eight polarization sensitive bolometers (PSBs). The TOD from the 12 bolometers can be combined to produce a single map at 217 GHz for any given period of time. Thus, we can produce 217-GHz maps for individual sky surveys (denoted S1, S2, S3, etc.), or by year (Y1, Y2), or split by half-mission (HM1, HM2). We can also produce a temperature map from each SWB and a temperature and polarization map from quadruplets of PSBs. For example, at 217 GHz we produce four temperature and two temperature+polarization maps. We refer to these maps as detectors-set maps (or "DetSets" for short); note that the DetSet maps can also be produced for any arbitrary time period. The high multipole likelihood used in the 2013 papers was computed by cross-correlating HFI DetSet maps for the "nominal" *Planck* mission extending over 15.5 months[8]. For the 2015 papers we use the full-mission *Planck* data, extending over 29 months for the HFI and 48 months for the LFI. In the *Planck* 2015 analysis, we have produced cross-year and cross-half-mission likelihoods in addition to a DetSet likelihood. The baseline 2015 *Planck* temperature-polarization likelihood is also a hybrid, matching the high-multipole likelihood at $\ell = 30$ to the *Planck* pixel-based likelihood at lower multipoles.

(4) The sky coverage used in the 2013 `CamSpec` likelihood was intentionally conservative, retaining effectively 49% of the

---

[7] Throughout this paper, we adopt the following labels for likelihoods: (i) *Planck* TT denotes the combination of the TT likelihood at multipoles $\ell \geq 30$ and a low-ℓ temperature-only likelihood based on the CMB map recovered with `Commander`; (ii) *Planck* TT+lowP further includes the *Planck* polarization data in the low-ℓ likelihood, as described in the main text; (iii) labels such as *Planck* TE+lowP denote the TE likelihood at $\ell \geq 30$ plus the polarization-only component of the map-based low-ℓ

Planck likelihood; and (iv) *Planck* TT,TE,EE+lowP denotes the combination of the likelihood at $\ell \geq 30$ using TT, TE, and EE spectra and the low-ℓ temperature+polarization likelihood. We make occasional use of combinations of the polarization likelihoods at $\ell \geq 30$ and the temperature+polarization data at low-ℓ, which we denote with labels such as *Planck* TE+lowT,P.

[8] Although we analysed a *Planck* full-mission temperature likelihood extensively, prior to the release of the 2013 papers.

sky at 100 GHz and 31% of the sky at 143 and 217 GHz[9]. This was done to ensure that on the first exposure of *Planck* cosmological results to the community, corrections for Galactic dust emission were demonstrably small and had negligible impact on cosmological parameters. In the 2015 analysis we make more aggressive use of the sky at each of these frequencies. We have also tuned the point-source masks to each frequency, rather than using a single point-source mask constructed from the union of the point source catalogues at 100, 143, 217, and 353 GHz. This results in many fewer point source holes in the 2015 analysis compared to the 2013 analysis.

(5) Most of the results in this paper are derived from a revised `Plik` likelihood, based on cross-half-mission spectra. The `Plik` likelihood has been modified since 2013 so that it is now similar to the `CamSpec` likelihood used in PCP13. Both likelihoods use similar approximations to compute the covariance matrices. The main difference is in the treatment of Galactic dust corrections in the analysis of the polarization spectra. The two likelihoods have been written independently and give similar (but not identical) results, as discussed further below. The `Plik` likelihood is discussed in Planck Collaboration XI (2016). The `CamSpec` likelihood is discussed in a separate paper (Efstathiou et al., in prep.).

(6) We have made minor changes to the foreground modelling and to the priors on some of the foreground parameters, as discussed in Sect. 2.3 and Planck Collaboration XI (2016).

Given these changes to data processing, mission length, sky coverage, etc., it is reasonable to ask whether the base ΛCDM parameters have changed significantly compared to the 2013 numbers. In fact, the parameter shifts are relatively small. The situation is summarized in Table 1. The second column of this table lists the *Planck*+WP parameters, as given in table 5 of PCP13. Since these numbers are based on the 2013 processing of the nominal mission and computed via a DetSet `CamSpec` likelihood, the column is labelled 2013N(DS). We now make a number of specific remarks about these comparisons.

(1) 4-K cooler line systematics. After the submission of PCP13 we found strong evidence that a residual in the 217×217 DetSet spectrum at $\ell \approx 1800$ was a systematic caused by electromagnetic interference between the Joule-Thomson 4-K cooler electronics and the bolometer readout electronics. This interference leads to a set of time-variable narrow lines in the power spectrum of the TOD. The data processing pipelines apply a filter to remove these lines; however, the filtering failed to reduce their impact on the power spectra to negligible levels. Incomplete removal of the 4-K cooler lines affects primarily the 217×217 PSB×PSB cross-spectrum in Survey 1. The presence of this systematic was reported in the revised versions of 2013 *Planck* papers. Using simulations and also comparison with the 2013 full-mission likelihood (in which the 217×217 power spectrum "dip" is strongly diluted by the additional sky surveys) we assessed that the 4-K line systematic was causing shifts in cosmological parameters of less than 0.5σ[10]. Column 3 in Table 1 lists the DetSet parameters for the full-mission 2013 data. This full-mission

likelihood uses more extensive sky coverage than the nominal mission likelihood (effectively 39% of sky at 217 GHz, 55% of sky at 143 GHz, and 63% of sky at 100 GHz); otherwise the methodology and foreground model are identical to the `CamSpec` likelihood described in PPL13. The parameter shifts are relatively small and consistent with the improvement in signal-to-noise of the full-mission spectra and the systematic shifts caused by the 217×217 dip in the nominal mission (for example, raising H_0 and n_s, as discussed in appendix C4 of PCP13).

(2) DetSets versus cross-surveys. In a reanalysis of the publicly released *Planck* maps, Spergel et al. (2015) constructed cross-survey (S1 × S2) likelihoods and found cosmological parameters for the base ΛCDM model that were close to (within approximately 1σ) the nominal mission parameters listed in Table 1. The Spergel et al. (2015) analysis differs substantially in sky coverage and foreground modelling compared to the 2013 *Planck* analysis and so it is encouraging that they find no major differences with the results presented by the *Planck* collaboration. On the other hand, they did not identify the reasons for the roughly 1σ parameter shifts. They argue that foreground modelling and the $\ell = 1800$ dip in the 217×217 DetSet spectrum can contribute towards some of the differences but cannot produce 1σ shifts, in agreement with the conclusions of PCP13. The 2013F(DS) likelihood disfavours the Spergel et al. (2015) cosmology (with parameters listed in their Table 3) by $\Delta\chi^2 = 11$, i.e., by about 2σ, and almost all of the $\Delta\chi^2$ is contributed by the multipole range 1000–1500, so the parameter shifts are not driven by cotemporal systematics resulting in correlated noise biases at high multipoles. However, as discussed in PPL13 and Planck Collaboration XI (2016), low-level correlated noise in the DetSet spectra affects *all* HFI channels at high multipoles where the spectra are noise dominated. The impact of this correlated noise on cosmological parameters is relatively small. This is illustrated by Col. 4 of Table 1 (labelled "2013F(CY)"), which lists the parameters of a 2013 `CamSpec` cross-year likelihood using the same sky coverage and foreground model as the DetSet likelihood used for Col. 3. The parameters from these two likelihoods are in good agreement (better than 0.2σ), illustrating that cotemporal systematics in the DetSets are at sufficiently low levels that there is very little effect on cosmological parameters. Nevertheless, in the 2015 likelihood analysis we apply corrections for correlated noise to the DetSet cross-spectra, as discussed in Planck Collaboration XI (2016), and typically find agreement in cosmological parameters between DetSet, cross-year, and cross-half-mission likelihoods to better than 0.5σ accuracy for a fixed likelihood code (and to better than 0.2σ accuracy for base ΛCDM).

(3) 2015 versus 2013 processing. Column 5 (labelled "2015F(CHM)") lists the parameters computed from the `CamSpec` cross-half-mission likelihood using the HFI 2015 data with revised absolute calibration and beam-transfer functions. We also replace the WP likelihood of the 2013 analysis with the *Planck* lowP likelihood. The 2015F(CHM) likelihood uses slightly more sky coverage (60%) at 217 GHz, compared to the 2013F(CY) likelihood and also uses revised point source masks. Despite these changes, the base ΛCDM parameters derived from the 2015 `CamSpec` likelihood are within $\approx 0.4\sigma$ of the 2013F(CY)

---

[9] These quantities are explicitly the apodized effective $f_{\mathrm{sky}}^{\mathrm{eff}}$, calculated as the average of the square of the apodized mask values (see Eq. (10)).

[10] The revised version of PCP13 also reported an error in the ordering of the beam-transfer functions applied to some of the 2013 217×217 DetSet cross-spectra, leading to an offset of a few $(\mu K)^2$ in the coadded 217×217 spectrum. As discussed in PCP13, this offset is largely ab-

sorbed by the foreground model and has negligible impact on the 2013 cosmological parameters.
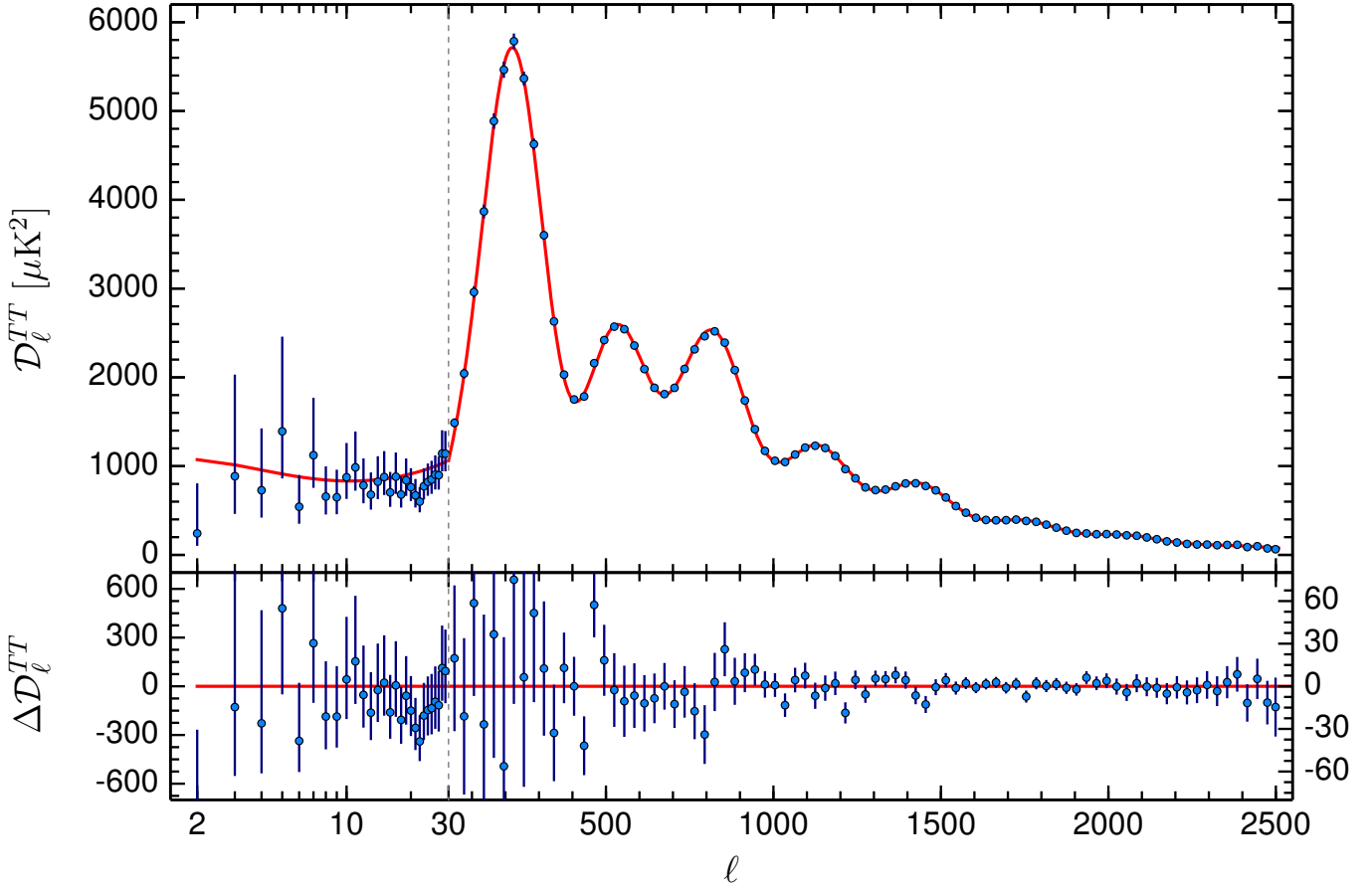
Fig. 1. *Planck* 2015 temperature power spectrum. At multipoles $\ell \geq 30$ we show the maximum likelihood frequency-averaged temperature spectrum computed from the `Plik` cross-half-mission likelihood, with foreground and other nuisance parameters determined from the MCMC analysis of the base ΛCDM cosmology. In the multipole range $2 \leq \ell \leq 29$, we plot the power spectrum estimates from the `Commander` component-separation algorithm, computed over 94% of the sky. The best-fit base ΛCDM theoretical spectrum fitted to the *Planck* TT+lowP likelihood is plotted in the *upper panel*. Residuals with respect to this model are shown in the *lower panel*. The error bars show $\pm 1\sigma$ uncertainties.

parameters, with the exception of θ_{MC}, which is lower by 0.67σ, τ, which is lower by 1σ, and $A_s e^{-2\tau}$, which is higher by about 4σ. The change in τ simply reflects the preference for a lower value of τ from the *Planck* LFI polarization data compared to the WMAP polarization likelihood in the form delivered by the WMAP team (see Sect. 3.4 for further discussion). The large upward shift in $A_s e^{-2\tau}$ reflects the change in the absolute calibration of the HFI. As noted in Sect. 2.3, the 2013 analysis did not propagate an error on the *Planck* absolute calibration through to cosmological parameters. Coincidentally, the changes to the absolute calibration compensate for the downward change in τ and variations in the other cosmological parameters to keep the parameter σ_8 largely unchanged from the 2013 value. This will be important when we come to discuss possible tensions between the amplitude of the matter fluctuations at low redshift estimated from various astrophysical data sets and the *Planck* CMB values for the base ΛCDM cosmology (see Sect. 5.6).

(4) Likelihoods. Constructing a high-multipole likelihood for *Planck*, particularly with TE and EE spectra, is complicated and difficult to check at the sub-σ level against numerical simulations because the simulations cannot model the foregrounds, noise properties, and low-level data processing of the real *Planck* data to sufficiently high accuracy. Within the *Planck* collaboration, we have tested the sensitivity of the

results to the likelihood methodology by developing several independent analysis pipelines. Some of these are described in Planck Collaboration XI (2016). The most highly developed of them are the `CamSpec` and revised `Plik` pipelines. For the 2015 *Planck* papers, the `Plik` pipeline was chosen as the baseline. Column 6 of Table 1 lists the cosmological parameters for base ΛCDM determined from the `Plik` cross-half-mission likelihood, together with the lowP likelihood, applied to the 2015 full-mission data. The sky coverage used in this likelihood is identical to that used for the `CamSpec` 2015F(CHM) likelihood. However, the two likelihoods differ in the modelling of instrumental noise, Galactic dust, treatment of relative calibrations, and multipole limits applied to each spectrum.

As summarized in Col. 8 of Table 1, the `Plik` and `CamSpec` parameters agree to within 0.2σ, except for n_s, which differs by nearly 0.5σ. The difference in n_s is perhaps not surprising, since this parameter is sensitive to small differences in the foreground modelling. Differences in n_s between `Plik` and `CamSpec` are systematic and persist throughout the grid of extended ΛCDM models discussed in Sect. 6. We emphasize that the `CamSpec` and `Plik` likelihoods have been written independently, though they are based on the same theoretical framework. None of the conclusions in this paper (including those based on the full "TT, TE, EE" likelihoods) would differ in any substantive way had we chosen to use the `CamSpec` likelihood in place of `Plik`.

The overall shifts of parameters between the `Plik` 2015 likelihood and the published 2013 nominal mission parameters are summarized in Col. 7 of Table 1. These shifts are within 0.7σ except for the parameters τ and $A_s e^{-2\tau}$, which are sensitive to the low-multipole polarization likelihood and absolute calibration.

In summary, the *Planck* 2013 cosmological parameters were pulled slightly towards lower H_0 and n_s by the $\ell \approx 1800$ 4-K line systematic in the 217×217 cross-spectrum, but the net effect of this systematic is relatively small, leading to shifts of 0.5σ or less in cosmological parameters. Changes to the low-level data processing, beams, sky coverage, etc., as well as the likelihood code also produce shifts of typically 0.5σ or less. The combined effect of these changes is to introduce parameter shifts relative to PCP13 of less than 0.7σ, with the exception of τ and $A_s e^{-2\tau}$. *The main scientific conclusions of PCP13 are therefore consistent with the 2015 Planck analysis.*

Parameters for the base ΛCDM cosmology derived from full-mission DetSet, cross-year, or cross-half-mission spectra are in extremely good agreement, demonstrating that residual (i.e., uncorrected) cotemporal systematics are at low levels. This is also true for the extensions of the ΛCDM model discussed in Sect. 6. It is therefore worth explaining why we have adopted the cross-half-mission likelihood as the baseline for this and other 2015 *Planck* papers. The cross-half-mission likelihood has lower signal-to-noise than the full-mission DetSet likelihood; however, the errors on the cosmological parameters from the two likelihoods are almost identical, as can be seen from the entries in Table 1. This is also true for extended ΛCDM models. However, for more complicated tests, such as searches for localized features in the power spectra (Planck Collaboration XX 2016), residual 4-K line systematic effects and residual uncorrected correlated noise at high multipoles in the DetSet likelihood can produce results suggestive of new physics (though not at a high significance level). We have therefore decided to adopt the cross-half-mission likelihood as the baseline for the 2015 analysis, sacrificing some signal-to-noise in favour of reduced systematics. For almost all of the models considered in this paper, the *Planck* results are limited by small systematics of various types, including systematic errors in modelling foregrounds, rather than by signal-to-noise.

The foreground-subtracted, frequency-averaged, cross-half-mission spectrum is plotted in Fig. 1, together with the `Commander` power spectrum at multipoles $\ell \leq 29$. The high multipole spectrum plotted in this figure is an approximate maximum likelihood solution based on equations (A24) and (A25) of PPL13, with the foregrounds and nuisance parameters for each spectrum fixed to the best-fit values of the base ΛCDM solution. Note that a different way of solving for the *Planck* CMB spectrum, by marginalizing over foreground and nuisance parameters, is presented in Sect. 4. The best-fit base ΛCDM model is plotted in the upper panel, while residuals with respect to this model are plotted in the lower panel. In this plot, there are only four bandpowers at $\ell \geq 30$ that differ from the best-fit model by more than 2σ. These are: $\ell = 434$ (-2.0σ); $\ell = 465$ (2.5σ); $\ell = 1214$ (-2.5σ); and $\ell = 1455$ (-2.1σ). The χ^2 of the coadded TT spectrum plotted in Fig. 1 relative to the best-fit base ΛCDM model is 2547 for 2479 degrees of freedom ($30 \leq \ell \leq 2500$), which is a 0.96σ fluctuation (PTE = 16.8%). These numbers confirm the extremely good fit of the base ΛCDM cosmology to the *Planck TT* data at high multipoles. The consistency of the *Planck* polarization spectra with base ΛCDM is discussed in Sect. 3.3.

PCP13 noted some mild internal tensions within the *Planck* data, for example, the preference of the phenomenological lensing parameter A_L (see Sect. 5.1) towards values greater than unity and a preference for a negative running of the scalar spectral index (see Sect. 6.2.2). These tensions were partly caused by the poor fit of base ΛCDM model to the temperature spectrum at multipoles below about 50. As noted by the WMAP team (Hinshaw et al. 2003), the temperature spectrum has a low quadrupole amplitude and a glitch in the multipole range $20 \lesssim \ell \lesssim 30$. These features can be seen in the *Planck* 2015 spectrum of Fig. 1. They have a similar (though slightly reduced) effect on cosmological parameters to those described in PCP13.

3.2. 545-GHz-cleaned spectra

As discussed in PCP13, unresolved extragalactic foregrounds (principally Poisson point sources and the clustered component of the CIB) contribute to the *Planck TT* spectra at high multipoles. The approach to modelling these foreground contributions in PCP13 is similar to that used by the ACT and SPT teams (Reichardt et al. 2012; Dunkley et al. 2013) in that the foregrounds are modelled by a set of physically motivated power spectrum template shapes with an associated set of adjustable nuisance parameters. This approach has been adopted as the baseline for the *Planck* 2015 analysis. The foreground model has been adjusted for this new analysis, in relatively minor ways, as summarized in Sect. 2.3 and described in further detail in Planck Collaboration XII (2016). Galactic dust emission also contributes to the temperature and polarization power spectra and must be subtracted from the spectra used to form the *Planck* likelihood. Unlike the extragalactic foregrounds, Galactic dust emission is anisotropic and so its impact can be reduced by appropriate masking of the sky. In PCP13, we intentionally adopted conservative masks, tuned for each of the frequencies used to form the likelihood, to keep dust emission at low levels. The results in PCP13 were therefore insensitive to the modelling of residual dust contamination.

In the 2015 analysis, we have extended the sky coverage at each of 100, 143, and 217 GHz, and so in addition to testing the accuracy of the extragalactic foreground model, it is important to test the accuracy of the Galactic dust model. As described in PPL13 and Planck Collaboration XII (2016) the Galactic dust templates used in the `CamSpec` and `Plik` likelihoods are derived by fitting the 545-GHz mask-differenced power spectra. Mask differencing isolates the anisotropic contribution of Galactic dust from the isotropic extragalactic components. For the extended sky coverage used in the 2015 likelihoods, the Galactic dust contributions are a significant fraction of the extragalactic foreground contribution in the 217×217 temperature spectrum at high multipoles, as illustrated in Fig. 2. Galactic dust dominates over all other foregrounds at multipoles $\ell \lesssim 500$ at HFI frequencies.

A simple and direct test of the parametric foreground modelling used in the `CamSpec` and `Plik` likelihoods is to compare results with a completely different approach in which the low-frequency maps are "cleaned" using higher frequency maps as foreground templates (see, e.g., Lueker et al. 2010). In a similar approach to Spergel et al. (2015), we can form cleaned maps at lower frequencies ν by subtracting a 545-GHz map as a template,

$$M^{T_\nu,\text{clean}} = (1 + \alpha^{T_\nu})M^{T_\nu} - \alpha^{T_\nu}M^{T_{\nu_t}}, \qquad (6)$$

where ν_t is the frequency of the template map $M^{T_{\nu_t}}$ and α^{T_ν} is the cleaning coefficient. Since the maps have different beams,
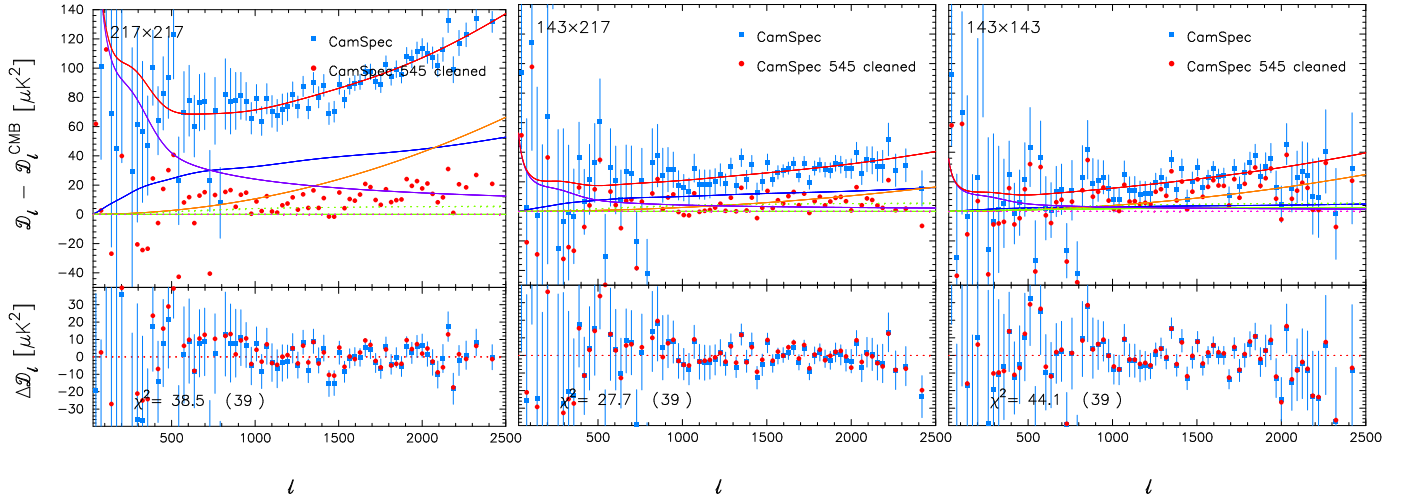
Fig. 2. Residual plots illustrating the accuracy of the foreground modelling. The blue points in the *upper panels* show the `CamSpec` 2015(CHM) spectra after subtraction of the best-fit ΛCDM spectrum. The residuals in the *upper panel* should be accurately described by the foreground model. Major foreground components are shown by the solid lines, colour coded as follows: total foreground spectrum (red); Poisson point sources (orange); clustered CIB (blue); thermal SZ (green); and Galactic dust (purple). Minor foreground components are shown by the dotted lines, colour-coded as follows: kinetic SZ (green); and tSZ×CIB cross-correlation (purple). The red points in the *upper panels* show the 545-GHz-cleaned spectra (minus the best-fit CMB as subtracted from the uncleaned spectra) that are fitted to a power-law residual foreground model, as discussed in the text. The *lower panels* show the spectra after subtraction of the best-fit foreground models. These agree to within a few $(\mu K)^2$. The χ^2 values of the residuals of the blue points, and the number of bandpowers, are listed in the *lower panels*.

the subtraction is actually done in the power spectrum domain:

$$
\begin{aligned}
\hat{C}^{T_{\nu_1} T_{\nu_2} \mathrm{clean}} = &\; (1 + \alpha^{T_{\nu_1}})(1 + \alpha^{T_{\nu_2}}) \hat{C}^{T_{\nu_1} T_{\nu_2}} \\
&- (1 + \alpha^{T_{\nu_1}}) \alpha^{T_{\nu_2}} \hat{C}^{T_{\nu_2} T_t} \\
&- (1 + \alpha^{T_{\nu_2}}) \alpha^{T_{\nu_1}} \hat{C}^{T_{\nu_1} T_t} + \alpha^{T_{\nu_1}} \alpha^{T_{\nu_2}} \hat{C}^{T_t T_t},
\end{aligned}
\tag{7}
$$

where $\hat{C}^{T_{\nu_1} T_{\nu_2}}$ etc. are the mask-deconvolved beam-corrected power spectra. The coefficients $\alpha^{T_{\nu_i}}$ are determined by minimizing

$$
\sum_{\ell=\ell_{\min}}^{\ell_{\max}} \sum_{\ell'=\ell_{\min}}^{\ell_{\max}} \hat{C}_{\ell}^{T_{\nu_i} T_{\nu_i} \mathrm{clean}} \left(\hat{\mathsf{M}}_{\ell \ell'}^{T_{\nu_i} T_{\nu_i}} \right)^{-1} \hat{C}_{\ell'}^{T_{\nu_i} T_{\nu_i} \mathrm{clean}},
\tag{8}
$$

where $\hat{\mathsf{M}}^{T_{\nu_i} T_{\nu_i}}$ is the covariance matrix of the estimates $\hat{C}^{T_{\nu_i} T_{\nu_i}}$. We choose $\ell_{\min} = 100$ and $\ell_{\max} = 500$ and compute the spectra in Eq. (7) by cross-correlating half-mission maps on the 60% mask used to compute the 217×217 spectrum. The resulting cleaning coefficients are $\alpha_{143}^T = 0.00194$ and $\alpha_{217}^T = 0.00765$; note that all of the input maps are in units of thermodynamic temperature. The cleaning coefficients are therefore optimized to remove Galactic dust at low multipoles, though by using 545 GHz as a dust template we find that the cleaning coefficients are almost constant over the multipole range 50–2500. We note, however, that this is not true if the 353- and 857-GHz maps are used as dust templates, as discussed in Efstathiou et al. (in prep.).

The 545-GHz-cleaned spectra are shown by the red points in Fig. 2 and can be compared directly to the "uncleaned" spectra used in the `CamSpec` likelihood (upper panels). As can be seen, Galactic dust emission is removed to high accuracy and the residual foreground contribution at high multipoles is strongly suppressed in the 217×217 and 143×217 spectra. Nevertheless, there remains small foreground contributions at high multipoles, which we model heuristically as power laws,

$$
\hat{\mathcal{D}}_{\ell} = A \left(\frac{\ell}{1500} \right)^{\epsilon},
\tag{9}
$$

with free amplitudes A and spectral indices ϵ. We construct another `CamSpec` cross-half-mission likelihood using exactly the same sky masks as the 2015F(CHM) likelihood, but using 545-GHz-cleaned 217×217, 143×217, and 143×143 spectra. We then use the simple model of Eq. (9) in the likelihood to remove residual unresolved foregrounds at high multipoles for each frequency combination. We do not clean the 100×100 spectrum and so for this spectrum we use the standard parametric foreground model in the likelihood. The lower panels in Fig. 2 show the residuals with respect to the best-fit base ΛCDM model and foreground solution for the uncleaned `CamSpec` spectra (blue points) and for the 545-GHz-cleaned spectra (red points). These residuals are almost identical, despite the very different approaches to Galactic dust removal and foreground modelling. The cosmological parameters from these two likelihoods are also in very good agreement, typically to better than 0.1σ, with the exception of n_s, which is lower in the cleaned likelihood by 0.26σ. It is not surprising, given the heuristic nature of the model (Eq. (9)), that n_s shows the largest shift. We can also remove the 100×100 spectrum from the likelihood entirely, with very little impact on cosmological parameters.

Further tests of map-based cleaning are presented in Planck Collaboration XI (2016), which additionally describes another independently written power-spectrum analysis pipeline (`MSPEC`) tuned to map-cleaned cross-spectrum analysis and using a more complex model for fitting residual foregrounds than the heuristic model of Eq. (9). Planck Collaboration XI (2016) also describes power spectrum analysis and cosmological parameters derived from component-separated *Planck* maps. However, the simple demonstration presented in this section shows that the details of modelling residual dust contamination and other foregrounds are under control in the 2015 *Planck* likelihood. A further strong argument that our TT results are insensitive to foreground modelling is presented in the next section, which compares the cosmological parameters derived from the TT, TE, and EE likelihoods. Unresolved foregrounds at high multipoles are completely negligible in the polarization spectra

and so the consistency of the parameters, particularly from the *TE* spectrum (which has higher signal-to-noise than the *EE* spectrum) provides an additional cross-check of the *TT* results.

Finally, one can ask why we have not chosen to use a 545-GHz-cleaned likelihood as the baseline for the 2015 *Planck* parameter analysis. Firstly, it would not make any difference to the results of this paper had we chosen to do so. Secondly, we feel that the parametric foreground model used in the baseline likelihood has a sounder physical basis. This allows us to link the amplitudes of the unresolved foregrounds across the various *Planck* frequencies with the results from other ways of studying foregrounds, including the higher resolution CMB experiments described in Sect. 4.

3.3. The 2015 Planck temperature and polarization spectra and likelihood

The coadded 2015 *Planck* temperature spectrum was introduced in Fig. 1. In this section, we present additional details and consistency checks of the temperature likelihood and describe the full mission *Planck TE* and *EE* spectra and likelihood; preliminary *Planck TE* and *EE* spectra were presented in PCP13. We then discuss the consistency of the cosmological parameters for base ΛCDM measured separately from the *TT*, *TE*, and *EE* spectra. For the most part, the discussion given in this section is specific to the Plik likelihood, which is used as the baseline in this paper. A more complete discussion of the Plik and other likelihoods developed by the *Planck* team is given in Planck Collaboration XI (2016).

3.3.1. Temperature spectra and likelihood

(1) Temperature masks. As in the 2013 analysis, the high-multipole *TT* likelihood uses the 100×100 , 143×143, 217×217, and 143×217 spectra. However, in contrast to the 2013 analysis, which used conservative sky masks to reduce the effects of Galactic dust emission, we make more aggressive use of sky in the 2015 analysis. The 2015 analysis retains 80%, 70%, and 60% of sky at 100 GHz, 143 GHz, and 217 GHz, respectively, before apodization. We also apply apodized point source masks to remove compact sources with a signal-to-noise threshold >5 at each frequency (see Planck Collaboration XXVI 2016 for a description of the *Planck* Catalogue of Compact Sources). Apodized masks are also applied to remove extended objects, and regions of high CO emission were masked at 100 GHz and 217 GHz (see Planck Collaboration X 2016). As an estimate of the effective sky area, we compute the following sum over pixels:

$$f_{\text{sky}}^{\text{eff}} = \frac{1}{4\pi} \sum w_i^2 \Omega_i, \tag{10}$$

where w_i is the weight of the apodized mask and Ω_i is the area of pixel i. All input maps are at HEALpix (Górski et al. 2005) resolution N_{side} = 2048. Equation (10) gives $f_{\text{sky}}^{\text{eff}}$ = 66.3% at 100 GHz, 57.4% at 143 GHz, and 47.1% at 217 GHz.

(2) Galactic dust templates. With the increased sky coverage used in the 2015 analysis, we take a slightly different approach to subtracting Galactic dust emission to that described in PPL13 and PCP13. The shape of the Galactic dust template is determined from mask-differenced power spectra estimated from the 545-GHz maps. The mask differencing removes the isotropic contribution from the CIB and point sources. The resulting dust template has a similar shape to

the template used in the 2013 analysis, with power-law behaviour $\mathcal{D}_\ell^{\text{dust}} \propto \ell^{-0.63}$ at high multipoles, but with a "bump" at $\ell \approx 200$ (as shown in Fig. 2). The absolute amplitude of the dust templates at 100, 143, and 217 GHz is determined by cross-correlating the temperature maps at these frequencies with the 545-GHz maps (with minor corrections for the CIB and point source contributions). This allows us to generate priors on the dust template amplitudes, which are treated as additional nuisance parameters when running MCMC chains (unlike the 2013 analysis, in which we fixed the amplitudes of the dust templates). The actual priors used in the Plik likelihood are Gaussians on $\mathcal{D}_{\ell=200}^{\text{dust}}$ with the following means and dispersions: $(7 \pm 2) \mu K^2$ for the 100×100 spectrum; $(9 \pm 2) \mu K^2$ for 143×143; $(21 \pm 8.5) \mu K^2$ for 143×217; and $(80 \pm 20) \mu K^2$ for 217×217. The MCMC solutions show small movements of the best-fit dust template amplitudes, but always within statistically acceptable ranges given the priors.

(3) Likelihood approximation and covariance matrices. The approximation to the likelihood function follows the methodology described in PPL13 and is based on a Gaussian likelihood assuming a fiducial theoretical power spectrum (a fit to Plik TT with prior τ = 0.07 ± 0.02). We have also included a number of small refinements to the covariance matrices. Foregrounds, including Galactic dust, are added to the fiducial theoretical power spectrum, so that the additional small variance associated with foregrounds is included, along with cosmic variance of the CMB, under the assumption that the foregrounds are Gaussian random fields. The 2013 analysis did not include corrections to the covariance matrices arising from leakage of low-multipole power to high multipoles via the point source holes; these can introduce errors in the covariance matrices of a few percent at $\ell \approx 300$, corresponding approximately to the first peak of the CMB spectrum. In the 2015 analysis we apply corrections to the fiducial theoretical power spectrum, based on Monte Carlo simulations, to correct for this effect. We also apply Monte Carlo based corrections to the analytic covariance matrices at multipoles $\ell \leq 50$, where the analytic approximations begin to become inaccurate even for large effective sky areas (see Efstathiou 2004). Finally, we add the uncertainties on the beam shapes to the covariance matrix following the methodology described in PPL13. The *Planck* beams are much more accurately characterized in the 2015 analysis, and so the beam corrections to the covariance matrices are extremely small. The refinements to the covariance matrices described in this paragraph are all relatively minor and have little impact on cosmological parameters.

(4) Binning. The baseline Plik likelihood uses binned temperature and polarization spectra. This is done because all frequency combinations of the *TE* and *EE* spectra are used in the Plik likelihood, leading to a large data vector of length 22 865 if the spectra are retained multipole-by-multipole. The baseline Plik likelihood reduces the size of the data vector by binning these spectra. The spectra are binned into bins of width $\Delta\ell = 5$ for $30 \leq \ell \leq 99$, $\Delta\ell = 9$ for $100 \leq \ell \leq 1503$, $\Delta\ell = 17$ for $1504 \leq \ell \leq 2013$ and $\Delta\ell = 33$ for $2014 \leq \ell \leq 2508$, with a weighting of C_ℓ proportional to $\ell(\ell + 1)$ over the bin widths. The bins span an odd number of multipoles, since for approximately azimuthal masks we expect a nearly symmetrical correlation function around the central multipole. The binning does not affect the determination of cosmological parameters in ΛCDM-type models (which have smooth power spectra), but significantly reduces

Table 2. Goodness-of-fit tests for the 2015 *Planck* temperature and polarization spectra.

Likelihood	Frequency	Multipole range	χ^2	$\chi^2/N_{\rm d.o.f.}$	$N_{\rm d.o.f.}$	$\Delta\chi^2/\sqrt{2N_{\rm d.o.f.}}$	PTE [%]
TT	100×100	30–1197	1234.37	1.06	1168	1.37	8.66
	143×143	30–1996	2034.45	1.03	1967	1.08	14.14
	143×217	30–2508	2566.74	1.04	2479	1.25	10.73
	217×217	30–2508	2549.66	1.03	2479	1.00	15.78
	Combined	30–2508	2546.67	1.03	2479	0.96	16.81
TE	100×100	30–999	1088.78	1.12	970	2.70	0.45
	100×143	30–999	1032.84	1.06	970	1.43	7.90
	100×217	505–999	526.56	1.06	495	1.00	15.78
	143×143	30–1996	2028.43	1.03	1967	0.98	16.35
	143×217	505–1996	1606.25	1.08	1492	2.09	2.01
	217×217	505–1996	1431.52	0.96	1492	−1.11	86.66
	Combined	30–1996	2046.11	1.04	1967	1.26	10.47
EE	100×100	30–999	1027.89	1.06	970	1.31	9.61
	100×143	30–999	1048.22	1.08	970	1.78	4.05
	100×217	505–999	479.72	0.97	495	−0.49	68.06
	143×143	30–1996	2000.90	1.02	1967	0.54	29.18
	143×217	505–1996	1431.16	0.96	1492	−1.11	86.80
	217×217	505–1996	1409.58	0.94	1492	−1.51	93.64
	Combined	30–1996	1986.95	1.01	1967	0.32	37.16

Notes. $\Delta\chi^2 = \chi^2 - N_{\rm d.o.f.}$ is the difference from the mean assuming that the best-fit base ΛCDM model (fitted to *Planck* TT+lowP) is correct and $N_{\rm d.o.f.}$ is the number of degrees of freedom (set equal to the number of multipoles). The sixth column expresses $\Delta\chi^2$ in units of the expected dispersion, $\sqrt{2N_{\rm d.o.f.}}$, and the last column lists the probability to exceed (PTE) the tabulated value of χ^2.

the size of the joint *TT*, *TE*, *EE* covariance matrix, speeding up the computation of the likelihood. However, for some specific purposes, e.g., searching for oscillatory features in the *TT* spectrum, or testing χ^2 statistics, we produce blocks of the likelihood multipole-by-multipole.

(5) Goodness of fit. The first five rows of Table 2 list χ^2 statistics for the *TT* spectra (multipole-by-multipole) relative to the *Planck* best-fit base ΛCDM model and foreground parameters (fitted to *Planck* TT+lowP). The first four entries list the statistics separately for each of the four spectra that form the *TT* likelihood and the fifth line (labelled "Combined") gives the χ^2 value for the maximum likelihood *TT* spectrum plotted in Fig. 1. Each of the individual spectra provides an acceptable fit to the base ΛCDM model, as does the frequency-averaged spectrum plotted in Fig. 1. This demonstrates the excellent consistency of the base ΛCDM model across frequencies. More detailed consistency checks of the *Planck* spectra are presented in Planck Collaboration XI (2016); however, as indicated by Table 2, we find no evidence for any inconsistencies between the foreground-corrected temperature power spectra computed for different frequency combinations. The temperature spectra are largely signal dominated over the multipole ranges listed in Table 2 and so the χ^2 values are insensitive to small errors in the *Planck* noise model used in the covariance matrices. As discussed in the next subsection, this is not true for the *TE* and *EE* spectra, which are noise dominated over much of the multipole range.

3.3.2. Polarization spectra and likelihood

In addition to the *TT* spectra, the 2015 *Planck* likelihood includes the *TE* and *EE* spectra. As discussed in Sect. 3.1, the *Planck* 2015 low-multipole polarization analysis is based on the LFI 70-GHz data. Here we discuss the *TE* and *EE* spectra that are used in the high-multipole likelihood, which are computed from the HFI data at 100, 143 and 217 GHz. As summarized in Planck Collaboration XI (2016), there is no evidence for any unresolved foreground components at high multipoles in the polarization spectra. We therefore include all frequency combinations in computing the *TE* and *EE* spectra to maximize the signal-to-noise[11].

(1) Masks and dust corrections. At low multipoles ($\ell \lesssim 300$) polarized Galactic dust emission is significant at all frequencies and is subtracted in a similar way to the dust subtraction in temperature, i.e., by including additional nuisance parameters quantifying the amplitudes of a power-law dust template with a slope constrained to $\mathcal{D}_\ell^{\rm dust} \propto \ell^{-0.40}$ for both *TE* and *EE* (Planck Collaboration Int. XXX 2016). Polarized synchrotron emission (which has been shown to be negligible at 100 GHz and higher frequencies for *Planck* noise levels, Fuskeland et al. 2014) is ignored. Gaussian priors on the polarization dust amplitudes are determined by cross-correlating the lower frequency maps with the 353-GHz polarization maps (the highest frequency polarized channel of the HFI) in a similar way to the determination of temperature dust priors. We use the temperature-based apodized masks in Q and U at each frequency, retaining 70%, 50%, and 41% of the sky at 100, 143, and 217 GHz, respectively, after apodization (slightly smaller than the temperature masks at 143 and 217 GHz). However, we do not apply point source or CO masks to the Q and U maps. The construction of the full *TT*, *TE*, *EE* likelihood is then a straightforward extension of the *TT* likelihood using the analytic covariance matrices given by Efstathiou (2006) and Hamimeche & Lewis (2008).

---

[11] In temperature, the 100×143 and 100×217 spectra are not included in the likelihood because the temperature spectra are largely signal dominated. These spectra therefore add little new information on the CMB, but would require additional nuisance parameters to correct for unresolved foregrounds at high multipoles.
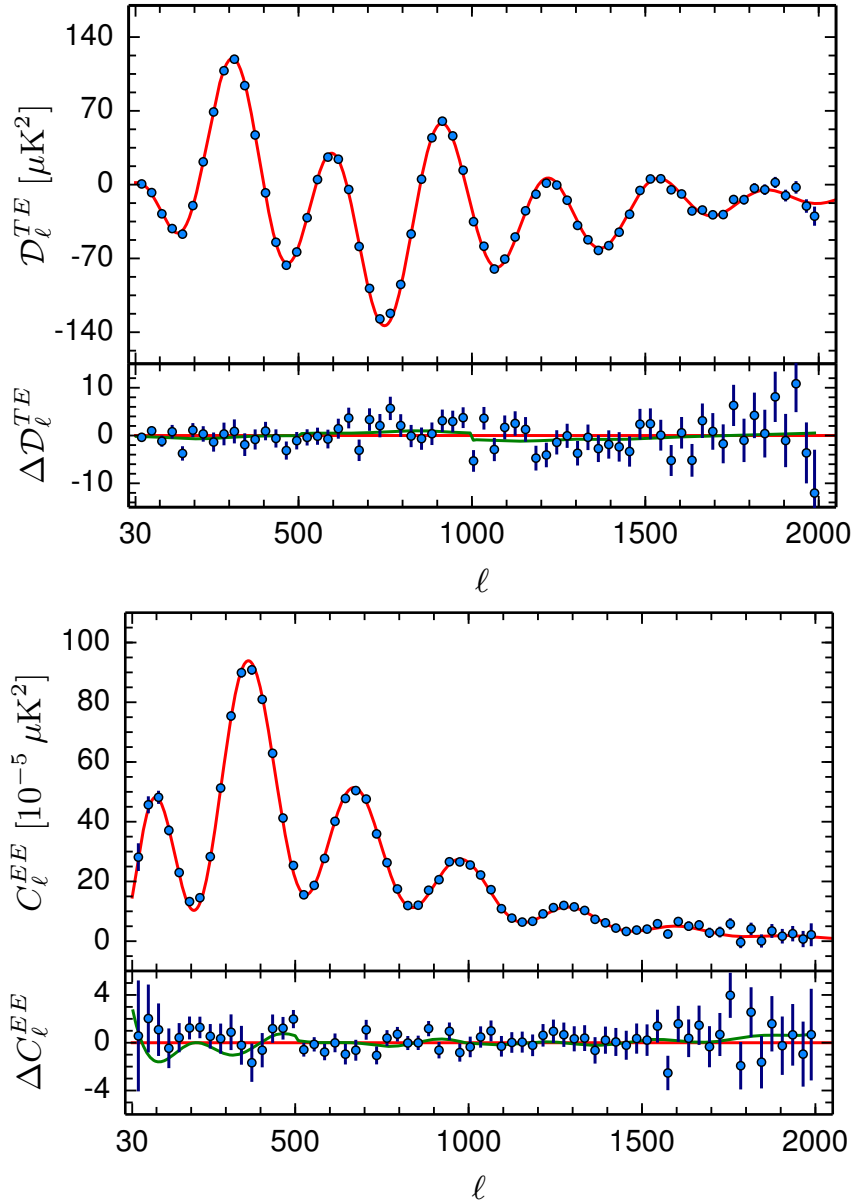
Fig. 3. Frequency-averaged *TE* and *EE* spectra (without fitting for temperature-to-polarization leakage). The theoretical *TE* and *EE* spectra plotted in the *upper panel* of each plot are computed from the *Planck* TT+lowP best-fit model of Fig. 1. Residuals with respect to this theoretical model are shown in the *lower panel* in each plot. The error bars show $\pm 1\sigma$ errors. The green lines in the *lower panels* show the best-fit temperature-to-polarization leakage model of Eqs. (11a) and (11b), fitted separately to the *TE* and *EE* spectra.

(2) Polarization spectra and residual systematics. Maximum likelihood frequency coadded *TE* and *EE* spectra are shown in Fig. 3. The theoretical curves plotted in these figures are the *TE* and *EE* spectra computed from the best-fit base ΛCDM model fitted to the *temperature* spectra (*Planck* TT+lowP), as plotted in Fig. 1. The lower panels in each figure show the residuals with respect to this model. The theoretical model provides a very good fit to the *TE* and *EE* spectra. Table 2 lists χ^2 statistics for the *TE* and *EE* spectra for each frequency combination (with the *TE* and *ET* spectra for each frequency combination coadded to form a single *TE* spectrum). Note that since the *TE* and *EE* spectra are noisier than the *TT* spectra, these values of χ^2 are sensitive to the procedure used to estimate *Planck* noise (see Planck Collaboration XI 2016 for further details). Some of these χ^2 values are unusually high, for example the 100×100 and 143×217 *TE* spectra and the 100×143 *EE*

spectrum all have low PTEs. The *Planck TE* and *EE* spectra for different frequency combinations are not as internally consistent as the *Planck TT* spectra. Inter-comparison of the *TE* and *EE* spectra at different frequencies is much more straightforward than for the temperature spectra because unresolved foregrounds are unimportant in polarization. The high χ^2 values listed in Table 2 therefore provide clear evidence of residual instrumental systematics in the *TE* and *EE* spectra.

With our present understanding of the *Planck* polarization data, we believe that the dominant source of systematic error in the polarization spectra is caused by beam mismatch that generates leakage from temperature to polarization (recalling that the HFI polarization maps are generated by differencing signals between quadruplets of polarization sensitive bolometers). In principle, with accurate knowledge of the beams this leakage could be described by effective

polarized beam window functions. For the 2015 papers, we use the TT beams rather than polarized beams, and characterize temperature-to-polarization leakage using a simplified model. The impact of beam mismatch on the polarization spectra in this model is

$$\Delta C_\ell^{TE} = \epsilon_\ell C_\ell^{TT}, \tag{11a}$$
$$\Delta C_\ell^{EE} = \epsilon_\ell^2 C_\ell^{TT} + 2\epsilon_\ell C_\ell^{TE}, \tag{11b}$$

where ϵ_ℓ is a polynomial in multipole. As a consequence of the *Planck* scanning strategy, pixels are visited approximately every six months, with a rotation of the focal plane by 180°, leading to a weak coupling to beam modes $b_{\ell m}$ with odd values of m. The dominant contributions are expected to come from modes with $m = 2$ and 4, describing the beam ellipticity. We therefore fit the spectra using a fourth-order polynomial,

$$\epsilon_\ell = a_0 + a_2\ell^2 + a_4\ell^4, \tag{12}$$

treating the coefficients a_0, a_2, and a_4 as nuisance parameters in the MCMC analysis. We have ignored the odd coefficients of the polynomial, which should be suppressed by our scanning strategy. We do however include a constant term in the polynomial to account for small deviations of the polarization efficiency from unity.

The fit is performed separately on the TE and EE spectra. A different polynomial is used for each cross-frequency spectrum. The coadded corrections are shown in the lower panels of Fig. 3. Empirically, we find that temperature-to-polarization leakage systematics tend to cancel in the coadded spectra. Although the best-fit leakage corrections to the coadded spectra are small, the corrections for individual frequency cross-spectra can be up to 3 times larger than those shown in Fig. 3. The model of Eqs. (11a) and (11b) is clearly crude, but gives us some idea of the impact of temperature-to-polarization leakage in the coadded spectra. With our present empirical understanding of leakage, we find a correlation between the polarization spectra that have the highest expected temperature-to-polarization leakage and those that display high χ^2 in Table 2. However, the characterization of this leakage is not yet accurate enough to reduce the χ^2 values for each frequency combination to acceptable levels.

As discussed in PCP13, each *Planck* data release and accompanying set of papers should be viewed as a snapshot of the state of the *Planck* analysis at the time of the release. For the 2015 release, we have a high level of confidence in the temperature power spectra. However, we have definite evidence for low-level systematics associated with temperature-to-polarization leakage in the polarization spectra. The tests described above suggest that these are at low levels of a few $(\mu K)^2$ in $\mathcal{D}_\ell$. However, temperature-to-polarization leakage can introduce correlated features in the spectra, as shown by the EE leakage model plotted in Fig. 3. Until we have a more accurate characterization of these systematics, we urge caution in the interpretation of features in the TE and EE spectra. For some of the 2015 papers, we use the TE and EE spectra, without leakage corrections. For most of the models considered in this paper, the TT spectra alone provide tight constraints and so we take a conservative approach and usually quote the TT results. However, as we will see, we find a high level of consistency between the *Planck TT* and full *Planck TT, TE, EE* likelihoods. Some models considered in Sect. 6 are, however, sensitive to the polarization blocks of the likelihood. Examples include constraints on isocurvature

modes, dark matter annihilation, and non-standard recombination histories. *Planck* 2015 constraints on these models should be viewed as preliminary, pending a more complete analysis of polarization systematics, which will be presented in the next series of *Planck* papers accompanying a third data release.

(3) TE and EE conditionals. Given the best-fit base ΛCDM cosmology and foreground parameters determined from the temperature spectra, one can test whether the TE and EE spectra are consistent with the TT spectra by computing conditional probabilities. Writing the data vector as

$$\hat{\boldsymbol{C}} = (\hat{\boldsymbol{C}}^{TT}, \hat{\boldsymbol{C}}^{TE}, \hat{\boldsymbol{C}}^{EE})^{\mathsf{T}} = (\hat{\boldsymbol{X}}_T, \hat{\boldsymbol{X}}_P)^{\mathsf{T}}, \tag{13}$$

where the quantities $\hat{\boldsymbol{C}}^{TT}$, $\hat{\boldsymbol{C}}^{TE}$, and $\hat{\boldsymbol{C}}^{EE}$ are the maximum likelihood freqency co-added foreground-corrected spectra. The covariance matrix of this vector can be partitioned as

$$\hat{\mathsf{M}} = \left(\begin{array}{c|c} \mathsf{M}_T & \mathsf{M}_{TP} \\ \hline \mathsf{M}_{TP}^{\mathsf{T}} & \mathsf{M}_P \end{array} \right). \tag{14}$$

The expected value of the polarization vector, given the observed temperature vector $\hat{\boldsymbol{X}}_T$ is

$$\hat{\boldsymbol{X}}_P^{\mathrm{cond}} = \hat{\boldsymbol{X}}_P^{\mathrm{theory}} + \mathsf{M}_{TP}^{\mathsf{T}}\mathsf{M}_T^{-1}(\hat{\boldsymbol{X}}_T - \hat{\boldsymbol{X}}_T^{\mathrm{theory}}), \tag{15}$$

with covariance

$$\hat{\mathsf{\Sigma}}_P = \mathsf{M}_P - \mathsf{M}_{TP}^{\mathsf{T}}\mathsf{M}_T^{-1}\mathsf{M}_{TP}. \tag{16}$$

In Eq. (15), X_T^{theory} and X_P^{theory} are the theoretical temperature and polarization spectra deduced from minimizing the *Planck* TT+lowP likelihood. Equations (15) and (16) give the expectation values and distributions of the polarization spectra conditional on the observed temperature spectra. These are shown in Fig. 4. Almost all of the data points sit within the $\pm 2\sigma$ bands and in the case of the TE spectra, the data points track the fluctuations expected from the TT spectra at multipoles $\ell \lesssim 1000$. Figure 4 therefore provides an important additional check of the consistency of the TE and EE spectra with the base ΛCDM cosmology.

(4) Likelihood implementation. Section 3.1 showed good consistency between the independently written CamSpec and Plik codes in temperature. The methodology used for the temperature likelihoods are very similar, but the treatment of the polarization spectra in the two codes differs substantially. CamSpec uses low-resolution CMB-subtracted 353-GHz polarization maps thresholded by $P = (Q^2 + U^2)^{1/2}$ to define diffuse Galactic polarization masks. The same apodized polarization mask, with an effective sky fraction $f_{\mathrm{sky}}^{\mathrm{eff}} = 48.8\%$ (as defined by Eq. (10)), is used for 100-, 143-, and 217-GHz Q and U maps. Since there are no unresolved extragalactic foregrounds detected in the TE and EE spectra, all of the different frequency combinations of TE and EE spectra are compressed into single TE and EE spectra (weighted by the inverse of the diagonals of the appropriate covariance matrices), after foreground cleaning using the 353-GHz maps[12] (generalizing the map cleaning technique described in Sect. 3.2 to polarization). This allows the construction of

---

[12] To reduce the impact of noise at 353 GHz, the map-based cleaning of the TE and EE spectra is applied at $\ell \le 300$. At higher multipoles, the polarized dust corrections are small and are subtracted as power laws fitted to the Galactic dust spectra at lower multipoles.
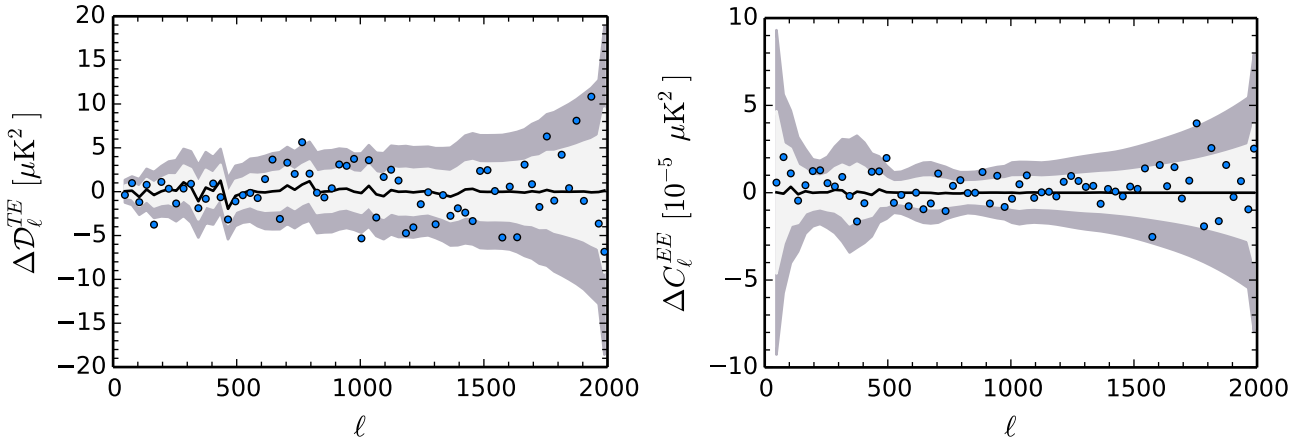
Fig. 4. Conditionals for the `Plik` TE and EE spectra, given the TT data computed from the `Plik` likelihood. The black lines show the expected TE and EE spectra *given the TT data*. The shaded areas show the ± 1 and $\pm 2\sigma$ ranges computed from Eq. (16). The blue points show the residuals for the measured TE and EE spectra.
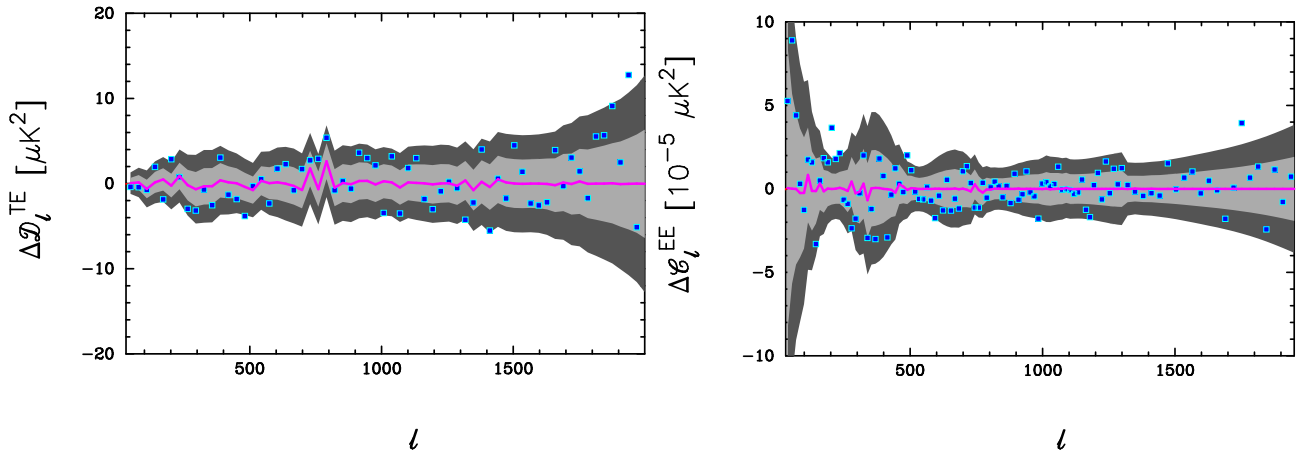

Fig. 5. Conditionals for the `CamSpec` TE and EE spectra, given the TT data computed from the `CamSpec` likelihood. As in Fig. 4, the shaded areas show ± 1 and $\pm 2\sigma$ ranges, computed from Eq. (16) and blue points show the residuals for the measured TE and EE spectra.

a full TT, TE, EE likelihood with no binning of the spectra and with no additional nuisance parameters in polarization. As noted in Sect. 3.1 the consistency of results from the polarization blocks of the `CamSpec` and `Plik` likelihoods is not as good as in temperature. Cosmological parameters from fits to the TE and EE `CamSpec` and `Plik` likelihoods can differ by up to about 1.5σ, although no major science conclusions would change had we chosen to use the `CamSpec` likelihood as the baseline in this paper. We will, however, sometimes quote results from `CamSpec` in addition to those from `Plik` to give the reader an indication of the uncertainties in polarization associated with different likelihood implementations. Figure 5 shows the `CamSpec` TE and EE residuals and error ranges conditional on the best-fit base ΛCDM and foreground model fitted to the `CamSpec` temperature+lowP likelihood. The residuals in both TE and EE are similar to those from `Plik`. The main difference can be seen at low multipoles in the EE spectrum, where `CamSpec` shows a higher dispersion, consistent with the error model, though there are several high points at $\ell \approx 200$ corresponding to the minimum in the EE spectrum, which may be caused by small errors in the subtraction of polarized Galactic emission using 353 GHz as a foreground template (and there are also differences in the covariance matrices at high multipoles caused by differences in the methods used in `CamSpec` and `Plik` to estimate noise). Generally, cosmological parameters determined from the `CamSpec` likelihood have smaller formal errors than

those from `Plik` because there are no nuisance parameters describing polarized Galactic foregrounds in `CamSpec`.

3.3.3. Consistency of cosmological parameters from the *TT*, *TE*, and *EE* spectra

The consistency between parameters of the base ΛCDM model determined from the `Plik` temperature and polarization spectra are summarized in Table 3 and in Fig. 6. As pointed out by Zaldarriaga et al. (1997) and Galli et al. (2014), precision measurements of the CMB polarization spectra have the potential to constrain cosmological parameters to higher accuracy than measurements of the TT spectra because the acoustic peaks are narrower in polarization and unresolved foreground contributions at high multipoles are much lower in polarization than in temperature. The entries in Table 3 show that cosmological parameters that do not depend strongly on τ are consistent between the TT and TE spectra, to within typically 0.5σ or better. Furthermore, the cosmological parameters derived from the TE spectra have comparable errors to the TT parameters. None of the conclusions in this paper would change in any significant way were we to use the TE parameters in place of the TT parameters. The consistency of the cosmological parameters for base ΛCDM between temperature and polarization therefore gives added confidence that *Planck* parameters are insensitive to the specific details of the foreground model that we have used to correct the TT spectra. The EE parameters are also typically within about

Table 3. Parameters of the base ΛCDM cosmology computed from the 2015 baseline *Planck* likelihoods, illustrating the consistency of parameters determined from the temperature and polarization spectra at high multipoles.

Parameter	[1] *Planck* TT+lowP	[2] *Planck* TE+lowP	[3] *Planck* EE+lowP	[4] *Planck* TT,TE,EE+lowP	$([1]-[4])/\sigma_{[1]}$
$\Omega_{\rm b}h^2$	0.02222 ± 0.00023	0.02228 ± 0.00025	0.0240 ± 0.0013	0.02225 ± 0.00016	-0.1
$\Omega_{\rm c}h^2$	0.1197 ± 0.0022	0.1187 ± 0.0021	$0.1150^{+0.0048}_{-0.0055}$	0.1198 ± 0.0015	0.0
$100\theta_{\rm MC}$	1.04085 ± 0.00047	1.04094 ± 0.00051	1.03988 ± 0.00094	1.04077 ± 0.00032	0.2
τ	0.078 ± 0.019	0.053 ± 0.019	$0.059^{+0.022}_{-0.019}$	0.079 ± 0.017	-0.1
$\ln(10^{10}A_{\rm s})$	3.089 ± 0.036	3.031 ± 0.041	$3.066^{+0.046}_{-0.041}$	3.094 ± 0.034	-0.1
$n_{\rm s}$	0.9655 ± 0.0062	0.965 ± 0.012	0.973 ± 0.016	0.9645 ± 0.0049	0.2
H_0	67.31 ± 0.96	67.73 ± 0.92	70.2 ± 3.0	67.27 ± 0.66	0.0
$\Omega_{\rm m}$	0.315 ± 0.013	0.300 ± 0.012	$0.286^{+0.027}_{-0.038}$	0.3156 ± 0.0091	0.0
σ_8	0.829 ± 0.014	0.802 ± 0.018	0.796 ± 0.024	0.831 ± 0.013	0.0
$10^9 A_{\rm s}e^{-2\tau}$	1.880 ± 0.014	1.865 ± 0.019	1.907 ± 0.027	1.882 ± 0.012	-0.1

Notes. Column (1) uses the TT spectra at low and high multipoles and is the same as Col. (6) of Table 1. Columns (2) and (3) use only the TE and EE spectra at high multipoles, and only polarization at low multipoles. Column (4) uses the full likelihood. The last column lists the deviations of the cosmological parameters determined from the *Planck* TT+lowP and *Planck* TT,TE,EE+lowP likelihoods.

1σ of the TT parameters, though because the EE spectra from *Planck* are noisier than the TT spectra, the errors on the EE parameters are significantly larger than those from TT. However, both the TE and EE likelihoods give lower values of τ, $A_{\rm s}$, and σ_8, by over 1σ compared to the TT solutions. Noticee that the TE and EE entries in Table 3 do not use any information from the temperature in the low-multipole likelihood. The tendency for higher values of σ_8, $A_{\rm s}$, and τ in the *Planck* TT+lowP solution is driven, in part, by the temperature power spectrum at low multipoles.

Columns (4) and (5) of Table 3 compare the parameters of the *Planck* TT likelihood with the full *Planck* TT, TE, EE likelihood. These are in agreement, shifting by less than 0.2σ. Although we have emphasized the presence of systematic effects in the *Planck* polarization spectra, which are not accounted for in the errors quoted in Col. (4) of Table 3, the consistency of the *Planck* TT and *Planck* TT, TE, EE parameters provides strong evidence that residual systematics in the polarization spectra have little impact on the scientific conclusions in this paper. The consistency of the base ΛCDM parameters from temperature and polarization is illustrated graphically in Fig. 6. As a rough rule-of-thumb, for base ΛCDM, or extensions to ΛCDM with spatially flat geometry, using the full *Planck* TT, TE, EE likelihood produces improvements in cosmological parameters of about the same size as adding BAO to the *Planck* TT+lowP likelihood.

3.4. Constraints on the reionization optical depth parameter τ

The reionization optical depth parameter τ provides an important constraint on models of early galaxy evolution and star formation. The evolution of the inter-galactic Lyα opacity measured in the spectra of quasars can be used to set limits on the epoch of reionization (Gunn & Peterson 1965). The most recent measurements suggest that the reionization of the inter-galactic medium was largely complete by a redshift $z \approx 6$ (Fan et al. 2006). The steep decline in the space density of Lyα-emitting galaxies over the redshift range $6 \lesssim z \lesssim 8$ also implies a low redshift of reionization (Choudhury et al. 2015). As a reference, for the *Planck* parameters listed in Table 3, instantaneous reionization at redshift $z = 7$ results in an optical depth of $\tau = 0.048$.

The optical depth τ can also be constrained from observations of the CMB. The WMAP9 results of Bennett et al. (2013) give $\tau = 0.089 \pm 0.014$, corresponding to an instantaneous

redshift of reionization $z_{\rm re} = 10.6 \pm 1.1$. The WMAP constraint comes mainly from the EE spectrum in the multipole range $\ell = 2-6$. It has been argued (e.g., Robertson et al. 2013, and references therein) that the high optical depth reported by WMAP cannot be produced by galaxies seen in deep redshift surveys, even assuming high escape fractions for ionizing photons, implying additional sources of photoionizing radiation from still fainter objects. Evidently, it would be useful to have an independent CMB measurement of τ.

The τ measurement from CMB polarization is difficult because it is a small signal, confined to low multipoles, requiring accurate control of instrumental systematics and polarized foreground emission. As discussed by Komatsu et al. (2009), uncertainties in modelling polarized foreground emission are comparable to the statistical error in the WMAP τ measurement. In particular, at the time of the WMAP9 analysis there was very little information available on polarized dust emission. This situation has been partially rectified by the 353-GHz polarization maps from *Planck* (Planck Collaboration Int. XXII 2015; Planck Collaboration Int. XXX 2016). In PPL13, we used preliminary 353-GHz *Planck* polarization maps to clean the WMAP Ka, Q, and V maps for polarized dust emission, using WMAP K-band as a template for polarized synchrotron emission. This lowered τ by about 1σ to $\tau = 0.075 \pm 0.013$, compared to $\tau = 0.089 \pm 0.013$ using the WMAP dust model[13]. However, given the preliminary nature of the *Planck* polarization analysis we decided for the *Planck* 2013 papers to use the WMAP polarization likelihood, as produced by the WMAP team.

In the 2015 papers, we use *Planck* polarization maps based on low-resolution LFI 70-GHz maps, excluding Surveys 2 and 4. These maps are foreground-cleaned using the LFI 30-GHz and HFI 353-GHz maps as polarized synchrotron and dust templates, respectively. These cleaned maps form the polarization part ("lowP") of the low-multipole *Planck* pixel-based likelihood, as described in Planck Collaboration XI (2016). The temperature part of this likelihood is provided by the `Commander` component-separation algorithm. The *Planck* low-multipole likelihood retains 46% of the sky in polarization and is completely independent of the WMAP polarization likelihood. In combination with the *Planck* high multipole TT likelihood, the *Planck*

---

[13] Neither of these error estimates reflect the true uncertainty in foreground removal.
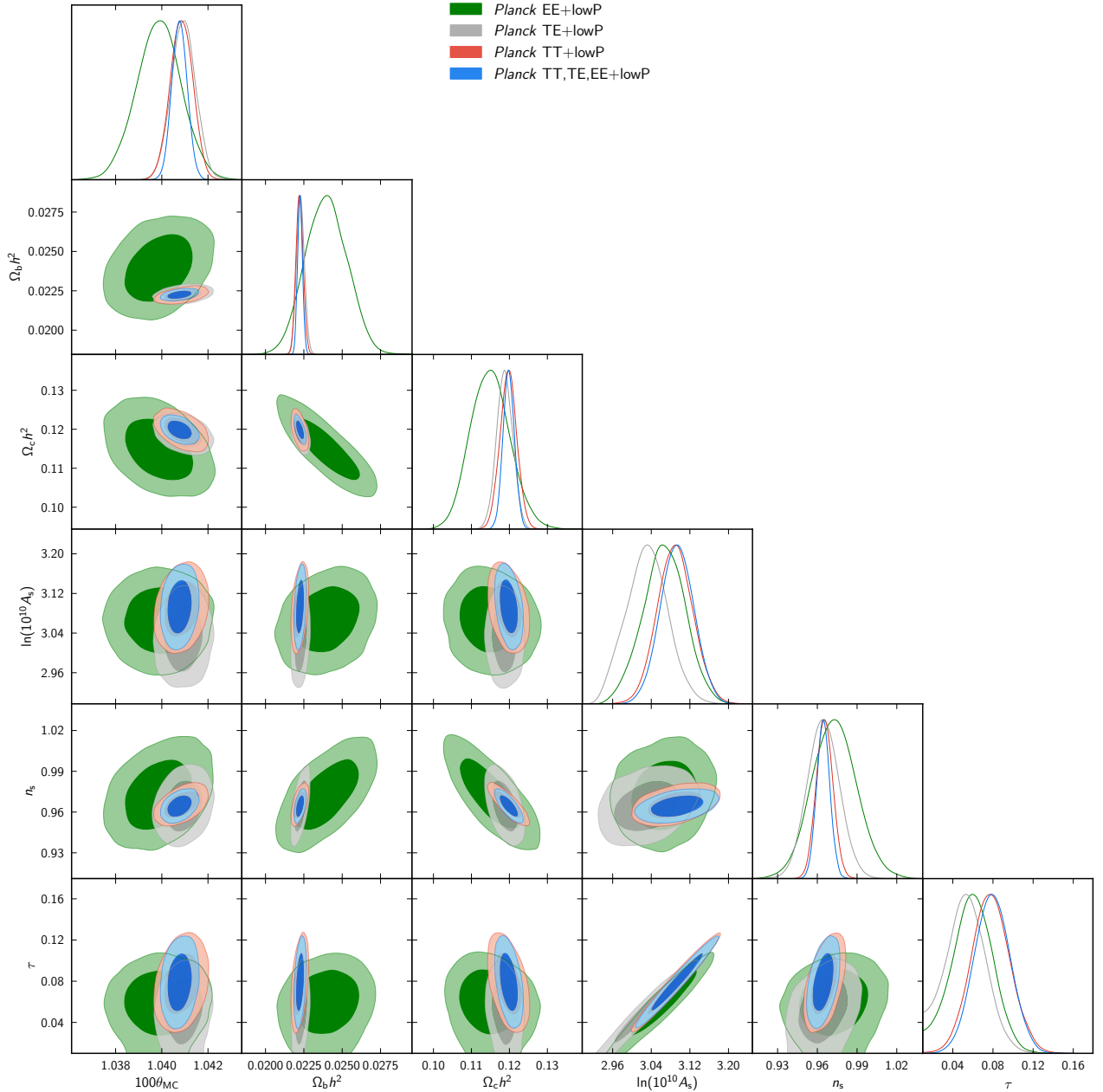
Fig. 6. Comparison of the base ΛCDM model parameter constraints from *Planck* temperature and polarization data.

low-multipole likelihood gives $\tau = 0.078 \pm 0.019$. This constraint is somewhat higher than the constraint $\tau = 0.067 \pm 0.022$ derived from the *Planck* low-multipole likelihood alone (see Planck Collaboration XI 2016 and also Sect. 5.1.2).

Following the 2013 analysis, we have used the 2015 HFI 353-GHz polarization maps as a dust template, together with the WMAP K-band data as a template for polarized synchrotron emission, to clean the low-resolution WMAP Ka, Q, and V maps (see Planck Collaboration XI 2016 for further details). For the purpose of cosmological parameter estimation, this data set is masked using the WMAP P06 mask, which retains 73% of the sky. The noise-weighted combination of the *Planck* 353-cleaned WMAP polarization maps yields $\tau = 0.071 \pm 0.013$ when combined with the *Planck TT* information in the range $2 \leq \ell \lesssim 2508$, consistent with the value of τ obtained from the LFI 70-GHz polarization maps. In fact, null tests described in Planck Collaboration XI (2016) demonstrate that the LFI and WMAP polarization data are statistically consistent. The HFI

polarization maps have higher signal-to-noise than the LFI and could, in principle, provide a third cross-check. However, at the time of writing, we are not yet confident that systematics in the HFI maps at low multipoles ($\ell \lesssim 20$) are at negligible levels. A discussion of HFI polarization at low multipoles will therefore be deferred to future papers[14].

Given the difficulty of making accurate CMB polarization measurements at low multipoles, it is useful to investigate other ways of constraining τ. Measurements of the temperature power spectrum provide a highly accurate measurement of the amplitude $A_s e^{-2\tau}$. However, as shown in PCP13 CMB *lensing* breaks the degeneracy between τ and A_s. The observed *Planck TT* spectrum is, of course, lensed, so the degeneracy between τ and A_s is partially broken when we fit models to the *Planck TT* likelihood. However, the degeneracy breaking is much stronger if we combine the *Planck* TT likelihood with the

[14] See Planck Collaboration Int. XLVI (2016), which has been submitted since this paper was written.
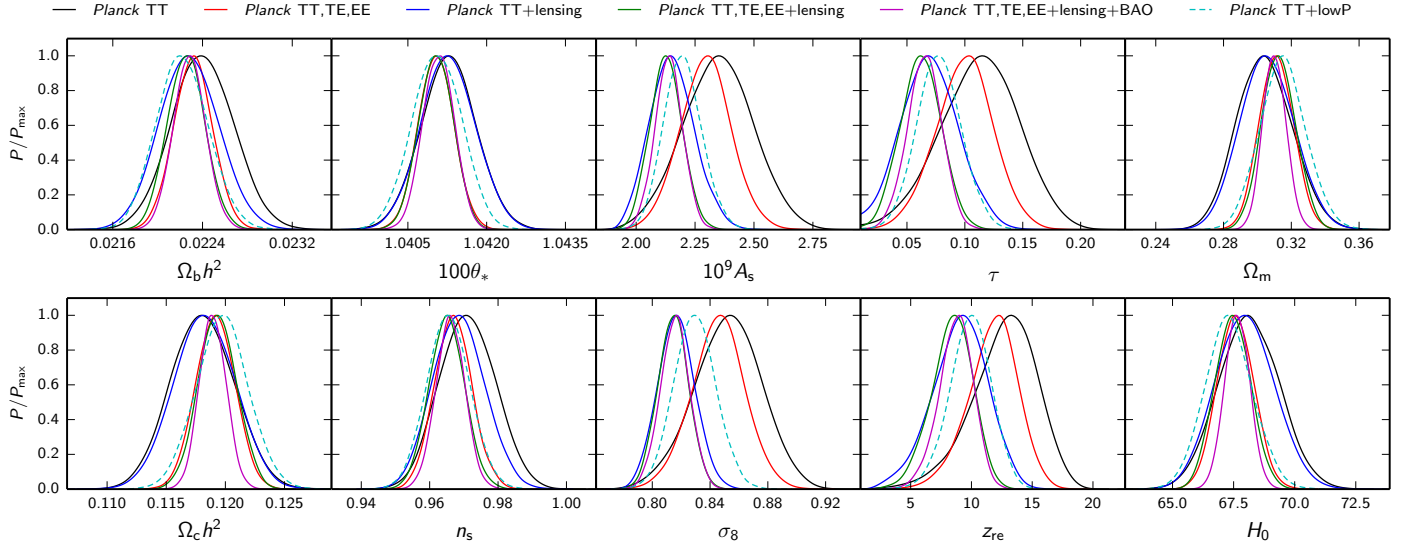
Fig. 7. Marginalized constraints on parameters of the base ΛCDM model for various data combinations, excluding low-multipole polarization, compared to the *Planck* TT+lowP constraints.

Planck lensing likelihood constructed from measurements of the power spectrum of the lensing potential $C_\ell^{\phi\phi}$. The 2015 *Planck* TT and lensing likelihoods are statistically more powerful than their 2013 counterparts and the corresponding determination of τ is more precise. The 2015 *Planck* lensing likelihood (labelled "lensing") is summarized in Sect. 5.1 and discussed in more detail in Planck Collaboration XV (2016). The constraints on τ and z_{re}[15] for various data combinations *excluding* low-multipole polarization data from *Planck* are summarized in Fig. 7 and compared with the baseline *Planck* TT+lowP parameters. This figure also shows the shifts of other parameters of the base ΛCDM cosmology, illustrating their sensitivity to changes in τ.

The *Planck* constraints on τ and z_{re} in the base ΛCDM model for various data combinations are:

$$\tau = 0.078^{+0.019}_{-0.019},\ z_{re} = 9.9^{+1.8}_{-1.6},\ \textit{Planck}\ \text{TT+lowP}, \quad (17a)$$

$$\tau = 0.070^{+0.024}_{-0.024},\ z_{re} = 9.0^{+2.5}_{-2.1},\ \textit{Planck}\ \text{TT+lensing}, \quad (17b)$$

$$\tau = 0.066^{+0.016}_{-0.016},\ z_{re} = 8.8^{+1.7}_{-1.4},\ \textit{Planck}\ \text{TT+lowP} \\ \text{+lensing}, \quad (17c)$$

$$\tau = 0.067^{+0.016}_{-0.016},\ z_{re} = 8.9^{+1.7}_{-1.4},\ \textit{Planck}\ \text{TT+lensing} \\ \text{+BAO}, \quad (17d)$$

$$\tau = 0.066^{+0.013}_{-0.013},\ z_{re} = 8.8^{+1.3}_{-1.2},\ \textit{Planck}\ \text{TT+lowP} \\ \text{+lensing+BAO}. \quad (17e)$$

The constraint from *Planck* TT+lensing+BAO on τ *is completely independent of low-multipole CMB polarization data* and agrees well with the result from *Planck* polarization (and has comparable precision). These results all indicate a lower redshift of reionization than the value $z_{re} = 11.1 \pm 1.1$ derived in PCP13, based on the WMAP9 polarization likelihood. The low values of τ from *Planck* are also consistent with the lower value of τ derived from the WMAP *Planck* 353-GHz-cleaned polarization likelihood, suggesting strongly that the WMAP9 value is biased slightly high by residual polarized dust emission.

The *Planck* results of Eqs. (17a)−(17e) provide evidence for a lower optical depth and redshift of reionization than inferred

from WMAP (Bennett et al. 2013), partially alleviating the difficulties in reionizing the intergalactic medium using starlight from high-redshift galaxies. A key goal of the *Planck* analysis over the next year is to assess whether these results are consistent with the HFI polarization data at low multipoles.

Given the consistency between the LFI and WMAP polarization maps when both are cleaned with the HFI 353-GHz polarization maps, we have also constructed a combined WMAP+*Planck* low-multipole polarization likelihood (denoted "lowP+WP"). This likelihood uses 73% of the sky and is constructed from a noise-weighted combination of LFI 70-GHz and WMAP Ka, Q, and V maps, as summarized in Sect. 3.1 and discussed in more detail in Planck Collaboration XI (2016). In combination with the *Planck* high-multipole TT likelihood, the combined lowP+WP likelihood gives $\tau = 0.074^{+0.011}_{-0.013}$, consistent with the individual LFI and WMAP likelihoods to within about 0.5σ.

The various *Planck* and *Planck*+WMAP constraints on τ are summarized in Fig. 8. The tightest of these constraints comes from the combined lowP+WP likelihood. It is therefore reasonable to ask why we have chosen to use the lowP likelihood as the baseline in this paper, which gives a higher statistical error on τ. The principal reason is to produce a *Planck* analysis, utilizing the LFI polarization data, that is independent of WMAP. All of the constraints shown in Fig. 8 are compatible with each other, and insofar as other cosmological parameters are sensitive to small changes in τ, it would make very little difference to the results in this paper had we chosen to use WMAP or *Planck*+WMAP polarization data at low multipoles.

4. Comparison of the *Planck* power spectrum with high-resolution experiments

In PCP13 we combined *Planck* with the small-scale measurements of the ground-based, high-resolution Atacama Cosmology Telescope (ACT) and South Pole Telescope (SPT). The primary role of using ACT and SPT was to set limits on foreground components that were poorly constrained by *Planck* alone and to provide more accurate constraints on the damping tail of the temperature power spectrum. In this paper, with the higher signal-to-noise levels of the full mission *Planck* data, we

---

[15] We use the same specific definition of z_{re} as in the 2013 papers, where reionization is assumed to be relatively sharp, with a mid-point parameterized by a redshift z_{re} and width $\Delta z_{re} = 0.5$. Unless otherwise stated we impose a flat prior on the optical depth with $\tau > 0.01$.
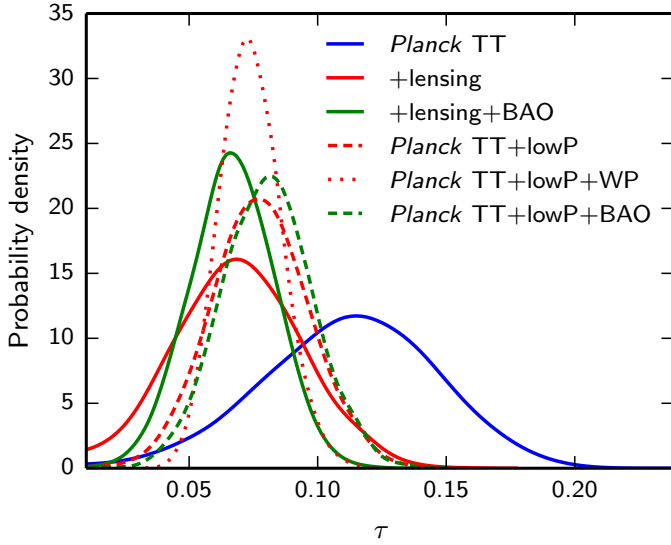
Fig. 8. Marginalized constraints on the reionization optical depth in the base ΛCDM model for various data combinations. Solid lines do not include low-multipole polarization; in these cases the optical depth is constrained by *Planck* lensing. The dashed/dotted lines include LFI polarization (+lowP), or the combination of LFI and WMAP polarization cleaned using 353 GHz as a dust template (+lowP+WP).
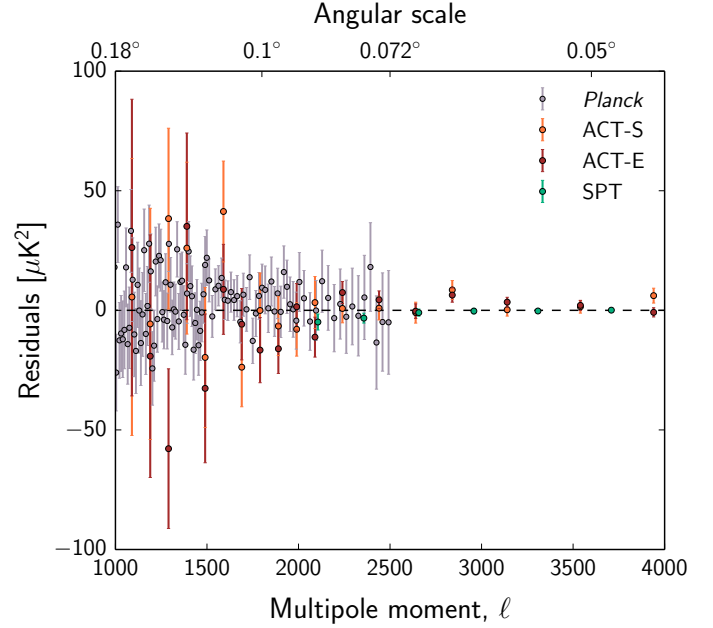

Fig. 9. Residual power with respect to the *Planck* TT+lowP ΛCDM best-fit model for the *Planck* (grey), ACT south (orange), ACT equatorial (red), and SPT (green) CMB bandpowers. The ACT and SPT bandpowers are scaled by the best-fit calibration factors.

have taken a different approach, using the ACT and SPT data to impose a prior on the thermal and kinetic SZ power spectrum parameters in the *Planck* foreground model as described in Sect. 2.3. In this section, we check the consistency of the temperature power spectra measured by *Planck*, ACT, and SPT, and test the effects of including the ACT and SPT data on the recovered CMB power spectrum.

We use the latest ACT temperature power spectra presented in Das et al. (2014), with a revised binning described in Calabrese et al. (2013) and final beam estimates in Hasselfield et al. (2013a). As in PCP13 we use ACT data in the range $1\,000 < \ell < 10\,000$ at 148 GHz, and $1\,500 < \ell < 10\,000$ for the 148×218 and 218-GHz spectra. We use SPT measurements in the range $2\,000 < \ell < 13\,000$ from the complete $2540\,\mathrm{deg}^2$ SPT-SZ survey at 95, 150, and 220 GHz presented in George et al. (2015).

Each of these experiments uses a foreground model to describe the multi-frequency power spectra. Here we implement a common foreground model to combine *Planck* with the high-multipole data, following a similar approach to PCP13 but with some refinements. Following the 2013 analysis, we solve for common nuisance parameters describing the tSZ, kSZ, and tSZ$\times$CIB components, extending the templates used for *Planck* to $\ell = 13\,000$ to cover the full ACT and SPT multipole range. As in PCP13, we use five point-source amplitudes to fit for the total dusty and radio Poisson power, namely $A_{148}^{\mathrm{PS,ACT}}$, $A_{218}^{\mathrm{PS,ACT}}$, $A_{95}^{\mathrm{PS,SPT}}$, $A_{150}^{\mathrm{PS,SPT}}$, and $A_{220}^{\mathrm{PS,SPT}}$. We rescale these amplitudes to cross-frequency spectra using point-source correlation coefficients, improving on the 2013 treatment by using different parameters for the ACT and SPT correlations, $r_{148 \times 218}^{\mathrm{PS,ACT}}$ and $r_{150 \times 220}^{\mathrm{PS,SPT}}$ (a single $r_{150 \times 220}^{\mathrm{PS}}$ parameter was used in 2013). We vary $r_{95 \times 150}^{\mathrm{PS,SPT}}$ and $r_{95 \times 220}^{\mathrm{PS,SPT}}$ as in 2013, and include dust amplitudes for ACT, with Gaussian priors as in PCP13.

As described in Sect. 2.3 we use a theoretically motivated clustered CIB model fitted to *Planck*+IRAS estimates of the CIB. The model at all frequencies in the range 95−220 GHz is

specified by a single amplitude A_{217}^{CIB}. The CIB power is well constrained by *Planck* data at $\ell < 2000$. At multipoles $\ell \gtrsim 3000$, the 1-halo component of the CIB model steepens and becomes degenerate with the Poisson power. This causes an underestimate of the Poisson levels for ACT and SPT, inconsistent with predictions from source counts. We therefore use the *Planck* CIB template only in the range $2 < \ell < 3000$, and extrapolate to higher multipoles using a power law $\mathcal{D}_\ell \propto \ell^{0.8}$. While this may not be a completely accurate model for the clustered CIB spectrum at high multipoles (see, e.g., Viero et al. 2013; Planck Collaboration XXX 2014), this extrapolation is consistent with the CIB model used in the analysis of ACT and SPT. We then need to extrapolate the *Planck* 217-GHz CIB power to the ACT and SPT frequencies. This requires converting the CIB measurement in the HFI 217-GHz channel to the ACT and SPT bandpasses assuming a spectral energy distribution; we use the CIB spectral energy distribution from Béthermin et al. (2012). Combining this model with the ACT and SPT bandpasses, we find that A_{217}^{CIB} has to be multiplied by 0.12 and 0.89 for ACT 148 and 218 GHz, and by 0.026, 0.14, and 0.91 for SPT 95, 150, and 220 GHz, respectively. With this model in place, the best-fit *Planck*, ACT, and SPT Poisson levels agree with those predicted from source counts, as discussed further in Planck Collaboration XI (2016).

The nuisance model includes seven calibration parameters as in PCP13 (four for ACT and three for SPT). The ACT spectra are internally calibrated using the WMAP 9-year maps, with 2% and 7% uncertainty at 148 and 218 GHz, while SPT calibrates using the *Planck* 2013 143-GHz maps, with 1.1%, 1.2%, and 2.2% uncertainty at 95, 150, and 220 GHz. To account for the increased 2015 *Planck* absolute calibration (2% higher in power) we increase the mean of the SPT map-based calibrations from 1.00 to 1.01.

This common foreground and calibration model fits the data well. We first fix the cosmology to that of the best-fit *Planck* TT+lowP base-ΛCDM model, and estimate the foreground
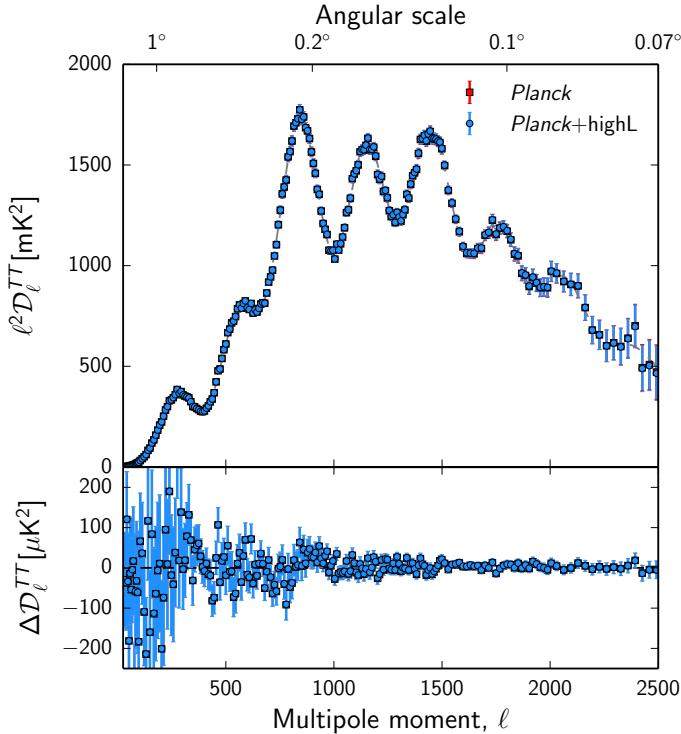
Fig. 10. *Planck* CMB power spectrum that is marginalized over foregrounds (red), including a prior on the thermal and kinetic SZ power. The inclusion of the full higher resolution ACT and SPT data (shown in blue) does not significantly decrease the errors.

and calibration parameters, finding a best-fitting χ^2 of 734 for 731 degrees of freedom (reduced $\chi^2 = 1.004$, PTE = 0.46). We then simultaneously estimate the *Planck*, ACT- (S: south, E: equatorial) and SPT CMB bandpowers, C_b, following the Gibbs sampling scheme of Dunkley et al. (2013) and Calabrese et al. (2013), marginalizing over the nuisance parameters.

To simultaneously solve for the *Planck*, ACT, and SPT CMB spectra, we extend the nuisance model described above, including the four *Planck* point source amplitudes, the dust parameters and the *Planck* 100-GHz and 217-GHz calibration parameters (relative to 143 GHz) with the same priors as used in the *Planck* multi-frequency likelihood analysis. For ACT and SPT, the calibration factors are defined for each frequency (rather than relative to a central frequency). Following Calabrese et al. (2013), we separate out the 148-GHz calibration for the ACT-(S,E) spectra and the 150-GHz calibration for SPT, estimating the CMB bandpowers as C_b/A_{cal}[16]. We impose Gaussian priors on A_{cal}: 1.00 ± 0.02 for ACT-(S,E); and 1.010 ± 0.012 for SPT. The estimated CMB spectrum will then have an overall calibration uncertainty for each of the ACT-S, ACT-E, and SPT spectra. We do not require the *Planck* CMB bandpowers to be the same as those for ACT or SPT, so that we can check for consistency between the three experiments.

In Fig. 9 we show the residual CMB power with respect to the *Planck* TT+lowP ΛCDM best-fit model for the three experiments. All of the data sets are consistent over the multipole range plotted in this figure. For ACT-S, we find $\chi^2 = 17.54$ (18 data points, PTE = 0.49); For ACT-E we find $\chi^2 = 23.54$ (18 data points, PTE = 0.17); and for SPT $\chi^2 = 5.13$ (six data points, PTE = 0.53).

---

[16] This means that the other calibration factors (e.g., ACT 218 GHz) are re-defined to be relative to 148 GHz (or 150 GHz for SPT) data.

Figure 10 shows the effect of including ACT and SPT data on the recovered *Planck* CMB spectrum. We find that including the ACT and SPT data does not reduce the *Planck* errors significantly. This is expected because the dominant small-scale foreground contributions for *Planck* are the Poisson source amplitudes, which are treated independently of the Poisson amplitudes for ACT and SPT. The high-resolution experiments do help tighten the CIB amplitude (which is reasonably well constrained by *Planck*) and the tSZ and kSZ amplitudes (which are subdominant foregrounds for *Planck*). The kSZ effect in particular is degenerate with the CMB, since both have blackbody components; imposing a prior on the allowed kSZ power (as discussed in Sect. 2.3) breaks this degeneracy. The net effect is that the errors on the recovered *Planck* CMB spectrum are only marginally reduced with the inclusion of the ACT and SPT data. This motivates our choice to include the information from ACT and SPT into the joint tSZ and kSZ prior applied to *Planck*.

The Gibbs sampling technique recovers a best-fit CMB spectrum marginalized over foregrounds and other nuisance parameters. The Gibbs samples can then be used to form a fast CMB-only *Planck* likelihood that depends on only one nuisance parameter, the overall calibration y_p. MCMC chains run using the CMB-only likelihood therefore converge much faster than using the full multi-frequency Plik likelihood. The CMB-only likelihood is also extremely accurate, even for extensions to the base ΛCDM cosmology and is discussed further in Planck Collaboration XI (2016).

5. Comparison of the *Planck* base ΛCDM model with other astrophysical data sets

5.1. CMB lensing measured by Planck

Gravitational lensing by large-scale structure leaves imprints on the CMB temperature and polarization that can be measured in high angular resolution, low-noise observations, such as those from *Planck*. The most relevant effects are a smoothing of the acoustic peaks and troughs in the TT, TE, and EE power spectra, the conversion of E-mode polarization to B-modes, and the generation of significant non-Gaussianity in the form of a nonzero connected 4-point function (see Lewis & Challinor 2006 for a review). The latter is proportional to the power spectrum $C_\ell^{\phi\phi}$ of the lensing potential ϕ, and so one can estimate this power spectrum from the CMB 4-point functions. In the 2013 *Planck* release, we reported a 10σ detection of the lensing effect in the TT power spectrum (see PCP13) and a 25σ measurement of the amplitude of $C_\ell^{\phi\phi}$ from the $TTTT$ 4-point function (Planck Collaboration XVII 2014). The power of such lensing measurements is that they provide sensitivity to parameters that affect the late-time expansion, geometry, and matter clustering (e.g., spatial curvature and neutrino masses) *from the CMB alone*.

Since the 2013 *Planck* release, there have been significant developments in the field of CMB lensing. The SPT team have reported a 7.7σ detection of lens-induced B-mode polarization based on the $EB\phi^{CIB}$ 3-point function, where ϕ^{CIB} is a proxy for the CMB lensing potential ϕ derived from CIB measurements (Hanson et al. 2013). The POLARBEAR collaboration (POLARBEAR Collaboration 2014b) and the ACT collaboration (van Engelen et al. 2015) have performed similar analyses at somewhat lower significance (POLARBEAR Collaboration 2014b). In addition, the first detections of the polarization 4-point function from lensing, at a significance of around 4σ, have been reported by the POLARBEAR (Ade et al. 2014) and

SPT ([Story et al. 2015](#)) collaborations, and the former have also made a direct measurement of the *BB* power spectrum due to lensing on small angular scales with a significance around 2σ ([POLARBEAR Collaboration 2014a](#)). Finally, the *BB* power spectrum from lensing has also been detected on degree angular scales, with similar significance, by the BICEP2 collaboration ([BICEP2 Collaboration 2014](#)); see also [BKP](#).

5.1.1. The *Planck* lensing likelihood

Lensing results from the full-mission *Planck* data are discussed in [Planck Collaboration XV (2016)](#)[17]. With approximately twice the amount of temperature data, and the inclusion of polarization, the noise levels on the reconstructed ϕ are a factor of about 2 better than in [Planck Collaboration XVII (2014)](#). The broadband amplitude of $C_\ell^{\phi\phi}$ is now measured to better than 2.5% accuracy, the most significant measurement of CMB lensing to date. Moreover, lensing B-modes are detected at 10σ, both through a correlation analysis with the CIB and via the *TTEB* 4-point function. Many of the results in this paper make use of the *Planck* measurements of $C_\ell^{\phi\phi}$. In particular, they provide an alternative route to estimate the optical depth (as already discussed in Sect. [3.4](#)), and to tightly constrain spatial curvature (Sect. [6.2.4](#)).

The estimation of $C_\ell^{\phi\phi}$ from the *Planck* full-mission data is discussed in detail in [Planck Collaboration XV (2016)](#). There are a number of significant changes from the 2013 analysis that are worth noting here.

- The lensing potential power spectrum is now estimated from lens reconstructions that use both temperature and polarization data in the multipole range $100 \leq \ell \leq 2048$. The likelihood used here is based on the power spectrum of a lens reconstruction derived from the minimum-variance combination of five quadratic estimators (*TT*, *TE*, *EE*, *TB*, and *EB*). The power spectrum is therefore based on 15 different 4-point functions.
- The results used here are derived from foreground-cleaned maps of the CMB synthesized from all nine *Planck* frequency maps with the `SMICA` algorithm, while the baseline 2013 results used a minimum-variance combination of the 143-GHz and 217-GHz nominal-mission maps. After masking the Galaxy and point-sources, 67.3% of the sky is retained for the lensing analysis.
- The lensing power spectrum is estimated in the multipole range $8 \leq \ell \leq 2048$. Multipoles $\ell < 8$ have large mean-field corrections due to survey anisotropy and are rather unstable to analysis choices; they are therefore excluded from all lensing results. Here, we use only the range $40 \leq \ell \leq 400$ (the same as used in the 2013 analysis), with eight bins each of width $\Delta\ell = 45$. This choice is based on the extensive suite of null tests reported in [Planck Collaboration XV (2016)](#). Nearly all tests are passed over the full multipole range $8 \leq \ell \leq 2048$, with the exception of a slight excess of curl modes in the *TT* reconstruction around $\ell = 500$. Given that the range $40 \leq \ell \leq 400$ contains most of the statistical power in the reconstruction, we have conservatively adopted this range for use in the *Planck* 2015 cosmology papers.
- To normalize $C_\ell^{\phi\phi}$ from the measured 4-point functions requires knowledge of the CMB power spectra. In practice, we normalize with fiducial spectra, but then correct for changes

in the true normalization at each point in parameter space within the likelihood. The exact renormalization scheme adopted in the 2013 analysis proved to be too slow for the extension to polarization, so we now use a linearized approximation, based on pre-computed response functions, which is very efficient within an MCMC analysis. Spot-checks have confirmed the accuracy of this approach.

- The measurement of $C_\ell^{\phi\phi}$ can be thought of as being derived from an optimal combination of trispectrum configurations. In practice, the expectation value of this combination at any multipole ℓ has a local part proportional to $C_\ell^{\phi\phi}$, but also a non-local ("$N^{(1)}$ bias") part that couples to a broad range of multipoles in $C_\ell^{\phi\phi}$ ([Kesden et al. 2003](#)); this non-local part comes from non-primary trispectrum couplings. In the *Planck* 2013 analysis we corrected for the $N^{(1)}$ bias by making a fiducial correction, but this ignores its parameter dependence. We improve on this in the 2015 analysis by correcting for errors in the fiducial $N^{(1)}$ bias at each point in parameter space within the lensing likelihood. As with the renormalization above, we linearize this $\delta N^{(1)}$ correction for efficiency. As a result, we no longer need to make an approximate correction in the $C_\ell^{\phi\phi}$ covariance matrix to account for the cosmological uncertainty in $N^{(1)}$.
- Beam uncertainties are no longer included in the covariance matrix of $C_\ell^{\phi\phi}$, since, with the improved knowledge of the beams, the estimated uncertainties are negligible for the lensing analysis. The only inter-bandpower correlations included in the $C_\ell^{\phi\phi}$ bandpower covariance matrix are from the uncertainty in the correction applied for the point-source 4-point function.

As in the 2013 analysis, we approximate the lensing likelihood as Gaussian in the estimated bandpowers, with a fiducial covariance matrix. Following the arguments in [Schmittfull et al. (2013)](#), it is a good approximation to ignore correlations between the 2- and 4-point functions; so, when combining the *Planck* power spectra with *Planck* lensing, we simply multiply their respective likelihoods.

It is also worth noting that the changes in absolute calibration of the *Planck* power spectra (around 2% between the 2013 and 2015 releases) do not directly affect the lensing results. The CMB 4-point functions do, of course, respond to any recalibration of the data, but in estimating $C_\ell^{\phi\phi}$ this dependence is removed by normalizing with theory spectra fit to the observed CMB spectra. The measured $C_\ell^{\phi\phi}$ bandpowers from the 2013 and current *Planck* releases can therefore be directly compared, and are in good agreement ([Planck Collaboration XV 2016](#)). Care is needed, however, in comparing consistency of the lensing measurements across data releases with the best-fitting model predictions. Changes in calibration translate directly into changes in $A_s e^{-2\tau}$, which, along with any change in the best-fitting optical depth, alter A_s, and hence the predicted lensing power. These changes from 2013 to the current release go in opposite directions, leading to a net decrease in A_s of 0.6%. This, combined with a small (0.15%) increase in θ_{eq}, reduces the expected $C_\ell^{\phi\phi}$ by approximately 1.5% for multipoles $\ell > 60$.

The *Planck* measurements of $C_\ell^{\phi\phi}$, based on the temperature and polarization 4-point functions, are plotted in Fig. [11](#) (with results of a temperature-only reconstruction included for comparison). The measured $C_\ell^{\phi\phi}$ are compared with the predicted lensing power from the best-fitting base ΛCDM model to the *Planck* TT+lowP data in this figure. The bandpowers that are

---

[17] In that paper we are careful to highlight the 4-point function origin of the lensing power spectrum reconstruction by using the index L; however, in this paper we use the notation ℓ.
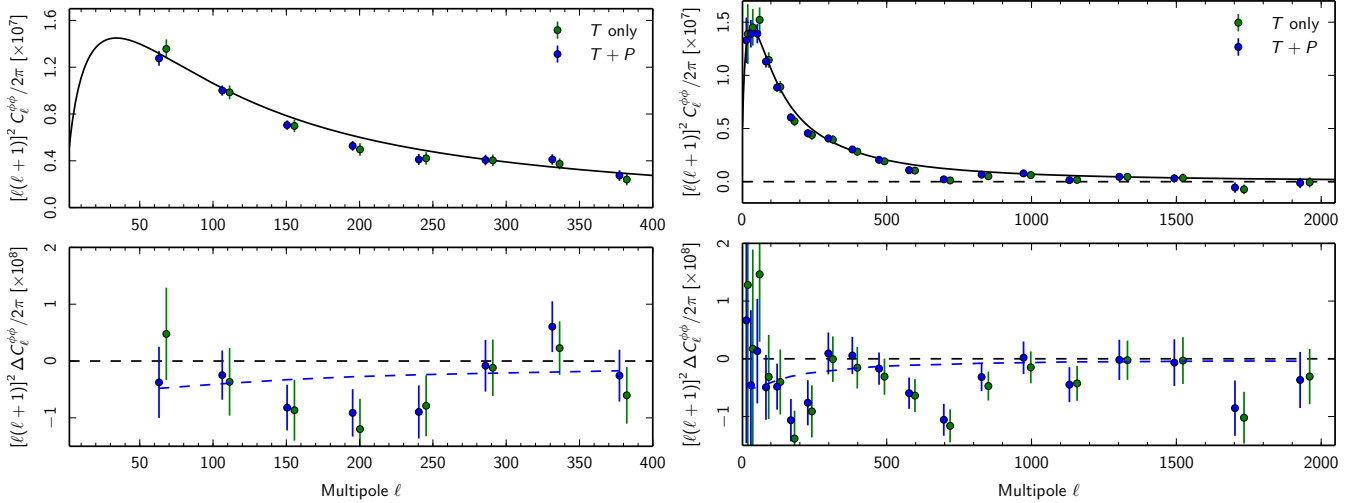
Fig. 11. *Planck* measurements of the lensing power spectrum compared to the prediction for the best-fitting base ΛCDM model to the *Planck* TT+lowP data. *Left:* the conservative cut of the *Planck* lensing data used throughout this paper, covering the multipole range $40 \leq \ell \leq 400$. *Right:* lensing data over the range $8 \leq \ell \leq 2048$, demonstrating the general consistency with the ΛCDM prediction over this extended multipole range. In both cases, green points are the power from lensing reconstructions using only temperature data, while blue points combine temperature and polarization. They are offset in ℓ for clarity and error bars are $\pm 1\sigma$. In *the top panels* the solid lines are the best-fitting base ΛCDM model to the *Planck* TT+lowP data with no renormalization or $\delta N^{(1)}$ correction applied (see text for explanation). The *bottom panels* show the difference between the data and the renormalized and $\delta N^{(1)}$-corrected theory bandpowers, which enter the likelihood. The mild preference of the lensing measurements for lower lensing power around $\ell = 200$ pulls the theoretical prediction for $C_\ell^{\phi\phi}$ downwards at the best-fitting parameters of a fit to the combined *Planck* TT+lowP+lensing data, shown by the dashed blue lines (always for the conservative cut of the lensing data, including polarization).

used in the conservative lensing likelihood adopted in this paper are shown in the left-hand plot, while bandpowers over the range $8 \leq \ell \leq 2048$ are shown in the right-hand plot, to demonstrate the general consistency with the ΛCDM prediction over the full multipole range. The difference between the measured bandpowers and the best-fit prediction are shown in the bottom panels. Here, the theory predictions are corrected in the same way as they are in the likelihood[18].

Figure 11 suggests that the *Planck* measurements of $C_\ell^{\phi\phi}$ are mildly in tension with the prediction of the best-fitting ΛCDM model. In particular, for the conservative multipole range $40 \leq \ell \leq 400$, the temperature+polarization reconstruction has $\chi^2 = 15.4$ (for eight degrees of freedom), with a PTE of 5.2%. For reference, over the full multipole range $\chi^2 = 40.8$ for 19 degrees of freedom (PTE of 0.3%); the large χ^2 is driven by a single bandpower ($638 \leq \ell \leq 762$), and excluding this gives an acceptable $\chi^2 = 26.8$ (PTE of 8%). We caution the reader that this multipole range is where the lensing reconstruction shows a mild excess of curl-modes (Planck Collaboration XV 2016), and for this reason we adopt the conservative multipole range for the lensing likelihood in this paper.

This simple χ^2 test does not account for the uncertainty in the predicted $C_\ell^{\phi\phi}$. In the ΛCDM model, the dominant uncertainty in the multipole range $40 \leq \ell \leq 400$ comes from that in A_s (1σ uncertainty of 3.7% for *Planck* TT+lowP), which itself derives from the uncertainty in the reionization optical depth, τ. The predicted rms lensing deflection from *Planck* TT+lowP data is $\langle d^2 \rangle^{1/2} = (2.50 \pm 0.05)$ arcmin, corresponding to a

3.6% uncertainty (1σ) in the amplitude of $C_\ell^{\phi\phi}$ (which improves to 3.1% uncertainty for the combined *Planck*+WP likelihood). Note that this is larger than the uncertainty on the measured amplitude, i.e., *the lensing measurement is more precise than the prediction from the CMB power spectra in even the simplest ΛCDM model*. This model uncertainty is reflected in a scatter in the χ^2 of the lensing data over the *Planck* TT+lowP chains, $\chi^2_{\rm lens} = 17.9 \pm 9.0$, which is significantly larger than the expected scatter in χ^2 at the true model, due to the uncertainties in the lensing bandpowers ($\sqrt{2N_{\rm d.o.f.}} = 4$). Following the treatment in PCP13, we can assess consistency more carefully by introducing a parameter $A_L^{\phi\phi}$ that scales the theory lensing trispectrum at every point in parameter space in a joint analysis of the CMB spectra and the lensing spectrum. We find

$$A_L^{\phi\phi} = 0.95 \pm 0.04 \quad (68\%, Planck \text{ TT+lowP+lensing}), \quad (18)$$

in good agreement with the expected value of unity. The posterior for $A_L^{\phi\phi}$, and other lensing amplitude measures discussed below, is shown in Fig. 12.

Given the precision of the measured $C_\ell^{\phi\phi}$ compared to the uncertainty in the predicted spectrum from fits to the *Planck* TT+lowP data, the structure in the residuals seen in Fig. 11 might be expected to pull parameters in joint fits. As discussed in Planck Collaboration XV (2016) and Pan et al. (2014), the primary parameter dependence of $C_\ell^{\phi\phi}$ at multipoles $\ell \gtrsim 100$ is through A_s and $\ell_{\rm eq}$ in ΛCDM models. Here, $\ell_{\rm eq} \propto 1/\theta_{\rm eq}$ is the angular multipole corresponding to the horizon size at matter-radiation equality observed at a distance χ_*. The combination $A_s \ell_{\rm eq}$ determines the mean-squared deflection $\langle d^2 \rangle$, while $\ell_{\rm eq}$ controls the shape of $C_\ell^{\phi\phi}$. For the parameter ranges of interest,

$$\delta C_\ell^{\phi\phi}/C_\ell^{\phi\phi} = \delta A_s/A_s + (n_\ell + 1)\delta \ell_{\rm eq}/\ell_{\rm eq}, \quad (19)$$

---

[18] In detail, the theory spectrum is binned in the same way as the data, renormalized to account for the (very small) difference between the CMB spectra in the best-fit model and the fiducial spectra used in the lensing analysis, and corrected for the difference in $N^{(1)}$, calculated for the best-fit and fiducial models (around a 4% change in $N^{(1)}$, since the fiducial-model $C_\ell^{\phi\phi}$ is higher by this amount than in the best-fit model).
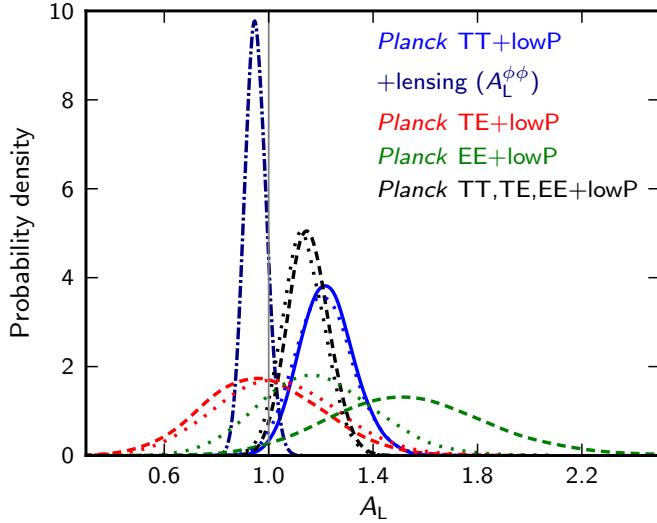
Fig. 12. Marginalized posterior distributions for measures of the lensing power amplitude. The dark-blue (dot-dashed) line is the constraint on the parameter $A_L^{\phi\phi}$, which scales the amplitude of the lensing power spectrum in the lensing likelihood for the *Planck* TT+lowP+lensing data combination. The other lines are for the A_L parameter, which scales the lensing power spectrum used to lens the CMB spectra, for the data combinations *Planck* TT+lowP (blue, solid), *Planck* TE+lowP (red, dashed), *Planck* EE+lowP (green, dashed), and *Planck* TT,TE,EE+lowP (black, dashed). The dotted lines show the A_L constraints when the `Plik` likelihood is replaced with `CamSpec`, highlighting that the preference for high A_L in the *Planck* EE+lowP data combination is not robust to the treatment of polarization on intermediate and small scales.

where n_ℓ arises (mostly) from the strong wavenumber dependence of the transfer function for the gravitational potential, with $n_\ell \approx 1.5$ around $\ell = 200$.

In joint fits to *Planck* TT+lowP+lensing, the main parameter changes from *Planck* TT+lowP alone are a 2.6% reduction in the best-fit A_s, with an accompanying reduction in the best-fit τ, to 0.067 (around 0.6σ; see Sect. 3.4). There is also a 0.7% reduction in ℓ_{eq}, achieved at fixed θ_* by reducing ω_m. These combine to reduce $C_\ell^{\phi\phi}$ by approximately 4% at $\ell = 200$, consistent with Eq. (19). The difference between the theory lensing spectrum at the best-fit parameters in the *Planck* TT+lowP and *Planck* TT+lowP+lensing fits are shown by the dashed blue lines in Fig. 11. In the joint fit, the χ^2 for the lensing bandpowers improves by 6, while the χ^2 for the *Planck* TT+lowP data degrades by only 1.2 (2.8 for the high-ℓ *TT* data and -1.6 for the low-ℓ *TEB* data).

The lower values of A_s and ω_m in the joint fit give a 2% reduction in σ_8, with

$$\sigma_8 = 0.815 \pm 0.009 \quad (68\%, Planck \text{ TT+lowP+lensing}), \quad (20)$$

as shown in Fig. 19. The decrease in matter density leads to a corresponding decrease in Ω_m, and at fixed θ_* (approximately $\propto \Omega_m h^3$) a 0.5σ increase in H_0, giving

$$\left.\begin{array}{l} H_0 = (67.8 \pm 0.9) \text{ km s}^{-1}\text{Mpc}^{-1} \\ \Omega_m = 0.308 \pm 0.012 \end{array}\right\} Planck \text{ TT+lowP+lensing.} \quad (21)$$

Joint *Planck*+lensing constraints on other parameters of the base ΛCDM cosmology are given in Table. 4.

Planck Collaboration XV (2016) discusses the effect on parameters of extending the lensing multipole range in joint fits with *Planck* TT+lowP. In the base ΛCDM model, using the full multipole range $8 \leq \ell \leq 2048$, the parameter combination $\sigma_8\Omega_m^{1/4} \approx (A_s\ell_{eq}^{2.5})^{1/2}$ (which is well determined by the lensing measurements) is pulled around 1σ lower that its value using the conservative lensing range, with a negligible change in the uncertainty. Around half of this shift comes from the 3.6σ outlying bandpower ($638 \leq \ell \leq 762$). In massive neutrino models, the total mass is similarly pulled higher by around 1σ when using the full lensing multipole range.

5.1.2. Detection of lensing in the CMB power spectra

The smoothing effect of lensing on the acoustic peaks and troughs of the *TT* power spectrum is detected at high significance in the *Planck* data. Following PCP13 (see also Calabrese et al. 2008), we introduce a parameter A_L, which scales the theory $C_\ell^{\phi\phi}$ power spectrum at each point in parameter space, and which is used to lens the CMB spectra[19]. The expected value for base ΛCDM is $A_L = 1$. The results of such an analysis for models with variable A_L is shown in Fig. 12. The marginalized constraint on A_L is

$$A_L = 1.22 \pm 0.10 \quad (68\%, Planck \text{ TT+lowP}). \quad (22)$$

This is very similar to the result from the 2013 *Planck* data reported in PCP13. The persistent preference for $A_L > 1$ is discussed in detail there. For the 2015 data, we find that $\Delta\chi^2 = -6.4$ between the best-fitting ΛCDM+A_L model and the best-fitting base ΛCDM model. There is roughly equal preference for high A_L from intermediate and high multipoles (i.e., the `Plik` likelihood; $\Delta\chi^2 = -2.6$) and from the low-ℓ likelihood ($\Delta\chi^2 = -3.1$), with a further small change coming from the priors.

Increases in A_L are accompanied by changes in all other parameters, with the general effect being to reduce the predicted CMB power on large scales, and in the region of the second acoustic peak, and to increase CMB power on small scales (see Fig. 13). A reduction in the high-ℓ foreground power compensates the CMB increase on small scales. Specifically, n_s is increased by 1% relative to the best-fitting base model and A_s is reduced by 4%, both of which lower the large-scale power to provide a better fit to the measured spectra around $\ell = 20$ (see Fig. 1). The densities ω_b and ω_c respond to the change in n_s, following the usual ΛCDM acoustic degeneracy, and $A_s e^{-2\tau}$ falls by 1%, attempting to reduce power in the damping tail due to the increase in n_s and reduction in the diffusion angle θ_D (which follows from the reduction in ω_m). The changes in A_s and $A_s e^{-2\tau}$ lead to a reduction in τ from 0.078 to 0.060. With these cosmological parameters, the lensing power is lower than in the base model, which additionally increases the CMB power in the acoustic peaks and reduces it in the troughs. This provides a poor fit to the measured spectra around the fourth and fifth peaks, but this can be mitigated by increasing A_L to give more smoothing from lensing than in the base model. However, A_L further increases power in the damping tail, but this is partly offset by reduction of the power in the high-ℓ foregrounds.

---

[19] We emphasize the difference between the phenomenological parameters A_L and $A_L^{\phi\phi}$ (introduced earlier). The amplitude A_L multiplies $C_\ell^{\phi\phi}$ when calculating both the lensed CMB theory spectra and the lensing likelihood, while $A_L^{\phi\phi}$ affects only the lensing likelihood by scaling the theory $C_\ell^{\phi\phi}$ when comparing with the power spectrum of the reconstructed lensing potential ϕ.
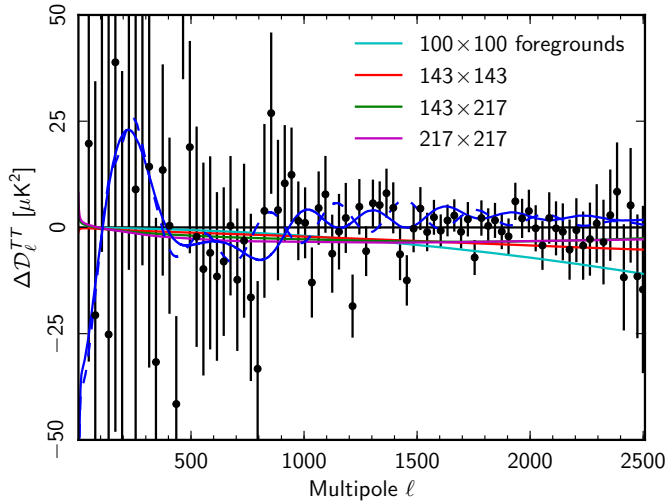
Fig. 13. Changes in the CMB TT spectrum and foreground spectra, between the best-fitting A_L model and the best-fitting base ΛCDM model to the *Planck* TT+lowP data. The solid blue line shows the difference between the A_L model and ΛCDM while the dashed line has the the same values of the other cosmological parameters, but with A_L set to unity, to highlight the changes in the spectrum arising from differences in the other parameters. Also shown are the changes in the best-fitting foreground contributions to the four frequency cross-spectra between the A_L model and the ΛCDM model. The data points (with $\pm 1\sigma$ errors) are the differences between the high-ℓ maximum-likelihood frequency-averaged CMB spectrum and the best-fitting ΛCDM model to the *Planck* TT+lowP data (as in Fig. 1). Note that the changes in the CMB spectrum and the foregrounds should be added when comparing to the residuals in the data points.

The trends in the TT spectrum that favour high A_L have a similar pull on parameters such as curvature (Sect. 6.2.4) and the dark energy equation of state (Sect. 6.3) in extended models. These parameters affect the late-time geometry and clustering and so alter the lensing power, but their effect on the primary CMB fluctuations is degenerate with changes in the Hubble constant (to preserve θ_*). The same parameter changes as those in A_L models are found in these extended models, but with, for example, the increase in A_L replaced by a reduction in Ω_K. Adding external data, however, such as the *Planck* lensing data or BAO (Sect. 5.2), pull these extended models back to base ΛCDM.

Finally, we note that lensing is also detected at lower significance in the polarization power spectra (see Fig. 12):

$$A_L = 0.98^{+0.21}_{-0.24} \quad (68\%, \textit{Planck} \text{ TE+lowP}), \quad (23a)$$

$$A_L = 1.54^{+0.28}_{-0.33} \quad (68\%, \textit{Planck} \text{ EE+lowP}). \quad (23b)$$

These results use only polarization at low multipoles, i.e., with no temperature data at multipoles $\ell < 30$. These are the first detections of lensing in the CMB polarization spectra, and reach almost 5σ in TE. We caution the reader that the A_L constraints from EE and low-ℓ polarization are rather unstable between high-ℓ likelihoods because of differences in the treatment of the polarization data (see Fig. 12, which compares constraints from the `Plik` and `CamSpec` polarization likelihoods). The result of replacing `Plik` with the `CamSpec` likelihood is $A_L = 1.19^{+0.20}_{-0.24}$, i.e., around 1σ lower than the result from `Plik` reported in Eq. (23b). If we additionally include the low-ℓ temperature data, A_L from TE increases:

$$A_L = 1.13 \pm 0.2 \quad (68\%, \textit{Planck} \text{ TE+lowT,P}). \quad (24)$$

The pull to higher A_L in this case is due to the reduction in TT power in these models on large scales (as discussed above).
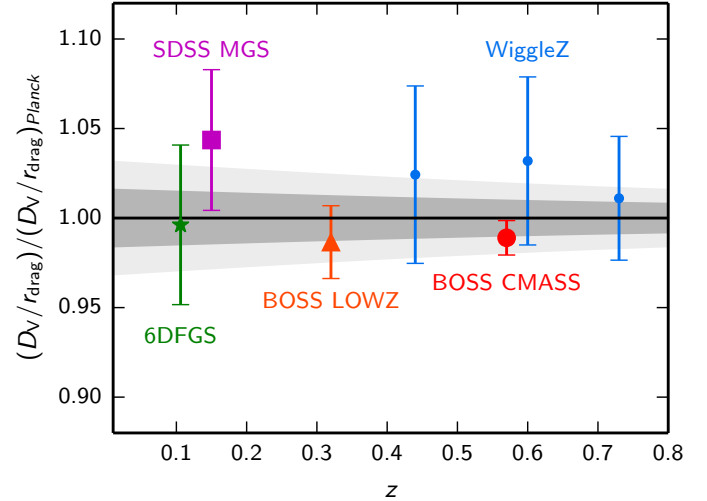
Fig. 14. Acoustic-scale distance ratio $D_V(z)/r_{drag}$ in the base ΛCDM model divided by the mean distance ratio from *Planck* TT+lowP+lensing. The points with 1σ errors are as follows: green star (6dFGS, Beutler et al. 2011); square (SDSS MGS, Ross et al. 2015); red triangle and large circle (BOSS "LOWZ" and CMASS surveys, Anderson et al. 2014); and small blue circles (WiggleZ, as analysed by Kazin et al. 2014). The grey bands show the 68% and 95% confidence ranges allowed by *Planck* TT+lowP+lensing.

5.2. Baryon acoustic oscillations

Baryon acoustic oscillation (BAO) measurements are geometric and largely unaffected by uncertainties in the nonlinear evolution of the matter density field and additional systematic errors that may affect other types of astrophysical data. As in PCP13, we therefore use BAO as a primary astrophysical data set to break parameter degeneracies from CMB measurements.

Figure 14 shows an updated version of Fig. 15 from PCP13. The plot shows the acoustic-scale distance ratio $D_V(z)/r_{drag}$ measured from a number of large-scale structure surveys with effective redshift z, divided by the mean acoustic-scale ratio in the base ΛCDM cosmology using *Planck* TT+lowP+lensing. Here r_{drag} is the comoving sound horizon at the end of the baryon drag epoch and D_V is a combination of the angular diameter distance $D_A(z)$ and Hubble parameter $H(z)$,

$$D_V(z) = \left[(1+z)^2 D_A^2(z) \frac{cz}{H(z)} \right]^{1/3}. \quad (25)$$

The grey bands in the figure show the $\pm 1\sigma$ and $\pm 2\sigma$ ranges allowed by *Planck* in the base ΛCDM cosmology.

The changes to the data points compared to figure 15 of PCP13 are as follows. We have replaced the SDSS DR7 measurements of Percival et al. (2010) with the recent analysis of the SDSS Main Galaxy Sample (MGS) of Ross et al. (2015) at $z_{eff} = 0.15$, and by the Anderson et al. (2014) analysis of the Baryon Oscillation Spectroscopic Survey (BOSS) "LOWZ" sample at $z_{eff} = 0.32$. Both of these analyses use peculiar velocity field reconstructions to sharpen the BAO feature and reduce the errors on D_V/r_{drag}. The blue points in Fig. 14 show a reanalysis of the WiggleZ redshift survey by Kazin et al. (2014) that applyies peculiar velocity reconstructions. These reconstructions cause small shifts in D_V/r_{drag} compared to the unreconstructed WiggleZ results of Blake et al. (2011) and lead to reductions in the errors on the distance measurements at $z_{eff} = 0.44$ and $z_{eff} = 0.73$. The point labelled "BOSS CMASS" at $z_{eff} = 0.57$
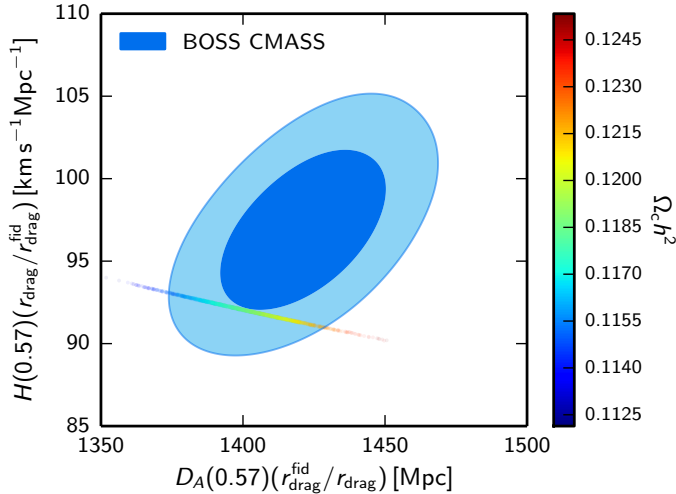
Fig. 15. 68% and 95% constraints on the angular diameter distance $D_A(z = 0.57)$ and Hubble parameter $H(z = 0.57)$ from the Anderson et al. (2014) analysis of the BOSS CMASS-DR11 sample. The fiducial sound horizon adopted by Anderson et al. (2014) is $r_{drag}^{fid} = 149.28$ Mpc. Samples from the *Planck* TT+lowP+lensing chains are plotted coloured by their value of $\Omega_c h^2$, showing consistency of the data, but also that the BAO measurement can tighten the *Planck* constraints on the matter density.

shows D_V/r_{drag} from the analysis of Anderson et al. (2014), updating the BOSS-DR9 analysis of Anderson et al. (2012) used in PCP13.

In fact, the Anderson et al. (2014) analysis solves jointly for the positions of the BAO feature in both the line-of-sight and transverse directions (the distortion in the transverse direction caused by the background cosmology is sometimes called the Alcock-Paczynski effect, Alcock & Paczynski 1979), leading to joint constraints on the angular diameter distance $D_A(z_{eff})$ and the Hubble parameter $H(z_{eff})$. These constraints, using the tabulated likelihood included in the `CosmoMC` module[20], are plotted in Fig. 15. Samples from the *Planck* TT+lowP+lensing chains are shown for comparison, coloured by the value of $\Omega_c h^2$. The length of the degeneracy line is set by the allowed variation in H_0 (or equivalently $\Omega_m h^2$). In the *Planck* TT+lowP+lensing ΛCDM analysis the line is defined approximately by

$$\frac{D_A(0.57)/r_{drag}}{9.384} \left(\frac{H(0.57)r_{drag}/c}{0.4582} \right)^{1.7} = 1.0000 \pm 0.0004, \quad (26)$$

which just grazes the BOSS CMASS 68% error ellipse plotted in Fig. 15. Evidently, the *Planck* base ΛCDM parameters are in good agreement with both the isotropized D_V BAO measurements plotted in Fig. 14, and with the anisotropic constraints plotted in Fig. 15.

In this paper, we use the 6dFGS, SDSS-MGS, and BOSS-LOWZ BAO measurements of D_V/r_{drag} (Beutler et al. 2011; Ross et al. 2015; Anderson et al. 2014) and the CMASS-DR11 anisotropic BAO measurements of Anderson et al. (2014). Since the WiggleZ volume partially overlaps that of the BOSS-CMASS sample, and the correlations have not been quantified, we do not use the WiggleZ results in this paper. It is clear from Fig. 14 that the combined BAO likelihood is dominated by the two BOSS measurements.

In the base ΛCDM model, the *Planck* data constrain the Hubble constant H_0 and matter density Ω_m to high precision:

$$\left. \begin{array}{l} H_0 = (67.3 \pm 1.0) \text{ km s}^{-1}\text{Mpc}^{-1} \\ \Omega_m = 0.315 \pm 0.013 \end{array} \right\} \textit{Planck} \text{ TT+lowP.} \quad (27)$$

With the addition of the BAO measurements, these constraints are strengthened significantly to

$$\left. \begin{array}{l} H_0 = (67.6 \pm 0.6) \text{ km s}^{-1}\text{Mpc}^{-1} \\ \Omega_m = 0.310 \pm 0.008 \end{array} \right\} \textit{Planck} \text{ TT+lowP+BAO.} \quad (28)$$

These numbers are consistent with the *Planck*+lensing constraints of Eq. (21). Section 5.4 discusses the consistency of these estimates of H_0 with direct measurements.

Although low-redshift BAO measurements are in good agreement with *Planck* for the base ΛCDM cosmology, this may not be true at high redshifts. Recently, BAO features have been measured in the flux-correlation function of the Lyα forest of BOSS quasars (Delubac et al. 2015) and in the cross-correlation of the Lyα forest with quasars (Font-Ribera et al. 2014). These observations give measurements of $c/(H(z)r_{drag})$ and $D_A(z)/r_{drag}$ (with somewhat lower precision) at $z = 2.34$ and $z = 2.36$, respectively. For example, from table II of Aubourg et al. (2015) the two Lyα BAO measurements combined give $c/(H(2.34)r_{drag}) = 9.14 \pm 0.20$, compared to the predictions of the base *Planck* ΛCDM cosmology of 8.586 ± 0.021, which are discrepant at the 2.7σ level. At present, it is not clear whether this discrepancy is caused by systematics in the Lyα BAO measurements (which are more complex and less mature than galaxy BAO measurements) or an indicator of new physics. As Aubourg et al. (2015) discuss, it is difficult to find a physical explanation for the Lyα BAO results without disrupting the consistency with the much more precise galaxy BAO measurements at lower redshifts.

5.3. Type Ia supernovae

Type Ia supernovae (SNe) are powerful probes of cosmology (Riess et al. 1998; Perlmutter et al. 1999) and particularly of the equation of state of dark energy. In PCP13, we used two samples of type Ia SNe, the "SNLS" compilation (Conley et al. 2011) and the "Union2.1" compilation (Suzuki et al. 2012). The SNLS sample was found to be in mild tension, at about the 2σ level, with the 2013 *Planck* base ΛCDM cosmology favouring a value of $\Omega_m \approx 0.23$ compared to the *Planck* value of $\Omega_m = 0.315 \pm 0.017$. Another consequence of this tension showed up in extensions to the base ΛCDM model, where the combination of *Planck* and the SNLS sample showed 2σ evidence for a "phantom" ($w < -1$) dark energy equation of state.

Following the submission of PCP13, Betoule et al. (2013) reported the results of an extensive campaign to improve the relative photometric calibrations between the SNLS and SDSS supernova surveys. The "Joint Light-curve Analysis" (JLA) sample, used in this paper, is constructed from the SNLS and SDSS SNe data, together with several samples of low redshift SNe[21].

---

[20] http://www.sdss3.org/science/boss_publications.php

[21] A `CosmoMC` likelihood model for the JLA sample is available at http://supernovae.in2p3.fr/sdss_snls_jla/ReadMe.html. The latest version in `CosmoMC` includes numerical integration over the nuisance parameters for use when calculating joint constraints using importance sampling; this can give different χ^2 values compared to parameter best fits.

Cosmological constraints from the JLA sample are discussed by Betoule et al. (2014) and residual biases associated with the photometry and light curve fitting are assessed by Mosher et al. (2014). For the base ΛCDM cosmology, Betoule et al. (2014) find $\Omega_m = 0.295 \pm 0.034$, consistent with the 2013 and 2015 *Planck* values for base ΛCDM. This relieves the tension between the SNLS and *Planck* data reported in PCP13. Given the consistency between *Planck* and the JLA sample for base ΛCDM, one can anticipate that the combination of these two data sets will constrain the dark energy equation of state to be close to $w = -1$ (see Sect. 6.3).

Since the submission of PCP13, first results from a sample of Type Ia SNe discovered with the Pan-STARRS survey have been reported by Rest et al. (2014) and Scolnic et al. (2014). The Pan-STARRS sample is still relatively small (consisting of 146 spectroscopically confirmed Type Ia SNe) and is not used in this paper.

5.4. The Hubble constant

CMB experiments provide indirect and highly model-dependent estimates of the Hubble constant. It is therefore important to compare CMB estimates with direct estimates of H_0, since any significant evidence of a tension could indicate the need for new physics. In PCP13, we used the Riess et al. (2011, hereafter R11) *Hubble* Space Telescope (HST) Cepheid+SNe based estimate of $H_0 = (73.8 \pm 2.4)$ km s^{-1}Mpc^{-1} as a supplementary "H_0-prior". This value was in tension at about the 2.5σ level with the 2013 *Planck* base ΛCDM value of H_0.

For the base ΛCDM model, CMB and BAO experiments consistently find a value of H_0 lower than the R11 value. For example, the 9-year WMAP data (Bennett et al. 2013; Hinshaw et al. 2013) give[22]:

$$H_0 = (69.7 \pm 2.1) \text{ km s}^{-1}\text{Mpc}^{-1}, \qquad \text{WMAP9}, \qquad (29a)$$
$$H_0 = (68.0 \pm 0.7) \text{ km s}^{-1}\text{Mpc}^{-1}, \qquad \text{WMAP9+BAO}. \qquad (29b)$$

These numbers can be compared with the *Planck* 2015 values given in Eqs. (27) and (28). The WMAP constraints are driven towards the *Planck* values by the addition of the BAO data and so there is persuasive evidence for a low H_0 in the base ΛCDM cosmology *independently of the high-multipole CMB results from Planck*. The 2015 *Planck* TT+lowP value is entirely consistent with the 2013 *Planck* value and so the tension with the R11 H_0 determination remains at about 2.4σ.

The tight constraint on H_0 in Eq. (29b) is an example of an "inverse distance ladder," where the CMB primarily constrains the sound horizon within a given cosmology, providing an absolute calibration of the BAO acoustic-scale (e.g., Percival et al. 2010; Cuesta et al. 2015; Aubourg et al. 2015, see also PCP13). In fact, in a recent paper Aubourg et al. (2015) use the 2013 *Planck* constraints on r_s in combination with BAO and the JLA SNe data to find $H_0 = (67.3 \pm 1.1)$ km s^{-1}Mpc^{-1}, in excellent agreement with the 2015 *Planck* value for base ΛCDM given in Eq. (27), *which is based on the Planck temperature power spectrum*. Note that by adding SNe data, the Aubourg et al. (2015) estimate of H_0 is insensitive to spatial curvature and to late time variations of the dark energy equation of state. Evidently, there are a number of lines of evidence that point to a lower value of H_0 than the direct determination of R11.

The R11 Cepheid data have been reanalysed by Efstathiou (2014, hereafter E14) using the revised geometric maser distance to NGC 4258 of Humphreys et al. (2013). Using NGC 4258 as a distance anchor, E14 finds

$$H_0 = (70.6 \pm 3.3) \text{ km s}^{-1}\text{Mpc}^{-1}, \qquad \text{NGC 4258}, \qquad (30)$$

which is within 1σ of the *Planck* TT estimate given in Eq. (27). In this paper we use Eq. (30) as a "conservative" H_0 prior.

R11 also use Large Magellanic Cloud Cepheids and a small sample of Milky Way Cepheids with parallax distances as alternative distance anchors to NGC 4258. The R11 H_0 prior used in PCP13 combines all three distance anchors. Combining the LMC and MW distance anchors, E14 finds

$$H_0 = (73.9 \pm 2.7) \text{ km s}^{-1}\text{Mpc}^{-1}, \qquad \text{LMC + MW}, \qquad (31)$$

under the assumption that there is no metallicity variation of the Cepheid period-luminosity relation. This is discrepant with Eq. (27) at about the 2.2σ level. However, neither the central value nor the error in Eq. (31) is reliable. The MW Cepheid sample is small and dominated by short period (<10 day) objects. The MW Cepheid sample therefore has very little overlap with the period range of SNe host galaxy Cepheids observed with HST. As a result, the MW solutions for H_0 are unstable (see Appendix A of E14). The LMC solution is sensitive to the metallicity dependence of the Cepheid period-luminosity relation which is poorly constrained by the R11 data. Furthermore, the estimate in Eq. (30) is based on a differential measurement, comparing HST photometry of Cepheids in NGC 4258 with those in SNe host galaxies. It is therefore less prone to photometric systematics, such as crowding corrections, than is the LMC+MW estimate of Eq. (31). It is for these reasons that we have adopted the prior of Eq. (30) in preference to using the LMC and MW distance anchors[23].

Direct measurements of the Hubble constant have a long and sometimes contentious history (see, e.g., Tammann et al. 2008). The controversy continues to this day and in the literature one can find "high" values, e.g., $H_0 = (74.3 \pm 2.6)$ km s^{-1}Mpc^{-1} (Freedman et al. 2012), and "low" values, e.g., $H_0 = (63.7 \pm 2.3)$ km s^{-1}Mpc^{-1} (Tammann & Reindl 2013). The key point that we wish to make is that the *Planck*-only estimates of Eqs. (21) and (27), and the *Planck*+BAO estimate of Eq. (28) all have small errors and are consistent. If a persuasive case can be made that a direct measurement of H_0 conflicts with these estimates, then this will be strong evidence for additional physics beyond the base ΛCDM model.

Finally, we note that in a recent analysis Bennett et al. (2014) derive a "concordance" value of $H_0 = (69.6 \pm 0.7)$ km s^{-1}Mpc^{-1} for base ΛCDM by combining WMAP9+SPT+ACT+BAO with a slightly revised version of the R11 H_0 value, (73.0 ± 2.4) km s^{-1}Mpc^{-1}. The Bennett et al. (2014) central value for H_0 differs from the *Planck* value of Eq. (28) by nearly 3% (or 2.5σ). The reason for this difference is that the *Planck* data are in tension with the Story et al. (2013) SPT data (as discussed in

---

[22] These numbers are taken from our parameter grid, which includes a neutrino mass of 0.06 eV and the same updated BAO compilation as Eq. (28) (see Sect. 5.2).

[23] As this paper was nearing completion, results from the Nearby Supernova Factory have been presented that indicate a correlation between the peak brightness of Type Ia SNe and the local star-formation rate (Rigault et al. 2015). These authors argue that this correlation introduces a systematic bias of around 1.8 km s^{-1}Mpc^{-1} in the SNe/Cepheid distance scale measurement of H_0. According to these authors, the estimate of Eq. (30) should be lowered to $H_0 = (68.8 \pm 3.3)$ km s^{-1}Mpc^{-1}, a downward shift of approximately 0.5σ. Clearly, further work needs to be done to assess the importance of such a bias on the distance scale. It is ignored in the rest of this paper.

Appendix B of PCP13; note that the tension is increased with the *Planck* full mission data) and with the revised R11 H_0 determination. Both tensions drive the Bennett et al. (2014) value of H_0 away from the *Planck* solution.

5.5. Additional data

5.5.1. Redshift space distortions

Transverse versus line-of-sight anisotropies in the redshift-space clustering of galaxies induced by peculiar motions can, potentially, provide a powerful way of constraining the growth rate of structure (e.g., Percival & White 2009). A number of studies of redshift-space distortions (RSD) have been conducted to measure the parameter combination $f\sigma_8(z)$, where for models with scale-independent growth

$$f(z) = \frac{\mathrm{d}\ln D}{\mathrm{d}\ln a}, \tag{32}$$

and D is the linear growth rate of matter fluctuations. Notice that the parameter combination $f\sigma_8$ is insensitive to differences between the clustering of galaxies and dark matter, i.e., to galaxy bias (Song & Percival 2009). In the base ΛCDM cosmology, the growth factor $f(z)$ is well approximated as $f(z) = \Omega_\mathrm{m}(z)^{0.545}$. More directly, in linear theory the quadrupole of the redshift-space clustering anisotropy actually probes the density-velocity correlation power spectrum, and we therefore define

$$f\sigma_8(z) \equiv \frac{\left[\sigma_8^{(vd)}(z)\right]^2}{\sigma_8^{(dd)}(z)}, \tag{33}$$

as an approximate proxy for the quantity actually being measured. Here $\sigma_8^{(vd)}$ measures the smoothed density-velocity correlation and is defined analogously to $\sigma_8 \equiv \sigma_8^{(dd)}$, but using the correlation power spectrum $P_{vd}(k)$, where $v = -\nabla\cdot\boldsymbol{v}_\mathrm{N}/H$ and $\boldsymbol{v}_\mathrm{N}$ is the Newtonian-gauge (peculiar) velocity of the baryons and dark matter, and d is the total matter density perturbation. This definition assumes that the observed galaxies follow the flow of the cold matter, not including massive neutrino velocity effects. For models close to ΛCDM, where the growth is nearly scale independent, it is equivalent to defining $f\sigma_8$ in terms of the growth of the baryon+CDM density perturbations (excluding neutrinos).

The use of RSD as a measure of the growth of structure is still under active development and is considerably more difficult than measuring the positions of BAO features. Firstly, adopting the wrong fiducial cosmology can induce an anisotropy in the clustering of galaxies, via the Alcock-Paczynski (AP) effect, which is strongly degenerate with the anisotropy induced by peculiar motions. Secondly, much of the RSD signal currently comes from scales where nonlinear effects and galaxy bias are significant and must be accurately modelled in order to relate the density and velocity fields (see, e.g., the discussions in Bianchi et al. 2012; Okumura et al. 2012; Reid et al. 2014; White et al. 2015).

Current constraints[24], assuming a *Planck* base ΛCDM model, are shown in Fig. 16. Neglecting the AP effect can lead to biased measurements of $f\sigma_8$ if the assumed cosmology differs, and to significant underestimation of the errors (Howlett et al. 2015). The analyses summarized in Fig. 16 solve simultaneously
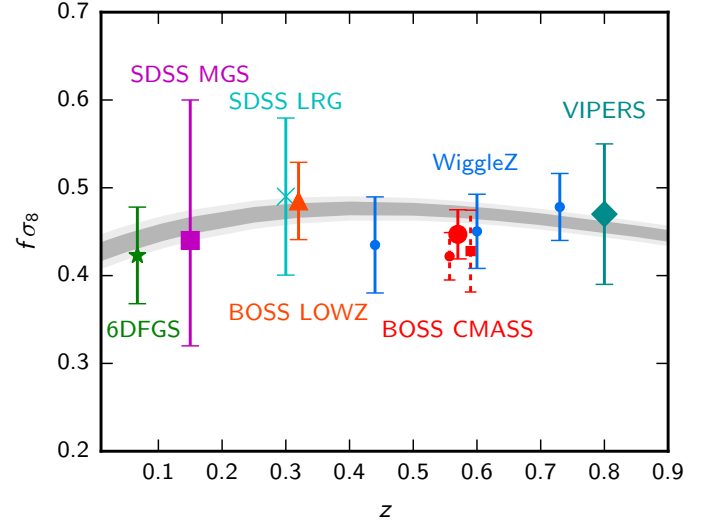
---

[24] The constraint of Chuang et al. (2016) plotted in the original version of this paper was subsequently shown to be in error. We therefore now show updated BOSS data points for DR12 from Chuang et al. (2016, for CMASS) and Gil-Marín et al. (2016, for LOWZ).


Fig. 16. Constraints on the growth rate of fluctuations from various redshift surveys in the base ΛCDM model: green star (6dFGRS, Beutler et al. 2012); purple square (SDSS MGS, Howlett et al. 2015); cyan cross (SDSS LRG, Oka et al. 2014); red triangle (BOSS LOWZ survey, Gil-Marín et al. 2016); large red circle (BOSS CMASS, as analysed by Samushia et al. 2014); blue circles (WiggleZ, Blake et al. 2012); and green diamond (VIPERS, de la Torre et al. 2013). The points with dashed red error bars correspond to alternative analyses of BOSS CMASS from Beutler et al. (2014a, small circle, offset for clarity) and Chuang et al. (2016, small square). Of the BOSS CMASS points, two are based on the same DR11 data set (Samushia et al. 2014; Beutler et al. 2014a), while the third is based on the more recent DR12 (Chuang et al. 2016), and are therefore not independent. The grey bands show the range allowed by *Planck* TT+lowP+lensing in the base ΛCDM model. Where available (for SDSS MGS and BOSS), we have plotted conditional constraints on $f\sigma_8$ assuming a *Planck* ΛCDM background cosmology. The WiggleZ points are plotted conditional on the mean *Planck* cosmology prediction for F_AP (evaluated using the covariance between $f\sigma_8$ and F_AP given in Blake et al. 2012). The 6dFGS point is at sufficiently low redshift that it is insensitive to the cosmology.

for RSD and the AP effect, except for the 6dFGS point (which is insensitive to cosmology) and the VIPERS point (which has a large error). The grey bands show the range allowed by *Planck* TT+lowP+lensing in the base ΛCDM model, and are consistent with the RSD data. The tightest constraints on $f\sigma_8$ in this figure come from the BOSS CMASS-DR11 analyses of Beutler et al. (2014a) and Samushia et al. (2014). The Beutler et al. (2014a) analysis is performed in Fourier space and shows a small bias in $f\sigma_8$ compared to numerical simulations when fitting over the wavenumber range $0.01-0.20\,h\,\mathrm{Mpc}^{-1}$. The Samushia et al. (2014) analysis is performed in configuration space and shows no evidence of biases when compared to numerical simulations. The updated DR12 CMASS result from Chuang et al. (2016) marginalizes over a polynomial model for systematic errors in the correlation function monopole, and is consistent with these and the *Planck* constraints, with a somewhat larger error bar.

The Samushia et al. (2014) results are expressed as a 3×3 covariance matrix for the three parameters $D_\mathrm{V}/r_\mathrm{drag}$, F_AP and $f\sigma_8$, evaluated at an effective redshift of $z_\mathrm{eff} = 0.57$, where F_AP is the "Alcock-Paczynski" parameter

$$F_\mathrm{AP}(z) = (1 + z)D_\mathrm{A}\frac{H(z)}{c}. \tag{34}$$

The principal degeneracy is between $f\sigma_8$ and F_AP and is illustrated in Fig. 17, compared to the constraint from *Planck*
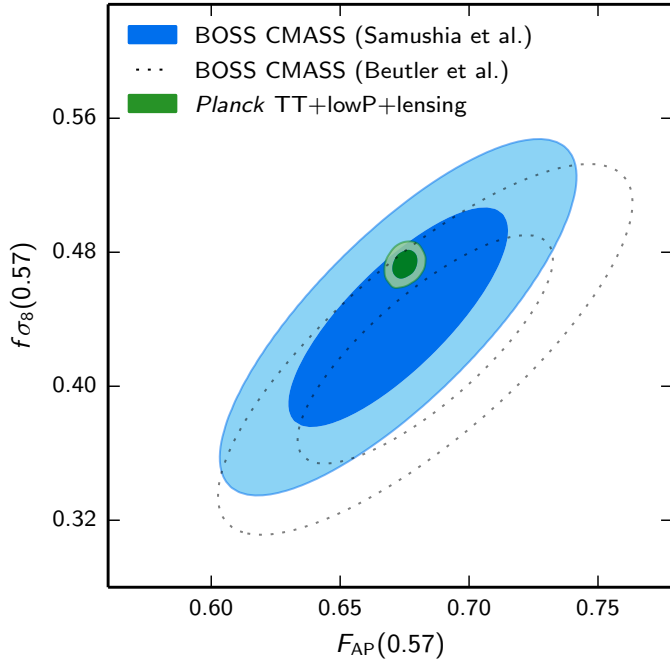
Fig. 17. 68% and 95% contours in the $f\sigma_8$–$F_{\rm AP}$ plane (marginalizing over $D_{\rm v}/r_{\rm s}$) for the CMASS-DR11 sample as analysed by Samushia et al. (2014, solid, our defult), and Beutler et al. (2014a, dotted). The green contours show the constraint from *Planck* TT+lowP+lensing in the base ΛCDM model.

TT+lowP+lensing for the base ΛCDM cosmology. The *Planck* results sit slightly high but overlap the 68% contour from Samushia et al. (2014). The *Planck* result lies about 1.5σ higher than the Beutler et al. (2014a) analysis of the BOSS CMASS sample.

RSD measurements are not used in combination with *Planck* in this paper. However, in the companion paper exploring dark energy and modified gravity (Planck Collaboration XIV 2016), the RSD/BAO measurements of Samushia et al. (2014) are used together with *Planck*. Where this is done, we *exclude* the Anderson et al. (2014) BOSS-CMASS results from the BAO likelihood. Since Samushia et al. (2014) do not apply a density field reconstruction in their analysis, the BAO constraints from BOSS-CMASS are then slightly weaker, though consistent, with those of Anderson et al. (2014).

5.5.2. Weak gravitational lensing

Weak gravitational lensing offers a potentially powerful technique for measuring the amplitude of the matter fluctuation spectrum at low redshifts. Currently, the largest weak lensing data set is provided by the CFHTLenS survey (Heymans et al. 2012; Erben et al. 2013). The first science results from this survey appeared shortly before the completion of PCP13 and it was not possible to do much more than offer a cursory comparison with the *Planck* 2013 results. As reported in PCP13, at face value the results from CFHTLenS appeared to be in tension with the *Planck* 2013 base ΛCDM cosmology at about the 2–3σ level. Since neither the CFHTLenS results nor the 2015 *Planck* results have changed significantly from those in PCP13, it is worth discussing this discrepancy in more detail in this paper.

Weak lensing data can be analysed in various ways. For example, one can compute two correlation functions from the ellipticities of pairs of images separated by angle θ, which are related
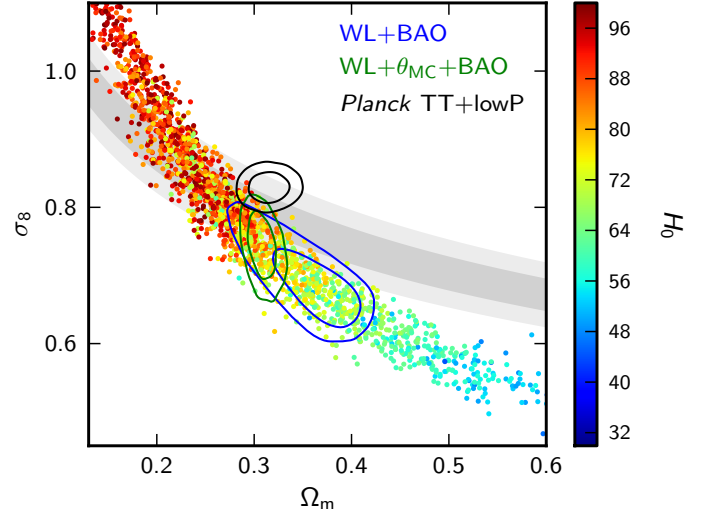
Fig. 18. Samples in the σ_8–$\Omega_{\rm m}$ plane from the H13 CFHTLenS data (with angular cuts as discussed in the text), coloured by the value of the Hubble parameter, compared to the joint constraints when the lensing data are combined with BAO (blue), and BAO with the CMB acoustic scale parameter fixed to $\theta_{\rm MC} = 1.0408$ (green). For comparison, the *Planck* TT+lowP constraint contours are shown in black. The grey bands show the constraint from *Planck* CMB lensing. We impose a weak prior on the primoridal amplitude, $2 < \ln(10^{10}A_{\rm s}) < 4$, which has some impact on the distribution of CFHTLenS-only samples.

to the convergence power spectrum $P^\kappa(\ell)$ of the survey at multipole ℓ via

$$\xi_\pm(\theta) = \frac{1}{2\pi}\int {\rm d}\ell\,\ell\, P^\kappa(\ell) J_\pm(\ell\theta), \qquad (35)$$

where the Bessel functions in (35) are $J_+ \equiv J_0$ and $J_- \equiv J_4$ (see, e.g., Bartelmann & Schneider 2001). Much of the information from the CFHTLenS survey correlation function analyses comes from wavenumbers at which the matter power spectrum is strongly nonlinear, complicating any direct comparison with *Planck*.

This can be circumventing by performing a 3D spherical harmonic analysis of the shear field, allowing one to impose lower limits on the wavenumbers that contribute to a weak lensing likelihood. This has been done by Kitching et al. (2014). Including only wavenumbers with $k \le 1.5\,h\,{\rm Mpc}^{-1}$, Kitching et al. (2014) find constraints in the σ_8–$\Omega_{\rm m}$ plane that are consistent with the results from *Planck*. However, by excluding modes with higher wavenumbers, the lensing constraints are weakened. When they increase the wavenumber cut-off to $k = 5\,h\,{\rm Mpc}^{-1}$ some tension with *Planck* begins to emerge (which these authors argue may be an indication of the effects of baryonic feedback in suppressing the matter power spectrum at small scales). The large-scale properties of CFHTLenS therefore seem broadly consistent with *Planck* and it is only as CFHTLenS probes higher wavenumbers, particular in the 2D and tomographic correlation function analyses (Heymans et al. 2013; Kilbinger et al. 2013; Fu et al. 2014; MacCrann et al. 2015), that apparently strong discrepancies with *Planck* appear.

The situation is summarized in Fig. 18. The sample points show parameter values in the σ_8–$\Omega_{\rm m}$ plane for the ΛCDM base model, computed from the Heymans et al. (2013, hereafter H13) tomographic measurements of $\xi_\pm$. These data consist of correlation function measurements in six photometric redshift bins extending over the redshift range 0.2–1.3. We use the blue galaxy

sample, since H13 find that this sample shows no evidence for intrinsic galaxy alignments (simplifying the comparison with theory) and we apply the "conservative" cuts of H13, intended to reduce sensitivity to the nonlinear part of the power spectrum; these cuts eliminate measurements with $\theta < 3'$ for any redshift combination that involves the lowest two redshift bins. Here we have used the `halofit` prescription of Takahashi et al. (2012) to model the nonlinear power spectrum, but do not include any model of baryon feedback or intrinsic alignments. For the lensing-only constraint we also impose additional priors in a similar way to the CMB lensing analysis described in Planck Collaboration XV (2016), i.e., Gaussian priors $\Omega_b h^2 = 0.0223 \pm 0.0009$ and $n_s = 0.96 \pm 0.02$, where the exact values (chosen to span reasonable ranges given CMB data) have little impact on the results. The sample range shown also restricts the Hubble parameter to $0.2 < h < 1$; note that when comparing with constraint contours, the location of the contours can change significantly depending on the H_0 prior range assumed. We also use a weak prior on the primoridal amplitude, $2 < \ln(10^{10} A_s) < 4$, which shows up the strong correlation between Ω_m–σ_8–H_0 in the region of parameter space relevant for comparison with *Planck*. In Fig. 18 we only show lensing contours after the samples have been projected into the space allowed by the BAO data (blue contours), or also additionally restricting to the reduced space where θ_{MC} is fixed to the *Planck* value, which is accurately measured. The black contours show the constraints from *Planck* TT+lowP.

The lensing samples just overlap with *Planck*, and superficially one might conclude that the two data sets are consistent. However, the weak lensing constraints approximately define a 1D degeneracy in the 3D Ω_m–σ_8–H_0 space, so consistency of the Hubble parameter at each point in the projected space must also be considered (see appendix E1 of Planck Collaboration XV 2016). Comparing the contours in Fig. 18 (the regions where the weak lensing constraints are consistent with BAO observations) the CFHTLenS data favour a lower value of σ_8 than the *Planck* data (and much of the area of the blue contours also has higher Ω_m). However, even with the conservative angular cuts applied by H13, the weak lensing constraints depend on the nonlinear model of the power spectrum and on the possible influence of baryonic feedback in reshaping the matter power spectrum at small spatial scales (Harnois-Déraps et al. 2015; MacCrann et al. 2015). The importance of these effects can be reduced by imposing even more conservative angular cuts on $\xi_\pm$, but of course, this weakens the statistical power of the weak lensing data. The CFHTLenS data are not used in combination with *Planck* in this paper (apart from specific cases in Sects. 6.3 and 6.4.4) and, in any case, would have little impact on most of the extended ΛCDM constraints discussed in Sect. 6. Weak lensing can, however, provide important constraints on dark energy and modified gravity. The CFHTLenS data are therefore used in combination with *Planck* in the companion paper (Planck Collaboration XIV 2016), which explores several `halofit` prescriptions and the impact of applying more conservative angular cuts to the H13 measurements.

5.5.3. Planck cluster counts

In 2013 we noted a possible tension between our primary CMB constraints and those from the *Planck* SZ cluster counts, with the clusters preferring lower values of σ_8 in the base ΛCDM model in some analyses (Planck Collaboration XX 2014). The comparison is interesting because the cluster counts directly measure σ_8 at low redshift; any tension could signal the need for extensions to the base model, such as non-minimal neutrino mass (though

see Sect. 6.4). However, limited knowledge of the scaling relation between SZ signal and mass have hampered the interpretation of this result.

With the full mission data we have created a larger catalogue of SZ clusters with a more accurate characterization of its completeness (Planck Collaboration XXIV 2016). By fitting the counts in redshift and signal-to-noise, we are able to simultaneously constrain the slope of the SZ signal–mass scaling relation and the cosmological parameters. A major uncertainty, however, remains the overall mass calibration, which in Planck Collaboration XX (2014) we quantified with a "hydrostatic bias" parameter, $(1 - b)$, with a fiducial value of 0.8 and a range $0.7 < (1 - b) < 1$ (consistent with some other studies, e.g., Simet et al. 2015). In the base ΛCDM model, the primary CMB constraints prefer a normalization below the lower end of this range, $(1 - b) \approx 0.6$. The recent, empirical normalization of the relation by the Weighing the Giants lensing programme (WtG; von der Linden et al. 2014) gives 0.69 ± 0.07 for the 22 clusters in common with the *Planck* cluster sample. This calibration reduces the tension with the primary CMB constraints in base ΛCDM. In contrast, correlating the entire *Planck* 2015 SZ cosmology sample with *Planck* CMB lensing gives $1/(1 - b) = 1.0 \pm 0.2$ (Planck Collaboration XXIV 2016), toward the upper end of the range adopted in Planck Collaboration XX (2014), although with a large uncertainty. An alternative lensing calibration analysis by the Canadian Cluster Comparison Project, which uses 37 clusters in common with the *Planck* cluster sample (Hoekstra et al. 2015) finds $(1 - b) = 0.76 \pm 0.05$ (stat.) $\pm$ 0.06 (syst.), which lies between the other two mass calibrations. These calibrations are not yet definitive and the situation will continue to evolve with improvements in mass measurements from larger samples of clusters.

A recent analysis of cluster counts for an X-ray-selected sample (REFLEX II) shows some tension with the *Planck* base ΛCDM cosmology (Böhringer et al. 2014). However, an analysis of cluster counts of X-ray-selected clusters by the WtG collaboration, incorporating the WtG weak lensing mass calibration, finds $\sigma_8(\Omega_m/0.3)^{0.17} = 0.81 \pm 0.03$, in good agreement with the *Planck* CMB results for base ΛCDM (Mantz et al. 2015). This raises the possibility that there may be systematic biases in the assumed scaling relations for SZ-selected clusters compared to X-ray-selected clusters (in addition to a possible mass calibration bias). Mantz et al. (2015) give a brief review of recent determinations of σ_8 from X-ray, optically-selected, and SZ-selected samples, to which we refer the reader. More detailed discussion of constraints from combining *Planck* cluster counts with primary CMB anisotropies and other data sets can be found in Planck Collaboration XXIV (2016).

5.6. Cosmic concordance?

Table 4 summarizes the cosmological parameters in the base ΛCDM for *Planck* combined with various data sets discussed in this section. Although we have seen from the survey presented above that base ΛCDM is consistent with a wide range of cosmological data, there are two areas of tension:

1. the Lyα BAO measurements at high redshift (Sect. 5.2);
2. the *Planck* CMB estimate of the amplitude of the fluctuation spectrum and the lower values inferred from weak lensing, and (possibly) cluster counts and redshift space distortions (Sect. 5.5).

The first point to note is that the astrophysical data in areas (1) and (2) are complex and more difficult to interpret than most of
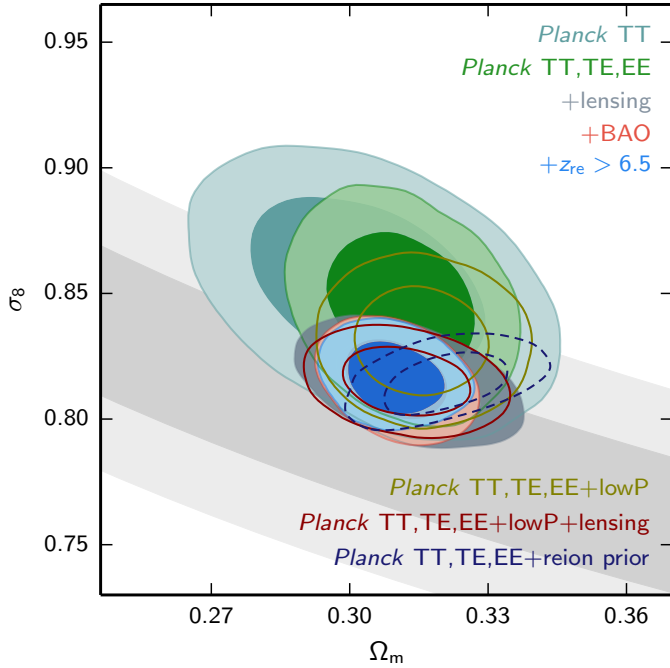
Fig. 19. Marginalized constraints on parameters of the base ΛCDM model without low-ℓ E-mode polarization (filled contours), compared to the constraints from using low-ℓ E-mode polarization (unfilled contours) or assuming a strong prior that reionization was at $z_{\mathrm{re}} = 7 \pm 1$ and $z_{\mathrm{re}} > 6.5$ ("reion prior", dashed contours). Grey bands show the constraint from CMB lensing alone.

the astrophysical data sets discussed in this section. The interpretation of the data in area (2) depends on nonlinear modelling of the power spectrum, and in the case of clusters and weak lensing, on uncertain baryonic physics. Understanding these effects more accurately sets a direction for future research.

It is, however, worth reviewing our findings on σ_8 and Ω_{m} from *Planck* assuming base ΛCDM. These are summarized in Fig. 19 and the following constraints:

$$\sigma_8 = 0.829 \pm 0.014, \quad \textit{Planck} \text{ TT+lowP}, \tag{36a}$$

$$\sigma_8 = 0.815 \pm 0.009, \quad \textit{Planck} \text{ TT+lowP+lensing}, \tag{36b}$$

$$\sigma_8 = 0.810 \pm 0.006, \quad \textit{Planck} \text{ TT+lensing}+z_{\mathrm{re}}. \tag{36c}$$

The last line imposes a Gaussian prior of $z_{\mathrm{re}} = 7 \pm 1$ with a limit $z_{\mathrm{re}} > 6.5$ on the reionization redshift in place of the reionization constraints from the lowP likelihood. As discussed in Sect. 3.4, such a low redshift of reionization is close to the lowest plausible value allowed by astrophysical data (though such low values are not favoured by either the WMAP or LFI polarization data). The addition of *Planck* lensing data pulls σ_8 down by about 1σ from the *Planck* TT+lowP value, so Eq. (36c) is the lowest possible range allowed by the *Planck* CMB data. As shown in Fig. 19, adding the TE and EE spectra at high multipoles does not change the *Planck* constraints. If a convincing case can be made that astrophysical data conflict with the estimate of Eq. (36c), then this will be powerful evidence for new physics beyond base ΛCDM with minimal-mass neutrinos.

A number of authors have interpreted the discrepancies in area (2) as evidence for new physics in the neutrino sector (e.g., Planck Collaboration XX 2014; Hamann & Hasenkamp 2013; Battye & Moss 2014; Battye et al. 2015; Wyman et al. 2014; Beutler et al. 2014b). They use various data combinations together with *Planck* to argue for massive neutrinos with mass

$\sum m_\nu \approx 0.3\,\text{eV}$ or for a single sterile neutrino with somewhat higher mass. The problem here is that any evidence for new neutrino physics is driven mainly by the additional astrophysical data, not by *Planck* CMB anisotropy measurements. In addition, the external data sets are not entirely consistent, so tensions remain. As discussed in PCP13 (see also Leistedt et al. 2014; Battye et al. 2015) *Planck* data usually favour base ΛCDM over extended models. Implications of the *Planck* 2015 data for neutrino physics are discussed in Sect. 6.4 and tensions between *Planck* and external data in various extended neutrino models are discussed further in Sect. 6.4.4.

As mentioned above, we do not use RSD or galaxy weak lensing measurements for combined constraints in this paper (apart from Sects. 6.3 and 6.4.4, where we use the CFHTLenS data) . They are, however, used in the paper exploring constraints on dark energy and modified gravity (Planck Collaboration XIV 2016). For some models discussed in that paper, the combination of *Planck*, RSD, and weak lensing data does prefer extensions to the base ΛCDM cosmology.

6. Extensions to the base ΛCDM model

6.1. Grid of models

The full grid results are available online[25]. Figure 20 and Table 5 summarize the constraints on one-parameter extensions to base ΛCDM. As in PCP13, we find no strong evidence in favour of any of these simple one-parameter extensions using *Planck* or *Planck* combined with BAO. The entire grid has been run using both the `Plik` and `CamSpec` likelihoods. As noted in Sect. 3, the parameters derived from these two TT likelihoods agree to better than 0.5σ for base ΛCDM. This level of agreement also holds for the extended models analysed in our grid. In Sect. 3 we also pointed out that we have definite evidence, by comparing spectra computed with different frequency combinations, of residual systematics in the TE and EE spectra. These systematics average down in the coadded TE and EE spectra, but the remaining level of systematics in these coadded spectra are not yet well quantified (though they are small). Thus, we urge the reader to treat parameters computed from the TT, TE, EE likelihoods with some caution. In the case of polarization, the agreement between the `Plik` and `CamSpec` TE and EE likelihoods is less good, with shifts in parameters of up to 1.5σ (though such large shifts are unusual). In general, the behaviour of the TT, TE, EE likelihoods is as shown in Fig. 20. For extended models, the addition of the *Planck* polarization data at high multipoles reduces the errors on extended parameters compared to the *Planck* temperature data and pulls the parameters towards those of base ΛCDM. A similar behaviour is seen if the *Planck* TT (or *Planck* TT, TE, EE) data are combined with BAO.

The rest of this section discusses the grid results in more detail and also reports results on some additional models (specifically dark matter annihilation, tests of the recombination history, and cosmic defects) that are not included in our grid.

6.2. Early-Universe physics

Arguably the most important result from 2013 *Planck* analysis was the finding that simple single-field inflationary models, with a tilted scalar spectrum $n_{\mathrm{s}} \approx 0.96$, provide a very good fit to

---

[25] See the Planck Legacy Archive, http://www.cosmos.esa.int/web/planck/pla, which contains considerably more detailed information than presented in this paper.

Table 4. Parameter 68% confidence limits for the base ΛCDM model from *Planck* CMB power spectra, in combination with lensing reconstruction ("lensing") and external data ("ext", BAO+JLA+H_0).

Parameter	TT+lowP 68% limits	TT+lowP+lensing 68% limits	TT+lowP+lensing+ext 68% limits	TT,TE,EE+lowP 68% limits	TT,TE,EE+lowP+lensing 68% limits	TT,TE,EE+lowP+lensing+ext 68% limits
$\Omega_{\rm b}h^2$	0.02222 ± 0.00023	0.02226 ± 0.00023	0.02227 ± 0.00020	0.02225 ± 0.00016	0.02226 ± 0.00016	0.02230 ± 0.00014
$\Omega_{\rm c}h^2$	0.1197 ± 0.0022	0.1186 ± 0.0020	0.1184 ± 0.0012	0.1198 ± 0.0015	0.1193 ± 0.0014	0.1188 ± 0.0010
$100\theta_{\rm MC}$	1.04085 ± 0.00047	1.04103 ± 0.00046	1.04106 ± 0.00041	1.04077 ± 0.00032	1.04087 ± 0.00032	1.04093 ± 0.00030
τ	0.078 ± 0.019	0.066 ± 0.016	0.067 ± 0.013	0.079 ± 0.017	0.063 ± 0.014	0.066 ± 0.012
$\ln(10^{10}A_{\rm s})$	3.089 ± 0.036	3.062 ± 0.029	3.064 ± 0.024	3.094 ± 0.034	3.059 ± 0.025	3.064 ± 0.023
$n_{\rm s}$	0.9655 ± 0.0062	0.9677 ± 0.0060	0.9681 ± 0.0044	0.9645 ± 0.0049	0.9653 ± 0.0048	0.9667 ± 0.0040
H_0	67.31 ± 0.96	67.81 ± 0.92	67.90 ± 0.55	67.27 ± 0.66	67.51 ± 0.64	67.74 ± 0.46
Ω_Λ	0.685 ± 0.013	0.692 ± 0.012	0.6935 ± 0.0072	0.6844 ± 0.0091	0.6879 ± 0.0087	0.6911 ± 0.0062
$\Omega_{\rm m}$	0.315 ± 0.013	0.308 ± 0.012	0.3065 ± 0.0072	0.3156 ± 0.0091	0.3121 ± 0.0087	0.3089 ± 0.0062
$\Omega_{\rm m}h^2$	0.1426 ± 0.0020	0.1415 ± 0.0019	0.1413 ± 0.0011	0.1427 ± 0.0014	0.1422 ± 0.0013	0.14170 ± 0.00097
$\Omega_{\rm m}h^3$	0.09597 ± 0.00045	0.09591 ± 0.00045	0.09593 ± 0.00045	0.09601 ± 0.00029	0.09596 ± 0.00030	0.09598 ± 0.00029
σ_8	0.829 ± 0.014	0.8149 ± 0.0093	0.8154 ± 0.0090	0.831 ± 0.013	0.8150 ± 0.0087	0.8159 ± 0.0086
$\sigma_8\Omega_{\rm m}^{0.5}$	0.466 ± 0.013	0.4521 ± 0.0088	0.4514 ± 0.0066	0.4668 ± 0.0098	0.4553 ± 0.0068	0.4535 ± 0.0059
$\sigma_8\Omega_{\rm m}^{0.25}$	0.621 ± 0.013	0.6069 ± 0.0076	0.6066 ± 0.0070	0.623 ± 0.011	0.6091 ± 0.0067	0.6083 ± 0.0066
$z_{\rm re}$	$9.9^{+1.8}_{-1.6}$	$8.8^{+1.7}_{-1.4}$	$8.9^{+1.3}_{-1.2}$	$10.0^{+1.7}_{-1.5}$	$8.5^{+1.4}_{-1.2}$	$8.8^{+1.2}_{-1.1}$
$10^9 A_{\rm s}$	$2.198^{+0.076}_{-0.085}$	2.139 ± 0.063	2.143 ± 0.051	2.207 ± 0.074	2.130 ± 0.053	2.142 ± 0.049
$10^9 A_{\rm s}e^{-2\tau}$	1.880 ± 0.014	1.874 ± 0.013	1.873 ± 0.011	1.882 ± 0.012	1.878 ± 0.011	1.876 ± 0.011
Age/Gyr	13.813 ± 0.038	13.799 ± 0.038	13.796 ± 0.029	13.813 ± 0.026	13.807 ± 0.026	13.799 ± 0.021
z_*	1090.09 ± 0.42	1089.94 ± 0.42	1089.90 ± 0.30	1090.06 ± 0.30	1090.00 ± 0.29	1089.90 ± 0.23
r_*	144.61 ± 0.49	144.89 ± 0.44	144.93 ± 0.30	144.57 ± 0.32	144.71 ± 0.31	144.81 ± 0.24
$100\theta_*$	1.04105 ± 0.00046	1.04122 ± 0.00045	1.04126 ± 0.00041	1.04096 ± 0.00032	1.04106 ± 0.00031	1.04112 ± 0.00029
$z_{\rm drag}$	1059.57 ± 0.46	1059.57 ± 0.47	1059.60 ± 0.44	1059.65 ± 0.31	1059.62 ± 0.31	1059.68 ± 0.29
$r_{\rm drag}$	147.33 ± 0.49	147.60 ± 0.43	147.63 ± 0.32	147.27 ± 0.31	147.41 ± 0.30	147.50 ± 0.24
$k_{\rm D}$	0.14050 ± 0.00052	0.14024 ± 0.00047	0.14022 ± 0.00042	0.14059 ± 0.00032	0.14044 ± 0.00032	0.14038 ± 0.00029
$z_{\rm eq}$	3393 ± 49	3365 ± 44	3361 ± 27	3395 ± 33	3382 ± 32	3371 ± 23
$k_{\rm eq}$	0.01035 ± 0.00015	0.01027 ± 0.00014	0.010258 ± 0.000083	0.01036 ± 0.00010	0.010322 ± 0.000096	0.010288 ± 0.000071
$100\theta_{\rm s,eq}$	0.4502 ± 0.0047	0.4529 ± 0.0044	0.4533 ± 0.0026	0.4499 ± 0.0032	0.4512 ± 0.0031	0.4523 ± 0.0023
f_{2000}^{143}	29.9 ± 2.9	30.4 ± 2.9	30.3 ± 2.8	29.5 ± 2.7	30.2 ± 2.7	30.0 ± 2.7
$f_{2000}^{143\times217}$	32.4 ± 2.1	32.8 ± 2.1	32.7 ± 2.0	32.2 ± 1.9	32.8 ± 1.9	32.6 ± 1.9
f_{2000}^{217}	106.0 ± 2.0	106.3 ± 2.0	106.2 ± 2.0	105.8 ± 1.9	106.2 ± 1.9	106.1 ± 1.8

Notes. While we see no evidence that systematic effects in polarization are biasing parameters in the base ΛCDM model, a conservative choice would be to use the parameter values listed in Col. 3 (i.e., for TT+lowP+lensing). Nuisance parameters are not listed here for brevity, but can be found in the extensive tables on the Planck Legacy Archive, http://pla.esac.esa.int/pla; however, the last three parameters listed here give a summary measure of the total foreground amplitude (in μK^2) at $\ell = 2000$ for the three high-ℓ temperature power spectra used by the likelihood. In all cases the helium mass fraction used is predicted by BBN from the baryon abundance (posterior mean $Y_{\rm P} \approx 0.2453$, with theoretical uncertainties in the BBN predictions dominating over the *Planck* error on $\Omega_{\rm b}h^2$). The Hubble constant is given in units of km s^{-1} Mpc^{-1}, while r_* is in Mpc and wavenumbers are in Mpc^{-1}.

Table 5. Constraints on 1-parameter extensions to the base ΛCDM model for combinations of *Planck* power spectra, *Planck* lensing, and external data (BAO+JLA+H_0, denoted "ext").

Parameter	TT	TT+lensing	TT+lensing+ext	TT, TE, EE	TT, TE, EE+lensing	TT, TE, EE+lensing+ext
Ω_K	$-0.052^{+0.049}_{-0.055}$	$-0.005^{+0.016}_{-0.017}$	$-0.0001^{+0.0054}_{-0.0052}$	$-0.040^{+0.038}_{-0.041}$	$-0.004^{+0.015}_{-0.015}$	$0.0008^{+0.0040}_{-0.0039}$
Σm_ν [eV]	<0.715	<0.675	<0.234	<0.492	<0.589	<0.194
$N_{\rm eff}$	$3.13^{+0.64}_{-0.63}$	$3.13^{+0.62}_{-0.61}$	$3.15^{+0.41}_{-0.40}$	$2.99^{+0.41}_{-0.39}$	$2.94^{+0.38}_{-0.38}$	$3.04^{+0.33}_{-0.33}$
$Y_{\rm P}$	$0.252^{+0.041}_{-0.042}$	$0.251^{+0.040}_{-0.039}$	$0.251^{+0.035}_{-0.036}$	$0.250^{+0.026}_{-0.027}$	$0.247^{+0.026}_{-0.027}$	$0.249^{+0.025}_{-0.026}$
$dn_{\rm s}/d\ln k$	$-0.008^{+0.016}_{-0.016}$	$-0.003^{+0.015}_{-0.015}$	$-0.003^{+0.015}_{-0.014}$	$-0.006^{+0.014}_{-0.014}$	$-0.002^{+0.013}_{-0.013}$	$-0.002^{+0.013}_{-0.013}$
$r_{0.002}$	<0.103	<0.114	<0.114	<0.0987	<0.112	<0.113
w	$-1.54^{+0.62}_{-0.50}$	$-1.41^{+0.64}_{-0.56}$	$-1.006^{+0.085}_{-0.091}$	$-1.55^{+0.58}_{-0.48}$	$-1.42^{+0.62}_{-0.56}$	$-1.019^{+0.075}_{-0.080}$

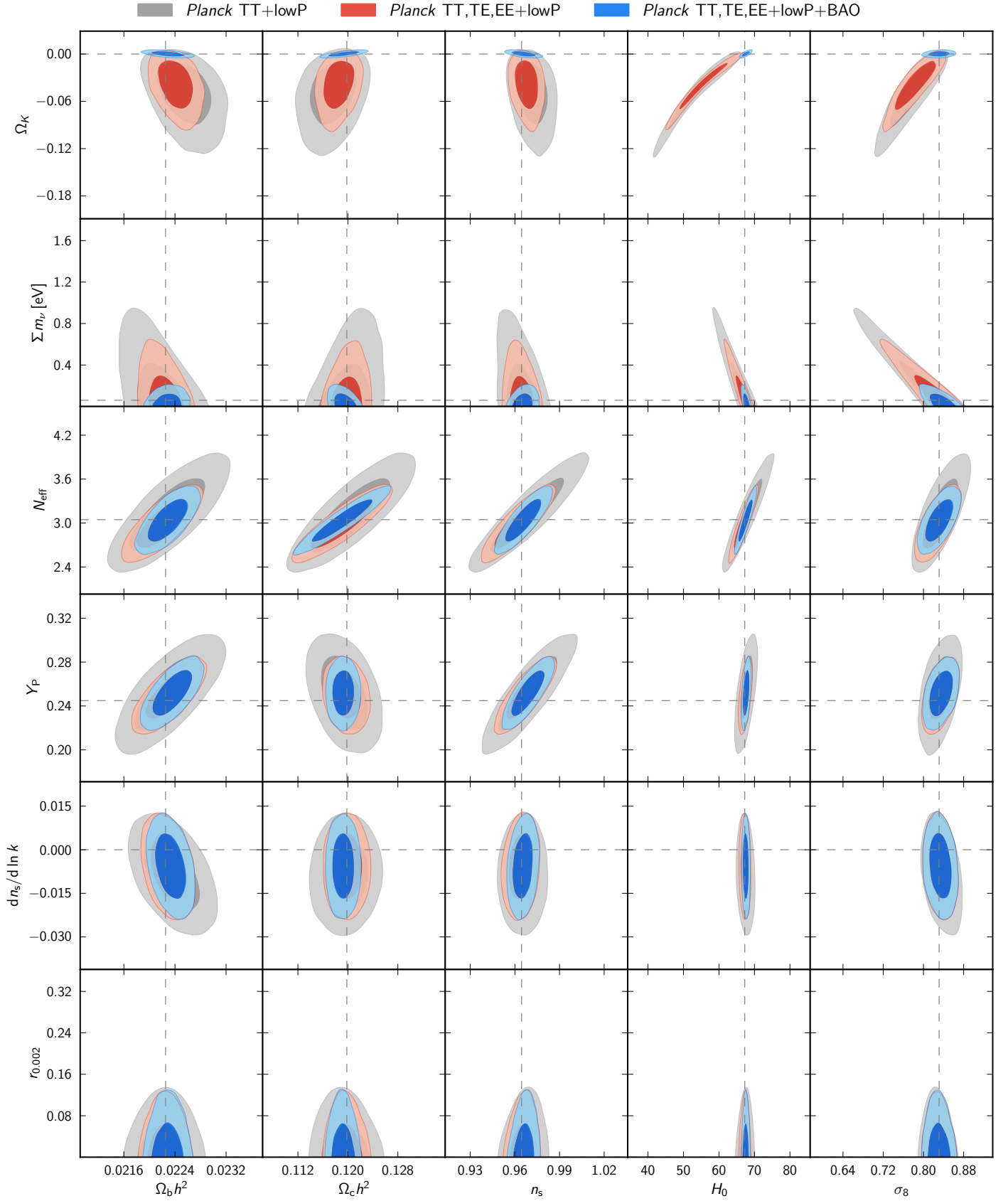**Notes.** All limits and confidence regions quoted here are 95%.

Fig. 20. 68% and 95% confidence regions on 1-parameter extensions of the base ΛCDM model for *Planck* TT+lowP (grey), *Planck* TT,TE,EE+lowP (red), and *Planck* TT,TE,EE+lowP+BAO (blue). Horizontal dashed lines correspond to the parameter values assumed in the base ΛCDM cosmology, while vertical dashed lines show the mean posterior values in the base model for *Planck* TT,TE,EE+lowP+BAO.

the *Planck* data. We found no evidence for a tensor component or running of the scalar spectral index, no strong evidence for isocurvature perturbations or features in the primordial power spectrum (Planck Collaboration XXII 2014), and no evidence for non-Gaussianity (Planck Collaboration XXIV 2014), cosmic strings or other topological defects (Planck Collaboration XXV 2014). On large angular scales, the *Planck* data showed some evidence for "anomalies" seen previously in the WMAP data (Bennett et al. 2011). These include a dip in the power spectrum in the multipole range $20 \lesssim \ell \lesssim 30$ (see Fig. 1) and some evidence for a departure from statistical isotropy on large angular scales (Planck Collaboration XXIII 2014). However, the statistical significance of these anomalies is not high enough to provide compelling evidence for new physics beyond simple single-field inflation.

The *Planck* 2013 results led to renewed interest in the R^2 inflationary model, originally introduced by Starobinsky (1980), and related inflationary models that have flat effective potentials of similar form (e.g., Kallosh & Linde 2013; Ferrara et al. 2013; Buchmuller et al. 2013; Ellis et al. 2013). A characteristic of these models is that they produce a red tilted scalar spectrum and a low tensor-to-scalar ratio. For reference, the Starobinsky model predicts (Starobinsky 1979; Mukhanov & Chibisov 1981)

$$n_{\rm s} \approx 1 - \frac{2}{N} \in (0.960, 0.967), \tag{37a}$$

$$r \approx \frac{12}{N^2} \in (0.003, 0.005), \tag{37b}$$

$$\frac{{\rm d}n_{\rm s}}{{\rm d}\ln k} \approx -\frac{2}{N^2} \in (-0.0008, -0.0006), \tag{37c}$$

where N is the number of e-foldings between the end of inflation and the time that our present day Hubble scale crossed the inflationary horizon, and numerical values are for the range $50 \le N \le 60$.

Although the *Planck* 2013 results stimulated theoretical work on inflationary models with low tensor-to-scalar ratios, the cosmological landscape became more complicated following the detection of a B-mode polarization anisotropy by the BICEP2 team (BICEP2 Collaboration 2014). If the BICEP2 signal were primarily caused by primordial gravitational waves, then the inferred tensor-to-scalar ratio would have been $r_{0.01} \approx 0.2$[26], apparently in conflict with the 2013 *Planck* 95% upper limit of $r_{0.002} < 0.11$, based on fits to the temperature power spectrum. Since the *Planck* constraints on r are highly model dependent (and fixed mainly by lower k) it is possible to reconcile these results by introducing additional parameters, such as large tilts or strong running of the spectral indices.

The situation has been clarified following a joint analysis of BICEP2/Keck observations and *Planck* polarization data reported in BKP. This analysis shows that polarized dust emission contributes a significant part of the BICEP2 signal. Correcting for polarized dust emission, BKP report a 95% upper limit of $r_{0.05} < 0.12$ on scale-invariant tensor modes, eliminating the tension between the BICEP2 and the *Planck* 2013 results. There is therefore no evidence for inflationary tensor modes from B-mode polarization measurements at this time (although the BKP analysis leaves open the possibility of a much higher tensor-to-scalar ratio than the prediction of Eq. (37b) for Starobinsky-type models).

The layout of the rest of this subsection is as follows. In Sect. 6.2.1 we review the *Planck* 2015 and *Planck*+BKP

---

[26] The pivot scale quoted here is roughly appropriate for the multipoles probed by BICEP2.

constraints on $n_{\rm s}$ and r. Constraints on the running of the scalar spectral index are presented in Sect. 6.2.2. Polarization data provide a powerful way of testing for isocurvature modes, as discussed in Sect. 6.2.3. Finally, Sect. 6.2.4 summarizes our results on spatial curvature. A discussion of specific inflationary models and tests for features in the primordial power spectrum can be found in Planck Collaboration XX (2016).

6.2.1. Scalar spectral index and tensor fluctuations

Primordial tensor fluctuations (gravitational waves) contribute to both the CMB temperature and polarization power spectra. Gravitational waves entering the horizon between recombination and the present day generate a tensor contribution to the large-scale CMB temperature anisotropy. In this data release, the strongest constraint on tensor modes from *Planck* data still comes from the CMB temperature spectrum at $\ell \lesssim 100$. The corresponding comoving wavenumbers probed by the *Planck* temperature spectrum have $k \lesssim 0.008 \, {\rm Mpc}^{-1}$, with very little sensitivity to higher wavenumbers because gravitational waves decay on sub-horizon scales. The precision of the *Planck* constraint is limited by cosmic variance of the large-scale anisotropies (which are dominated by the scalar component), and it is also model dependent. In polarization, in addition to B-modes, the EE and TE spectra also contain a signal from tensor modes coming from the last-scattering and reionization epochs. However, in this release the addition of *Planck* polarization constraints at $\ell \ge 30$ do not significantly change the results from temperature and low-ℓ polarization (see Table 5).

Figure 21 shows the 2015 *Planck* constraint in the $n_{\rm s}$–r plane, adding r as a 1-parameter extension to base ΛCDM. For base ΛCDM ($r = 0$), the value of $n_{\rm s}$ is

$$n_{\rm s} = 0.9655 \pm 0.0062, \qquad \textit{Planck} \ {\rm TT+lowP}. \tag{38}$$

We highlight this number here since $n_{\rm s}$, a key parameter for inflationary cosmology, shows one of the largest shifts of any parameter in base ΛCDM between the *Planck* 2013 and *Planck* 2015 analyses (about 0.7σ). As explained in Sect. 3.1, part of this shift was caused by the $\ell \approx 1800$ systematic in the nominal-mission 217×217 spectrum used in PCP13.

The red contours in Fig. 21 show the constraints from *Planck* TT+lowP. These are similar to the constraints shown in Fig. 23 of PCP13, but with $n_{\rm s}$ shifted to slightly higher values. The addition of BAO or the *Planck* lensing data to *Planck* TT+lowP lowers the value of $\Omega_c h^2$, which, at fixed θ_*, increases the small-scale CMB power. To maintain the fit to the *Planck* temperature power spectrum for models with $r = 0$, these parameter shifts are compensated by a change in the amplitude $A_{\rm s}$ and the tilt $n_{\rm s}$ (by about 0.4σ). The increase in $n_{\rm s}$ to match the observed power on small scales leads to a decrease in the scalar power on large scales, allowing room for a slightly larger contribution from tensor modes. The constraints shown by the blue contours in Fig. 21, which combine *Planck* lensing, BAO, and other astrophysical data, are therefore tighter in the $n_{\rm s}$ direction and shifted to slightly higher values, but marginally weaker in the r-direction. The 95% limits on $r_{0.002}$ are

$$r_{0.002} < 0.10, \qquad \textit{Planck} \ {\rm TT+lowP}, \tag{39a}$$

$$r_{0.002} < 0.11, \qquad \textit{Planck} \ {\rm TT+lowP+lensing+ext}, \tag{39b}$$

consistent with the results reported in PCP13. Here we assume the second-order slow-roll consistency relation for the tensor spectral index. The result in Eqs. (39a) and (39b) are mildly
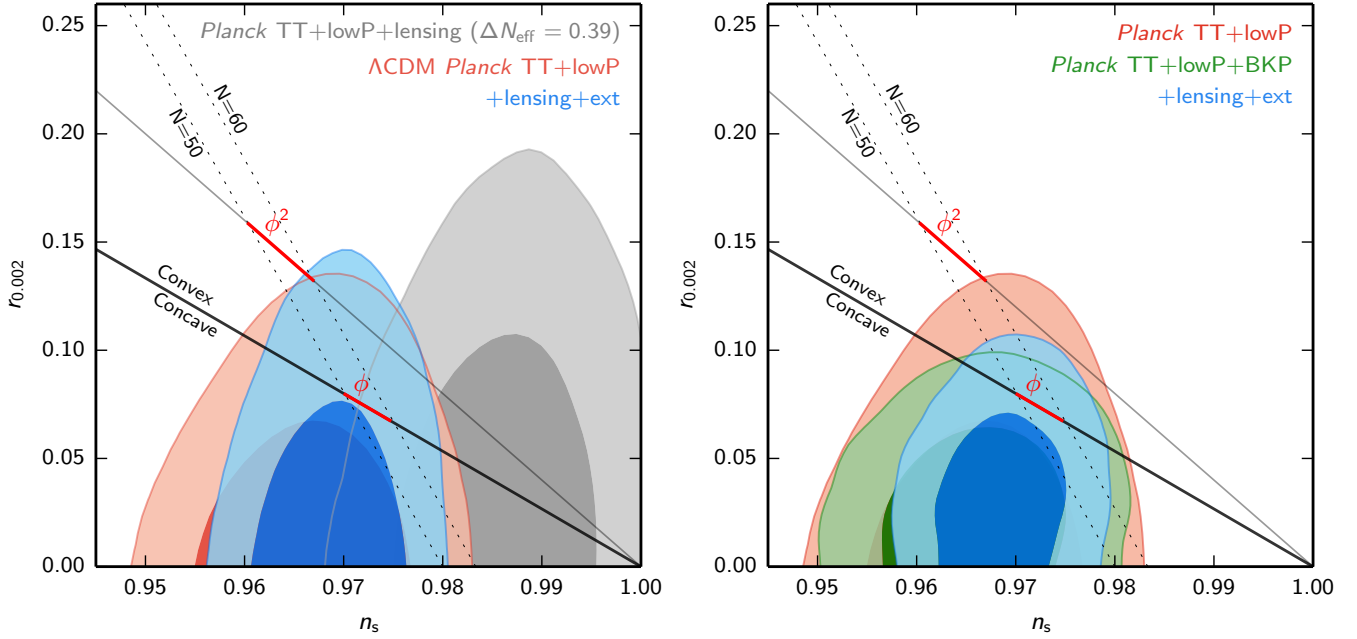
Fig. 21. *Left*: constraints on the tensor-to-scalar ratio $r_{0.002}$ in the ΛCDM model, using *Planck* TT+lowP and *Planck* TT+lowP+lensing+BAO+JLA+H_0 (red and blue, respectively) assuming negligible running and the inflationary consistency relation. The result is model-dependent; for example, the grey contours show how the results change if there were additional relativistic degrees of freedom with $\Delta N_{\rm eff} = 0.39$ (disfavoured, but not excluded, by *Planck*). Dotted lines show loci of approximately constant e-folding number N, assuming simple $V \propto (\phi/m_{\rm Pl})^p$ single-field inflation. Solid lines show the approximate $n_{\rm s}$–r relation for quadratic and linear potentials, to first order in slow roll; red lines show the approximate allowed range assuming $50 < N < 60$ and a power-law potential for the duration of inflation. The solid black line (corresponding to a linear potential) separates concave and convex potentials. *Right*: equivalent constraints in the ΛCDM model when adding B-mode polarization results corresponding to the default configuration of the BICEP2/Keck Array+*Planck* (BKP) likelihood. These exclude the quadratic potential at a higher level of significance compared to the *Planck*-alone constraints.

scale dependent, with equivalent limits on $r_{0.05}$ being weaker by about 5%.

PCP13 noted a mismatch between the best-fit base ΛCDM model and the temperature power spectrum at multipoles $\ell \lesssim 40$, partly driven by the dip in the multipole range $20 \lesssim \ell \lesssim 30$. If this mismatch is simply a statistical fluctuation of the ΛCDM model (and there is no compelling evidence to think otherwise), the strong *Planck* limit (compared to forecasts) is the result of chance low levels of scalar mode confusion. On the other hand, if the dip represents a failure of the ΛCDM model, the 95% limits of Eqs. (39a) and (39b) may be underestimates. These issues are considered at greater length in Planck Collaboration XX (2016) and will not be discussed further in this paper.

As mentioned above, the *Planck* temperature constraints on r are model-dependent and extensions to ΛCDM can give significantly different results. For example, extra relativistic degrees of freedom increase the small-scale damping of the CMB anisotropies at a fixed angular scale, which can be compensated by increasing $n_{\rm s}$, allowing a larger tensor mode. This is illustrated by the grey contours in Fig. 21, which show the constraints for a model with $\Delta N_{\rm eff} = 0.39$. Although this value of $\Delta N_{\rm eff}$ is disfavoured by the *Planck* data (see Sect. 6.4.1) it is not excluded at a high significance level.

This example emphasizes the need for direct tests of tensor modes based on measurements of a large-scale B-mode pattern in CMB polarization. *Planck* B-mode constraints from the 100- and 143-GHz HFI channels, presented in Planck Collaboration XI (2016), give a 95% upper limit of $r \lesssim 0.27$. However, at present the tightest B-mode constraints on r come from the BKP analysis of the BICEP2/Keck field, which covers approximately $400\,{\rm deg}^2$ centred on RA = $0^{\rm h}$,

Dec = $-57\overset{\circ}{.}5$. These measurements probe the peak of the B-mode power spectrum at around $\ell = 100$, corresponding to gravitational waves with $k \approx 0.01\,{\rm Mpc}^{-1}$ that enter the horizon during recombination (i.e., somewhat smaller than the scales that contribute to the *Planck* temperature constraints on r). The results of BKP give a posterior for r that peaks at $r_{0.05} \approx 0.05$, but is consistent with $r_{0.05} = 0$. Thus, at present there is no convincing evidence of a primordial B-mode signal. At these low values of r, there is no longer any tension with *Planck* temperature constraints.

The analysis of BKP constrains r defined relative to a fixed fiducial B-mode spectrum, and on its own does not give a useful constraint on either the scalar amplitude or $n_{\rm s}$. A combined analysis of the *Planck* CMB spectra and the BKP likelihood can, self-consistently, give constraints in the $n_{\rm s}$–r plane, as shown in the right-hand panel of Fig. 21. The BKP likelihood pulls the contours to slightly non-zero values of r, with best fits of around $r_{0.002} \approx 0.03$, but at very low levels of statistical significance. The BKP likelihood also rules out the upper tail of r values allowed by *Planck* alone. The joint *Planck*+BKP likelihood analyses give the 95% upper limits

$$r_{0.002} < 0.08, \quad \textit{Planck}~{\rm TT+lowP+BKP}, \tag{40a}$$

$$r_{0.002} < 0.09, \quad \textit{Planck}~{\rm TT+lowP+lensing+ext+BKP}. \tag{40b}$$

The exact values of these upper limits are weakly dependent on the details of the foreground modelling applied in the BKP analysis (see BKP for further details). The results given here are for the baseline 2-parameter model, varying the B-mode dust amplitude and frequency scaling, using the lowest five B-mode bandpowers.
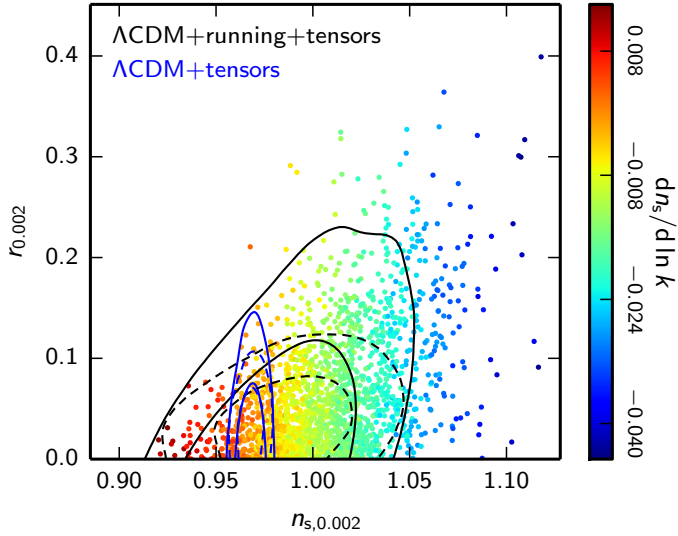
Fig. 22. Constraints on the tensor-to-scalar ratio $r_{0.002}$ in the ΛCDM model with running, using *Planck* TT+lowP (samples, coloured by the running parameter), and *Planck* TT+lowP+lensing+BAO (black contours). Dashed contours show the corresponding constraints also including the BKP B-mode likelihood. These are compared to the constraints when the running is fixed to zero (blue contours). Parameters are plotted at $k = 0.002\,\mathrm{Mpc}^{-1}$, which is approximately the scale at which *Planck* probes tensor fluctuations; however, the scalar tilt is only constrained well on much smaller scales. The inflationary slow-roll consistency relation is used here for n_t (though the range of running allowed is much larger than would be expected in most slow-roll models).

Allowing a running of the scalar spectral index as an additional free parameter weakens the *Planck* constraints on $r_{0.002}$, as shown in Fig. 22. The coloured samples in Fig. 22 illustrate how a negative running allows the large-scale scalar spectral index $n_{s,0.002}$ to shift towards higher values, lowering the scalar power on large scales relative to small scales, thereby allowing a larger tensor contribution. However adding the BKP likelihood, which directly constrains the tensor amplitude on smaller scales, significantly reduces the extent of this degeneracy leading to a 95% upper limit of $r_{0.002} < 0.10$ even in the presence of running (i.e., similar to the results of Eqs. (40a) and (40b)).

The *Planck*+BKP joint analysis rules out a quadratic inflationary potential ($V(\phi) \propto m^2\phi^2$, predicting $r \approx 0.16$) at over 99% confidence and reduces the allowed range of the parameter space for models with convex potentials. Starobinsky-type models are an example of a wider class of inflationary theories in which $n_s - 1 = O(1/N)$ is not a coincidence, yet $r = O(1/N^2)$ (Roest 2014; Creminelli et al. 2015). These models have concave potentials, and include a variety of string-inspired models with exponential potentials. Models with $r = O(1/N)$ are, however, still allowed by the data, including a simple linear potential and fractional-power monomials, as well as regions of parameter space in between where $n_s - 1 = O(1/N)$ is just a coincidence. Models that have sub-Planckian field evolution, so satisfying the Lyth bound (Lyth 1997; Garcia-Bellido et al. 2014), will typically have $r \lesssim 2 \times 10^{-5}$ for $n_s \approx 0.96$, and are also consistent with the tensor constraints shown in Fig. 21. For further discussion of the implications of the *Planck* 2015 data for a wide range of inflationary models see Planck Collaboration XX (2016).

In summary, the *Planck* limits on r are consistent with the BKP limits from B-mode measurements. Both data sets are consistent with $r = 0$; however, the combined data sets yield an upper limit to the tensor-to-scalar ratio of $r \approx 0.09$ at the 95% level.

The *Planck* temperature constraints on r are limited by cosmic variance. The only way of improving these limits, or potentially detecting gravitational waves with $r \lesssim 0.09$, is through direct B-mode detection. The *Planck* 353-GHz polarization maps (Planck Collaboration Int. XXX 2016) show that at frequencies of around 150 GHz, Galactic dust emission is an important contaminant at the $r \approx 0.05$ level even in the cleanest regions of the sky. BKP demonstrates further that on small regions of the sky covering a few hundred square degrees (typical of ground based B-mode experiments), the *Planck* 353-GHz maps are of limited use as monitors of polarized Galactic dust emission because of their low signal-to-noise level. To achieve limits substantially below $r \approx 0.05$ will require observations of comparably high sensitivity over a range of frequencies, and with increased sky coverage. The forthcoming measurements from Keck Array and BICEP3 at 95 GHz and the Keck Array receivers at 220 GHz should offer significant improvements on the current constraints. A number of other ground-based and sub-orbital experiments should also return high precision B-mode data within the next few years (see Abazajian et al. 2015a, for a review).

6.2.2. Scale dependence of primordial fluctuations

In simple single-field models of inflation, the running of the spectral index is of second order in inflationary slow-roll parameters and is typically small, $|dn_s/d\ln k| \approx (n_s - 1)^2 \approx 10^{-3}$ (Kosowsky & Turner 1995). Nevertheless, it is possible to construct models that produce a large running over a wavenumber range accessible to CMB experiments, whilst simultaneously achieving enough e-folds of inflation to solve the horizon problem. Inflation with an oscillatory potential of sufficiently long period, perhaps related to axion monodromy, is an example (Silverstein & Westphal 2008; Meerburg 2014; Czerny et al. 2014; Minor & Kaplinghat 2015).

As reviewed in PCP13, previous CMB experiments, either on their own or in combination with other astrophysical data, have sometimes given hints of a non-zero running at about the 2σ level (Spergel et al. 2003; Hinshaw et al. 2013; Hou et al. 2014). The results of PCP13 showed a slight preference for negative running at the 1.4σ level, driven almost entirely by the mismatch between the CMB temperature power spectrum at high multipoles and the spectrum at multipoles $\ell \lesssim 50$.

The 2015 *Planck* results (Fig. 23) are similar to those in PCP13. Adding running as an additional parameter to base ΛCDM with $r = 0$, we find

$$\frac{dn_s}{d\ln k} = -0.0084 \pm 0.0082, \quad \textit{Planck}\ \mathrm{TT+lowP}, \tag{41a}$$

$$\frac{dn_s}{d\ln k} = -0.0057 \pm 0.0071, \quad \textit{Planck}\ \mathrm{TT, TE, EE+lowP}. \tag{41b}$$

There is a slight preference for negative running, which, as in PCP13, is driven by the mismatch between the high and low multipoles in the temperature power spectrum. However, in the 2015 *Planck* data the tension between high and low multipoles is reduced somewhat, primarily because of changes to the HFI beams at multipoles $\ell \lesssim 200$ (see Sect. 3.1). A consequence of this reduced tension can be seen in the 2015 constraints on models that
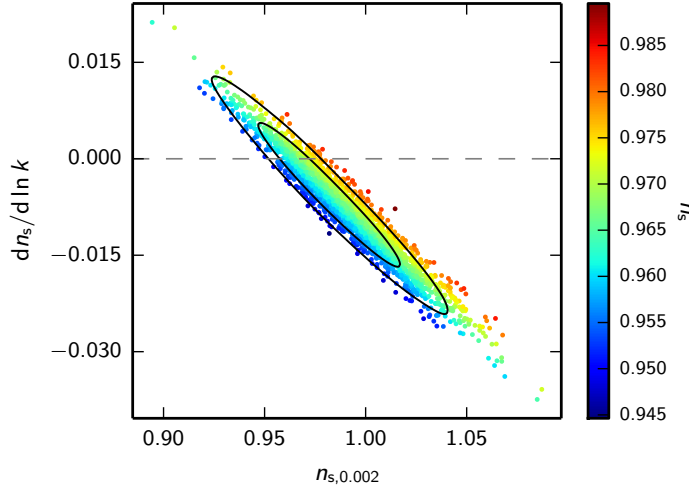
Fig. 23. Constraints on the running of the scalar spectral index in the ΛCDM model, using *Planck* TT+lowP (samples, coloured by the spectral index at $k = 0.05 \, \text{Mpc}^{-1}$), and *Planck* TT,TE,EE+lowP (black contours). The *Planck* data are consistent with zero running, but also allow for significant negative running, which gives a positive tilt on large scales and hence less power on large scales.
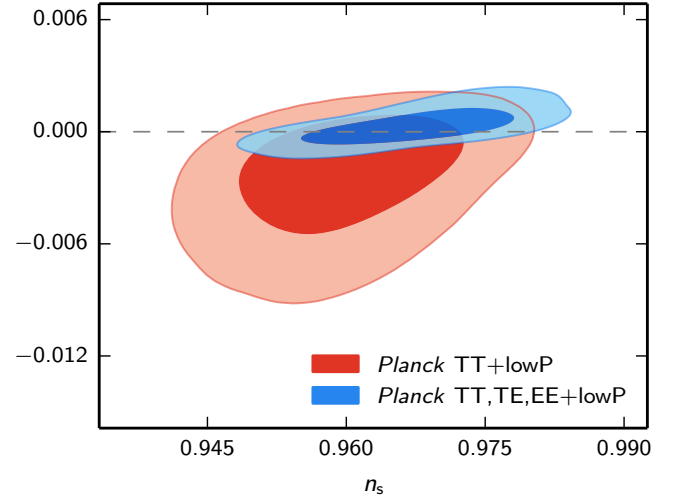

Fig. 24. Constraints on the correlated matter isocurvature mode amplitude parameter α, where $\alpha = 0$ corresponds to purely adiabatic perturbations. The *Planck* temperature data slightly favour negative values, since this lowers the large-scale anisotropies; however, the polarization signal from an isocurvature mode is distinctive and the *Planck* polarization data significantly shrink the allowed region around the value $\alpha = 0$ corresponding to adiabatic perturbations.

include tensor fluctuations in addition to running:

$$\frac{dn_s}{d\ln k} = -0.0126^{+0.0098}_{-0.0087}, \quad Planck \ \text{TT+lowP}, \tag{42a}$$

$$\frac{dn_s}{d\ln k} = -0.0085 \pm 0.0076, \quad Planck \ \text{TT, TE, EE+lowP}, \tag{42b}$$

$$\frac{dn_s}{d\ln k} = -0.0065 \pm 0.0076, \quad Planck \ \text{TT+lowP+lensing}$$
$$+\text{ext+BKP}. \tag{42c}$$

PCP13 found an approximately 2σ pull towards negative running for these models. This tension is reduced to about 1σ with the 2015 *Planck* data, and to lower values when we include the BKP likelihood, which reduces the range of allowed tensor amplitudes.

In summary, the *Planck* data are consistent with zero running of the scalar spectral index. However, as illustrated in Fig. 23, the *Planck* data still allow running at roughly the 10^{-2} level, i.e., an order of magnitude higher than expected in simple inflationary models. One way of potentially improving these constraints is to extend the wavenumber range from CMB scales to smaller scales using additional astrophysical data, for example by using measurements of the Lyα flux power spectrum of high-redshift quasars (as in the first year WMAP analysis, Spergel et al. 2003). Palanque-Delabrouille et al. (2015) have recently reported an analysis of a large sample of quasar spectra from the SDSSIII/BOSS survey. These authors find a low value of the scalar spectral index $n_s = 0.928 \pm 0.012$ (stat.) $\pm$ (0.02) (syst.) on scales of $k \approx 1 \, \text{Mpc}^{-1}$. To extract physical parameters, the Lyα power spectra need to be calibrated against numerical hydrodynamical simulations. The large systematic error in this spectral index determination is dominated by the fidelity of the hydrodynamic simulations and by the splicing used to achieve high resolution over large scales. These uncertainties need to be reduced before addressing the consistency of Lyα results with CMB measurements of the running of the spectral index.

6.2.3. Isocurvature perturbations

A key prediction of single-field inflation is that the primordial perturbations are adiabatic. More generally, the observed fluctuations will be adiabatic in any model in which the curvature perturbations were the only super-horizon perturbations left by the time that dark matter (and other matter) first decoupled, or was produced by decay. The different matter components then all have perturbations proportional to the curvature perturbation, so there are no isocurvature perturbations. However, it is possible to produce an observable amount of isocurvature modes by having additional degrees of freedom present during inflation and through reheating. For example, the curvaton model can generate correlated adiabatic and isocurvature modes from a second field (Mollerach 1990; Lyth & Wands 2002).

Isocurvature modes describe relative perturbations between the different species (Bucher et al. 2001b), with perhaps the simplest being a perturbation in the baryonic or dark matter sector (relative to the radiation). However, only one total matter isocurvature mode is observable in the linear CMB (in the accurate approximation in which the baryons are pressureless); a compensated mode (between the baryons and the cold dark matter) with $\delta\rho_b = -\delta\rho_c$ has no net density perturbation, and produces no CMB anisotropies (Gordon & Lewis 2003; Grin et al. 2011; Grin et al. 2014). It is possible to generate isocurvature modes in the neutrino sector; however, this requires interaction of an additional perturbed super-horizon field with neutrinos after they have decoupled, and hence is harder to achieve. Finally, neutrino velocity potential and vorticity modes are other possible consistent perturbations to the photon-neutrino fluid after neutrino decoupling. However, they are essentially impossible to excite, since they consist of photon and neutrino fluids coherently moving in opposite directions on super-horizon scales (although the relative velocity would have been zero before neutrino decoupling).

Planck Collaboration XXII (2014) presented constraints on a variety of general isocurvature models using the *Planck* temperature data, finding consistency with adiabaticity, though with
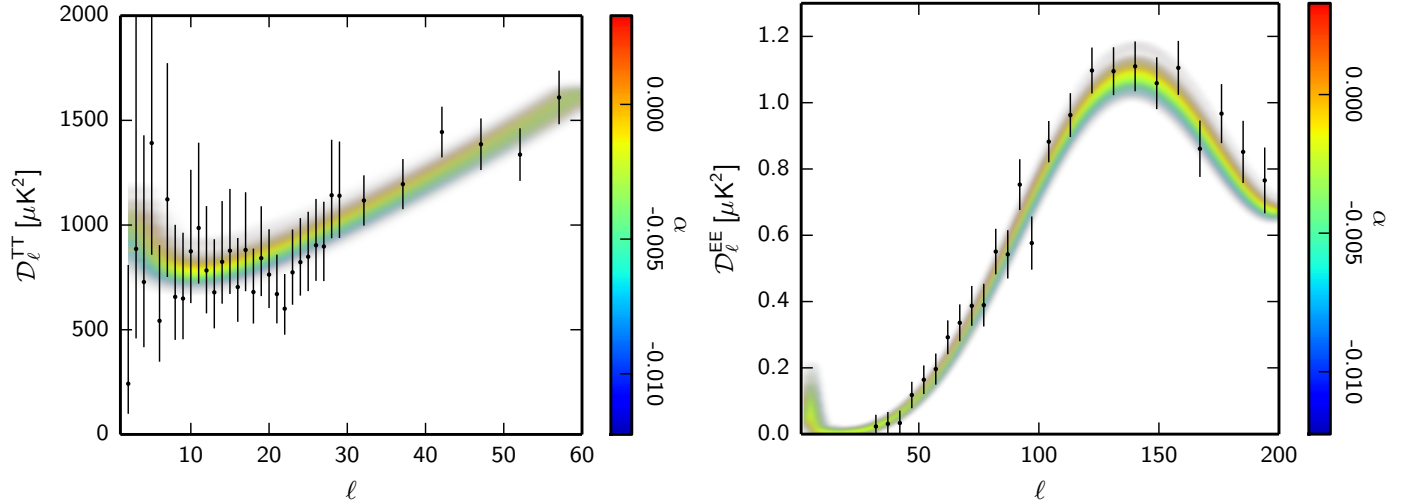
Fig. 25. Power spectra drawn from the *Planck* TT+lowP posterior for the correlated matter isocurvature model, colour-coded by the value of the isocurvature amplitude parameter α, compared to the *Planck* data points. The *left-hand figure* shows how the negatively-correlated modes lower the large-scale temperature spectrum, slightly improving the fit at low multipoles. Including polarization, the negatively-correlated modes are disfavoured, as illustrated at the first acoustic peak in *EE* on the right-hand plot. Data points at $\ell < 30$ are not shown for polarization, as they are included with both the default temperature (i.e., TT+lowP) and polarization (i.e., TT,TE,EE+lowP) likelihood combinations.

some mild preference for isocurvature models that reduce the power at low multipoles to provide a better match to the *Planck* temperature spectrum at $\ell \lesssim 50$. For matter isocurvature perturbations, the photons are initially unperturbed but perturbations develop as the Universe becomes more matter dominated. As a result, the phase of the acoustic oscillations differs from adiabatic modes; this is most clearly distinctive with the addition of polarization data (Bucher et al. 2001a).

An extended analysis of isocurvature models is given in Planck Collaboration XX (2016). Here we focus on a simple illustrative case of a totally-correlated matter isocurvature mode. We define an isocurvature amplitude parameter α, such that[27]

$$S_{\mathrm{m}} = \mathrm{sgn}(\alpha) \sqrt{\frac{|\alpha|}{1 - |\alpha|}} \zeta, \qquad (43)$$

where ζ is the primordial curvature perturbation. Here S_{m} is the total matter isocurvature mode, defined as the observable sum of the baryon and CDM isocurvature modes, i.e., $S_{\mathrm{m}} = S_{\mathrm{c}} + S_{\mathrm{b}}(\rho_{\mathrm{b}}/\rho_{\mathrm{c}})$, where

$$S_i \equiv \frac{\delta \rho_i}{\rho_i} - \frac{3 \delta \rho_\gamma}{4 \rho_\gamma}. \qquad (44)$$

All modes are assumed to have a power spectrum with the same spectral index n_{s}, so that α is independent of scale. For positive α this agrees with the definitions in Bean et al. (2006) and Larson et al. (2011) for α_{-1}, but also allows for the correlation to have the opposite sign. Approximately, $\mathrm{sgn}(\alpha) \alpha^2 \approx B_{\mathrm{c}}$, where B_{c} is the CDM version of the amplitude defined as in Amendola et al. (2002). Note that in our conventions, negative values of α *lower* the Sachs-Wolfe contribution to the large-scale *TT* power spectrum. We caution the reader that this convention differs from some others, e.g., Larson et al. (2011).

Planck constraints on the correlated isocurvature amplitude are shown in Fig. 24, with and without high-multipole polarization. The corresponding marginalized limit from the temperature

data is

$$\alpha = -0.0025^{+0.0035}_{-0.0047} \quad (95\%, \textit{Planck} \text{ TT+lowP}), \qquad (45)$$

which is significantly tightened around zero when *Planck* polarization information is included at high multipoles:

$$\alpha = 0.0003^{+0.0016}_{-0.0012} \quad (95\%, \textit{Planck} \text{ TT,TE,EE+lowP}). \qquad (46)$$

This strongly limits the isocurvature contribution to be less than about 3% of the adiabatic modes. Figure 25 shows how models with negative correlation parameter, α, fit the temperature data at low multipoles slightly better than models with $\alpha = 0$; however, these models are disfavoured from the corresponding change in the polarization acoustic peaks.

In this model most of the gain in sensitivity comes from relatively large scales, $\ell \lesssim 300$, where the correlated isocurvature modes with delayed phase change the first polarization acoustic peak ($\ell \approx 140$) significantly more than in temperature (Bucher et al. 2001a). The polarization data are not entirely robust to systematics on these scales, but in this case the result appears to be quite stable between the different likelihood codes. However, it should be noted that a particularly low point in the *TE* spectrum at $\ell \approx 160$ (see Fig. 3) pulls in the direction of positive α, and could be giving an artificially strong constraint if this were caused by an unidentified systematic.

6.2.4. Curvature

The simplifying assumptions of large-scale homogeneity and isotropy lead to the familiar Friedman-Lemaître-Robertson-Walker (FLRW) metric that appears to be an accurate description of our Universe. The base ΛCDM cosmology assumes an FLRW metric with a flat 3-space. This is a very restrictive assumption that needs to be tested empirically. In this subsection, we investigate constraints on the parameter Ω_K, where for ΛCDM models $\Omega_K \equiv 1 - \Omega_{\mathrm{m}} - \Omega_\Lambda$. For FLRW models $\Omega_K > 0$ corresponds to negatively-curved 3-geometries while $\Omega_K < 0$ corresponds to positively-curved 3-geometries. Even with perfect data within our past lightcone, our inference of the curvature

---

[27] Planck Collaboration XX (2016) gives equivalent one-tailed constraints on $\beta_{\mathrm{iso}} = |\alpha|$, where the correlated and anti-correlated cases are considered separately.
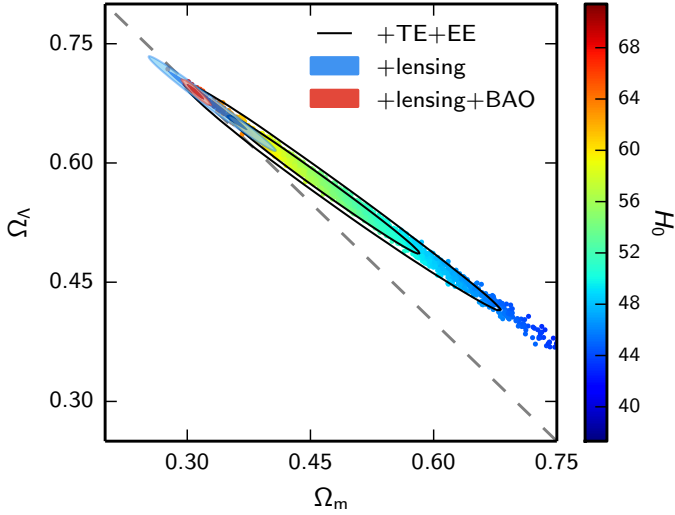
Fig. 26. Constraints in the Ω_m–Ω_Λ plane from the *Planck* TT+lowP data (samples; colour-coded by the value of H_0) and *Planck* TT,TE,EE+lowP (solid contours). The geometric degeneracy between Ω_m and Ω_Λ is partially broken because of the effect of lensing on the temperature and polarization power spectra. These limits are improved significantly by the inclusion of the *Planck* lensing reconstruction (blue contours) and BAO (solid red contours). The red contours tightly constrain the geometry of our Universe to be nearly flat.

Fig. 27. Samples from the distribution of the dark energy parameters w_0 and w_a using *Planck* TT+lowP+BAO+JLA data, colour-coded by the value of the Hubble parameter H_0. Contours show the corresponding 68% and 95% limits. Dashed grey lines intersect at the point in parameter space corresponding to a cosmological constant.

Ω_K is limited by the cosmic variance of curvature perturbations that are still super-horizon at the present, since these cannot be distinguished from background curvature within our observable volume.

The parameter Ω_K decreases exponentially with time during inflation, but grows only as a power law during the radiation and matter-dominated phases, so the standard inflationary prediction has been that curvature should be unobservably small today. Nevertheless, by fine-tuning parameters it is possible to devise inflationary models that generate open (e.g., Bucher et al. 1995; Linde 1999) or closed universes (e.g., Linde 2003). Even more speculatively, there has been interest recently in multiverse models, in which topologically-open "pocket universes" form by bubble nucleation (e.g., Coleman & De Luccia 1980; Gott 1982) between different vacua of a "string landscape" (e.g., Freivogel et al. 2006; Bousso et al. 2015). Clearly, the detection of a significant deviation from $\Omega_K = 0$ would have profound consequences for inflation theory and fundamental physics.

The *Planck* power spectra give the constraint

$$\Omega_K = -0.052^{+0.049}_{-0.055} \quad (95\%, Planck\ \text{TT+lowP}). \qquad (47)$$

The well-known geometric degeneracy (Bond et al. 1997; Zaldarriaga et al. 1997) allows for the small-scale linear CMB spectrum to remain almost unchanged if changes in Ω_K are compensated by changes in H_0 to obtain the same angular diameter distance to last scattering. The *Planck* constraint is therefore mainly determined by the (wide) priors on H_0, and the effect of lensing smoothing on the power spectra. As discussed in Sect. 5.1, the *Planck* temperature power spectra show a slight preference for more lensing than expected in the base ΛCDM cosmology, and since positive curvature increases the amplitude of the lensing signal, this preference also drives Ω_K towards negative values.

Taken at face value, Eq. (47) represents a detection of positive curvature at just over 2σ, largely via the impact of lensing on the power spectra. One might wonder whether this is mainly

a parameter volume effect, but that is not the case, since the best fit closed model has $\Delta\chi^2 \approx 6$ relative to base ΛCDM, and the fit is improved over almost all the posterior volume, with the mean improvement being $\langle\Delta\chi^2\rangle \approx 5$ (very similar to the phenomenological case of ΛCDM+A_L). Addition of the *Planck* polarization spectra shifts Ω_K towards zero by $\Delta\Omega_K \approx 0.015$:

$$\Omega_K = -0.040^{+0.038}_{-0.041} \quad (95\%, Planck\ \text{TT,TE,EE+lowP}), \qquad (48)$$

but Ω_K remains negative at just over 2σ.

What's more, the lensing reconstruction from *Planck* measures the lensing amplitude directly and, as discussed in Sect. 5.1, this does *not* prefer more lensing than base ΛCDM. The combined constraint shows impressive consistency with a flat universe:

$$\Omega_K = -0.005^{+0.016}_{-0.017} \quad (95\%, Planck\ \text{TT+lowP+lensing}). \qquad (49)$$

The dramatic improvement in the error bar is another illustration of the power of the lensing reconstruction from *Planck*.

The constraint can be sharpened further by adding external data that break the main geometric degeneracy. Combining the *Planck* data with BAO, we find

$$\Omega_K = 0.000 \pm 0.005 \quad (95\%,\ Planck\ \text{TT+lowP+lensing+BAO}). \qquad (50)$$

This constraint is unchanged at the quoted precision if we add the JLA supernovae data and the H_0 prior of Eq. (30).

Figure 26 illustrates these results in the Ω_m–Ω_Λ plane. We adopt Eq. (50) as our most reliable constraint on spatial curvature. Our Universe appears to be spatially flat to a 1σ accuracy of 0.25%.

6.3. Dark energy

The physical explanation for the observed accelerated expansion of the Universe is currently not known. In standard ΛCDM the acceleration is provided by a cosmological constant, i.e., an additional fluid satisfying an equation of state $w \equiv p_{DE}/\rho_{DE} = -1$.

However, there are many possible alternatives, typically described either in terms of extra degrees of freedom associated with scalar fields or modifications of general relativity on cosmological scales (for reviews see, e.g., Copeland et al. 2006; Tsujikawa 2010). A detailed study of these models and the constraints imposed by *Planck* and other data are presented in a separate paper, Planck Collaboration XIV (2016).

Here we will limit ourselves to the most basic extensions of ΛCDM, which can be phenomenologically described in terms of the equation of state parameter w alone. Specifically we will use the `camb` implementation of the "parameterized post-Friedmann" (PPF) framework of Hu & Sawicki (2007) and Fang et al. (2008) to test whether there is any evidence that w varies with time. This framework aims to recover the behaviour of canonical (i.e., those with a standard kinetic term) scalar field cosmologies minimally coupled to gravity when $w \geq -1$, and accurately approximates them for values $w \approx -1$. In these models the speed of sound is equal to the speed of light, so that the clustering of the dark energy inside the horizon is strongly suppressed. The advantage of using the PPF formalism is that it is possible to study the phantom domain, $w < -1$, including transitions across the "phantom barrier", $w = -1$, which is not possible for canonical scalar fields.

The CMB temperature data alone do not tightly constrain w, because of a strong geometrical degeneracy, even for spatially-flat models. From *Planck* we find

$$w = -1.54^{+0.62}_{-0.50} \quad (95\%, \text{*Planck* TT+lowP}), \tag{51}$$

i.e., almost a 2σ shift into the phantom domain. This is partly, but not entirely, a parameter volume effect, with the average effective χ^2 improving by $\langle \Delta\chi^2 \rangle \approx 2$ compared to base ΛCDM. This is consistent with the preference for a higher lensing amplitude discussed in Sect. 5.1.2, improving the fit in the $w < -1$ region, where the lensing smoothing amplitude becomes slightly larger. However, the lower limit in Eq. (51) is largely determined by the (arbitrary) prior $H_0 < 100$ km s^{-1}Mpc^{-1}, chosen for the Hubble parameter. Much of the posterior volume in the phantom region is associated with extreme values for cosmological parameters, which are excluded by other astrophysical data. The mild tension with base ΛCDM disappears as we add more data that break the geometrical degeneracy. Adding *Planck* lensing and BAO, JLA and H_0 ("ext") gives the 95% constraints

$$w = -1.023^{+0.091}_{-0.096} \quad \text{*Planck* TT+lowP+ext,} \tag{52a}$$

$$w = -1.006^{+0.085}_{-0.091} \quad \text{*Planck* TT+lowP+lensing+ext,} \tag{52b}$$

$$w = -1.019^{+0.075}_{-0.080} \quad \text{*Planck* TT, TE, EE+lowP+lensing+ext.} \tag{52c}$$

The addition of *Planck* lensing, or using the full *Planck* temperature+polarization likelihood together with the BAO, JLA, and H_0 data does not substantially improve the constraint of Eq. (52a). All of these data set combinations are compatible with the base ΛCDM value of $w = -1$. In PCP13, we conservatively quoted $w = -1.13^{+0.24}_{-0.25}$, based on combining *Planck* with BAO, as our most reliable limit on w. The errors in Eqs. (52a)−(52c) are substantially smaller, mainly because of the addition of the JLA SNe data, which offer a sensitive probe of the dark energy equation of state at $z \lesssim 1$. In PCP13, the addition of the SNLS SNe data pulled w into the phantom domain at the 2σ level, reflecting the tension between the SNLS sample and the *Planck* 2013 base ΛCDM parameters. As noted in Sect. 5.3, this discrepancy is no longer present, following improved photometric calibrations of the SNe data in the JLA sample. One consequence of this is the tightening of the errors in Eqs. (52a)−(52c) around the ΛCDM value $w = -1$ when we combine the JLA sample with *Planck*.

If w differs from -1, it is likely to change with time. We consider here the case of a Taylor expansion of w at first order in the scale factor, parameterized by

$$w = w_0 + (1 - a)w_a. \tag{53}$$

More complex models of dynamical dark energy are discussed in Planck Collaboration XIV (2016). Figure 27 shows the 2D marginalized posterior distribution for w_0 and w_a for the combination *Planck*+BAO+JLA. The JLA SNe data are again crucial in breaking the geometrical degeneracy at low redshift and with these data we find no evidence for a departure from the base ΛCDM cosmology. The points in Fig. 27 show samples from these chains colour-coded by the value of H_0. From these MCMC chains, we find $H_0 = (68.2 \pm 1.1)$ km s^{-1}Mpc^{-1}. Much higher values of H_0 would favour the phantom regime, $w < -1$.

As pointed out in Sects. 5.5.2 and 5.6 the CFHTLenS weak lensing data are in tension with the *Planck* base ΛCDM parameters. Examples of this tension can be seen in investigations of dark energy and modified gravity, since some of these models can modify the growth rate of fluctuations from the base ΛCDM predictions. This tension can be seen even in the simple model of Eq. (53). The green regions in Fig. 28 show 68% and 95% contours in the w_0−w_a plane for *Planck* TT+lowP combined with the CFHTLenS H13 data. In this example, we have applied ultra-conservative cuts, excluding ξ_- entirely and excluding measurements with $\theta < 17'$ in ξ_+ for all tomographic redshift bins. As discussed in Planck Collaboration XIV (2016), with these cuts the CFHTLenS data are insensitive to modelling the nonlinear evolution of the power spectrum, but this reduction in sensitivity comes at the expense of reducing the statistical power of the weak lensing data. Nevertheless, Fig. 28 shows that the combination of *Planck*+CFHTLenS pulls the contours into the phantom domain and is discrepant with base ΛCDM at about the 2σ level. The *Planck*+CFHTLenS data also favour a high value of H_0. If we add the (relatively weak) H_0 prior of Eq. (30), the contours (shown in cyan) in Fig. 28 shift towards $w = -1$. It therefore seems unlikely that the tension between *Planck* and CFHTLenS can be resolved by allowing a time-variable equation of state for dark energy.

A much more extensive investigation of models of dark energy and also models of modified gravity can be found in Planck Collaboration XIV (2016). The main conclusions of that analysis are:

- an investigation of more general time-variations of the equation of state shows a high degree of consistency with $w = -1$;
- a study of several dark energy and modified gravity models either finds compatibility with base ΛCDM, or mild tensions, which are driven mainly by external data sets.

6.4. Neutrino physics and constraints on relativistic components

In the following subsections, we update *Planck* constraints on the mass of standard (active) neutrinos, additional relativistic degrees of freedom, models with a combination of the two, and models with massive sterile neutrinos. In each subsection we emphasize the *Planck*-only constraint, and the implications of the *Planck* result for late-time cosmological parameters measured from other observations. We then give a brief discussion of tensions between *Planck* and some discordant external data, and
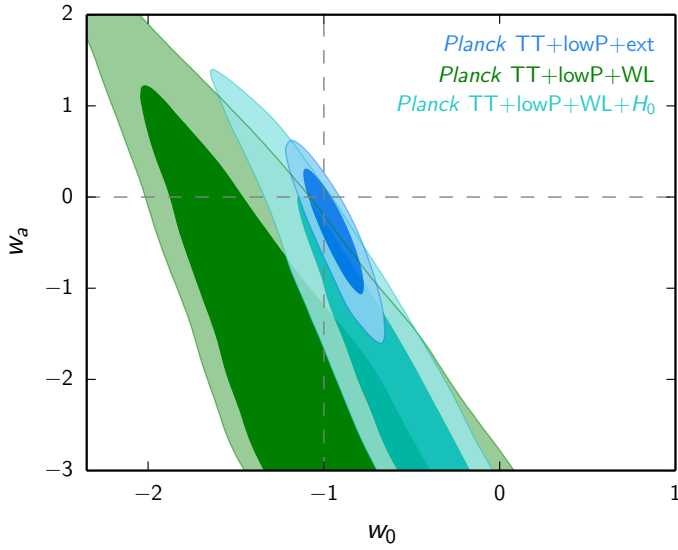
Fig. 28. Marginalized posterior distributions for (w_0, w_a) for various data combinations. We show *Planck* TT+lowP in combination with BAO, JLA, H_0 ("ext"), and two data combinations that add the CFHTLenS data with ultra-conservative cuts as described in the text (denoted "WL"). Dashed grey lines show the parameter values corresponding to a cosmological constant.
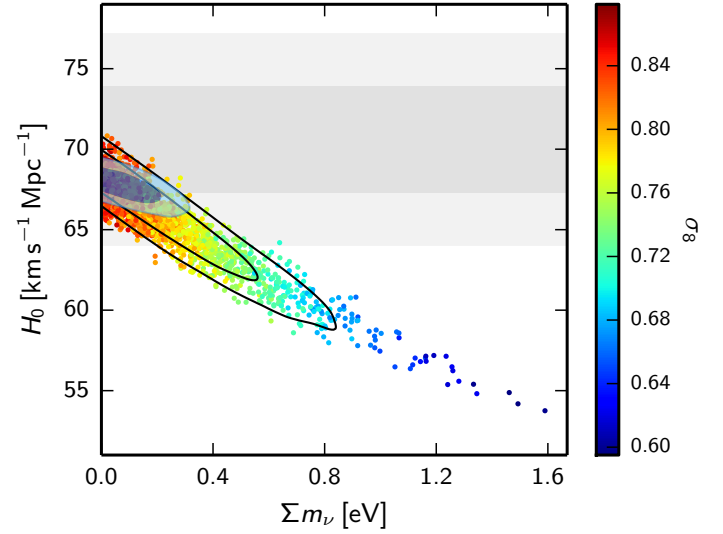

Fig. 29. Samples from the *Planck* TT+lowP posterior in the $\sum m_\nu$–H_0 plane, colour-coded by σ_8. Higher $\sum m_\nu$ damps the matter fluctuation amplitude σ_8, but also decreases H_0. The grey bands show the direct measurement, $H_0 = (70.6 \pm 3.3)$ km s^{-1}Mpc^{-1}, Eq. (30). Solid black contours show the constraint from *Planck* TT+lowP+lensing (which mildly prefers larger masses), and filled contours show the constraints from *Planck* TT+lowP+lensing+BAO.

assess whether any of these model extensions can help to resolve them. Finally we provide constraints on neutrino interactions.

6.4.1. Constraints on the total mass of active neutrinos

Detection of neutrino oscillations has proved that neutrinos have mass (see, e.g., Lesgourgues & Pastor 2006 and Nakamura & Petcov 2014 for reviews). The *Planck* base ΛCDM model assumes a normal mass hierarchy with $\sum m_\nu \approx 0.06$ eV (dominated by the heaviest neutrino mass eigenstate) but there are other possibilities, including a degenerate hierarchy with $\sum m_\nu \gtrsim 0.1$ eV. At this time there are no compelling theoretical reasons to strongly prefer any of these possibilities, so allowing for larger neutrino masses is perhaps one of the most well-motivated extensions to base ΛCDM considered in this paper. There has also been significant interest recently in larger neutrino masses as a possible way to lower σ_8 (the late-time fluctuation amplitude), and thereby reconcile *Planck* with weak lensing measurements and the abundance of rich clusters (see Sects. 5.5 and 5.6). Though model dependent, neutrino mass constraints from cosmology are already significantly stronger than those from tritium β-decay experiments (see, e.g., Drexlin et al. 2013).

Here we give constraints assuming three species of degenerate massive neutrinos, neglecting the small differences in mass expected from the observed mass splittings. At the level of sensitivity of *Planck* this is an accurate approximation, but note that it does not quite match continuously on to the base ΛCDM model (which assumes two massless and one massive neutrino with $\sum m_\nu = 0.06$ eV). We assume that the neutrino mass is constant, and that the distribution function is Fermi-Dirac with zero chemical potential.

Masses well below 1 eV have only a mild effect on the shape of the CMB power spectra, since they became non-relativistic after recombination. The effect on the background cosmology can be compensated by changes in H_0, to ensure the same observed acoustic peak scale θ_*. There is, however, some sensitivity of

the CMB anisotropies to neutrino masses as the neutrinos start to become less relativistic at recombination (modifying the early ISW effect), and from the late-time effect of lensing on the power spectrum. The *Planck* power spectrum (95%) constraints are

$$\sum m_\nu < 0.72 \text{ eV} \quad Planck \text{ TT+lowP,} \tag{54a}$$

$$\sum m_\nu < 0.21 \text{ eV} \quad Planck \text{ TT+lowP+BAO,} \tag{54b}$$

$$\sum m_\nu < 0.49 \text{ eV} \quad Planck \text{ TT, TE, EE+lowP,} \tag{54c}$$

$$\sum m_\nu < 0.17 \text{ eV} \quad Planck \text{ TT, TE, EE+lowP+BAO.} \tag{54d}$$

The *Planck* TT+lowP constraint has a broad tail to high masses, as shown in Fig. 29, which also illustrates the acoustic scale degeneracy with H_0. Larger masses imply a lower σ_8 through the effects of neutrino free-streaming on structure formation, but the larger masses also require a lower Hubble constant, leading to possible tensions with direct measurements of H_0. Masses below about 0.4 eV can provide an acceptable fit to the direct H_0 measurements, and adding the BAO data helps to break the acoustic scale degeneracy and tightens the constraint on $\sum m_\nu$ substantially. Adding *Planck* polarization data at high multipoles produces a relatively small improvement to the *Planck* TT+lowP+BAO constraint (and the improvement is even smaller with the alternative CamSpec likelihood), so we consider the *TT* results to be our most reliable constraints.

The constraint of Eq. (54b) is consistent with the 95% limit of $\sum m_\nu < 0.23$ eV reported in PCP13 for *Planck*+BAO. The limits are similar because the linear CMB is insensitive to the mass of neutrinos that are relativistic at recombination. There is little to be gained from improved measurement of the CMB temperature power spectra, though improved external data can help to break the geometric degeneracy to higher precision. CMB lensing can also provide additional information at lower redshifts, and future high-resolution CMB polarization measurements that accurately reconstruct the lensing potential can probe much smaller masses (see, e.g. Abazajian et al. 2015b).

As discussed in detail in PCP13 and Sect. 5.1, the *Planck* CMB power spectra prefer somewhat more lensing smoothing than predicted in ΛCDM (allowing the lensing amplitude to vary gives $A_{\rm L} > 1$ at just over 2σ). The neutrino mass constraint from the power spectra is therefore quite tight, since increasing the neutrino mass lowers the predicted smoothing even further compared to base ΛCDM. On the other hand the lensing reconstruction data, which directly probes the lensing power, prefers lensing amplitudes slightly below (but consistent with) the base ΛCDM prediction (Eq. (18)). The *Planck*+lensing constraint therefore pulls the constraints slightly away from zero towards higher neutrino masses, as shown in Fig. 30. Although the posterior has less weight at zero, the lensing data are incompatible with very large neutrino masses so the *Planck*+lensing 95% limit is actually tighter than the *Planck* TT+lowP result:

$$\sum m_\nu < 0.68 \text{ eV} \quad (95\%, Planck \text{ TT+lowP+lensing}). \tag{55}$$

Adding the polarization spectra improves this constraint slightly to

$$\sum m_\nu < 0.59 \text{ eV} \quad (95\%, Planck \text{ TT,TE,EE+lowP+lensing}). \tag{56}$$

We take the combined constraint that further includes BAO, JLA, and H_0 ("ext") as our best limit:

$$\left.\begin{array}{l} \sum m_\nu < 0.23 \text{ eV} \\ \Omega_\nu h^2 < 0.0025 \end{array}\right\} \; 95\%, Planck \text{ TT+lowP+lensing+ext}. \tag{57}$$

This is slightly weaker than the constraint from *Planck* TT,TE,EE+lowP+lensing+BAO (which is tighter in both the `CamSpec` and `Plik` likelihoods), but is immune to low level systematics that might affect the constraints from the *Planck* polarization spectra. Equation (57) is therefore a conservative limit. Marginalizing over the range of neutrino masses, the *Planck* constraints on the late-time parameters are[28]

$$\left.\begin{array}{l} H_0 = 67.7 \pm 0.6 \\ \sigma_8 = 0.810^{+0.015}_{-0.012} \end{array}\right\} \; Planck \text{ TT+lowP+lensing+ext}. \tag{58}$$

For this restricted range of neutrino masses, the impact on the other cosmological parameters is small and, in particular, low values of σ_8 will remain in tension with the parameter space preferred by *Planck*.

The constraint of Eq. (57) is weaker than the constraint of Eq. (54b) excluding lensing, but there is no good reason to disregard the *Planck* lensing information while retaining other astrophysical data. The CMB lensing signal probes very-nearly linear scales and passes many consistency checks over the multipole range used in the *Planck* lensing likelihood (see Sect. 5.1 and Planck Collaboration XV 2016). The situation with galaxy weak lensing is rather different, as discussed in Sect. 5.5.2. In addition to possible observational systematics, the weak lensing data probe lower redshifts than CMB lensing, and smaller spatial scales, where uncertainties in modelling nonlinearities in the matter power spectrum and baryonic feedback become important (Harnois-Déraps et al. 2015).

---

[28] To simplify the displayed equations, H_0 is given in units of km s^{-1}Mpc^{-1} in this section.
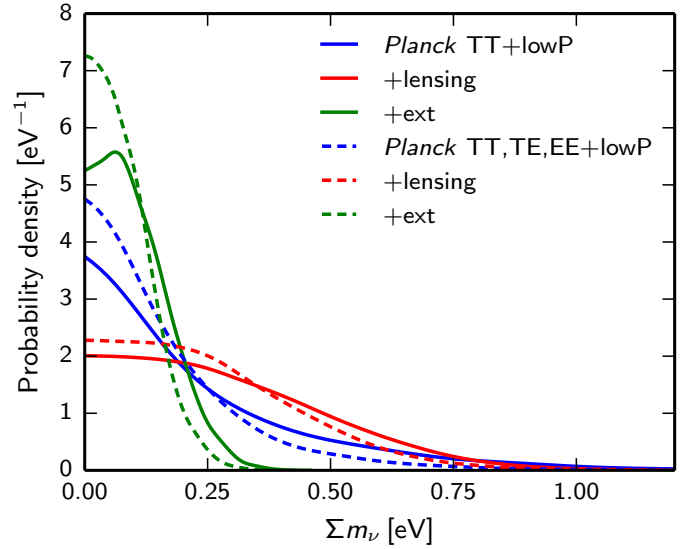
Fig. 30. Constraints on the sum of the neutrino masses for various data combinations.

A larger range of neutrino masses was found by Beutler et al. (2014b) using a combination of RSD, BAO, and weak lensing information. The tension between the RSD results and base ΛCDM was subsequently reduced following the analysis of Samushia et al. (2014), as shown in Fig. 17. Galaxy weak lensing and some cluster constraints remain in tension with base ΛCDM, and we discuss possible neutrino resolutions of these problems in Sect. 6.4.4.

Another way of potentially improving neutrino mass constraints is to use measurements of the Lyα flux power spectrum of high-redshift quasars. Palanque-Delabrouille et al. (2015) have recently reported an analysis of a large sample of quasar spectra from the SDSSIII/BOSS survey. When combining their results with 2013 Planck data, these authors find a bound $\sum m_\nu < 0.15$ eV (95% CL), compatible with the results presented in this section.

An exciting future prospect is the possible direct detection of non-relativistic cosmic neutrinos by capture on tritium, for example with the PTOLEMY experiment (Cocco et al. 2007; Betts et al. 2013; Long et al. 2014). Unfortunately, for the mass range $\sum m_\nu < 0.23$ eV preferred by *Planck*, detection with the first generation experiment will be extremely difficult.

6.4.2. Constraints on $N_{\rm eff}$

Dark radiation density in the early Universe is usually parameterized by $N_{\rm eff}$, defined so that the total relativistic energy density in neutrinos and any other dark radiation is given in terms of the photon density ρ_γ at $T \ll 1$ MeV by

$$\rho = N_{\rm eff} \frac{7}{8} \left(\frac{4}{11}\right)^{4/3} \rho_\gamma. \tag{59}$$

The numerical factors in this equation are included so that $N_{\rm eff} = 3$ for three standard model neutrinos that were thermalized in the early Universe and decoupled well before electron-positron annihilation. The standard cosmological prediction is actually $N_{\rm eff} = 3.046$, since neutrinos are not completely decoupled at electron-positron annihilation and are subsequently slightly heated (Mangano et al. 2002).
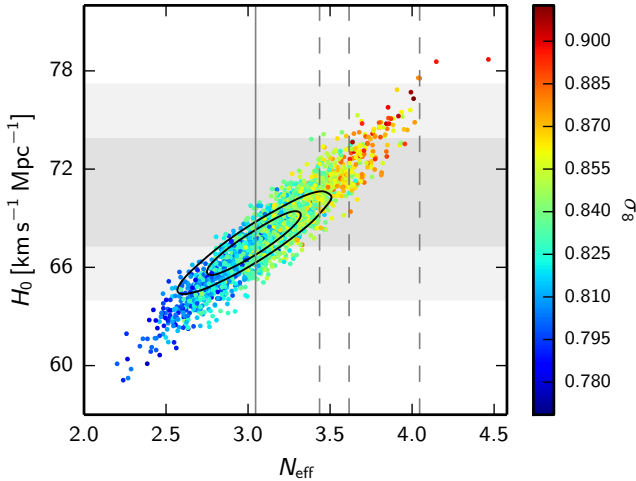
Fig. 31. Samples from *Planck* TT+lowP chains in the N_{eff}–H_0 plane, colour-coded by σ_8. The grey bands show the constraint $H_0 = (70.6 \pm 3.3)$ km s^{-1}Mpc^{-1} of Eq. (30). Notice that higher N_{eff} brings H_0 into better consistency with direct measurements, but increases σ_8. Solid black contours show the constraints from *Planck* TT,TE,EE+lowP+BAO. Models with $N_{eff} < 3.046$ (left of the solid vertical line) require photon heating after neutrino decoupling or incomplete thermalization. Dashed vertical lines correspond to specific fully-thermalized particle models, for example one additional massless boson that decoupled around the same time as the neutrinos ($\Delta N_{eff} \approx 0.57$), or before muon annihilation ($\Delta N_{eff} \approx 0.39$), or an additional sterile neutrino that decoupled around the same time as the active neutrinos ($\Delta N_{eff} \approx 1$).

In this section we focus on additional energy density from massless particles. In addition to massless sterile neutrinos, a variety of other particles could contribute to N_{eff}. We assume that the additional massless particles are produced well before recombination, and neither interact nor decay, so that their energy density scales with the expansion exactly like massless neutrinos. An additional $\Delta N_{eff} = 1$ could correspond to a fully thermalized sterile neutrino that decoupled at $T \lesssim 100$ MeV; for example, any sterile neutrino with mixing angles large enough to provide a potential resolution to short-baseline reactor neutrino oscillation anomalies would most likely thermalize rapidly in the early Universe. However, this solution to the neutrino oscillation anomalies requires approximately 1-eV sterile neutrinos, rather than the massless case considered in this section; exploration of the two parameters N_{eff} and $\sum m_\nu$ is reported in Sect. 6.4.3. For a review of sterile neutrinos see Abazajian et al. (2012).

More generally the additional radiation does not need to be fully thermalized, for example there are many possible models of non-thermal radiation production via particle decays (see, e.g., Hasenkamp & Kersten 2013; Conlon & Marsh 2013). The radiation could also be produced at temperatures $T > 100$ MeV, in which case typically $\Delta N_{eff} < 1$ for each additional species, since heating by photon production at muon annihilation (corresponding to $T \approx 100$ MeV) decreases the fractional importance of the additional component at the later times relevant for the CMB. For particles produced at $T \gg 100$ MeV the density would be diluted even more by numerous phase transitions and particle annihilations, and give $\Delta N_{eff} \ll 1$. Furthermore, if the particle is not fermionic, the factors entering the entropy conservation equation are different, and even thermalized particles could give specific fractional values of ΔN_{eff}. For example Weinberg (2013) considers the case of a thermalized massless boson, which contributes $\Delta N_{eff} = 4/7 \approx 0.57$ if it decouples in the range 0.5 MeV $< T < 100$ MeV like the

neutrinos, or $\Delta N_{eff} \approx 0.39$ if it decouples at $T > 100$ MeV (before the photon production at muon annihilation, hence undergoing fractional dilution).

In this paper we follow the usual phenomenological approach, where one constrains N_{eff} as a free parameter with a wide flat prior, although we comment on a few discrete cases separately below. Values of $N_{eff} < 3.046$ are less well motivated, since they would require the standard neutrinos to be incompletely thermalized or additional photon production after neutrino decoupling, but we include this range for completeness.

Figure 31 shows that *Planck* is entirely consistent with the standard value $N_{eff} = 3.046$. However, a significant density of additional radiation is still allowed, with the (68%) constraints

$$N_{eff} = 3.13 \pm 0.32 \quad \textit{Planck} \text{ TT+lowP,} \tag{60a}$$

$$N_{eff} = 3.15 \pm 0.23 \quad \textit{Planck} \text{ TT+lowP+BAO,} \tag{60b}$$

$$N_{eff} = 2.99 \pm 0.20 \quad \textit{Planck} \text{ TT, TE, EE+lowP,} \tag{60c}$$

$$N_{eff} = 3.04 \pm 0.18 \quad \textit{Planck} \text{ TT, TE, EE+lowP+BAO.} \tag{60d}$$

Notice the significantly tighter constraint with the inclusion of *Planck* high-ℓ polarization, with $\Delta N_{eff} < 1$ at over 4σ from *Planck* alone. This constraint is not very stable between likelihoods, with the CamSpec likelihood giving a roughly 0.8σ *lower* value of N_{eff}. However, the strong limit from polarization is also consistent with the joint *Planck* TT+lowP+BAO result, so Eq. (60b) leads to the robust conclusion that $\Delta N_{eff} < 1$ at over 3σ. The addition of *Planck* lensing has very little effect on this constraint.

For $N_{eff} > 3$, the *Planck* data favour higher values of the Hubble parameter than the *Planck* base ΛCDM value, which as discussed in Sect. 5.4 may be in better agreement with some direct measurements of H_0. This is because *Planck* accurately measures the acoustic scale r_*/D_A; increasing N_{eff} means (via the Friedmann equation) that the early Universe expands faster, so the sound horizon at recombination, r_*, is smaller and hence recombination has to be closer (larger H_0 and hence smaller D_A) for it to subtend the same angular size observed by *Planck*. However, models with $N_{eff} > 3$ and a higher Hubble constant also have higher values of the fluctuation amplitude σ_8, as shown by the coloured samples in Fig. 31. As a result, these models *increase* the tensions between the CMB measurements and astrophysical measurements of σ_8 discussed in Sect. 5.6. It therefore seems unlikely that additional radiation alone can help to resolve tensions with large-scale structure data.

The energy density in the early Universe can also be probed by the predictions of BBN. In particular $\Delta N_{eff} > 0$ increases the primordial expansion rate, leading to earlier freeze-out, with a higher neutron density and hence a greater abundance of helium and deuterium after BBN has completed. A detailed discussion of the implications of *Planck* for BBN is given in Sect. 6.5. Observations of both the primordial helium and deuterium abundance are compatible with the predictions of standard BBN for the *Planck* base ΛCDM value of the baryon density. The *Planck*+BBN constraints on N_{eff} (Eqs. (75) and (76)) are compatible, and slightly tighter than Eq. (60b).

Although there is a large continuous range of plausible N_{eff} values, it is worth mentioning briefly a few of the discrete values from fully thermalized models. This serves as an indication of how strongly *Planck* prefers base ΛCDM, and also how the inferred values of other cosmological parameters might be affected by this particular extension to base ΛCDM. As discussed above, one fully thermalized neutrino ($\Delta N_{eff} \approx 1$) is ruled out at over 3σ, and is disfavoured by $\Delta\chi^2 \approx 8$ compared to base ΛCDM by *Planck* TT+lowP, and much more strongly in combination with

Planck high-ℓ polarization or BAO data. The thermalized boson models that give $\Delta N_{\rm eff} = 0.39$ or $\Delta N_{\rm eff} = 0.57$ are disfavoured by $\Delta\chi^2 \approx 1.5$ and $\Delta\chi^2 \approx 3$, respectively, and are therefore not strongly excluded. We focus on the former, since it is also consistent with the *Planck* TT+lowP+BAO constraint at 2σ. As shown in Fig. 31, larger $N_{\rm eff}$ corresponds to a region of parameter space with significantly higher Hubble parameter,

$$H_0 = 70.6 \pm 1.0 \quad (68\%, \textit{Planck TT+lowP}; \Delta N_{\rm eff} = 0.39). \quad (61)$$

This can be compared to the direct measurements of H_0 discussed in Sect. 5.4. Evidently, Eq. (61) is consistent with the H_0 prior adopted in this paper (Eq. (30)), but this example shows that an accurate direct measurement of H_0 can potentially provide evidence for new physics beyond that probed by *Planck*. As shown in Fig. 31, the $\Delta N_{\rm eff} = 0.39$ cosmology also has a significantly higher small-scale fluctuation amplitude and the spectral index $n_{\rm s}$ is also bluer, with

$$\left.\begin{array}{l} \sigma_8 = 0.850 \pm 0.015 \\ n_{\rm s} = 0.983 \pm 0.006 \end{array}\right\} \quad \textit{Planck TT+lowP}; \Delta N_{\rm eff} = 0.39. \quad (62)$$

The σ_8 range in this model is higher than preferred by the *Planck* lensing likelihood in base ΛCDM. However, the fit to the *Planck* lensing likelihood is model dependent and the lensing degeneracy direction also associates high H_0 and low $\Omega_{\rm m}$ values with higher σ_8. The joint *Planck* TT+lowP+lensing constraint does pull σ_8 down slightly to $\sigma_8 = 0.84 \pm 0.01$ and provides an acceptable fit to the *Planck* data. For *Planck* TT+lowP+lensing, the difference in χ^2 between the best fit base ΛCDM model and the extension with $\Delta N_{\rm eff} = 0.39$ is only $\Delta\chi^2_{\rm CMB} \approx 2$. The higher spectral index with $\Delta N_{\rm eff} = 0.39$ gives a decrease in large-scale power, fitting the low $\ell < 30$ *Planck TT* spectrum better by $\Delta\chi^2 \approx 1$, but at the same time the high-ℓ data prefer $\Delta N_{\rm eff} \approx 0$. Correlations with other cosmological parameters can be seen in Fig. 20. Clearly, a very effective way of testing these models would be to obtain reliable, accurate, astrophysical measurements of H_0 and σ_8.

In summary, models with $\Delta N_{\rm eff} = 1$ are disfavoured by *Planck* combined with BAO data at about the 3σ level. Models with fractional changes of $\Delta N_{\rm eff} \approx 0.39$ are mildly disfavoured by *Planck*, but require higher H_0 and σ_8 compared to base ΛCDM.

6.4.3. Simultaneous constraints on $N_{\rm eff}$ and neutrino mass

As discussed in the previous sections, neither a higher neutrino mass nor additional radiation density alone can resolve all of the tensions between *Planck* and other astrophysical data. However, the presence of additional massive particles, such as massive sterile neutrinos, could potentially improve the situation by introducing enough freedom to allow higher values of the Hubble constant *and* lower values of σ_8. As mentioned in Sect. 6.4.2, massive sterile neutrinos offer a possible solution to reactor neutrino oscillation anomalies (Kopp et al. 2013; Giunti et al. 2013) and this has led to significant recent interest in this class of models (Hamann & Hasenkamp 2013; Wyman et al. 2014; Battye & Moss 2014; Leistedt et al. 2014; Bergström et al. 2014; MacCrann et al. 2015). Alternatively, active neutrinos could have significant degenerate masses above the minimal baseline value together with additional massless particles contributing to $N_{\rm eff}$. Many more complicated scenarios could also be envisaged.

In the case of massless radiation density, the cosmological predictions are independent of the actual form of the distribution
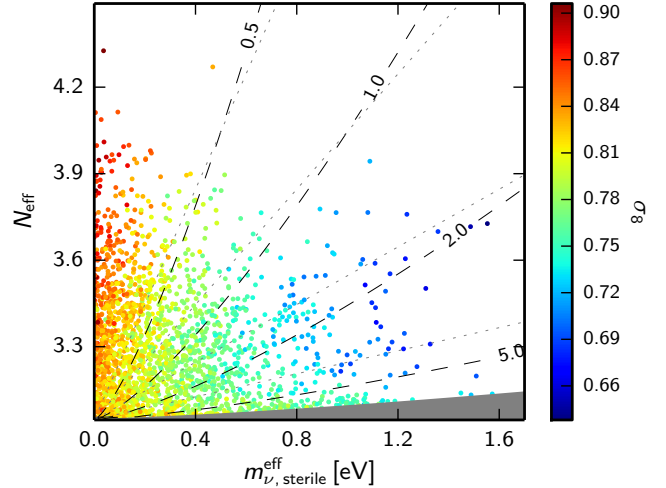

Fig. 32. Samples from *Planck* TT+lowP in the $N_{\rm eff}$–$m^{\rm eff}_{\nu,\,\rm sterile}$ plane, colour-coded by σ_8, for models with one massive sterile neutrino family, with effective mass $m^{\rm eff}_{\nu,\,\rm sterile}$, and the three active neutrinos as in the base ΛCDM model. The physical mass of the sterile neutrino in the thermal scenario, $m^{\rm thermal}_{\rm sterile}$, is constant along the grey dashed lines, with the indicated mass in eV; the grey shading shows the region excluded by our prior $m^{\rm thermal}_{\rm sterile} < 10$ eV, which cuts out most of the area where the neutrinos behave nearly like dark matter. The physical mass in the Dodelson-Widrow scenario, $m^{\rm DW}_{\rm sterile}$, is constant along the dotted lines (with the value indicated on the adjacent dashed lines).

function, since all particles travel at the speed of light. However, for massive particles the results are more model dependent. To formulate a well-defined model, we follow PCP13 and consider the case of one massive sterile neutrino parameterized by $m^{\rm eff}_{\nu,\,\rm sterile} \equiv (94.1\,\Omega_{\nu,\rm sterile}h^2)$ eV, in addition to the two approximately massless and one massive neutrino of the baseline model. For thermally-distributed sterile neutrinos, $m^{\rm eff}_{\nu,\,\rm sterile}$ is related to the true mass via

$$m^{\rm eff}_{\nu,\,\rm sterile} = (T_{\rm s}/T_\nu)^3 m^{\rm thermal}_{\rm sterile} = (\Delta N_{\rm eff})^{3/4} m^{\rm thermal}_{\rm sterile}, \quad (63)$$

and for the cosmologically-equivalent Dodelson-Widrow (DW) case (Dodelson & Widrow 1994) the relation is given by

$$m^{\rm eff}_{\nu,\,\rm sterile} = \chi_{\rm s}\, m^{\rm DW}_{\rm sterile}, \quad (64)$$

with $\Delta N_{\rm eff} = \chi_{\rm s}$. We impose a prior on the physical thermal mass, $m^{\rm thermal}_{\rm sterile} < 10$ eV, when generating parameter chains, to exclude regions of parameter space in which the particles are so massive that their effect on the CMB spectra is identical to that of cold dark matter. Although we consider only the specific case of one massive sterile neutrino with a thermal (or DW) distribution, our constraints will be reasonably accurate for other models, for example eV-mass particles produced as non-thermal decay products (Hasenkamp 2014).

Figure 32 shows that although *Planck* is perfectly consistent with no massive sterile neutrinos, a significant region of parameter space with fractional $\Delta N_{\rm eff}$ is allowed, where σ_8 is lower than in the base ΛCDM model. This is also the case for massless sterile neutrinos combined with massive active neutrinos. In the single massive sterile model, the combined constraints are

$$\left.\begin{array}{l} N_{\rm eff} < 3.7 \\ m^{\rm eff}_{\nu,\,\rm sterile} < 0.52 \text{ eV} \end{array}\right\} \quad 95\%, \textit{Planck TT+lowP+lensing+BAO}.$$
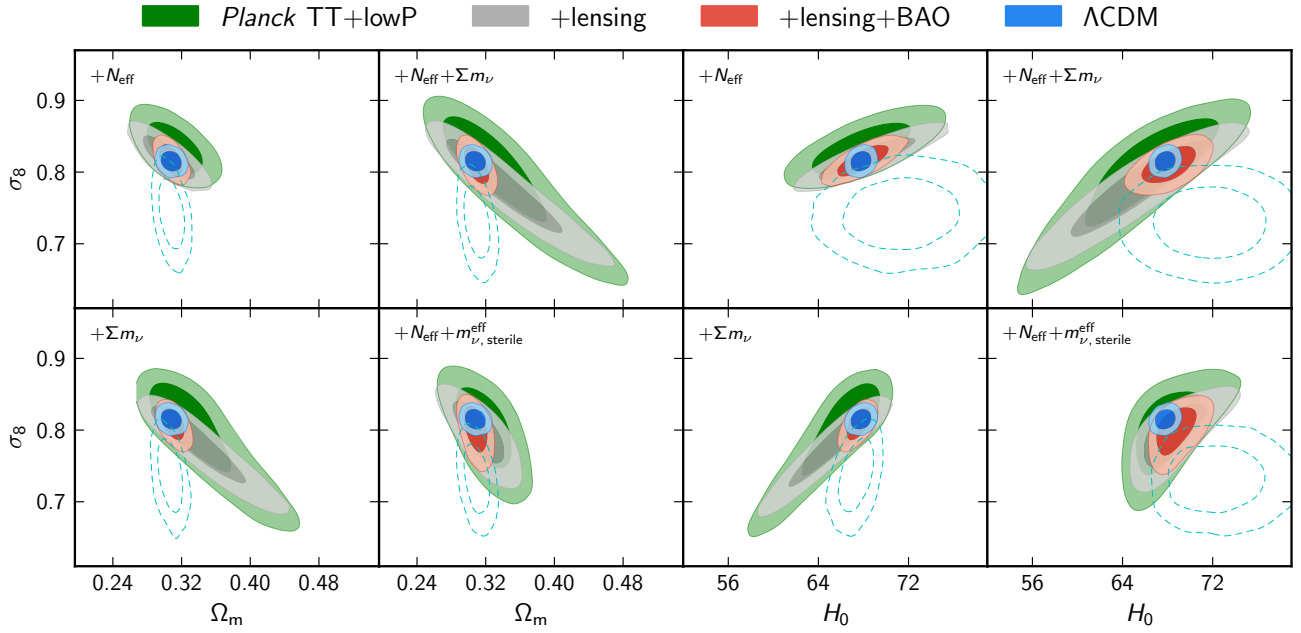
$$(65)$$

Fig. 33. 68% and 95% constraints from *Planck* TT+lowP (green), *Planck* TT+lowP+lensing (grey), and *Planck* TT+lowP+lensing+BAO (red) on the late-Universe parameters H_0, σ_8, and Ω_m in various neutrino extensions of the base ΛCDM model. The blue contours show the base ΛCDM constraints from *Planck* TT+lowP+lensing+BAO. The dashed cyan contours show joint constraints from the H13 CFHTLenS galaxy weak lensing likelihood (with angular cuts as in Fig. 18) at constant CMB acoustic scale θ_{MC} (fixed to the *Planck* TT+lowP ΛCDM best fit) combined with BAO and the Hubble constant measurement of Eq. (30). These additional constraints break large parameter degeneracies in the weak lensing likelihood that would otherwise obscure the comparison with the *Planck* contours. Here priors on other parameters applied to the CFHTLenS analysis are as described in Sect. 5.5.2.

The upper tail of $m_{\nu,\,sterile}^{eff}$ is largely associated with high physical masses near to the prior cutoff; if instead we restrict to the region where $m_{sterile}^{thermal} < 2$ eV the constraint is

$$\left.\begin{array}{l} N_{eff} < 3.7 \\ m_{\nu,\,sterile}^{eff} < 0.38 \text{ eV} \end{array}\right\} \text{ 95\%, } \textit{Planck } \text{TT+lowP+lensing+BAO.}$$

(66)

Massive sterile neutrinos with mixing angles large enough to help resolve the reactor anomalies would typically imply full thermalization in the early Universe, and hence give $\Delta N_{eff} = 1$ for each additional species. Such a high value of N_{eff}, especially combined with $m_{sterile} \approx 1$ eV, as required by reactor anomaly solutions, were virtually ruled out by previous cosmological data (Mirizzi et al. 2013; Archidiacono et al. 2013a; Gariazzo et al. 2013). This conclusion is strengthened by the analysis presented here, since $N_{eff} = 4$ is excluded at greater than 99% confidence. Unfortunately, there does not appear to be a consistent resolution to the reactor anomalies, unless thermalization of the massive neutrinos can be suppressed, for example, by large lepton asymmetry, new interactions, or particle decay (see Gariazzo et al. 2014; Bergström et al. 2014, and references therein).

We have also considered the case of additional radiation and degenerate massive active neutrinos, with the combined constraint

$$\left.\begin{array}{l} N_{eff} = 3.2 \pm 0.5 \\ \sum m_\nu < 0.32 \text{ eV} \end{array}\right\} \text{ 95\%, } \textit{Planck } \text{TT+lowP+lensing+BAO.}$$

(67)

Again *Planck* shows no evidence for a deviation from the base ΛCDM model.

6.4.4. Neutrino models and tension with external data

The extended models discussed in this section allow *Planck* to be consistent with a wider range of late-Universe parameters than in base ΛCDM. Figure 33 summarizes the constraints on Ω_m, σ_8, and H_0 for the various models that we have considered. The inferred Hubble parameter can increase or decrease, as required to maintain the observed acoustic scale, depending on the relative contribution of additional radiation (changing the sound horizon) and neutrino mass (changing mainly the angular diameter distance). However, all of the models follow similar degeneracy directions in the Ω_m–σ_8 and H_0–σ_8 planes, so these models remain predictive: *large common areas of the parameter space are excluded in all of these models*. The two-parameter extensions are required to fit substantially lower values of σ_8 without also decreasing H_0 below the values determined from direct measurements, but the scope for doing this is clearly limited.

External data sets need to be reanalysed consistently in extended models, since the extensions change the growth of structure, angular distances, and the matter-radiation equality scale. For example, the dashed lines in Fig. 33 show how different models affect the CFHTLenS galaxy weak lensing constraints from Heymans et al. (2013) (see Sect. 5.5.2), when restricted to the region of parameter space consistent with the *Planck* acoustic scale measurements and the local Hubble parameter. The filled green, grey, and red contours in Fig. 33 show the CMB constraints on these models for various data combinations. The tightest of these constraints comes from the *Planck* TT+lowP+lensing+BAO combination. The blue contours show the constraints in the base ΛCDM cosmology. The red contours are broader than the blue contours and there is greater overlap with the CFHTLenS contours, *but this offers only a marginal improvement compared to base ΛCDM* (compare with Fig. 18; see also the discussions in Leistedt et al. 2014 and Battye et al. 2015). For each of these models, the CFHTLenS results prefer

lower values of σ_8. Allowing for a higher neutrino mass lowers σ_8 from *Planck*, but does not help alleviate the discrepancy with the CFHTLenS data, since the *Planck* data prefer a lower value of H_0. A joint analysis of the CFHTLenS likelihood with *Planck* TT+lowP shows a $\Delta\chi^2 < 1$ preference for the extended neutrino models compared to base ΛCDM, and the fits to *Planck* TT+lowP are worse in all cases. In base ΛCDM the CFHTLenS data prefer a region of parameter space $\Delta\chi^2 \approx 4$ away from the *Planck* TT+lowP+CFHTLenS joint fit, indicative of the tension between the data sets. This is only slightly relieved to $\Delta\chi^2 \approx 3$ in the extended models.

In summary, modifications to the neutrino sector alone cannot easily explain the discrepancies between *Planck* and other astrophysical data described in Sect. 5.5, including the inference of a low value of σ_8 from rich cluster counts.

6.4.5. Testing perturbations in the neutrino background

As shown in the previous sections, the *Planck* data provide evidence for a cosmic neutrino background at a very high significance level. Neutrinos affect the CMB anisotropies at the background level, by changing the expansion rate before recombination and hence relevant quantities such as the sound horizon and the damping scales. Neutrinos also affect the CMB anisotropies via their perturbations. Perturbations in the neutrino background are coupled through gravity to the perturbations in the photon background, and can be described (for massless neutrinos) by the following set of equations (Hu 1998; Hu et al. 1999; Trotta & Melchiorri 2005; Archidiacono et al. 2011):

$$\dot{\delta}_\nu = \frac{\dot{a}}{a}\left(1 - 3c_{\text{eff}}^2\right)\left(\delta_\nu + 3\frac{\dot{a}}{a}\frac{q_\nu}{k}\right) - k\left(q_\nu + \frac{2}{3k}\dot{h}\right), \tag{68a}$$

$$\dot{q}_\nu = k\,c_{\text{eff}}^2\left(\delta_\nu + 3\frac{\dot{a}}{a}\frac{q_\nu}{k}\right) - \frac{\dot{a}}{a}q_\nu - \frac{2}{3}k\pi_\nu, \tag{68b}$$

$$\dot{\pi}_\nu = 3k\,c_{\text{vis}}^2\left(\frac{2}{5}q_\nu + \frac{4}{15k}(\dot{h} + 6\dot{\eta})\right) - \frac{3}{5}kF_{\nu,3}, \tag{68c}$$

$$\dot{F}_{\nu,\ell} = \frac{k}{2\ell+1}\left(\ell F_{\nu,\ell-1} - (\ell+1)F_{\nu,\ell+1}\right), \quad (\ell \geq 3). \tag{68d}$$

Here dots denote derivatives with respect to conformal time, δ_ν is the neutrino density contrast, q_ν is the neutrino velocity perturbation, π_ν the anisotropic stress, $F_{\nu,\ell}$ are higher-order moments of the neutrino distribution function, and h and η are the scalar metric perturbations in the synchronous gauge. In these equations, c_{eff}^2 is the neutrino sound speed in its own reference frame and c_{vis}^2 parameterizes the anisotropic stress. For standard non-interacting massless neutrinos $c_{\text{eff}}^2 = c_{\text{vis}}^2 = 1/3$. Any deviation from the expected values could provide a hint of non-standard physics in the neutrino sector.

A greater (lower) neutrino sound speed would increase (decrease) the neutrino pressure, leading to a lower (higher) perturbation amplitude. On the other hand, changing c_{vis}^2 alters the viscosity of the neutrino fluid. For $c_{\text{vis}}^2 = 0$, the neutrinos act as a perfect fluid, supporting undamped acoustic oscillations.

Several previous studies have used this approach to constrain c_{eff}^2 and c_{vis}^2 using cosmological data (see, e.g., Trotta & Melchiorri 2005; Smith et al. 2012; Archidiacono et al. 2013b; Gerbino et al. 2013; Audren et al. 2015), with the motivation that deviations from the expected values could be a hint of non-standard physics in the neutrino sector. Non-standard interactions could involve, for example, neutrino coupling with
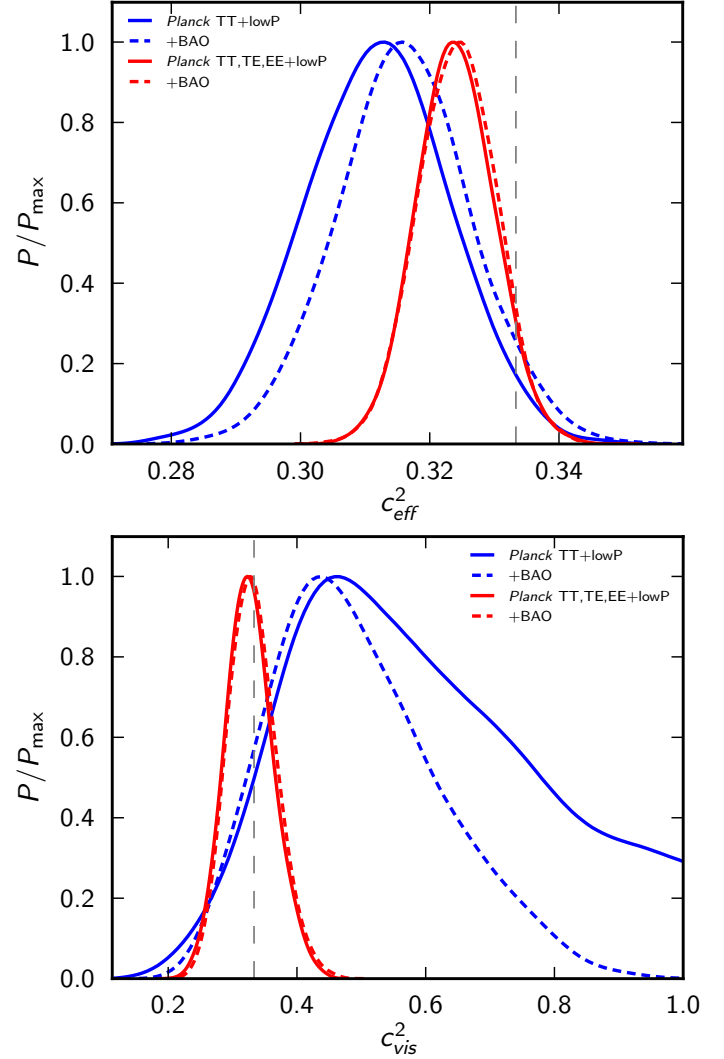

Fig. 34. 1D posterior distributions for the neutrino perturbation parameters c_{eff}^2 (*top*) and c_{vis}^2 (*bottom*). Dashed vertical lines indicate the conventional values $c_{\text{eff}}^2 = c_{\text{vis}}^2 = 1/3$.

light scalar particles (Hannestad 2005; Beacom et al. 2004; Bell 2005; Sawyer 2006). If neutrinos are strongly coupled at recombination, this would result in a lower value for c_{vis}^2 than in the standard model. Alternatively, the presence of early dark energy that mimics a relativistic component at recombination could possibly lead to a value for c_{eff}^2 that differs from $1/3$ (see, e.g., Calabrese et al. 2011).

In this analysis, for simplicity, we assume $N_{\text{eff}} = 3.046$ and massless neutrinos. By using an equivalent parameterization for massive neutrinos (Audren et al. 2015) we have checked that assuming one massive neutrino with $\Sigma m_\nu \approx 0.06\,\text{eV}$, as in the base model used throughout this paper, has no impact on the constraints on c_{eff}^2 and c_{vis}^2 reported in this section[29]. We adopt a flat prior between zero and unity for both c_{vis}^2 and c_{eff}^2.

The top and bottom panels of Fig. 34 show the posterior distributions of c_{eff}^2 and c_{vis}^2 from *Planck* TT+lowP, *Planck* TT+lowP+BAO, *Planck* TT,TE,EE+lowP, and *Planck* TT,TE,EE+lowP+BAO. The mean values and 68% errors on c_{eff}^2

---

[29] We also do not explore extended cosmologies in this section, since no significant degeneracies are expected between $(\sum m_\nu, N_{\text{eff}}, w, \text{d}n_s/\text{d}\ln k)$ and $(c_{\text{eff}}^2, c_{\text{vis}}^2)$ (Audren et al. 2015).

and c_{vis}^2 are

$$c_{\mathrm{eff}}^2 = 0.312 \pm 0.011$$
$$c_{\mathrm{vis}}^2 = 0.47_{-0.12}^{+0.26}$$
$$\left.\right\} \quad Planck \ \mathrm{TT+lowP}, \qquad (69a)$$

$$c_{\mathrm{eff}}^2 = 0.316 \pm 0.010$$
$$c_{\mathrm{vis}}^2 = 0.44_{-0.10}^{+0.15}$$
$$\left.\right\} \quad Planck \ \mathrm{TT+lowP+BAO}, \qquad (69b)$$

$$c_{\mathrm{eff}}^2 = 0.3240 \pm 0.0060$$
$$c_{\mathrm{vis}}^2 = 0.327 \pm 0.037$$
$$\left.\right\} \quad Planck \ \mathrm{TT,TE,EE+lowP}, \qquad (69c)$$

$$c_{\mathrm{eff}}^2 = 0.3242 \pm 0.0059$$
$$c_{\mathrm{vis}}^2 = 0.331 \pm 0.037$$
$$\left.\right\} \quad Planck \ \mathrm{TT,TE,EE+lowP+BAO}. \qquad (69d)$$

Constraints on these parameters are consistent with the conventional values $c_{\mathrm{eff}}^2 = c_{\mathrm{vis}}^2 = 1/3$. A vanishing value of c_{vis}^2, which might imply a strong interaction between neutrinos and other species, is excluded at more than the 95% level arising from the *Planck* temperature data. This conclusion is greatly strengthened (to about 9σ) when *Planck* polarization data are included. As discussed in Bashinsky & Seljak (2004), neutrino anisotropic stresses introduce a phase shift in the CMB angular power spectra, which is more visible in polarization than temperature because of the sharper acoustic peaks. This explains why we see such a dramatic reduction in the error on c_{vis}^2 when including polarization data.

The precision of our results is consistent with the forecasts discussed in Smith et al. (2012), and we find strong evidence, purely from CMB observations, for neutrino anisotropies with the standard values $c_{\mathrm{vis}}^2 = 1/3$ and $c_{\mathrm{eff}}^2 = 1/3$.

6.5. Primordial nucleosynthesis

6.5.1. Details of analysis approach

Standard big bang nucleosynthesis (BBN) predicts light element abundances as a function of parameters relevant to the CMB, such as the baryon-to-photon density ratio $\eta_{\mathrm{b}} \equiv n_{\mathrm{b}}/n_{\gamma}$, the radiation density parameterized by N_{eff}, and the chemical potential of the electron neutrinos. In PCP13, we presented consistency checks between the *Planck* 2013 results, light element abundance data, and standard BBN. The goal of Sect. 6.5.2 below is to update these results and to provide improved tests of the standard BBN model. In Sect. 6.5.3 we show how *Planck* data can be used to constrain nuclear reaction rates, and in Sect. 6.5.4 we will present the most stringent CMB bounds to date on the primordial helium fraction.

For simplicity, our analysis assumes a negligible leptonic asymmetry in the electron neutrino sector. For a fixed photon temperature today (which we take to be $T_0 = 2.7255 \ \mathrm{K}$), η_{b} can be related to $\omega_{\mathrm{b}} \equiv \Omega_{\mathrm{b}} h^2$, up to a small (and negligible) uncertainty associated with the primordial helium fraction. Standard BBN then predicts the abundance of each light element as a function of only two parameters, ω_{b} and $\Delta N_{\mathrm{eff}} \equiv N_{\mathrm{eff}} - 3.046$, with a theoretical error coming mainly from uncertainties in the neutron lifetime and a few nuclear reaction rates.

We will confine our discussion to BBN predictions for the primordial abundances[30] of ^{4}He and deuterium, expressed,

respectively as $Y_{\mathrm{P}}^{\mathrm{BBN}} = 4n_{\mathrm{He}}/n_{\mathrm{b}}$ and $y_{\mathrm{DP}} = 10^5 n_{\mathrm{D}}/n_{\mathrm{H}}$. We will not discuss other light elements, such as tritium and lithium, because the observed abundance measurements and their interpretation is more controversial (see Fields et al. 2014, for a recent review). As in PCP13, the BBN predictions for $Y_{\mathrm{P}}^{\mathrm{BBN}}(\omega_{\mathrm{b}}, \Delta N_{\mathrm{eff}})$ and $y_{\mathrm{DP}}(\omega_{\mathrm{b}}, \Delta N_{\mathrm{eff}})$ are given by Taylor expansions obtained with the `PArthENoPE` code (Pisanti et al. 2008), similar to the ones presented in Iocco et al. (2009), but updated by the `PArthENoPE` team with the latest observational data on nuclear rates and on the neutron life-time:

$$Y_{\mathrm{P}}^{\mathrm{BBN}} = 0.2311 + 0.9502\omega_{\mathrm{b}} - 11.27\omega_{\mathrm{b}}^2$$
$$+ \Delta N_{\mathrm{eff}} \left(0.01356 + 0.008581\omega_{\mathrm{b}} - 0.1810\omega_{\mathrm{b}}^2\right)$$
$$+ \Delta N_{\mathrm{eff}}^2 \left(-0.0009795 - 0.001370\omega_{\mathrm{b}} + 0.01746\omega_{\mathrm{b}}^2\right), \quad (70)$$

$$y_{\mathrm{DP}} = 18.754 - 1534.4\omega_{\mathrm{b}} + 48656\omega_{\mathrm{b}}^2 - 552670\omega_{\mathrm{b}}^3$$
$$+ \Delta N_{\mathrm{eff}} \left(2.4914 - 208.11\omega_{\mathrm{b}} + 6760.9\omega_{\mathrm{b}}^2 - 78007\omega_{\mathrm{b}}^3\right)$$
$$+ \Delta N_{\mathrm{eff}}^2 \left(0.012907 - 1.3653\omega_{\mathrm{b}} + 37.388\omega_{\mathrm{b}}^2 - 267.78\omega_{\mathrm{b}}^3\right). \quad (71)$$

By averaging over several measurements, the Particle Data Group 2014 (Olive et al. 2014) estimates the neutron life-time to be $\tau_{\mathrm{n}} = (880.3 \pm 1.1) \ \mathrm{s}$ at 68% CL[31]. The expansions in Eqs. (70) and (71) are based on this central value, and we assume that Eq. (70) predicts the correct helium fraction up to a standard error $\sigma(Y_{\mathrm{P}}^{\mathrm{BBN}}) = 0.0003$, obtained by propagating the error on τ_{n}.

The uncertainty on the deuterium fraction is dominated by that on the rate of the reaction $\mathrm{d}(\mathrm{p}, \gamma)^3\mathrm{He}$. For that rate, in PCP13 we relied on the result of Serpico et al. (2004), obtained by fitting several experiments. The expansions of Eqs. (70) and (71) now adopt the latest experimental determination by Adelberger et al. (2011) and use the best-fit expression in their Eq. (29). We also rely on the uncertainty quoted in Adelberger et al. (2011) and propagate it to the deuterium fraction. This gives a standard error $\sigma(y_{\mathrm{DP}}) = 0.06$, which is more conservative than the error adopted in PCP13.

6.5.2. Primordial abundances from *Planck* data and standard BBN

We first investigate the consistency of standard BBN and the CMB by fixing the radiation density to its standard value, i.e., $N_{\mathrm{eff}} = 3.046$, based on the assumption of standard neutrino decoupling and no extra light relics. We can then use *Planck* data to measure ω_{b}, assuming base ΛCDM, and test for consistency with experimental abundance measurements. The 95% CL bounds obtained for the base ΛCDM model for various data

---

[30] BBN calculations usually refer to nucleon number density fractions rather than mass fractions. To avoid any ambiguity with the helium mass fraction Y_{P}, normally used in CMB physics, we use superscripts to distinguish between the two definitions $Y_{\mathrm{P}}^{\mathrm{CMB}}$ and $Y_{\mathrm{P}}^{\mathrm{BBN}}$. Typically, $Y_{\mathrm{P}}^{\mathrm{BBN}}$ is about 0.5% higher than $Y_{\mathrm{P}}^{\mathrm{CMB}}$.

[31] However, the most recent individual measurement by Yue et al. (2013) gives $\tau_{\mathrm{n}} = [887.8 \pm 1.2 \ (\mathrm{stat.}) \pm 1.9 \ (\mathrm{syst.})] \ \mathrm{s}$, which is discrepant at 3.3σ with the previous average (including only statistical errors). Hence one should bear in mind that systematic effects could be underestimated in the Particle Data Group result. Adopting the central value of Yue et al. (2013) would shift our results by a small amount (by a factor of 1.0062 for Y_{P} and 1.0036 for y_{DP}).
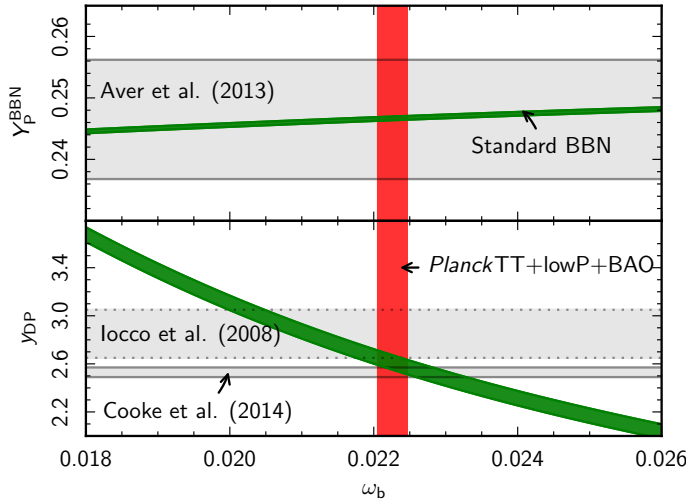
Fig. 35. Predictions of standard BBN for the primordial abundance of ^{4}He (*top*) and deuterium (*bottom*), as a function of the baryon density ω_b. The width of the green stripes corresponds to 68% uncertainties on nuclear reaction rates and on the neutron lifetime. The horizontal bands show observational bounds on primordial element abundances compiled by various authors, and the red vertical band shows the *Planck* TT+lowP+BAO bounds on ω_b (all with 68% errors). The BBN predictions and CMB results shown here assume $N_{eff} = 3.046$ and no significant lepton asymmetry.

combinations are

$$\omega_b = \begin{cases} 0.02222^{+0.00045}_{-0.00043} & Planck\ \mathrm{TT+lowP}, \\ 0.02226^{+0.00040}_{-0.00039} & Planck\ \mathrm{TT+lowP+BAO}, \\ 0.02225^{+0.00032}_{-0.00030} & Planck\ \mathrm{TT,TE,EE+lowP}, \\ 0.02229^{+0.00029}_{-0.00027} & Planck\ \mathrm{TT,TE,EE+lowP+BAO}, \end{cases} \tag{72}$$

corresponding to a predicted primordial ^{4}He number density fraction (95% CL) of

$$Y_P^{BBN} = \begin{cases} 0.24665^{+(0.00020)\ 0.00063}_{-(0.00019)\ 0.00063} & Planck\ \mathrm{TT+lowP}, \\ 0.24667^{+(0.00018)\ 0.00063}_{-(0.00018)\ 0.00063} & Planck\ \mathrm{TT+lowP+BAO}, \\ 0.24667^{+(0.00014)\ 0.00062}_{-(0.00014)\ 0.00062} & Planck\ \mathrm{TT,TE,EE+lowP}, \\ 0.24668^{+(0.00013)\ 0.00061}_{-(0.00013)\ 0.00061} & Planck\ \mathrm{TT,TE,EE+lowP+BAO}, \end{cases} \tag{73}$$

and deuterium fraction (95% CL)

$$y_{DP} = \begin{cases} 2.620^{+(0.083)\ 0.15}_{-(0.085)\ 0.15} & Planck\ \mathrm{TT+lowP}, \\ 2.612^{+(0.075)\ 0.14}_{-(0.074)\ 0.14} & Planck\ \mathrm{TT+lowP+BAO}, \\ 2.614^{+(0.057)\ 0.13}_{-(0.060)\ 0.13} & Planck\ \mathrm{TT,TE,EE+lowP}, \\ 2.606^{+(0.051)\ 0.13}_{-(0.054)\ 0.13} & Planck\ \mathrm{TT,TE,EE+lowP+BAO}. \end{cases} \tag{74}$$

The first set of error bars (in parentheses) in Eqs. (73) and (74) reflect only the uncertainty on ω_b. The second set includes the theoretical uncertainty on the BBN predictions, added in quadrature to the errors from ω_b. The total errors in the predicted helium abundances are dominated by the BBN uncertainty, as in PCP13. For deuterium, the *Planck* 2015 results improve the determination of ω_b to the point where the theoretical errors are

comparable or larger than the errors from the CMB. In other words, for base ΛCDM the predicted abundances cannot be improved substantially by further measurements of the CMB. This also means that *Planck* results can, in principle, be used to investigate nuclear reaction rates that dominate the theoretical uncertainty (see Sect. 6.5.3).

The results of Eqs. (73) and (74) are well within the ranges indicated by the latest measurements of primordial abundances, as illustrated in Fig. 35. The helium data compilation of Aver et al. (2013) gives $Y_P^{BBN} = 0.2465 \pm 0.0097$ (68% CL), and the *Planck* prediction is near the middle of this range[32]. As summarized by Aver et al. (2013) and Peimbert (2008), helium abundance measurements derived from emission lines in low-metallicity H II regions are notoriously difficult and prone to systematic errors. As a result, many discrepant helium abundance measurements can be found in the literature. Izotov et al. (2014) have reported $Y_P^{BBN} = 0.2551 \pm 0.0022$, which is discrepant with the base ΛCDM predictions by 3.4σ. Such a high helium fraction could be accommodated by increasing N_{eff} (see Fig. 36 and Sect. 6.5.4); however, at present it is not clear whether the error quoted by Izotov et al. (2014) accurately reflects systematic uncertainties, including in particular the error in extrapolating to zero metallicity.

Historically, deuterium abundance measurements have shown excess scatter over that expected from statistical errors, indicating the presence of systematic uncertainties in the observations. Figure 35 shows the data compilation of Iocco et al. (2009), $y_{DP} = 2.87 \pm 0.22$ (68% CL), which includes measurements based on damped Lyα and Lyman limit systems. We also show the more recent results by Cooke et al. (2014; see also Pettini & Cooke 2012) based on their observations of low-metallicity damped Lyα absorption systems in two quasars (SDSS J1358+6522, $z_{abs} = 3.06726$ and SDSS J1419+0829, $z_{abs} = 3.04973$) and a reanalysis of archival spectra of damped Lyα systems in three further quasars that satisfy strict selection criteria. The Cooke et al. (2014) analysis gives $y_{DP} = 2.53 \pm 0.04$ (68% CL), somewhat lower than the central Iocco et al. (2009) value, and with a much smaller error. The Cooke et al. (2014) value is almost certainly the more reliable measurement, as evidenced by the consistency of the deuterium abundances of the five systems in their analysis. The *Planck* base ΛCDM predictions of Eq. (74) lie within 1σ of the Cooke et al. (2014) result. This is a remarkable success for the standard theory of BBN.

It is worth noting that the *Planck* data are so accurate that ω_b is insensitive to the underlying cosmological model. In our grid of extensions to base ΛCDM the largest degradation of the error in ω_b is in models that allow N_{eff} to vary. In these models, the mean value of ω_b is almost identical to that for base ΛCDM, but the error on ω_b increases by about 30%. The value of ω_b is stable to even more radical changes to the cosmology, for example, adding general isocurvature modes (Planck Collaboration XX 2016).

If we relax the assumption that $N_{eff} = 3.046$ (but adhere to the hypothesis that electron neutrinos have a standard distribution, with a negligible chemical potential), BBN predictions depend on both parameters (ω_b and N_{eff}). Following the same methodology as in Sect. 6.4.4 of PCP13, we can identify the region of the ω_b–N_{eff} parameter space that is compatible with direct measurements of the primordial helium and deuterium

---

[32] A substantial part of this error comes from the regression to zero metallicity. The mean of the 17 measurements analysed by Aver et al. (2013) is $\langle Y_P^{BBN} \rangle = 0.2535 \pm 0.0036$, i.e., about 1.7σ higher than the *Planck* predictions of Eq. (73).
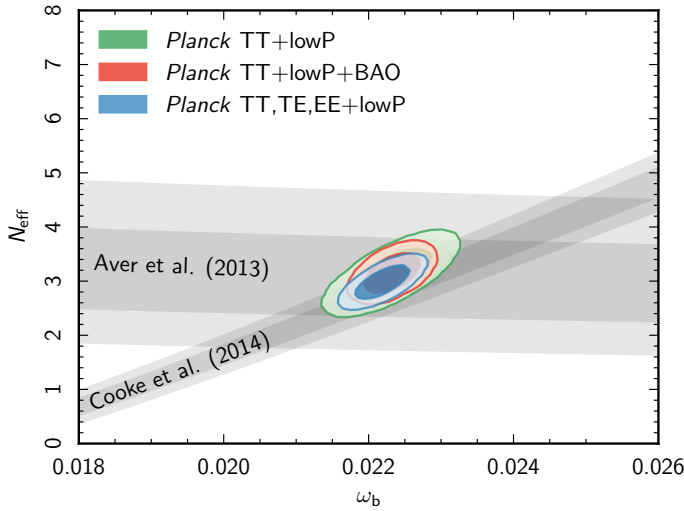
Fig. 36. Constraints in the ω_b–N_{eff} plane from *Planck* and *Planck*+BAO data (68% and 95% contours) compared to the predictions of BBN, given primordial element abundance measurements. We show the 68% and 95% confidence regions derived from ^{4}He bounds compiled by Aver et al. (2013) and from deuterium bounds compiled by Cooke et al. (2014). In the CMB analysis, N_{eff} is allowed to vary as an additional parameter to base ΛCDM, with Y_P fixed as a function of ω_b and N_{eff}, according to BBN predictions. These constraints assume no significant lepton asymmetry.

abundances, including the BBN theoretical errors. This is illustrated in Fig. 36 for the N_{eff} extension to base ΛCDM. The region preferred by CMB observations lies at the intersection between the helium and deuterium abundance 68% CL preferred regions and is compatible with the standard value of N_{eff} = 3.046. This confirms the beautiful agreement between CMB and BBN physics. Figure 36 also shows that the *Planck* polarization data help in reducing the degeneracy between ω_b and N_{eff}.

We can actually make a more precise statement by combining the posterior distribution on ω_b and N_{eff}) obtained for *Planck* with that inferred from helium and deuterium abundance, including observational and theoretical errors. This provides joint CMB+BBN predictions on these parameters. After marginalizing over ω_b, the 95% CL preferred ranges for N_{eff} are

$$N_{\text{eff}} = \begin{cases} 3.11^{+0.59}_{-0.57} & \text{He+}Planck\text{ TT+lowP,} \\ 3.14^{+0.44}_{-0.43} & \text{He+}Planck\text{ TT+lowP+BAO,} \\ 2.99^{+0.39}_{-0.39} & \text{He+}Planck\text{ TT,TE,EE+lowP,} \end{cases} \quad (75)$$

when combining *Planck* with the helium abundance estimated by Aver et al. (2013), or

$$N_{\text{eff}} = \begin{cases} 2.95^{+0.52}_{-0.52} & \text{D+}Planck\text{ TT+lowP,} \\ 3.01^{+0.38}_{-0.37} & \text{D+}Planck\text{ TT+lowP+BAO,} \\ 2.91^{+0.37}_{-0.37} & \text{D+}Planck\text{ TT,TE,EE+lowP,} \end{cases} \quad (76)$$

when combining with the deuterium abundance measured by Cooke et al. (2014). These bounds represent the best currently-available estimates of N_{eff} and are remarkably consistent with the standard model prediction.

The allowed region in ω_b–N_{eff} space does not increase significantly when other parameters are allowed to vary at the same time. From our grid of extended models, we have checked that this conclusion holds in models with neutrino masses, tensor fluctuations, or running of the scalar spectral index, for example.

6.5.3. Constraints from *Planck* and deuterium observations on nuclear reaction rates

We have seen that primordial element abundances estimated from direct observations are consistent with those inferred from *Planck* data under the assumption of standard BBN. However, the *Planck* determination of ω_b is so precise that the theoretical errors in the BBN predictions are now a dominant source of uncertainty. As noted by Cooke et al. (2014), one can begin to think about using CMB measurements together with accurate deuterium abundance measurements to learn about the underlying BBN physics.

While for helium the theoretical error comes mainly from the uncertainties in the neutron lifetime, for deuterium it is dominated by uncertainties in the radiative capture process $d(p, \gamma)^3$He, converting deuterium into helium. The present experimental uncertainty for the S-factor at low energy (relevant for BBN), is in the range $6{-}10\%$ (Ma et al. 1997). However, as noted by several authors (see, e.g., Nollett & Holder 2011; Di Valentino et al. 2014) the best-fit value of $S(E)$ inferred from experimental data in the range $30\,\text{keV} \leq E \leq 300\,\text{keV}$ is about $5{-}10\%$ lower than theoretical expectations (Viviani et al. 2000; Marcucci et al. 2005). The `PArthENoPE` BBN code assumes the lower experimental value for $d(p, \gamma)^3$He, and this might explain why the deuterium abundance determined by Cooke et al. (2014) is slightly lower than the value inferred by *Planck*.

To investigate this further, following the methodology of Di Valentino et al. (2014), we perform a combined analysis of *Planck* and deuterium observations, to constrain the value of the $d(p, \gamma)^3$He reaction rate. As in Di Valentino et al. (2014), we parameterize the thermal rate $R_2(T)$ of the $d(p, \gamma)^3$He process in the `PArthENoPE` code by introducing a rescaling factor A_2 of the experimental rate $R_2^{\text{ex}}(T)$, i.e., $R_2(T) = A_2 R_2^{\text{ex}}(T)$, and solve for A_2 using various *Planck*+BAO data combinations, given the Cooke et al. (2014) deuterium abundance measurements.

Assuming the base ΛCDM model we find (68% CL)

$$\begin{aligned} A_2 &= 1.106 \pm 0.071 & Planck\text{ TT+lowP,} & \quad (77a) \\ A_2 &= 1.098 \pm 0.067 & Planck\text{ TT+lowP+BAO,} & \quad (77b) \\ A_2 &= 1.110 \pm 0.062 & Planck\text{ TT, TE, EE+lowP,} & \quad (77c) \\ A_2 &= 1.109 \pm 0.058 & Planck\text{ TT, TE, EE+lowP+BAO.} & \quad (77d) \end{aligned}$$

The posteriors for A_2 are shown in Fig. 37. These results suggest that the $d(p, \gamma)^3$He reaction rate may be have been underestimated by about 10%. Evidently, tests of the standard BBN picture appear to have reached the point where they are limited by uncertainties in nuclear reaction rates. There is therefore a strong case to improve the precision of experimental measurements (e.g., Anders et al. 2014) and theoretical computations of key nuclear reaction rates relevant for BBN.

6.5.4. Model-independent bounds on the helium fraction from *Planck*

Instead of inferring the primordial helium abundance from BBN codes using $(\omega_b, N_{\text{eff}})$ constraints from *Planck*, we can measure it directly, since variations in Y_P^{BBN} modify the density of free electrons between helium and hydrogen recombination and therefore affect the damping tail of the CMB anisotropies.
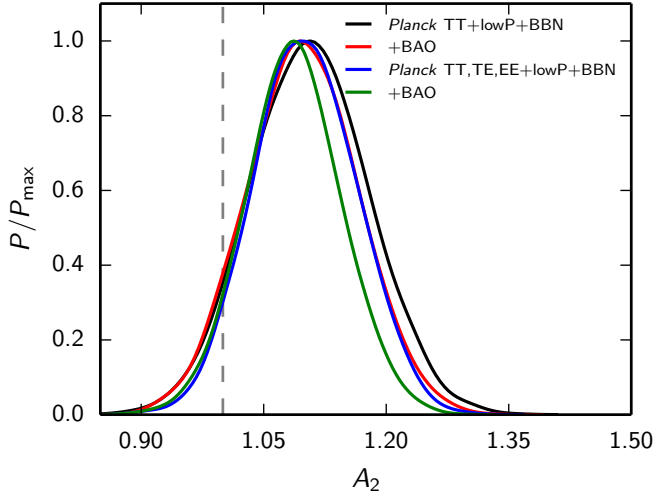
Fig. 37. Posteriors for the A_2 reaction rate parameter for various data combinations. The vertical dashed line shows the value $A_2 = 1$ that corresponds to the current experimental estimate of the d(p, γ)^{3}He rate used in the `PArthENoPE` BBN code.

If we allow $Y_{\rm P}^{\rm CMB}$ to vary as an additional parameter to base ΛCDM, we find the following constraints (at 95% CL):

$$Y_{\rm P}^{\rm BBN} = \begin{cases} 0.253^{+0.041}_{-0.042} & Planck\ {\rm TT+lowP}, \\ 0.255^{+0.036}_{-0.038} & Planck\ {\rm TT+lowP+BAO}, \\ 0.251^{+0.026}_{-0.027} & Planck\ {\rm TT,TE,EE+lowP}, \\ 0.253^{+0.025}_{-0.026} & Planck\ {\rm TT,TE,EE+lowP+BAO}. \end{cases}$$
(78)

Joint constraints on $Y_{\rm P}^{\rm BBN}$ and $\omega_{\rm b}$ are shown in Fig. 38. The addition of *Planck* polarization measurements results in a substantial reduction in the uncertainty on the helium fraction. In fact, the standard deviation on $Y_{\rm P}^{\rm BBN}$ in the case of *Planck* TT,TE,EE+lowP is only 30% larger than the observational error quoted by Aver et al. (2013). As emphasized throughout this paper, the systematic effects in the *Planck* polarization spectra, although at low levels, have not been accurately characterized at this time. Readers should therefore treat the polarization constraints with some caution. Nevertheless, as shown in Fig. 38, all three data combinations agree well with the observed helium abundance measurements and with the predictions of standard BBN.

There is a well-known parameter degeneracy between $Y_{\rm P}$ and the radiation density (see the discussion in PCP13). Helium abundance predictions from the CMB are therefore particularly sensitive to the addition of the parameter $N_{\rm eff}$ to base ΛCDM. Allowing both $Y_{\rm P}^{\rm BBN}$ and $N_{\rm eff}$ to vary we find the following constraints (at 95% CL):

$$Y_{\rm P}^{\rm BBN} = \begin{cases} 0.252^{+0.058}_{-0.065} & Planck\ {\rm TT+lowP}, \\ 0.251^{+0.058}_{-0.064} & Planck\ {\rm TT+lowP+BAO}, \\ 0.263^{+0.034}_{-0.037} & Planck\ {\rm TT,TE,EE+lowP}, \\ 0.262^{+0.035}_{-0.037} & Planck\ {\rm TT,TE,EE+lowP+BAO}. \end{cases}$$
(79)

Contours in the $Y_{\rm P}^{\rm BBN}$–$N_{\rm eff}$ plane are shown in Fig. 39. Here again, the impact of *Planck* polarization data is important, and helps to substantially reduce the degeneracy between these two
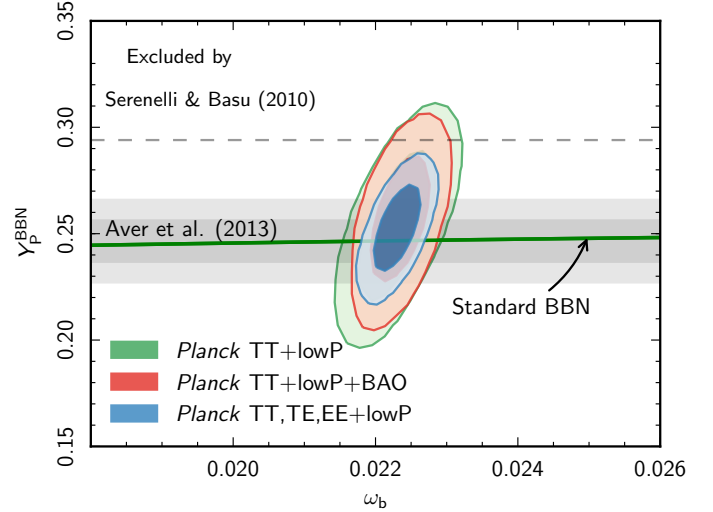
Fig. 38. Constraints in the $\omega_{\rm b}$–$Y_{\rm P}^{\rm BBN}$ plane from *Planck* and *Planck*+BAO, compared to helium abundance measurements. Here 68% and 95% contours are plotted for the CMB(+BAO) data combinations when $Y_{\rm P}^{\rm BBN}$ is allowed to vary as an additional parameter to base ΛCDM. The horizontal band shows observational bounds on ^{4}He compiled by Aver et al. (2013) with 68% and 95% errors, while the dashed line at the top of the figure delineates the conservative 95% upper bound inferred from the Solar helium abundance by Serenelli & Basu (2010). The green stripe shows the predictions of standard BBN for the primordial abundance of ^{4}He as a function of the baryon density. Both BBN predictions and CMB results assume $N_{\rm eff} = 3.046$ and no significant lepton asymmetry.
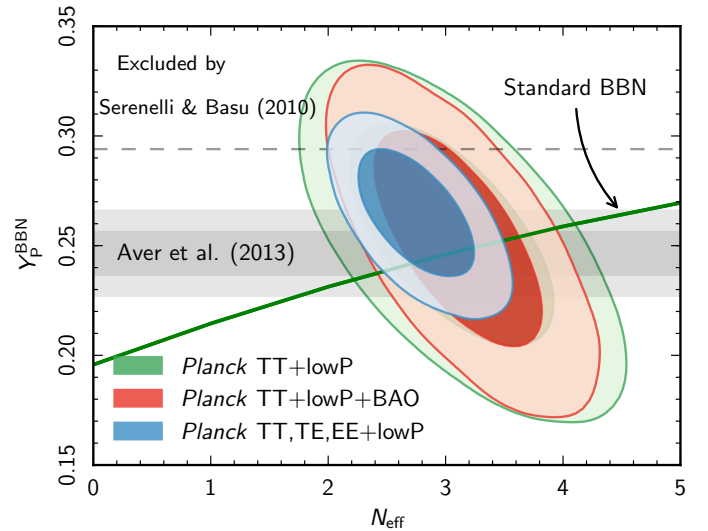
Fig. 39. As in Fig. 38, but now allowing $Y_{\rm P}^{\rm BBN}$ and $N_{\rm eff}$ to vary as parameter extensions to base ΛCDM.

parameters. The *Planck* TT,TE,EE+lowP contours are in very good agreement with standard BBN and $N_{\rm eff} = 3.046$. However, even if we relax the assumption of standard BBN, the CMB does not allow high values of $N_{\rm eff}$. It is therefore difficult to accommodate an extra thermalized relativistic species, even if the standard BBN prior on the helium fraction is relaxed.

6.6. Dark matter annihilation

Energy injection from dark matter (DM) annihilation can alter the recombination history, leading to changes in the

temperature and polarization power spectra of the CMB (e.g., Chen & Kamionkowski 2004; Padmanabhan & Finkbeiner 2005). As demonstrated in several papers (e.g., Galli et al. 2009a; Slatyer et al. 2009; Finkbeiner et al. 2012), CMB anisotropies offer an opportunity to constrain the nature of DM. Furthermore, CMB experiments such as *Planck* can achieve limits on the annihilation cross-section that are relevant for the interpretation of the rise in the cosmic-ray positron fraction at energies $\gtrsim 10\,\mathrm{GeV}$ observed by PAMELA, *Fermi*, and AMS (Adriani et al. 2009; Ackermann et al. 2012; Aguilar et al. 2014). The CMB constraints are complementary to those determined from other astrophysical probes, such as the γ-ray observations of dwarf galaxies by the *Fermi* satellite (Ackermann et al. 2014).

The way in which DM annihilations heat and ionize the gaseous background depends on the nature of the cascade of particles produced following annihilation and, in particular, on the production of $e^\pm$ pairs and photons that couple to the gas. The fraction of the rest mass energy that is injected into the gas can be modelled by an "efficiency factor", $f(z)$, which is typically in the range $0.01-1$ and depends on redshift[33]. Computations of $f(z)$ for various annihilation channels can be found in Slatyer et al. (2009), Hütsi et al. (2009), and Evoli et al. (2013). The rate of energy release per unit volume by annihilating DM can therefore be written as

$$\frac{\mathrm{d}E}{\mathrm{d}t\mathrm{d}V}(z) = 2\,g\,\rho_{\mathrm{crit}}^2 c^2 \Omega_{\mathrm{c}}^2 (1+z)^6 p_{\mathrm{ann}}(z), \tag{80}$$

where p_{ann} is defined as

$$p_{\mathrm{ann}}(z) \equiv f(z)\frac{\langle\sigma v\rangle}{m_\chi}. \tag{81}$$

Here ρ_{crit} the critical density of the Universe today, m_χ is the mass of the DM particle, and $\langle\sigma v\rangle$ is the thermally-averaged annihilation cross-section times the velocity (explicitly the so-called Møller velocity); we will refer to this quantity loosely as the "cross-section" hereafter. In Eq. (80), g is a degeneracy factor that is equal to 1/2 for Majorana particles and 1/4 for Dirac particles. In this paper, the constraints will refer to Majorana particles. Note that to produce the observed dark matter density from thermal DM relics requires an annihilation cross-section of $\langle\sigma v\rangle \approx 3 \times 10^{-26}\,\mathrm{cm}^3\,\mathrm{s}^{-1}$ (assuming s-wave annihilation) at the time of freeze-out (see, e.g., the review by Profumo 2013).

Both the amplitude and redshift dependence of the efficiency factor $f(z)$ depend on the details of the annihilation process (e.g., Slatyer et al. 2009). The functional shape of $f(z)$ can be taken into account using generalized parameterizations or principal components (Finkbeiner et al. 2012; Hutsi et al. 2011), similar to the analysis of the recombination history presented in Sect. 6.7.4. However, as shown in Galli et al. (2011), Giesen et al. (2012), and Finkbeiner et al. (2012), to a first approximation the redshift dependence of $f(z)$ can be ignored, since current CMB data (including *Planck*) are sensitive to energy injection over a relatively narrow range of redshift, typically $z \approx 1000-600$. The effects of DM annihilation can therefore be reasonably well parameterized by a single constant parameter, p_{ann} (with $f(z)$ set to a constant f_{eff}), which encodes the dependence on the properties of the DM particles. In the following, we calculate constraints on the p_{ann} parameter, assuming that it is constant, and then project these constraints on to

Table 6. Constraints on p_{ann} in units of $\mathrm{cm}^3\,\mathrm{s}^{-1}\,\mathrm{GeV}^{-1}$.

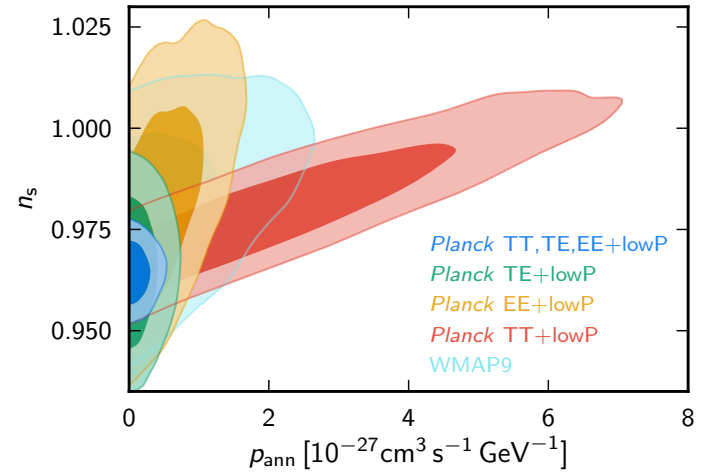| Data combinations	p_{ann} (95% upper limits)
TT+lowP	$<.7 \times 10^{-27}$
EE+lowP	$<1.4 \times 10^{-27}$
TE+lowP	$<5.9 \times 10^{-28}$
TT+lowP+lensing	$<4.4 \times 10^{-27}$
TT,TE,EE+lowP	$< 4.1 \times 10^{-28}$
TT,TE,EE+lowP+lensing	$<3.4 \times 10^{-28}$
TT,TE,EE+lowP+ext	$<3.5 \times 10^{-28}$

Fig. 40. 2D marginal distributions in the $p_{\mathrm{ann}}-n_{\mathrm{s}}$ plane for *Planck* TT+lowP (red), *Planck* EE+lowP (yellow), *Planck* TE+lowP (green), and *Planck* TT,TE,EE+lowP (blue) data combinations. We also show the constraints obtained using WMAP9 data (light blue).

a particular dark matter model assuming $f_{\mathrm{eff}} \equiv f(z = 600)$, since the effect of dark matter annihilation peaks at $z \approx 600$ (see Finkbeiner et al. 2012). The $f(z)$ functions used here are those calculated in Slatyer et al. (2009), with the updates described in Galli et al. (2013) and Madhavacheril et al. (2014). Finally, we estimate the fractions of injected energy that affect the gaseous background, from heating, ionizations, or Lyα excitations, using the updated calculations described in Galli et al. (2013) and Valdes et al. (2010), following Shull & van Steenberg (1985).

We compute the theoretical angular power spectrum in the presence of DM annihilations by modifying the `recfast` routine (Seager et al. 1999) in the `camb` code as in Galli et al. (2011)[34]. We then add p_{ann} as an additional parameter to those of the base ΛCDM cosmology. Table 6 shows the constraints for various data combinations.

The constraints on p_{ann} from the *Planck* TT+lowP spectra are about 3 times weaker than the 95% limit of $p_{\mathrm{ann}} < 2.1 \times 10^{-27}\,\mathrm{cm}^3\,\mathrm{s}^{-1}\,\mathrm{GeV}^{-1}$ derived from WMAP9, which includes WMAP polarization data at low multipoles. On the other hand, the *Planck TE* or *EE* spectra improve the constraints on p_{ann} by about an order of magnitude compared to those from *Planck TT* alone. This is because the main effect of dark matter annihilation is to increase the width of last scattering, leading to a suppression of the amplitude of the peaks, both in

---

[33] To maintain consistency with other papers on dark matter annihilation, we retain the notation $f(z)$ for the efficiency factor in this section; it should not be confused with the growth rate factor introduced in Eq. (32).

[34] We checked that we obtain similar results using either the `HyRec` code (Ali-Haimoud & Hirata 2011), as detailed in Giesen et al. (2012), or `CosmoRec` (Chluba & Thomas 2011), instead of `recfast`.
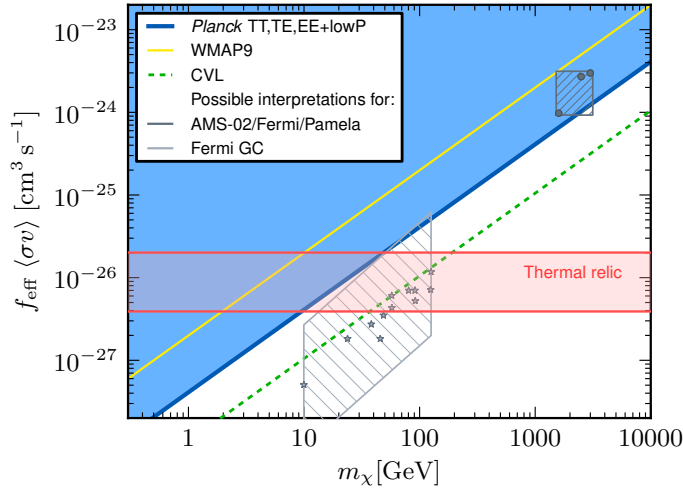
Fig. 41. Constraints on the self-annihilation cross-section at recombination, $\langle\sigma v\rangle_{z_*}$, times the efficiency parameter, f_{eff} (Eq. (81)). The blue area shows the parameter space excluded by the *Planck TT, TE, EE*+lowP data at 95% CL. The yellow line indicates the constraint using WMAP9 data. The dashed green line delineates the region ultimately accessible to a cosmic-variance-limited experiment with angular resolution comparable to that of *Planck*. The horizontal red band includes the values of the thermal-relic cross-section multiplied by the appropriate f_{eff} for different DM annihilation channels. The dark grey circles show the best-fit DM models for the PAMELA/AMS-02/*Fermi* cosmic-ray excesses, as calculated in Cholis & Hooper (2013, caption of their figure 6). The light grey stars show the best-fit DM models for the *Fermi* Galactic centre γ-ray excess, as calculated by Calore et al. (2015, their tables I, II, and III), with the light grey area indicating the astrophysical uncertainties on the best-fit cross-sections.

temperature and polarization. As a result, the effects of DM annihilation on the power spectra at high multipole are degenerate with other parameters of base ΛCDM, such as n_s and A_s (Chen & Kamionkowski 2004; Padmanabhan & Finkbeiner 2005). At large angular scales ($\ell \lesssim 200$), however, dark matter annihilation can produce an enhancement in polarization, caused by the increased ionization fraction in the freeze-out tail following recombination. As a result, large-angle polarization information is crucial for breaking the degeneracies between parameters, as illustrated in Fig. 40. The strongest constraints on p_{ann} therefore come from the full *Planck* temperature and polarization likelihood and there is little improvement if other astrophysical data, or *Planck* lensing, are added[35].

We verified the robustness of the *Planck* TT,TE,EE+lowP constraint by also allowing other parameter extensions of base ΛCDM (N_{eff}, $dn_s/d\ln k$, or Y_P) to vary together with p_{ann}. We found that the constraint is weakened by up to 20%. Furthermore, we have verified that we obtain consistent results when relaxing the priors on the amplitudes of the Galactic dust templates or if we use the `CamSpec` likelihood instead of the baseline `Plik` likelihood.

Figure 41 shows the constraints from WMAP9, *Planck* TT,TE,EE+lowP, and a forecast for a cosmic-variance-limited experiment with similar angular resolution to *Planck*[36]. The

---

[35] It is interesting to note that the constraint derived from *Planck* TT,TE,EE+lowP is consistent with the forecast given in Galli et al. (2009a), $p_{\text{ann}} < 3 \times 10^{-28} \text{ cm}^3 \text{ s}^{-1} \text{ GeV}^{-1}$.

[36] We assumed here that the cosmic-variance-limited experiment would measure the angular power spectra up to a maximum multipole of $\ell_{\text{max}} = 2500$, observing a sky fraction $f_{\text{sky}} = 0.65$.

horizontal red band includes the values of the thermal-relic cross-section multiplied by the appropriate f_{eff} for different DM annihilation channels. For example, the upper red line corresponds to $f_{\text{eff}} = 0.67$, which is appropriate for a DM particle of mass $m_\chi = 10$ GeV annihilating into e^+e^-, while the lower red line corresponds to $f_{\text{eff}} = 0.13$, for a DM particle annihilating into $2\pi^+\pi^-$ through an intermediate mediator (see, e.g., Arkani-Hamed et al. 2009). The *Planck* data exclude at 95% confidence level a thermal relic cross-section for DM particles of mass $m_\chi \lesssim 44$ Gev annihilating into e^+e^- ($f_{\text{eff}} \approx 0.6$), $m_\chi \lesssim 16$ GeV annihilating into $\mu^+\mu^-$ or $b\bar{b}$ ($f_{\text{eff}} \approx 0.2$), and $m_\chi \lesssim 11$ GeV annihilating into $\tau^+\tau^-$ ($f_{\text{eff}} \approx 0.15$).

The dark grey shaded area in Fig. 41 shows the approximate allowed region of parameter space, as calculated by Cholis & Hooper (2013) on the assumption that the PAMELA, AMS, and *Fermi* cosmic-ray excesses are caused by DM annihilation; the dark grey dots indicate the best-fit dark matter models described in that paper (for a recent discussion on best-fitting models, see also Boudaud et al. 2015). The favoured value of the cross-section is about two orders of magnitude higher than the thermal relic cross-section ($\approx 3 \times 10^{-26} \text{ cm}^3 \text{ s}^{-1}$). Attempts to reconcile such a high cross-section with the relic abundance of DM include a Sommerfeld enhanced cross-section (that may saturate at $\langle\sigma v\rangle \approx 10^{-24} \text{ cm}^3 \text{ s}^{-1}$) or non-thermal production of DM (see, e.g., the discussion by Madhavacheril et al. 2014). Both of these possibilities are strongly disfavoured by the *Planck* data. We cannot, however, exclude more exotic possibilities, such as DM annihilation through a p-wave channel with a cross-section that scales as v^2 (Diamanti et al. 2014). Since the relative velocity of DM particles at recombination is many orders of magnitude smaller than in the Galactic halo, such a model cannot be constrained using CMB data.

Observations from the *Fermi* Large Area Telescope of extended γ-ray emission towards the centre of the Milky Way, peaking at energies of around $1-3$ GeV, have been interpreted as evidence for annihilating DM (e.g.,Goodenough & Hooper 2009; Gordon & Macías 2013; Daylan et al.2016; Abazajian et al. 2014; Lacroix et al. 2014). The light grey stars in Fig. 41 show specific models of DM annihilation designed to fit the *Fermi* γ-ray excess (Calore et al. 2015), while the light grey box shows the uncertainties of the best-fit cross-sections due to imprecise knowledge of the Galactic DM halo profile. Although the interpretation of the *Fermi* excess remains controversial (because of uncertainties in the astrophysical backgrounds), DM annihilation remains a possible explanation. The best-fit models of Calore et al. (2015) are consistent with the *Planck* constraints on DM annihilation.

6.7. Testing recombination physics with Planck

The cosmological recombination process determines how CMB photons decoupled from baryons around redshift $z \approx 10^3$, when the Universe was about 400 000 years old. The importance of this transition on the CMB anisotropies has long been recognized (Sunyaev & Zeldovich 1970; Peebles & Yu 1970). The most advanced computations of the ionization history (e.g., Ali-Haïmoud & Hirata 2010; Ali-Haimoud & Hirata 2011; Chluba & Thomas 2011; Chluba et al. 2012) account for many subtle atomic physics and radiative transfer effects that were not included in the earliest calculations (Zeldovich et al. 1968; Peebles 1968).

With precision data from *Planck*, we are sensitive to sub-percent variations of the free electron fraction

around last-scattering (e.g., Hu et al. 1995; Seager et al. 2000; Seljak et al. 2003). Quantifying the impact of uncertainties in the ionization history around the maximum of the Thomson visibility function on predictions of the CMB power spectra is thus crucial for the scientific interpretation of data from *Planck*. In particular, for tests of models of inflation and extensions to ΛCDM, the interpretation of the CMB data can be significantly compromised by inaccuracies in the recombination calculation (e.g., Wong et al. 2008; Rubiño-Martín et al. 2010; Shaw & Chluba 2011). This problem can be approached in two ways, either by using modified recombination models with a specific physical process (or parameter) in mind, or in a semi-blind, model-independent way. Both approaches provide useful insights in assessing the robustness of the results from *Planck*.

Model-dependent limits on varying fundamental constants (Kaplinghat et al. 1999; Scóccola et al. 2009; Galli et al. 2009b), annihilating or decaying particles (e.g., Chen & Kamionkowski 2004; Padmanabhan & Finkbeiner 2005; Zhang et al. 2006, and Sect. 6.6), or more general sources of extra ionization and excitation photons (Peebles et al. 2000; Doroshkevich et al. 2003; Galli et al. 2008), have been discussed extensively in the literature.

As already discussed in PCP13, the choice for *Planck* has been to use the rapid calculations of the `recfast` code, modified using corrections calculated with the more precise codes. To start this sub-section we quantify the effect on the analysis of *Planck* data of the remaining uncertainties in the standard recombination history obtained with different recombination codes (Sect. 6.7.1). We also derive CMB anisotropy-based measurements of the hydrogen 2s−1s two-photon decay rate, $A_{2s \to 1s}$ (Sect. 6.7.2), and the average CMB temperature, T_0 derived at the last-scattering epoch (Sect. 6.7.3). These two parameters strongly affect the recombination history but are usually kept fixed when fitting models to CMB data (as in the analyses described in previous sections). Section 6.7.4 describes model-independent constraints on perturbed recombination scenarios. A discussion of these cases provides both a test of the consistency of the CMB data with the standard recombination scenario and also a demonstration of the impressive sensitivity of *Planck* to small variations in the ionization history at $z \approx 1100$.

6.7.1. Comparison of different recombination codes

Even for pre-*Planck* data, it was realized that the early recombination calculations of Zeldovich et al. (1968) and Peebles (1968) had to be improved. This led to the development of the widely-used and computationally quick `recfast` code (Seager et al. 1999, 2000). However, for *Planck*, the recombination model of `recfast` in its original form is not accurate enough. Percent-level corrections, due to detailed radiative transfer and atomic physics effects have to be taken into account. Ignoring these effects can bias the inferred cosmological parameters, some by as much as a few standard deviations.

The recombination problem was solved as a common effort of several groups (Dubrovich & Grachev 2005; Kholupenko et al. 2007; Chluba & Sunyaev 2006b; Rubiño-Martín et al. 2006; Karshenboim & Ivanov 2008; Wong & Scott 2007; Switzer & Hirata 2008; Grin & Hirata 2010; Ali-Haïmoud & Hirata 2010). This work was undertaken, to a large extent, in preparation for the precision data from *Planck*. Both `CosmoRec` (Chluba & Thomas 2011) and `HyRec` (Ali-Haimoud & Hirata 2011) allow fast and precise computations of the ionization history, explicitly capturing the physics of the recombination problem. For the standard cosmology, the ionization histories

obtained from these two codes in their default settings agree to within 0.05% for hydrogen recombination ($600 \lesssim z \lesssim 1600$) and 0.35% during helium recombination[37] ($1600 \lesssim z \lesssim 3000$). The effect of these small differences on the CMB power spectra is $\lesssim 0.1\%$ at $\ell < 4000$ and so has a negligible impact on the interpretation of precision CMB data; for the standard six parameters of base ΛCDM, we find that the largest effect is a bias in $\ln(10^{10}A_s)$ at the level of $0.04\sigma \approx 0.0012$ for *Planck* TT,TE,EE+lowP+BAO.

For *Planck* analyses, the recombination model of `recfast` is used by default. In `recfast`, the precise dynamics of recombination is not modelled physically, but approximated with fitting-functions calibrated against the full recombination calculations assuming a reference cosmology (Seager et al. 1999, 2000; Wong et al. 2008). At the level of precision required for *Planck*, the `recfast` approach is sufficiently accurate, provided that the cosmologies are close to base ΛCDM (Rubiño-Martín et al. 2010; Shaw & Chluba 2011). Comparing the latest version of `recfast` (`camb` version) with `CosmoRec`, we find agreement to within 0.2% for hydrogen recombination ($600 \lesssim z \lesssim 1600$) and 0.2% during helium recombination for the standard ionization history. The effect on the CMB power spectra is $\lesssim 0.15\%$ at $\ell < 4000$, although with slightly more pronounced shifts in the peak positions than when comparing `CosmoRec` and `HyRec`. For the base ΛCDM model, we find that the largest bias is on n_s, at the level of 0.15σ (≈ 0.0006) for *Planck* TT,TE,EE+lowP+BAO. Although this is about 5 times larger than the difference in n_s between `CosmoRec` and `HyRec`, this bias is nevertheless unimportant at the current level of precision (and smaller than the differences seen from different likelihoods, see Sect. 3.1).

Finally we compare `CosmoRec` with `recfast` in its original form (i.e., before recalibrating the fitting-functions on refined recombination calculations). For base ΛCDM, we expect to see biases of $\Delta\Omega_b h^2 \approx -2.1\sigma \approx -0.00028$ and $\Delta n_s \approx -3.3\sigma \approx -0.012$ (Shaw & Chluba 2011). Using the actual data (*Planck* TT,TE,EE+lowP+BAO) we find biases of $\Delta\Omega_b h^2 \approx -1.8\sigma \approx -0.00024$ and $\Delta n_s \approx -2.6\sigma \approx -0.010$, very close to the expected values. This illustrates explicitly the importance of the improvements of `CosmoRec` and `HyRec` over the original version of `recfast` for the interpretation of *Planck* data. However, `CosmoRec` and `HyRec` themselves are much more computationally intensive than the modified `recfast`, which is why we use `recfast` in most *Planck* cosmological analyses.

6.7.2. Measuring $A_{2s \to 1s}$ with *Planck*

The crucial role of the 2s−1s two-photon decay channel for the dynamics of hydrogen recombination has been appreciated since the early days of CMB research (Zeldovich et al. 1968; Peebles 1968). Recombination is an out-of-equilibrium process and energetic photons emitted in the far Wien tail of the CMB by Lyman continuum and series transitions keep the primordial plasma ionized for a much longer period than expected from simple equilibrium recombination physics. Direct recombinations to the ground state of hydrogen are prohibited, causing a modification of the free electron number density, N_e, by only $\Delta N_e/N_e \approx 10^{-6}$ around $z \approx 10^3$ (Chluba & Sunyaev 2007). Similarly, the slow escape of photons from the Lyα resonance reduces the effective Ly-α transition rate to $A_{2p \to 1s}^* \approx 1-10\,\mathrm{s}^{-1}$ (by more than seven orders of magnitude), making it comparable to the vacuum

---

[37] Helium recombination is treated in more detail by `CosmoRec` (e.g., Rubiño-Martín et al. 2008; Chluba et al. 2012), which explains most of the difference.

2s−1s two-photon decay rate of $A_{2s\to1s} \approx 8.22\,\mathrm{s}^{-1}$. About 57% of all hydrogen atoms in the Universe became neutral through the 2s−1s channel (e.g., Wong et al. 2006; Chluba & Sunyaev 2006a), and subtle effects, such as the induced 2s−1s two-photon decay and Lyα re-absorption, need to be considered in precision recombination calculations (Chluba & Sunyaev 2006b; Kholupenko & Ivanchik 2006; Hirata 2008).

The high sensitivity of the recombination process to the 2s−1s two-photon transition rate also implies that instead of simply adopting a value for $A_{2s\to1s}$ from theoretical computations (Breit & Teller 1940; Spitzer & Greenstein 1951; Goldman 1989) one can directly determine it with CMB data. From the theoretical point of view it would be surprising to find a value that deviates significantly from $A_{2s\to1s} = 8.2206\,\mathrm{s}^{-1}$, derived from the most detailed computation (Labzowsky et al. 2005). However, laboratory measurements of this transition rate are extremely challenging (O'Connell et al. 1975; Krüger & Oed 1975; Cesar et al. 1996). The most stringent limit is for the differential decay rate, $A_{2s\to1s}(\lambda)\,\mathrm{d}\lambda = (1.5 \pm 0.65)\,\mathrm{s}^{-1}$ (a 43% error) at wavelengths $\lambda = 255.4{-}232.0\,\mathrm{nm}$, consistent with the theoretical value of $A_{2s\to1s}(\lambda)\,\mathrm{d}\lambda = 1.02\,\mathrm{s}^{-1}$ in the same wavelength range (Krüger & Oed 1975). With precision data from *Planck* we are in a position to perform the best measurement to date, using cosmological data to inform us about atomic transition rates at last scattering (as also emphasized by Mukhanov et al. 2012).

The 2s−1s two-photon rate affects the CMB anisotropies only through its effect on the recombination history. A larger value of $A_{2s\to1s}$, accelerates recombination, allowing photons and baryons to decouple earlier, an effect that shifts the acoustic peaks towards smaller scales. In addition, slightly less damping occurs, as in the case of the stimulated 2s−1s two-photon decays (Chluba & Sunyaev 2006b). This implies that for flat cosmologies, variations of $A_{2s\to1s}$ correlate with $\Omega_c h^2$ and H_0 (which affect the distance to the last scattering surface), while $A_{2s\to1s}$ anti-correlates with $\Omega_b h^2$ and n_s (which modify the slope of the damping tail). Despite these degeneracies, one expects that *Planck* will provide a measurement of $A_{2s\to1s}$ to within $\pm 0.5\,\mathrm{s}^{-1}$, corresponding to an approximately 6% uncertainty (Mukhanov et al. 2012).

In Fig. 42, we show the marginalized posterior for $A_{2s\to1s}$ from *Planck* and for *Planck* combined with BAO. Using CosmoRec to compute the recombination history, we find

$$A_{2s\to1s} = 7.70 \pm 1.01\,\mathrm{s}^{-1} \quad Planck\ \mathrm{TT+lowP}, \tag{82a}$$
$$A_{2s\to1s} = 7.72 \pm 0.60\,\mathrm{s}^{-1} \quad Planck\ \mathrm{TT, TE, EE+lowP}, \tag{82b}$$
$$A_{2s\to1s} = 7.71 \pm 0.99\,\mathrm{s}^{-1} \quad Planck\ \mathrm{TT+lowP+BAO}, \tag{82c}$$
$$A_{2s\to1s} = 7.75 \pm 0.61\,\mathrm{s}^{-1} \quad Planck\ \mathrm{TT, TE, EE+lowP}$$
$$\hspace{4cm} \mathrm{+BAO}. \tag{82d}$$

These results are in very good agreement with the theoretical value, $A_{2s\to1s} = 8.2206\,\mathrm{s}^{-1}$. For *Planck* TT,TE,EE+lowP+BAO, approximately 8% precision is reached using cosmological data. These constraints are not sensitive to the addition of BAO, or other external data (JLA+H_0). The slight shift away from the theoretical value is accompanied by small (fractions of a σ) shifts in n_s, $\Omega_c h^2$, and H_0, to compensate for the effects of $A_{2s\to1s}$ on the distance to the last scattering surface and damping tail. This indicates that additional constraints on the acoustic scale are required to fully break degeneracies between these parameters and their effects on the CMB power spectrum, a task that could be achieved in the future using large-scale structure surveys and next generation CMB experiments.
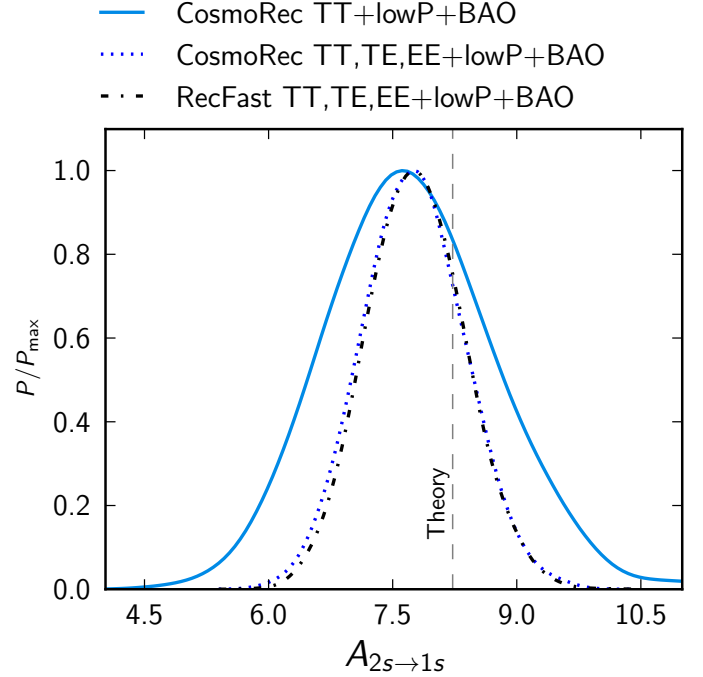

Fig. 42. Marginalized posterior for $A_{2s\to1s}$, obtained using CosmoRec, with and without small-scale polarization data. We find good agreement with the theoretical value of $A_{2s\to1s} = 8.2206\,\mathrm{s}^{-1}$. For comparison, we also show the result for *Planck* TT,TE,EE+lowP+BAO obtained with recfast, emphasizing the consistency of different treatments.

The values for $A_{2s\to1s}$ quoted above were obtained using CosmoRec. When varying $A_{2s\to1s}$, the range of cosmologies becomes large enough to potentially introduce a mismatch of the recfast fitting-functions that could affect the posterior. In particular, with recfast the 2s−1s two-photon and Lyα channels are not treated separately, so that changes specific to the 2s−1s decay channel propagate inconsistently[38]. However, repeating the analysis with recfast, we find $A_{2s\to1s} = 7.78 \pm 0.58\,\mathrm{s}^{-1}$ (see Fig. 42), for *Planck* TT,TE,EE+lowP+BAO, which is in excellent agreement with CosmoRec, showing that these effects can be neglected.

6.7.3. Measuring T_0 at last-scattering with *Planck*

Our best constraint on the CMB monopole temperature comes from the measurements of the CMB spectrum with COBE/FIRAS, giving a 0.02% determination of T_0 (Fixsen et al. 1996; Fixsen 2009). Other constraints from molecular lines typically reach 1% precision (see Table 2 in Fixsen 2009, for an overview), while independent BBN constraints provide 5−10% limits (Simha & Steigman 2008; Jeong et al. 2014).

The CMB anisotropies provide additional ways of determining the value of T_0 (for fixed values of N_{eff} and Y_P). One is through the energy distribution of the CMB anisotropies (Fixsen et al. 1996; Fixsen 2003; Chluba 2014) and another through their power spectra (Opher & Pelinson 2004, 2005; Chluba 2014). Even small changes in T_0, compatible with the COBE/FIRAS error, affect the ionization history at the 0.5% level around last-scattering, propagating to a roughly 0.1%

---

[38] One effect is that by increasing $A_{2s\to1s}$ fewer Lyα photons are produced. This reduces the Lyα feedback correction to the 2s−1s channel, which further accelerates recombination, an effect that is not captured with recfast in the current implementation.
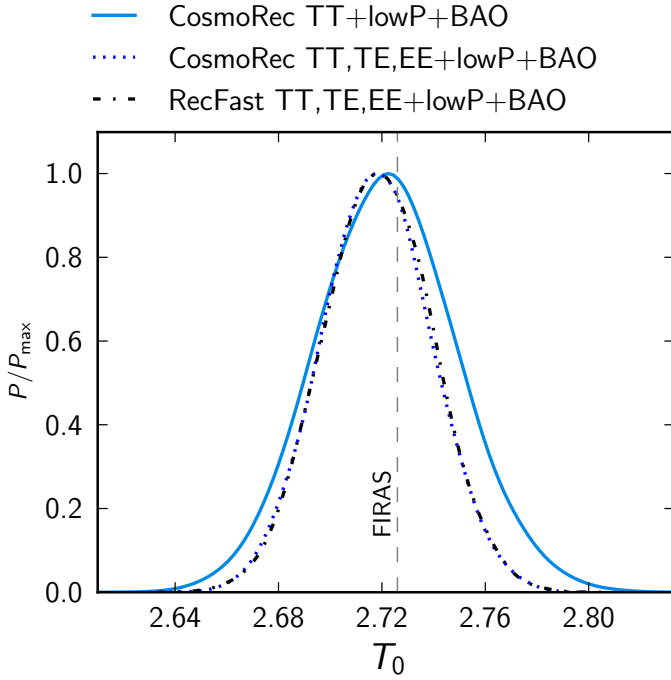
Fig. 43. Marginalized posterior for T_0. We find excellent agreement with the COBE/FIRAS measurement. For comparison, we show the result for *Planck* TT,TE,EE+lowP+BAO obtained using both `CosmoRec` and `recfast`, emphasizing the consistency of different treatments.

uncertainty in the CMB power spectrum (Chluba & Sunyaev 2008). Overall, the effect of this uncertainty on the parameters of ΛCDM models is small (Hamann & Wong 2008); however, without prior knowledge of T_0 from the COBE/FIRAS measurement, the situation would change significantly.

The CMB monopole affects the CMB anisotropies in several ways. Most importantly, for larger T_0, photons decouple from baryons at lower redshift, since more ionizing photons are present in the Wien-tail of the CMB. This effect is amplified because of the exponential dependence of the atomic level populations on the ratio of the ionization potentials and CMB temperature. In addition, increasing T_0 lowers the expansion timescale of the Universe and the redshift of matter-radiation equality, while increasing the photon sound speed. Some of these effects are also produced by varying N_{eff}; however, the effects of T_0 on the ionization history and photon sound speed are distinct.

With CMB data alone, the determination of T_0 is degenerate with other parameters, but the addition of other data sets breaks this degeneracy. Marginalized posterior distributions for T_0 are shown in Fig. 43. Using `CosmoRec`, we find

$$T_0 = 2.722 \pm 0.027 \,\mathrm{K} \quad Planck \,\,\mathrm{TT+lowP+BAO}, \tag{83a}$$

$$T_0 = 2.718 \pm 0.021 \,\mathrm{K} \quad Planck \,\,\mathrm{TT, TE, EE+lowP+BAO}, \tag{83b}$$

and similar results are obtained with `recfast`. This is in excellent agreement with the COBE/FIRAS measurement, $T_0 = 2.7255 \pm 0.0006$ K (Fixsen et al. 1996; Fixsen 2009). These measurements of T_0 reach a precision that is comparable to the accuracy obtained with interstellar molecules. Since the systematics of these independent methods are very different, this result demonstrates the consistency of all these data. Allowing T_0 to vary causes the errors of the other cosmological parameters to increase. The strongest effect is on θ_{MC}, which is highly degenerate with T_0. The error on θ_{MC} increases by a factor of roughly 25 if T_0 is allowed to vary. The error on $\Omega_b h^2$ increases by a

factor of about 4, while the errors on n_s and $\Omega_c h^2$ increase by factors of $1.5-2$, and the other cosmological parameters are largely unaffected by variations in T_0. Because of the strong degeneracy with θ_{MC}, no constraint on T_0 can be obtained using *Planck* data alone. External data, such as BAO, are therefore required to break this geometric degeneracy.

It is important to emphasize that the CMB measures the temperature at a redshift of $z \approx 1100$, so the comparison with measurements of T_0 at the present day is effectively a test of the constancy of aT_{CMB}, where $a \approx 1/1100$ is the scale-factor at the time of last-scattering. It is remarkable that we are able to test the constancy of $aT_{\mathrm{CMB}} \equiv T_0$ over such a large dynamic range in redshift. Of course, if we did find that aT_{CMB} around recombination were discrepant with T_0 now, then we would need to invent a finely-tuned late-time photon injection mechanism[39] to explain the anomaly. Fortunately, the data are consistent with the standard $T_{\mathrm{CMB}} \propto (1 + z)$ scaling of the CMB temperature.

Another approach to measuring aT_{CMB} is through the thermal Sunyaev-Zeldovich effect in rich clusters of galaxies at various redshifts (Fabbri et al. 1978; Rephaeli 1980), although it is unclear how one would interpret a failure of this test without an explicit model. In practice this approach is consistent with a scaling $aT_{\mathrm{CMB}} = \mathrm{constant}$, but with lower precision than obtained here from *Planck* (e.g., Battistelli et al. 2002; Luzzi et al. 2009; Saro et al. 2014; Hurier et al. 2014). A simple $T_{\mathrm{CMB}} = T_0(1 + z)^{1-\beta}$ modification to the standard temperature redshift relation is frequently discussed in the literature (though this case is not justified by any physical model and is difficult to realize without creating a CMB spectral distortion, see Chluba 2014). For this parameterization we find

$$\beta = (0.2 \pm 1.4) \times 10^{-3} \quad Planck \,\,\mathrm{TT+lowP+BAO}, \tag{84a}$$

$$\beta = (0.4 \pm 1.1) \times 10^{-3} \quad Planck \,\,\mathrm{TT, TE, EE+lowP+BAO}, \tag{84b}$$

where we have adopted a recombination redshift of $z_* = 1100$[40]. Because of the long lever-arm in redshift afforded by the CMB, this is an improvement over earlier constraints by more than an order of magnitude (e.g., Hurier et al. 2014).

In a self-consistent picture, changes of T_0 would also affect the BBN era. We might therefore consider a simultaneous variation of N_{eff} and Y_P to reflect the variation of the neutrino energy density accompanying a putative variation in the photon energy density. Since we find aT_{CMB} at recombination to be highly consistent with the observed CMB temperature from COBE/FIRAS, considering this extra variation seems unnecessary. Instead, we may view the aT_{CMB} variation investigated here as further support for the limits discussed in Sects. 6.4 and 6.5.

6.7.4. Semi-blind perturbed recombination analysis

The high sensitivity of small-scale CMB anisotropies to the ionization history of the Universe around the epoch of recombination allows us to constrain possible deviations from the standard recombination scenario in a model-independent way (Farhang et al. 2012, 2013). The method relies on an eigen-analysis (often referred to as a principle component analysis) of perturbations in the free electron fraction, $X_e(z) = N_e/N_H$, where N_H denotes the number density of hydrogen nuclei. The eigenmodes selected are specific to the data used in the analysis.

---

[39] Pure energy release in the form of heating of ordinary matter would leave a Compton y-distortion (Zeldovich & Sunyaev 1969) at these late times (Burigana et al. 1991; Hu & Silk 1993; Chluba & Sunyaev 2012).
[40] The test depends on the logarithm of the redshift and so is insensitive to the precise value adopted for z_*.

Table 7. Standard parameters and the first three X_e-modes, as determined for *Planck* TT,TE,EE+lowP+BAO.

Parameter	+ 1 mode	+ 2 modes	+ 3 modes
$\Omega_b h^2$ . . .	0.02229 ± 0.00017	0.02237 ± 0.00018	0.02237 ± 0.00019
$\Omega_c h^2$ . . .	0.1190 ± 0.0010	0.1186 ± 0.0011	0.1187 ± 0.0012
H_0	67.64 ± 0.48	67.80 ± 0.51	67.80 ± 0.56
τ	0.065 ± 0.012	0.068 ± 0.013	0.068 ± 0.013
n_s	0.9667 ± 0.0053	0.9677 ± 0.0055	0.9678 ± 0.0067
$\ln(10^{10}A_s)$	3.062 ± 0.023	3.066 ± 0.024	3.066 ± 0.024
μ_1	-0.03 ± 0.12	0.03 ± 0.14	0.02 ± 0.15
μ_2	. . .	-0.17 ± 0.18	-0.18 ± 0.19
μ_3	. . .	. . .	-0.02 ± 0.88

Similar approaches have been used to constrain deviations of the reionization history from the simplest models (Mortonson & Hu 2008) and annihilating dark matter scenarios (Finkbeiner et al. 2012), both with the prior assumption that the standard recombination physics is fully understood, as well as for constraining trajectories in inflation Planck Collaboration XX (2016) and dark energy Planck Collaboration XIV (2016) parameterizations.

Here, we use *Planck* data to find preferred ionization fraction trajectories $X_e(z)$ composed of low-order perturbation eigenmodes to the standard history (X_e-modes). The X_e-modes are constructed through the eigen-decomposition of the inverse of the Fisher information matrix for base ΛCDM (the six cosmological parameters and the nuisance parameters) and recombination perturbation parameters (see Farhang et al. 2012, for details). This procedure allows us to estimate the errors on the eigenmode amplitudes, μ_i, providing a rank ordering of the X_e-modes and their information content.

The first three X_e-modes for *Planck* TT,TE,EE+lowP are illustrated in Fig. 44, together with their impact on the differential visibility function. Figure 45 shows the response of the CMB temperature and polarization power spectra to these eigenmodes. The first mode mainly leads to a change in the width and height of the Thomson visibility function (bottom panel of Fig. 44). This implies less diffusion damping, which is also reflected in the modifications to the CMB power spectra (as shown in Fig. 45). The second mode causes the visibility maximum to shift towards higher redshifts for $\mu_2 > 0$, which leads to a shift of the CMB extrema to smaller scales; however, for roughly constant width of the visibility function it also introduces less damping at small scales. The third mode causes a combination of changes in both the position and width of the visibility function, with a pronounced effect on the location of the acoustic peaks. For the analysis of *Planck* data combinations, we only use X_e-modes that are optimized for *Planck* TT,TE,EE+lowP.

We modified `CosmoMC` to estimate the mode amplitudes. The results for *Planck* TT,TE,EE+lowP+BAO are presented in Table 7. Although all mode amplitudes are consistent with standard recombination, adding the second X_e-mode causes mild shifts in H_0 and τ. For *Planck* TT+lowP, we find $\mu_1 = -0.11 \pm 0.51$ and $\mu_2 = -0.23 \pm 0.50$, using the *Planck* TT,TE,EE+lowP eigenmodes, again consistent with the standard recombination scenario. Adding the polarization data improves the errors by more than a factor of 2. However, the mode amplitudes are insensitive to the addition of external data.

With pre-*Planck* data, only the amplitude, μ_1, of the first eigenmode could be constrained. The corresponding change in the ionization history translates mainly into a change in the slope of the CMB damping tail, with this mode resembling the first mode determined using *Planck* data (Fig. 44).
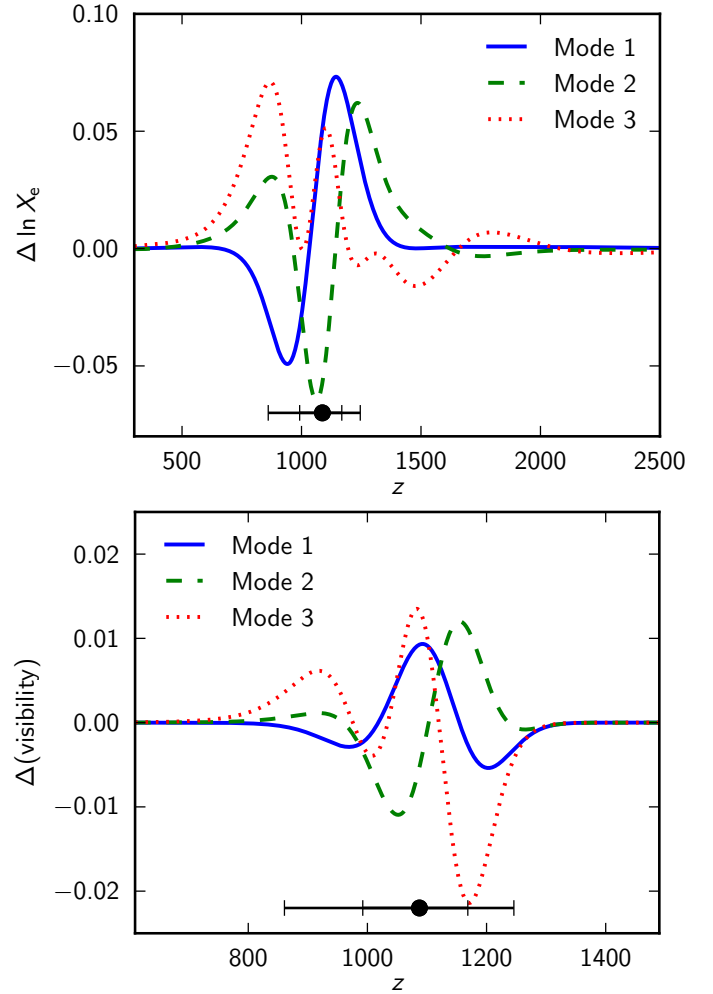

Fig. 44. Eigen-modes of the recombination history, marginalized over the standard six cosmological and *Planck* nuisance parameters. The *upper panel* shows the first three X_e-modes constructed for *Planck* TT,TE,EE+lowP data. The *lower panel* show changes in the differential visibility corresponding to 1σ deviations from the standard recombination scenario for the first three X_e-modes. The maximum of the Thomson visibility function and width are indicated in both figures.

The WMAP9+SPT data gave a non-zero value for the first eigenmode at about 2σ, $\mu_1^{SPT} = -0.80 \pm 0.37$. However, the WMAP9+ACT data gave $\mu_1^{ACT} = 0.14 \pm 0.45$ and the combined pre-*Planck* data (WMAP+ACT+SPT) gave $\mu_1^{pre} = -0.44 \pm 0.33$, both consistent with the standard recombination scenario (Calabrese et al. 2013). The variation among these results is another manifestation of the tensions between different pre-*Planck* CMB data, as discussed in PCP13.

Although not optimal for *Planck* data, we also compute the amplitudes of the first three X_e-modes constructed for the WMAP9+SPT data set. This provides a more direct comparison with the pre-*Planck* constraints. For *Planck* TT,TE,EE+lowP+BAO we obtain $\mu_1^{SPT} = -0.10 \pm 0.13$ and $\mu_2^{SPT} = -0.13 \pm 0.18$. The mild tension of the pre-*Planck* data with the standard recombination scenario disappears when using *Planck* data. This is especially impressive, since the errors have improved by more than a factor of 2. By projecting onto the *Planck* modes, we find that the first two SPT modes can be expressed as $\mu_1^{SPT} \approx 0.69\mu_1 + 0.66\mu_2 \approx -0.09$ and $\mu_2^{SPT} \approx -0.70\mu_1 + 0.64\mu_2 \approx -0.13$, which emphasizes the consistency of the results. Adding the first three SPT modes,
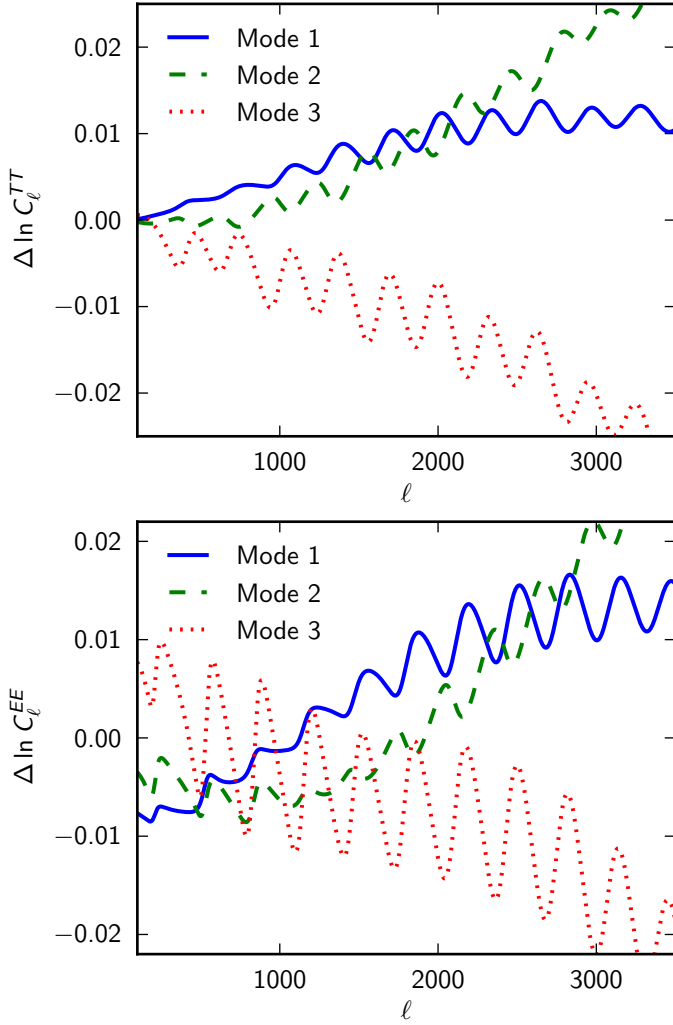
Fig. 45. Changes in the *TT* (*upper panel*) and *EE* (*lower panel*) power spectra caused by a 1σ deviation from the standard recombination scenario for the first three X_e-modes (see Fig. 44).

we obtain $\mu_1^{\mathrm{SPT}} = -0.09 \pm 0.13$, $\mu_2^{\mathrm{SPT}} = -0.14 \pm 0.21$, and $\mu_3^{\mathrm{SPT}} = -0.12 \pm 0.86$, which again is consistent with the standard model of recombination. The small changes in the mode amplitudes when adding the third mode arise because the SPT modes are not optimal for *Planck* and so are correlated.

6.8. Cosmic defects

Topological defects are a generic by-product of symmetry-breaking phase transitions and a common phenomenon in condensed matter systems. Cosmic defects of various types can be formed in phase transitions in the early Universe (Kibble 1976). In particular, cosmic strings can be produced in some supersymmetric and grand-unified theories at the end of inflation (Jeannerot et al. 2003), as well as in higher-dimensional theories (e.g., Polchinski 2005). Constraints on the abundance of cosmic strings and other defects therefore place limits on a range of models of the early Universe. More discussion on the formation, evolution, and cosmological role of topological defects can be found, for example, in the reviews by Vilenkin & Shellard (2000), Hindmarsh & Kibble (1995), and Copeland & Kibble (2010).
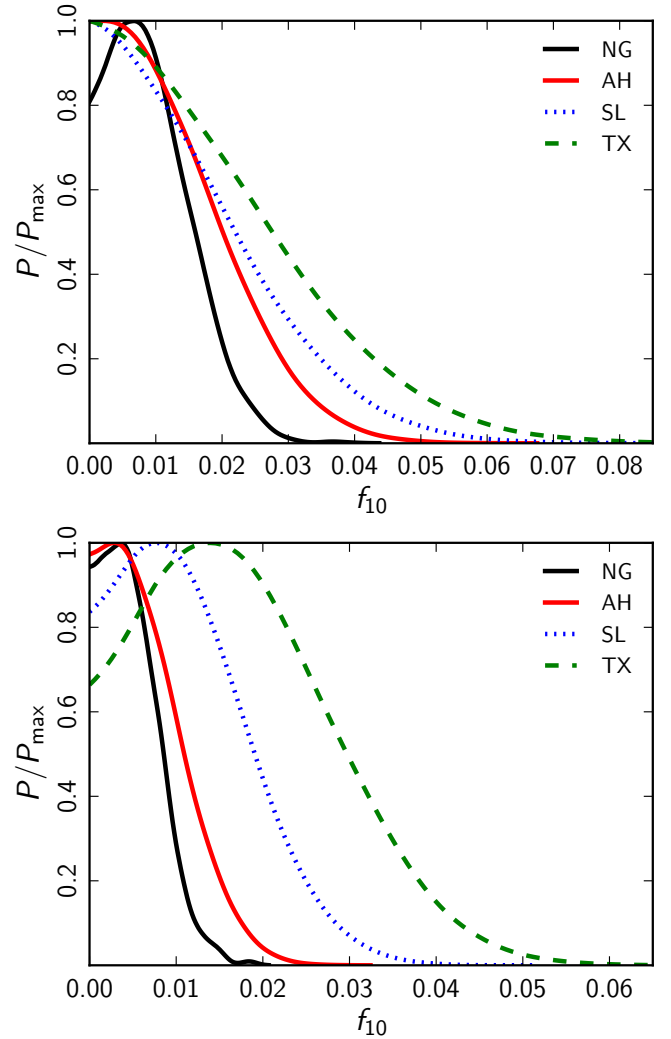
Fig. 46. Marginalized posterior distributions for the fractional contribution, f_{10}, of the defect contribution to the temperature power spectrum at $\ell = 10$ (see the text for the precise definition). Here we show the constraints for the Nambu-Goto cosmic strings (NG, solid black), field-theory simulations of Abelian-Higgs cosmic strings (AH, solid red), semi-local strings (SL, dotted blue), and global textures (TX, dashed green). The *upper panel* shows the 1D posterior for the *Planck*+lowP data, while constraints shown in the *lower panel* additionally use the *TE* and *EE* data.

In this section we revisit the power spectrum-based constraints on the abundance of cosmic strings and other topological defects using the 2015 *Planck* data, including *Planck* polarization measurements. The general approach follows that described in the *Planck* 2013 analysis of cosmic defects (Planck Collaboration XXV 2014), so here we focus on the updated constraints rather than on details of the methodology.

Topological defects are non-perturbative excitations of the underlying field theory and their study requires numerical simulations. Unfortunately, since the Hubble scale, c/H_0, is over 50 orders of magnitude greater that the thickness of a GUT-scale string, approximately $(\hbar/\mu c)^{1/2}$ with μ the mass per unit length of the string, it is impractical to simulate the string dynamics exactly in the late Universe. For this reason one needs to make approximations. One approach considers the limit of an infinitely thin string, which corresponds to using the Nambu-Goto ("NG") action for the string dynamics. In an alternative approach, the actual field dynamics for a given model are solved on a lattice.

Table 8. 95% upper limits on the parameter f_{10} and on the derived parameter $G\mu/c^2$ for the defect models discussed in the text.

Defect type	TT+lowP		TT,TE,EE+lowP	
	f_{10}	$G\mu/c^2$	f_{10}	$G\mu/c^2$
NG	<0.020	$< 1.8 \times 10^{-7}$	<0.011	$<1.3 \times 10^{-7}$
AH	<0.030	$< 3.3 \times 10^{-7}$	<0.015	$<2.4 \times 10^{-7}$
SL	<0.039	$<10.6 \times 10^{-7}$	<0.024	$<8.5 \times 10^{-7}$
TX	<0.047	$< 9.8 \times 10^{-7}$	<0.036	$<8.6 \times 10^{-7}$

Notes. We show results for *Planck* TT+lowP data as well as for *Planck* TT, TE, EE+lowP.

In this case it is necessary to resolve the string core, which generally requires more computationally intensive simulations than in the NG approach. Lattice simulations, however, can include additional physics, such as field radiation that is not present in NG simulations. Here we will use field-theory simulations of the Abelian-Higgs action ("AH"); details of these simulations are discussed in Bevis et al. (2007, 2010).

The field-theory approach also allows one to simulate theories in which the defects are not cosmic strings and so cannot be described by the NG action. Examples include semi-local strings ("SL", Urrestilla et al. 2008) and global defects. Here we will specifically consider the breaking of a global $O(4)$ symmetry resulting in texture defects ("TX").

For the field-theory defects, we measure the energy-momentum tensor from the simulations and insert it as an additional constituent into a modified version of the CMBEASY Boltzmann code (Doran 2005) to predict the defect contribution to the CMB temperature and polarization power spectra (see, e.g., Durrer et al. 2002). The same approach can be applied to NG strings, but rather than using simulations directly, we model the strings using the unconnected segment model ("USM", Albrecht et al. 1999; Pogosian & Vachaspati 1999). In this model, strings are represented by a set of uncorrelated straight segments, with scaling properties chosen to match those determined from numerical simulations. In this case, the string energy-momentum tensor can be computed analytically and used as an active source in a modified Boltzmann code. For this analysis we use CMBACT version 4 [41], whereas Planck Collaboration XXV (2014) used version 3. There have been several improvements to the code since the 2013 analysis, including a correction to the normalization of vector mode spectra. However, the largest change comes from an improved treatment of the scaling properties. The string correlation length and velocity are described by an updated velocity-dependent one-scale model (Martins & Shellard 2002), which provides better agreement with numerical simulations. Small-scale structure of the string, which was previously a free parameter, is accounted for by the one-scale model.

The CMB power spectra from defects are proportional to $(G\mu/c^2)^2$. We scale the computed template CMB spectra, and add these to the inflationary and foreground power spectra, to form the theory spectra that enter the likelihood. In practice, we parameterize the defects with their relative contribution to the TT spectrum at multipole $\ell = 10$, $f_{10} \equiv C_{10}^{TT(\text{defect})}/C_{10}^{TT(\text{total})}$. We vary f_{10} and the standard six parameters of the base ΛCDM model, using CosmoMC. We also report our results in terms of the derived parameter $G\mu/c^2$.

The constraints on f_{10} and the inferred limits on $G\mu/c^2$ are summarized in Table 8. The marginalized 1D posterior distribution functions are shown in Fig. 46. For *Planck* TT+lowP we find that the results are similar to the *Planck*+WP constraints reported in Planck Collaboration XXV (2014), for the AH model, or somewhat better for SL and TX. However, the addition of the *Planck* high-ℓ TE and EE polarization data leads to a significant improvement compared to the 2013 constraints.

For the NG string model, the results based on *Planck* TT+lowP are slightly weaker than the 2013 *Planck*+WP constraints. This is caused by a difference in the updated defect spectrum from the USM model, which has a less pronounced peak and shifts towards the AH spectrum. With the inclusion of polarization, *Planck* TT,TE,EE+lowP improves the upper limit on f_{10} by a factor of 2, as for the AH model. The differences between the AH and NG results quoted here can be regarded as a rough indication of the uncertainty in the theoretical string power spectra.

In summary, we find no evidence for cosmic defects from the *Planck* 2015 data, with tighter limits than before.

7. Conclusions[42]

(1) The six-parameter base ΛCDM model continues to provide a very good match to the more extensive 2015 *Planck* data, including polarization. This is the most important conclusion of this paper.

(2) The 2015 *Planck* TT, TE, EE, and lensing spectra are consistent with each other under the assumption of the base ΛCDM cosmology. However, when comparing the TE and EE spectra computed for different frequency combinations, we find evidence for systematic effects caused by temperature-to-polarization leakage. These effects are at low levels and have little impact on the science conclusions of this paper.

(3) We have presented the first results on polarization from the LFI at low multipoles. The LFI polarization data, together with *Planck* lensing and high-multipole temperature data, gives a reionization optical depth of $\tau = 0.066 \pm 0.016$ and a reionization redshift of $z_{\text{re}} = 8.8^{+1.7}_{-1.4}$. These numbers are in good agreement with those inferred from the WMAP9 polarization data cleaned for polarized dust emission using HFI 353-GHz maps. They are also in good agreement with results from *Planck* temperature and lensing data, i.e., excluding any information from polarization at low multipoles.

(4) The absolute calibration of the *Planck* 2015 HFI spectra is higher by 2% (in power) compared to 2013, largely resolving the calibration difference noted in PCP13 between WMAP and *Planck*. In addition, there have been a number of small changes to the low-level *Planck* processing and more accurate calibrations of the HFI beams. The 2015 *Planck* likelihood also makes more aggressive use of sky than in PCP13 and incorporates some refinements to the modelling of unresolved foregrounds. Apart from differences in τ (caused by switching to the LFI low-multipole polarization likelihood, as described in item 3 above) and the amplitude-τ combination $A_s e^{-2\tau}$ (caused by the change in absolute calibration), the 2015 parameters for base ΛCDM are in good agreement with those reported in PCP13.

(5) The *Planck* TT, TE, and EE spectra are accurately described by a purely adiabatic spectrum of fluctuations with

[42] As in the abstract, here we quote 68% confidence limits on measured parameters and 95% upper limits on other parameters.

a spectral tilt $n_s = 0.968 \pm 0.006$, consistent with the predictions of single-field inflationary models. Combining *Planck* data with BAO, we find tight limits on the spatial curvature of the Universe, $|\Omega_K| < 0.005$, again consistent with the inflationary prediction of a spatially-flat Universe.

(6) The *Planck* data show no evidence for tensor modes. Adding a tensor amplitude as a one-parameter extension to base ΛCDM, we derive a 95% upper limit of $r_{0.002} < 0.11$. This is consistent with the *B*-mode polarization analysis reported in BKP, resolving the apparent discrepancy between the *Planck* constraints on r and the BICEP2 results reported by BICEP2 Collaboration (2014). In fact, by combining the *Planck* and BKP likelihoods, we find an even tighter constraint, $r_{0.002} < 0.09$, strongly disfavouring inflationary models with a $V(\phi) \propto \phi^2$ potential.

(7) The *Planck* data show no evidence for any significant running of the spectral index. We also set strong limits on a possible departure from a purely adiabatic spectrum, either through an admixture of fully-correlated isocurvature modes or from cosmic defects.

(8) The *Planck* best-fit base ΛCDM cosmology (we quote numbers for *Planck* TT+lowP+lensing here) is in good agreement with results from BAO surveys, and with the recent JLA sample of Type Ia SNe. The Hubble constant in this cosmology is $H_0 = (67.8 \pm 0.9)$ km s^{-1}Mpc^{-1}, consistent with the direct measurement of H_0 of Eq. (30) used as an H_0 prior in this paper. The *Planck* base ΛCDM cosmology is also consistent with the recent analysis of redshift-space distortions of the BOSS CMASS-DR11 data by Samushia et al. (2014) and Beutler et al. (2014a). The amplitude of the present-day fluctuation spectrum, σ_8, of the *Planck* base ΛCDM cosmology is higher than inferred from weak lensing measurements from the CFHTLenS survey (Heymans et al. 2012; Erben et al. 2013) and, possibly, from counts of rich clusters of galaxies (including *Planck* cluster counts reported in Planck Collaboration XXIV 2016). The *Planck* base ΛCDM cosmology is also discordant with Lyα BAO measurements at $z \approx 2.35$ (Delubac et al. 2015; Font-Ribera et al. 2014). At present, the reasons for these tensions are unclear.

(9) By combining the *Planck* TT+lowP+lensing data with other astrophysical data, including the JLA supernovae, the equation of state for dark energy is constrained to $w = -1.006 \pm 0.045$ and is therefore compatible with a cosmological constant, as assumed in the base ΛCDM cosmology.

(10) We have presented a detailed analysis of possible extensions to the neutrino sector of the base ΛCDM model. Combining *Planck* TT+lowP+lensing with BAO we find $N_{eff} = 3.15 \pm 0.23$ for the effective number of relativistic degrees of freedom, consistent with the value $N_{eff} = 3.046$ of the standard model. The sum of neutrino masses is constrained to $\sum m_\nu < 0.23$ eV. The *Planck* data strongly disfavour fully thermalized sterile neutrinos with $m_{sterile} \approx 1$ eV that have been proposed as a solution to reactor neutrino oscillation anomalies. From *Planck*, we find no evidence for new neutrino physics. Standard neutrinos with masses larger than those in the minimal mass hierarchy are still allowed, and could be detectable in combination with future astrophysical and CMB lensing data.

(11) The standard theory of big bang nucleosynthesis, with $N_{eff} = 3.046$ and negligible leptonic asymmetry in the electron neutrino sector, is in excellent agreement with *Planck* data and observations of primordial light element abundances. This agreement is particularly striking for deuterium, for which accurate primordial abundance measurements have been reported recently (Cooke et al. 2014). The BBN theoretical predictions for deuterium are now dominated by uncertainties in nuclear reaction rates (principally the d(p, γ)^{3}He radiative capture process), rather than from *Planck* uncertainties in the physical baryon density $\omega_b \equiv \Omega_b h^2$.

(12) We have investigated the temperature and polarization signatures associated with annihilating dark matter and possible deviations from the standard recombination history. Again, we find no evidence for new physics from the *Planck* data.

In summary, the *Planck* temperature and polarization spectra presented in Figs. 1 and 3 are more precise (and accurate) than those from any previous CMB experiment, and improve on the 2013 spectra presented in PCP13. Yet we find no signs for any significant deviation from the base ΛCDM cosmology. Similarly, the analysis of 2015 *Planck* data reported in Planck Collaboration XVII (2016) sets unprecedentedly tight limits on primordial non-Gaussianity. The *Planck* results offer powerful evidence in favour of simple inflationary models, which provide an attractive mechanism for generating the slightly tilted spectrum of (nearly) Gaussian adiabatic perturbations that match our data to such high precision. In addition, the *Planck* data show that the neutrino sector of the theory is consistent with the assumptions of the base ΛCDM model and that the dark energy is compatible with a cosmological constant. If there is new physics beyond base ΛCDM, then the corresponding observational signatures in the CMB are weak and difficult to detect. This is the legacy of the *Planck* mission for cosmology.

References

Abazajian, K. N., Acero, M. A., Agarwalla, S. K., et al. 2012, ArXiv e-prints [arXiv:1204.5379]

Abazajian, K. N., Arnold, K., Austermann, J., et al. 2015a, Astropart. Phys., 63, 55

Abazajian, K. N., Arnold, K., Austermann, J., et al. 2015b, Astropart. Phys., 63, 66

Abazajian, K. N., Canac, N., Horiuchi, S., & Kaplinghat, M. 2014, Phys. Rev. D, 90, 023526

Ackermann, M., Ajello, M., Allafort, A., et al. 2012, Phys. Rev. Lett., 108, 011103

Ackermann, M., Albert, A., Anderson, B., et al. 2014, Phys. Rev. D, 89, 042001

Addison, G. E., Dunkley, J., & Spergel, D. N. 2012, MNRAS, 427, 1741

Ade, P. A. R., Akiba, Y., Anthony, A. E., et al. 2014, Phys. Rev. Lett., 113, 021301

Adelberger, E., Balantekin, A., Bemmerer, D., et al. 2011, Rev. Mod. Phys., 83, 195

Adriani, O., Barbarino, G. C., Bazilevskaya, G. A., et al. 2009, Nature, 458, 607

Aguilar, M., Aisa, D., Alvino, A., et al. 2014, Phys. Rev. Lett., 113, 121102

Albrecht, A., Battye, R. A., & Robinson, J. 1999, Phys. Rev. D, 59, 023508
Alcock, C., & Paczynski, B. 1979, Nature, 281, 358
Ali-Haïmoud, Y., & Hirata, C. M. 2010, Phys. Rev. D, 82, 063521
Ali-Haimoud, Y., & Hirata, C. M. 2011, Phys. Rev. D, 83, 043513
Amendola, L., Gordon, C., Wands, D., & Sasaki, M. 2002, Phys. Rev. Lett., 88, 211302
Anders, M., Trezzi, D., Menegazzo, R., et al. 2014, Phys. Rev. Lett., 113, 042501
Anderson, L., Aubourg, E., Bailey, S., et al. 2012, MNRAS, 427, 3435
Anderson, L., Aubourg, É., Bailey, S., et al. 2014, MNRAS, 441, 24
Archidiacono, M., Calabrese, E., & Melchiorri, A. 2011, Phys. Rev. D, 84, 123008
Archidiacono, M., Fornengo, N., Giunti, C., Hannestad, S., & Melchiorri, A. 2013a, Phys. Rev. D, 87, 125034
Archidiacono, M., Giusarma, E., Melchiorri, A., & Mena, O. 2013b, Phys. Rev. D, 87, 103519
Arkani-Hamed, N., Finkbeiner, D. P., Slatyer, T. R., & Weiner, N. 2009, Phys. Rev. D, 79, 015014
Aubourg, E., Bailey, S., Bautista, J. E., et al. 2015, Phys. Rev. D, 92, 123516
Audren, B., Lesgourgues, J., Benabed, K., & Prunet, S. 2013, J. Cosmology Astropart. Phys., 2, 001
Audren, B., Bellini, E., Cuesta, A. J., et al. 2015, JCAP, 1503, 036
Aver, E., Olive, K. A., Porter, R., & Skillman, E. D. 2013, JCAP, 1311, 017
Bartelmann, M., & Schneider, P. 2001, Phys. Rep., 340, 291
Bashinsky, S., & Seljak, U. 2004, Phys. Rev. D, 69, 083002
Battistelli, E. S., De Petris, M., Lamagna, L., et al. 2002, ApJ, 580, L101
Battye, R. A., & Moss, A. 2014, Phys. Rev. Lett., 112, 051303
Battye, R. A., Charnock, T., & Moss, A. 2015, Phys. Rev. D, 91, 103508
Beacom, J. F., Bell, N. F., & Dodelson, S. 2004, Phys. Rev. Lett., 93, 121302
Bean, R., Dunkley, J., & Pierpaoli, E. 2006, Phys. Rev. D, 74, 063503
Bell, N. F. 2005, Nucl. Phys. B Proc. Suppl., 138, 76
Bennett, C. L., Halpern, M., Hinshaw, G., et al. 2003, ApJS, 148, 1
Bennett, C. L., Hill, R. S., Hinshaw, G., et al. 2011, ApJS, 192, 17
Bennett, C. L., Larson, D., Weiland, J. L., et al. 2013, ApJS, 208, 20
Bennett, C. L., Larson, D., Weiland, J. L., & Hinshaw, G. 2014, ApJ, 794, 135
Benson, B. A., de Haan, T., Dudley, J. P., et al. 2013, ApJ, 763, 147
Bergström, J., Gonzalez-Garcia, M. C., Niro, V., & Salvado, J. 2014, JHEP, 10, 104
Béthermin, M., Daddi, E., Magdis, G., et al. 2012, ApJ, 757, L23
Betoule, M., Marriner, J., Regnault, N., et al. 2013, A&A, 552, A124
Betoule, M., Kessler, R., Guy, J., et al. 2014, A&A, 568, A22
Betts, S., et al. 2013, in Community Summer Study 2013: Snowmass on the Mississippi (CSS2013) Minneapolis, MN, USA, July 29–August 6
Beutler, F., Blake, C., Colless, M., et al. 2011, MNRAS, 416, 3017
Beutler, F., Blake, C., Colless, M., et al. 2012, MNRAS, 423, 3430
Beutler, F., Saito, S., Seo, H.-J., et al. 2014a, MNRAS, 443, 1065
Beutler, F., Saito, S., Brownstein, J. R., et al. 2014b, MNRAS, 444, 3501
Bevis, N., Hindmarsh, M., Kunz, M., & Urrestilla, J. 2007, Phys. Rev. D, 75, 065015
Bevis, N., Hindmarsh, M., Kunz, M., & Urrestilla, J. 2010, Phys. Rev. D, 82, 065004
Bianchi, D., Guzzo, L., Branchini, E., et al. 2012, MNRAS, 427, 2420
BICEP2 Collaboration. 2014, Phys. Rev. Lett., 112, 241101
BICEP2/Keck Array and Planck Collaborations 2015, Phys. Rev. Lett., 114, 101301
Blake, C., Kazin, E. A., Beutler, F., et al. 2011, MNRAS, 418, 1707
Blake, C., Brough, S., Colless, M., et al. 2012, MNRAS, 425, 405
Böhringer, H., Chon, G., & Collins, C. A. 2014, A&A, 570, A31
Bond, J., Efstathiou, G., & Tegmark, M. 1997, MNRAS, 291, L33
Boudaud, M., Aupetit, S., Caroff, S., et al. 2015, A&A, 575, A67
Bousso, R., Harlow, D., & Senatore, L. 2015, Phys. Rev. D, 91, 083527
Breit, G., & Teller, E. 1940, ApJ, 91, 215
Bucher, M., Goldhaber, A. S., & Turok, N. 1995, Phys. Rev. D, 52, 3314
Bucher, M., Moodley, K., & Turok, N. 2001a, Phys. Rev. Lett., 87, 191301
Bucher, M., Moodley, K., & Turok, N. 2001b, Phys. Rev. D, 62, 083508
Buchmuller, W., Domcke, V., & Kamada, K. 2013, Phys. Lett. B, 726, 467
Burigana, C., Danese, L., & de Zotti, G. 1991, A&A, 246, 49
Calabrese, E., Slosar, A., Melchiorri, A., Smoot, G. F., & Zahn, O. 2008, Phys. Rev. D, 77, 123531
Calabrese, E., de Putter, R., Huterer, D., Linder, E. V., & Melchiorri, A. 2011, Phys. Rev. D, 83, 023011
Calabrese, E., Hlozek, R. A., Battaglia, N., et al. 2013, Phys. Rev. D, 87, 103012
Calore, F., Cholis, I., McCabe, C., & Weniger, C. 2015, Phys. Rev. D, 91, 063003
Cesar, C. L., Fried, D. G., Killian, T. C., et al. 1996, Phys. Rev. Lett., 77, 255
Chen, X.-L., & Kamionkowski, M. 2004, Phys. Rev. D, 70, 043502
Chluba, J. 2014, MNRAS, 443, 1881
Chluba, J., & Sunyaev, R. A. 2006a, A&A, 458, L29
Chluba, J., & Sunyaev, R. A. 2006b, A&A, 446, 39
Chluba, J., & Sunyaev, R. A. 2007, A&A, 475, 109

Chluba, J., & Sunyaev, R. A. 2008, A&A, 478, L27
Chluba, J., & Sunyaev, R. A. 2012, MNRAS, 419, 1294
Chluba, J., & Thomas, R. M. 2011, MNRAS, 412, 748
Chluba, J., Fung, J., & Switzer, E. R. 2012, MNRAS, 423, 3227
Cholis, I., & Hooper, D. 2013, Phys. Rev. D, 88, 023013
Choudhury, T. R., Puchwein, E., Haehnelt, M. G., & Bolton, J. S. 2015, MNRAS, 452, 261
Chuang, C.-H., Prada, F, Pellejero-Ibanez, M., et al. 2016, MNRAS, 461, 3781
Cocco, A. G., Mangano, G., & Messina, M. 2007, JCAP, 0706, 015
Coleman, S. R., & De Luccia, F. 1980, Phys. Rev. D, 21, 3305
Conley, A., Guy, J., Sullivan, M., et al. 2011, ApJS, 192, 1
Conlon, J. P., & Marsh, M. C. D. 2013, JHEP, 1310, 214
Cooke, R., Pettini, M., Jorgenson, R. A., Murphy, M. T., & Steidel, C. C. 2014, ApJ, 781, 31
Copeland, E. J., & Kibble, T. 2010, Proc. Roy. Soc. Lond. A, 466, 623
Copeland, E. J., Sami, M., & Tsujikawa, S. 2006, Int. J. Mod. Phys. D, 15, 1753
Creminelli, P., Dubovsky, S., López Nacir, D., et al. 2015, Phys. Rev. D, 92, 123528
Cuesta, A. J., Verde, L., Riess, A., & Jimenez, R. 2015, MNRAS, 448, 3463
Czerny, M., Kobayashi, T., & Takahashi, F. 2014, Phys. Lett. B, 735, 176
Das, S., Louis, T., Nolta, M. R., et al. 2014, JCAP, 4, 14
Daylan, T., Finkbeiner, D. P., Hooper, D., et al. 2016, Phys. Dark Univ., 12, 1
de la Torre, S., Guzzo, L., Peacock, J. A., et al. 2013, A&A, 557, A54
Delubac, T., Bautista, J. E., Busca, N. G., et al. 2015, A&A, 574, A59
Di Valentino, E., Gustavino, C., Lesgourgues, J., et al. 2014, Phys. Rev. D, 90, 023543
Diamanti, R., Lopez-Honorez, L., Mena, O., Palomares-Ruiz, S., & Vincent, A. C. 2014, JCAP, 1402, 017
Dodelson, S., & Widrow, L. M. 1994, Phys. Rev. Lett., 72, 17
Doran, M. 2005, JCAP, 0510, 011
Doroshkevich, A. G., Naselsky, I. P., Naselsky, P. D., & Novikov, I. D. 2003, ApJ, 586, 709
Drexlin, G., Hannen, V., Mertens, S., & Weinheimer, C. 2013, Adv. High Energy Phys., 2013, 293986
Dubrovich, V. K., & Grachev, S. I. 2005, Astron. Lett., 31, 359
Dunkley, J., Calabrese, E., Sievers, J., et al. 2013, JCAP, 7, 25
Durrer, R., Kunz, M., & Melchiorri, A. 2002, Phys. Rept., 364, 1
Efstathiou, G. 2004, MNRAS, 349, 603
Efstathiou, G. 2006, MNRAS, 370, 343
Efstathiou, G. 2014, MNRAS, 440, 1138
Efstathiou, G., & Migliaccio, M. 2012, MNRAS, 423, 2492
Ellis, J., Nanopoulos, D. V., & Olive, K. A. 2013, Phys. Rev. Lett., 111, 111301
Erben, T., Hildebrandt, H., Miller, L., et al. 2013, MNRAS, 433, 2545
Evoli, C., Pandolfi, S., & Ferrara, A. 2013, MNRAS, 433, 1736
Fabbri, R., Melchiorri, F., & Natale, V. 1978, Ap&SS, 59, 223
Fan, X., Strauss, M. A., Becker, R. H., et al. 2006, AJ, 132, 117
Fang, W., Hu, W., & Lewis, A. 2008, Phys. Rev. D, 78, 087303
Farhang, M., Bond, J. R., & Chluba, J. 2012, ApJ, 752, 88
Farhang, M., Bond, J. R., Chluba, J., & Switzer, E. R. 2013, ApJ, 764, 137
Ferrara, S., Kallosh, R., Linde, A., & Porrati, M. 2013, Phys. Rev. D, 88, 085038
Fields, B. D., Molaro, P., & Sarkar, S. 2014, Chin. Phys. C, 38, 339
Finkbeiner, D. P., Galli, S., Lin, T., & Slatyer, T. R. 2012, Phys. Rev. D, 85, 043522
Fixsen, D. J. 2003, ApJ, 594, L67
Fixsen, D. J. 2009, ApJ, 707, 916
Fixsen, D. J., Cheng, E. S., Gales, J. M., et al. 1996, ApJ, 473, 576
Flauger, R., Hill, J. C., & Spergel, D. N. 2014, JCAP, 8, 39
Font-Ribera, A., Kirkby, D., Busca, N., et al. 2014, JCAP, 5, 27
Freedman, W. L., Madore, B. F., Scowcroft, V., et al. 2012, ApJ, 758, 24
Freivogel, B., Kleban, M., Rodriguez Martinez, M., & Susskind, L. 2006, JHEP, 0603, 039
Fu, L., Kilbinger, M., Erben, T., et al. 2014, MNRAS, 441, 2725
Fuskeland, U., Wehus, I. K., Eriksen, H. K., & Næss, S. K. 2014, ApJ, 790, 104
Galli, S., Bean, R., Melchiorri, A., & Silk, J. 2008, Phys. Rev. D, 78, 063532
Galli, S., Iocco, F., Bertone, G., & Melchiorri, A. 2009a, Phys. Rev. D, 80, 023505
Galli, S., Melchiorri, A., Smoot, G. F., & Zahn, O. 2009b, Phys. Rev. D, 80, 023508
Galli, S., Iocco, F., Bertone, G., & Melchiorri, A. 2011, Phys. Rev. D, 84, 027302
Galli, S., Slatyer, T. R., Valdes, M., & Iocco, F. 2013, Phys. Rev. D, 88, 063502
Galli, S., Benabed, K., Bouchet, F., et al. 2014, Phys. Rev. D, 90, 063504
Garcia-Bellido, J., Roest, D., Scalisi, M., & Zavala, I. 2014, Phys. Rev. D, 90, 123539
Gariazzo, S., Giunti, C., & Laveder, M. 2013, JHEP, 1311, 211
Gariazzo, S., Giunti, C., & Laveder, M. 2014, ArXiv e-prints [arXiv:1404.6160]
George, E. M., Reichardt, C. L., Aird, K. A., et al. 2015, ApJ, 799, 177

Gerbino, M., Di Valentino, E., & Said, N. 2013, Phys. Rev. D, 88, 063538
Giesen, G., Lesgourgues, J., Audren, B., & Ali-Haimoud, Y. 2012, JCAP, 1212, 008
Gil-Marín, H., Percival, W. J., Brownstein, J. R., et al. 2016, MNRAS, 460, 4188
Giunti, C., Laveder, M., Li, Y., & Long, H. 2013, Phys. Rev. D, 88, 073008
Goldman, S. P. 1989, Phys. Rev. A, 40, 1185
Goodenough, L., & Hooper, D. 2009, ArXiv e-prints [arXiv:0910.2998]
Gordon, C., & Lewis, A. 2003, Phys. Rev. D, 67, 123513
Gordon, C., & Macías, O. 2013, Phys. Rev. D, 88, 083521
Górski, K. M., Hivon, E., Banday, A. J., et al. 2005, ApJ, 622, 759
Gott, J. 1982, Nature, 295, 304
Grin, D., & Hirata, C. M. 2010, Phys. Rev. D, 81, 083005
Grin, D., Dore, O., & Kamionkowski, M. 2011, Phys. Rev. D, 84, 123003
Grin, D., Hanson, D., Holder, G. P., Doré, O., & Kamionkowski, M. 2014, Phys. Rev. D, 89, 023006
Gunn, J. E., & Peterson, B. A. 1965, ApJ, 142, 1633
Hamann, J., & Hasenkamp, J. 2013, JCAP, 1310, 044
Hamann, J., & Wong, Y. Y. Y. 2008, JCAP, 3, 25
Hamimeche, S., & Lewis, A. 2008, Phys. Rev. D, 77, 103013
Hannestad, S. 2005, JCAP, 0502, 011
Hanson, D., Hoover, S., Crites, A., et al. 2013, Phys. Rev. Lett., 111, 141301
Harnois-Déraps, J., van Waerbeke, L., Viola, M., & Heymans, C. 2015, MNRAS, 450, 1212
Hasenkamp, J. 2014, JCAP, 1409, 048
Hasenkamp, J., & Kersten, J. 2013, JCAP, 1308, 024
Hasselfield, M., Moodley, K., Bond, J. R., et al. 2013a, ApJS, 209, 17
Hasselfield, M., Hilton, M., Marriage, T. A., et al. 2013b, JCAP, 1307, 008
Heymans, C., Van Waerbeke, L., Miller, L., et al. 2012, MNRAS, 427, 146
Heymans, C., Grocutt, E., Heavens, A., et al. 2013, MNRAS, 432, 2433
Hindmarsh, M., & Kibble, T. 1995, Rept. Prog. Phys., 58, 477
Hinshaw, G., Spergel, D. N., Verde, L., et al. 2003, ApJS, 148, 135
Hinshaw, G., Larson, D., Komatsu, E., et al. 2013, ApJS, 208, 19
Hirata, C. M. 2008, Phys. Rev. D, 78, 023001
Hoekstra, H., Herbonnet, R., Muzzin, A., et al. 2015, MNRAS, 449, 685
Hou, Z., Reichardt, C. L., Story, K. T., et al. 2014, ApJ, 782, 74
Howlett, C., Ross, A., Samushia, L., Percival, W., & Manera, M. 2015, MNRAS, 449, 848
Hu, W. 1998, ApJ, 506, 485
Hu, W., & Sawicki, I. 2007, Phys. Rev. D, 76, 104043
Hu, W., & Silk, J. 1993, Phys. Rev. D, 48, 485
Hu, W., Scott, D., Sugiyama, N., & White, M. 1995, Phys. Rev. D, 52, 5498
Hu, W., Eisenstein, D. J., Tegmark, M., & White, M. 1999, Phys. Rev. D, 59, 023512
Humphreys, E. M. L., Reid, M. J., Moran, J. M., Greenhill, L. J., & Argon, A. L. 2013, ApJ, 775, 13
Hurier, G., Aghanim, N., Douspis, M., & Pointecouteau, E. 2014, A&A, 561, A143
Hutsi, G., Chluba, J., Hektor, A., & Raidal, M. 2011, A&A, 535, A26
Hütsi, G., Hektor, A., & Raidal, M. 2009, A&A, 505, 999
Iocco, F., Mangano, G., Miele, G., Pisanti, O., & Serpico, P. D. 2009, Phys. Rep., 472, 1
Izotov, Y., Thuan, T., & Guseva, N. 2014, MNRAS, 445, 778
Jeannerot, R., Rocher, J., & Sakellariadou, M. 2003, Phys. Rev. D, 68, 103514
Jeong, D., Pradler, J., Chluba, J., & Kamionkowski, M. 2014, Phys. Rev. Lett., 113, 061301
Kallosh, R., & Linde, A. 2013, JCAP, 6, 28
Kaplinghat, M., Scherrer, R. J., & Turner, M. S. 1999, Phys. Rev. D, 60, 023516
Karshenboim, S. G., & Ivanov, V. G. 2008, Astron. Lett., 34, 289
Kazin, E. A., Koda, J., Blake, C., et al. 2014, MNRAS, 441, 3524
Kesden, M., Cooray, A., & Kamionkowski, M. 2003, Phys. Rev. D, 67, 123507
Kholupenko, E. E., & Ivanchik, A. V. 2006, Astron. Lett., 32, 795
Kholupenko, E. E., Ivanchik, A. V., & Varshalovich, D. A. 2007, MNRAS, 378, L39
Kibble, T. 1976, J. Phys. A, 9, 1387
Kilbinger, M., Fu, L., Heymans, C., et al. 2013, MNRAS, 430, 2200
Kitching, T. D., Heavens, A. F., Alsing, J., et al. 2014, MNRAS, 442, 1326
Komatsu, E., Dunkley, J., Nolta, M. R., et al. 2009, ApJS, 180, 330
Kopp, J., Machado, P. A. N., Maltoni, M., & Schwetz, T. 2013, JHEP, 1305, 050
Kosowsky, A., & Turner, M. S. 1995, Phys. Rev. D, 52, 1739
Krüger, H., & Oed, A. 1975, Phys. Lett. A, 54, 251
Labzowsky, L. N., Shonin, A. V., & Solovyev, D. A. 2005, J. Phys. B Atomic Mol. Phys., 38, 265
Lacroix, T., Boehm, C., & Silk, J. 2014, Phys. Rev. D, 90, 043508
Larson, D., Dunkley, J., Hinshaw, G., et al. 2011, ApJS, 192, 16
Leistedt, B., Peiris, H. V., & Verde, L. 2014, Phys. Rev. Lett., 113, 041301
Lesgourgues, J. 2011, ArXiv e-prints [arXiv:1104.2932]
Lesgourgues, J., & Pastor, S. 2006, Phys. Rep., 429, 307
Lewis, A. 2013, Phys. Rev. D, 87, 103529
Lewis, A., & Bridle, S. 2002, Phys. Rev. D, 66, 103511
Lewis, A., & Challinor, A. 2006, Phys. Rep., 429, 1
Lewis, A., Challinor, A., & Lasenby, A. 2000, ApJ, 538, 473
Linde, A. 1999, Phys. Rev. D, 59, 023503
Linde, A. 2003, JCAP, 5, 2
Long, A. J., Lunardini, C., & Sabancilar, E. 2014, JCAP, 1408, 038
Lueker, M., Reichardt, C. L., Schaffer, K. K., et al. 2010, ApJ, 719, 1045
Luzzi, G., Shimon, M., Lamagna, L., et al. 2009, ApJ, 705, 1122
Lyth, D. H. 1997, Phys. Rev. Lett., 78, 1861
Lyth, D., & Wands, D. 2002, Phys. Lett. B, 524, 5
Ma, L., Karwowski, H. J., Brune, C. R., et al. 1997, Phys. Rev. C, 55, 588
MacCrann, N., Zuntz, J., Bridle, S., Jain, B., & Becker, M. R. 2015, MNRAS, 451, 2877
Madhavacheril, M. S., Sehgal, N., & Slatyer, T. R. 2014, Phys. Rev. D, 89, 103508
Mandelbaum, R., Slosar, A., Baldauf, T., et al. 2013, MNRAS, 432, 1544
Mangano, G., Miele, G., Pastor, S., & Peloso, M. 2002, Phys. Lett. B, 534, 8
Mantz, A. B., von der Linden, A., Allen, S. W., et al. 2015, MNRAS, 446, 2205
Marcucci, L., Viviani, M., Schiavilla, R., Kievsky, A., & Rosati, S. 2005, Phys. Rev. C, 72, 014001
Martins, C., & Shellard, E. 2002, Phys. Rev. D, 65, 043514
McCarthy, I. G., Le Brun, A. M. C., Schaye, J., & Holder, G. P. 2014, MNRAS, 440, 3645
Meerburg, P. D. 2014, Phys. Rev. D, 90, 063529
Minor, Q. E., & Kaplinghat, M. 2015, Phys. Rev. D, 91, 063504
Mirizzi, A., Mangano, G., Saviano, N., et al. 2013, Phys. Lett. B, 726, 8
Mollerach, S. 1990, Phys. Rev. D, 42, 313
Mortonson, M. J., & Hu, W. 2008, ApJ, 672, 737
Mortonson, M. J., & Seljak, U. 2014, JCAP, 10, 35
Mosher, J., Guy, J., Kessler, R., et al. 2014, ApJ, 793, 16
Mukhanov, V. F., & Chibisov, G. V. 1981, JETPL, 33, 532
Mukhanov, V., Kim, J., Naselsky, P., Trombetti, T., & Burigana, C. 2012, JCAP, 6, 40
Nakamura, K., & Petcov, S. T. 2014, in Chin. Phys. C, 38, Rev. Part. Phys., ed. K. Olive, 090001
Nollett, K. M., & Holder, G. P. 2011, ArXiv e-prints [arXiv:1112.2683]
O'Connell, D., Kollath, K. J., Duncan, A. J., & Kleinpoppen, H. 1975, J. Phys. B Atom. Mol. Phys., 8, L214
Oka, A., Saito, S., Nishimichi, T., Taruya, A., & Yamamoto, K. 2014, MNRAS, 439, 2515
Okumura, T., Seljak, U., & Desjacques, V. 2012, JCAP, 11, 14
Olive, K. A., Agashe, K., Amsler, C., et al. 2014, Chin. Phys., C38, 090001
Opher, R., & Pelinson, A. 2004, Phys. Rev. D, 70, 063529
Opher, R., & Pelinson, A. 2005, MNRAS, 362, 167
Padmanabhan, N., & Finkbeiner, D. P. 2005, Phys. Rev. D, 72, 023508
Palanque-Delabrouille, N., Yèche, C., Lesgourgues, J., et al. 2015, JCAP, 1502, 045
Pan, Z., Knox, L., & White, M. 2014, MNRAS, 445, 2941
Peebles, P. J. E. 1968, ApJ, 153, 1
Peebles, P. J. E., & Yu, J. T. 1970, ApJ, 162, 815
Peebles, P. J. E., Seager, S., & Hu, W. 2000, ApJ, 539, L1
Peimbert, M. 2008, Current Science, 95, 1165
Percival, W. J., & White, M. 2009, MNRAS, 393, 297
Percival, W. J., Reid, B. A., Eisenstein, D. J., et al. 2010, MNRAS, 401, 2148
Perlmutter, S., Aldering, G., Goldhaber, G., et al. 1999, ApJ, 517, 565
Pettini, M., & Cooke, R. 2012, MNRAS, 425, 2477
Pisanti, O., Cirillo, A., Esposito, S., et al. 2008, Comput. Phys. Commun., 178, 956
Planck Collaboration I. 2014, A&A, 571, A1
Planck Collaboration XV. 2014, A&A, 571, A15
Planck Collaboration XVI. 2014, A&A, 571, A16
Planck Collaboration XVII. 2014, A&A, 571, A17
Planck Collaboration XX. 2014, A&A, 571, A20
Planck Collaboration XXII. 2014, A&A, 571, A22
Planck Collaboration XXIII. 2014, A&A, 571, A23
Planck Collaboration XXIV. 2014, A&A, 571, A24
Planck Collaboration XXV. 2014, A&A, 571, A25
Planck Collaboration XXX. 2014, A&A, 571, A30
Planck Collaboration XXXI. 2014, A&A, 571, A31
Planck Collaboration I. 2016, A&A, 594, A1
Planck Collaboration II. 2016, A&A, 594, A2
Planck Collaboration III. 2016, A&A, 594, A3
Planck Collaboration IV. 2016, A&A, 594, A4
Planck Collaboration V. 2016, A&A, 594, A5
Planck Collaboration VI. 2016, A&A, 594, A6
Planck Collaboration VII. 2016, A&A, 594, A7
Planck Collaboration VIII. 2016, A&A, 594, A8
Planck Collaboration IX. 2016, A&A, 594, A9

Planck Collaboration X. 2016, A&A, 594, A10
Planck Collaboration XI. 2016, A&A, 594, A11
Planck Collaboration XII. 2016, A&A, 594, A12
Planck Collaboration XIII. 2016, A&A, 594, A13
Planck Collaboration XIV. 2016, A&A, 594, A14
Planck Collaboration XV. 2016, A&A, 594, A15
Planck Collaboration XVI. 2016, A&A, 594, A16
Planck Collaboration XVII. 2016, A&A, 594, A17
Planck Collaboration XVIII. 2016, A&A, 594, A18
Planck Collaboration XIX. 2016, A&A, 594, A19
Planck Collaboration XX. 2016, A&A, 594, A20
Planck Collaboration XXI. 2016, A&A, 594, A21
Planck Collaboration XXII. 2016, A&A, 594, A22
Planck Collaboration XXIII. 2016, A&A, 594, A23
Planck Collaboration XXIV. 2016, A&A, 594, A24
Planck Collaboration XXV. 2016, A&A, 594, A25
Planck Collaboration XXVI. 2016, A&A, 594, A26
Planck Collaboration XXVII. 2016, A&A, 594, A27
Planck Collaboration XXVIII. 2016, A&A, 594, A28
Planck Collaboration Int. XVI. 2014, A&A, 566, A54
Planck Collaboration Int. XXII. 2015, A&A, 576, A107
Planck Collaboration Int. XXX. 2016, A&A, 586, A133
Planck Collaboration Int. XLVI. 2016, A&A, in press,
    DOI: 10.1051/0004-6361/201628890
Pogosian, L., & Vachaspati, T. 1999, Phys. Rev. D, 60, 083504
POLARBEAR Collaboration 2014a, ApJ, 794, 171
POLARBEAR Collaboration 2014b, Phys. Rev. Lett., 112, 131302
Polchinski, J. 2005, Int. J. Mod. Phys. A, 20, 3413
Profumo, S. 2013, ArXiv e-prints [arXiv:1301.0952]
Reichardt, C. L., Shaw, L., Zahn, O., et al. 2012, ApJ, 755, 70
Reid, B. A., Seo, H.-J., Leauthaud, A., Tinker, J. L., & White, M. 2014, MNRAS,
    444, 476
Rephaeli, Y. 1980, ApJ, 241, 858
Rest, A., Scolnic, D., Foley, R. J., et al. 2014, ApJ, 795, 44
Riess, A. G., Filippenko, A. V., Challis, P., et al. 1998, AJ, 116, 1009
Riess, A. G., Macri, L., Casertano, S., et al. 2011, ApJ, 730, 119
Rigault, M., Aldering, G., Kowalski, M., et al. 2015, ApJ, 802, 20
Robertson, B. E., Furlanetto, S. R., Schneider, E., et al. 2013, ApJ, 768, 71
Roest, D. 2014, JCAP, 1401, 007
Ross, A. J., Samushia, L., Howlett, C., et al. 2015, MNRAS, 449, 835
Rubiño-Martín, J. A., Chluba, J., & Sunyaev, R. A. 2006, MNRAS, 371, 1939
Rubiño-Martín, J. A., Chluba, J., & Sunyaev, R. A. 2008, A&A, 485, 377
Rubiño-Martín, J. A., Chluba, J., Fendt, W. A., & Wandelt, B. D. 2010, MNRAS,
    403, 439
Samushia, L., Reid, B. A., White, M., et al. 2014, MNRAS, 439, 3504
Saro, A., Liu, J., Mohr, J. J., et al. 2014, MNRAS, 440, 2610
Sawyer, R. F. 2006, Phys. Rev. D, 74, 043527
Schmittfull, M. M., Challinor, A., Hanson, D., & Lewis, A. 2013, Phys. Rev. D,
    88, 063012
Scóccola, C. G., Landau, S. J., & Vucetich, H. 2009, Mem. Soc. Astron. It., 80,
    814
Scolnic, D., Rest, A., Riess, A., et al. 2014, ApJ, 795, 45
Seager, S., Sasselov, D. D., & Scott, D. 1999, ApJ, 523, L1
Seager, S., Sasselov, D. D., & Scott, D. 2000, ApJS, 128, 407
Seljak, U., Sugiyama, N., White, M., & Zaldarriaga, M. 2003, Phys. Rev. D, 68,
    083507
Serenelli, A. M., & Basu, S. 2010, ApJ, 719, 865
Serpico, P. D., Esposito, S., Iocco, F., et al. 2004, JCAP, 0412, 010
Shaw, J. R., & Chluba, J. 2011, MNRAS, 415, 1343
Shull, J. M., & van Steenberg, M. E. 1985, ApJ, 298, 268
Silverstein, E., & Westphal, A. 2008, Phys. Rev. D, 78, 106003
Simet, M., Battaglia, N., Mandelbaum, R., & Seljak, U. 2015, ArXiv e-prints
    [arXiv:1502.01024]
Simha, V., & Steigman, G. 2008, JCAP, 6, 16
Slatyer, T. R., Padmanabhan, N., & Finkbeiner, D. P. 2009, Phys. Rev. D, 80,
    043526
Smith, R. E., Peacock, J. A., Jenkins, A., et al. 2003, MNRAS, 341, 1311
Smith, T. L., Das, S., & Zahn, O. 2012, Phys. Rev. D, 85, 023001
Smoot, G. F., Bennett, C. L., Kogut, A., et al. 1992, ApJ, 396, L1
Song, Y.-S., & Percival, W. J. 2009, JCAP, 10, 4
Spergel, D. N., Verde, L., Peiris, H. V., et al. 2003, ApJS, 148, 175
Spergel, D. N., Flauger, R., & Hložek, R. 2015, Phys. Rev. D, 91, 023518
Spitzer, Jr., L., & Greenstein, J. L. 1951, ApJ, 114, 407
Starobinsky, A. A. 1979, JETPL, 30, 682
Starobinsky, A. A. 1980, Phys. Lett. B, 91, 99
Story, K. T., Reichardt, C. L., Hou, Z., et al. 2013, ApJ, 779, 86
Story, K. T., Hanson, D., Ade, P. A. R., et al. 2015, ApJ, 810, 50
Sunyaev, R. A., & Zeldovich, Y. B. 1970, Ap&SS, 7, 3

Suzuki, N., Rubin, D., Lidman, C., et al. 2012, ApJ, 746, 85
Switzer, E. R., & Hirata, C. M. 2008, Phys. Rev. D, 77, 083006
Takahashi, R., Sato, M., Nishimichi, T., Taruya, A., & Oguri, M. 2012, ApJ, 761,
    152
Tammann, G. A., & Reindl, B. 2013, A&A, 549, A136
Tammann, G. A., Sandage, A., & Reindl, B. 2008, A&ARv, 15, 289
Trac, H., Bode, P., & Ostriker, J. P. 2011, ApJ, 727, 94
Trotta, R., & Melchiorri, A. 2005, Phys. Rev. Lett., 95, 011305
Tsujikawa, S. 2010, Lect. Notes Phys., 800, 99
Urrestilla, J., Bevis, N., Hindmarsh, M., Kunz, M., & Liddle, A. R. 2008, JCAP,
    0807, 010
Valdes, M., Evoli, C., & Ferrara, A. 2010, MNRAS, 404, 1569
van Engelen, A., Sherwin, B. D., Sehgal, N., et al. 2015, ApJ, 808, 7
Viero, M. P., Wang, L., Zemcov, M., et al. 2013, ApJ, 772, 77
Vilenkin, A., & Shellard, E. 2000, Cosmic Strings and Other Topological
    Defects, Cambridge Monographs on Mathematical Physics (Cambridge
    University Press)
Viviani, M., Kievsky, A., Marcucci, L. E., Rosati, S., & Schiavilla, R. 2000,
    Phys. Rev. C, 61, 064001
von der Linden, A., Mantz, A., Allen, S. W., et al. 2014, MNRAS, 443, 1973
Weinberg, S. 2013, Phys. Rev. Lett., 110, 241301
White, M., Reid, B., Chuang, C.-H., et al. 2015, MNRAS, 447, 234
Wong, W. Y., & Scott, D. 2007, MNRAS, 375, 1441
Wong, W. Y., Seager, S., & Scott, D. 2006, MNRAS, 367, 1666
Wong, W. Y., Moss, A., & Scott, D. 2008, MNRAS, 386, 1023
Wyman, M., Rudd, D. H., Vanderveld, R. A., & Hu, W. 2014, Phys. Rev. Lett.,
    112, 051302
Yue, A., Dewey, M., Gilliam, D., et al. 2013, Phys. Rev. Lett., 111, 222501
Zaldarriaga, M., Spergel, D. N., & Seljak, U. 1997, ApJ, 488, 1
Zeldovich, Y. B., Kurt, V. G., & Syunyaev, R. A. 1968, Zhurnal Eksperimental
    noi i Teoreticheskoi Fiziki, 55, 278
Zeldovich, Y. B., & Sunyaev, R. A. 1969, Ap&SS, 4, 301
Zhang, L., Chen, X., Lei, Y.-A., & Si, Z.-G. 2006, Phys. Rev. D, 74, 103519

[1] APC, AstroParticule et Cosmologie, Université Paris Diderot,
    CNRS/IN2P3, CEA/lrfu, Observatoire de Paris, Sorbonne Paris
    Cité, 10 rue Alice Domon et Léonie Duquet, 75205 Paris Cedex 13,
    France
[2] Aalto University Metsähovi Radio Observatory and Dept of Radio
    Science and Engineering, PO Box 13000, 00076 AALTO, Finland
[3] African Institute for Mathematical Sciences, 6-8 Melrose Road,
    Muizenberg, 7945 Cape Town, South Africa
[4] Agenzia Spaziale Italiana Science Data Center, via del Politecnico
    snc, 00133 Roma, Italy
[5] Aix Marseille Université, CNRS, LAM (Laboratoire
    d'Astrophysique de Marseille) UMR 7326, 13388 Marseille,
    France
[6] Aix Marseille Université, Centre de Physique Théorique, 163
    Avenue de Luminy, 13288 Marseille, France
[7] Astrophysics Group, Cavendish Laboratory, University of Cam-
    bridge, J J Thomson Avenue, Cambridge CB3 0HE, UK
[8] Astrophysics & Cosmology Research Unit, School of Mathe-
    matics, Statistics & Computer Science, University of KwaZulu-
    Natal, Westville Campus, Private Bag X54001, 4000 Durban, South
    Africa
[9] Atacama Large Millimeter/submillimeter Array, ALMA Santi-
    ago Central Offices, Alonso de Cordova 3107, Vitacura, Casilla
    763 0355, Santiago, Chile
[10] CGEE, SCS Qd 9, Lote C, Torre C, 4° andar, Ed. Parque Cidade
    Corporate, CEP 70308-200, Brasília, DF, Brazil
[11] CITA, University of Toronto, 60 St. George St., Toronto, ON M5S
    3H8, Canada
[12] CNRS, IRAP, 9 Av. colonel Roche, BP 44346, 31028 Toulouse
    Cedex 4, France
[13] CRANN, Trinity College, Dublin, Ireland
[14] California Institute of Technology, Pasadena, California, USA
[15] Centre for Theoretical Cosmology, DAMTP, University of Cam-
    bridge, Wilberforce Road, Cambridge CB3 0WA, UK
[16] Centro de Estudios de Física del Cosmos de Aragón (CEFCA),
    Plaza San Juan, 1, planta 2, 44001 Teruel, Spain
[17] Computational Cosmology Center, Lawrence Berkeley National
    Laboratory, Berkeley, California, USA

[18] Consejo Superior de Investigaciones Científicas (CSIC), 28049 Madrid, Spain

[19] DSM/Irfu/SPP, CEA-Saclay, 91191 Gif-sur-Yvette Cedex, France

[20] DTU Space, National Space Institute, Technical University of Denmark, Elektrovej 327, 2800 Kgs. Lyngby, Denmark

[21] Département de Physique Théorique, Université de Genève, 24, Quai E. Ansermet, 1211 Genève 4, Switzerland

[22] Departamento de Astrofísica, Universidad de La Laguna (ULL), 38206 La Laguna, Tenerife, Spain

[23] Departamento de Física, Universidad de Oviedo, Avda. Calvo Sotelo s/n, 33007 Oviedo, Spain

[24] Department of Astronomy and Astrophysics, University of Toronto, 50 Saint George Street, 38100 Toronto, Ontario, Canada

[25] Department of Astrophysics/IMAPP, Radboud University Nijmegen, PO Box 9010, 6500 GL Nijmegen, The Netherlands

[26] Department of Physics & Astronomy, University of British Columbia, 6224 Agricultural Road, Vancouver, British Columbia, Canada

[27] Department of Physics and Astronomy, Dana and David Dornsife College of Letter, Arts and Sciences, University of Southern California, Los Angeles, CA 90089, USA

[28] Department of Physics and Astronomy, Johns Hopkins University, Bloomberg Center 435, 3400 N. Charles St., Baltimore, MD 21218, USA

[29] Department of Physics and Astronomy, University College London, London WC1E 6BT, UK

[30] Department of Physics and Astronomy, University of Sussex, Brighton BN1 9QH, UK

[31] Department of Physics, Florida State University, Keen Physics Building, 77 Chieftan Way, Tallahassee, Florida, USA

[32] Department of Physics, Gustaf Hällströmin katu 2a, University of Helsinki, 00560 Helsinki, Finland

[33] Department of Physics, Princeton University, Princeton, New Jersey, NJ 08540, USA

[34] Department of Physics, University of California, Berkeley, California, CA 94720, USA

[35] Department of Physics, University of California, One Shields Avenue, Davis, California, CA 93106, USA

[36] Department of Physics, University of California, Santa Barbara, California, USA

[37] Department of Physics, University of Illinois at Urbana-Champaign, 1110 West Green Street, Urbana, Illinois, IL 61801 USA

[38] Dipartimento di Fisica e Astronomia G. Galilei, Università degli Studi di Padova, via Marzolo 8, 35131 Padova, Italy

[39] Dipartimento di Fisica e Scienze della Terra, Università di Ferrara, via Saragat 1, 44122 Ferrara, Italy

[40] Dipartimento di Fisica, Università La Sapienza, P. le A. Moro 2, 00185 Roma, Italy

[41] Dipartimento di Fisica, Università degli Studi di Milano, via Celoria, 16, 20133 Milano, Italy

[42] Dipartimento di Fisica, Università degli Studi di Trieste, via A. Valerio 2, 34127 Trieste, Italy

[43] Dipartimento di Matematica, Università di Roma Tor Vergata, via della Ricerca Scientifica, 1, 00185 Roma, Italy

[44] Discovery Center, Niels Bohr Institute, Blegdamsvej 17, 1165 Copenhagen, Denmark

[45] Discovery Center, Niels Bohr Institute, Copenhagen University, Blegdamsvej 17, 1165 Copenhagen, Denmark

[46] European Southern Observatory, ESO Vitacura, Alonso de Cordova 3107, Vitacura, Casilla 19001, Santiago, Chile

[47] European Space Agency, ESAC, Planck Science Office, Camino bajo del Castillo, s/n, Urbanización Villafranca del Castillo, Villanueva de la Cañada, 28691 Madrid, Spain

[48] European Space Agency, ESTEC, Keplerlaan 1, 2201 AZ Noordwijk, The Netherlands

[49] Gran Sasso Science Institute, INFN, viale F. Crispi 7, 67100 L'Aquila, Italy

[50] HGSFP and University of Heidelberg, Theoretical Physics Department, Philosophenweg 16, 69120 Heidelberg, Germany

[51] Haverford College Astronomy Department, 370 Lancaster Avenue, Haverford, Pennsylvania, USA

[52] Helsinki Institute of Physics, Gustaf Hällströmin katu 2, University of Helsinki, 00560 Helsinki, Finland

[53] INAF−Osservatorio Astrofisico di Catania, via S. Sofia 78, 95123 Catania, Italy

[54] INAF−Osservatorio Astronomico di Padova, Vicolo dell'Osservatorio 5, 35131 Padova, Italy

[55] INAF−Osservatorio Astronomico di Roma, via di Frascati 33, 00040 Monte Porzio Catone, Italy

[56] INAF−Osservatorio Astronomico di Trieste, via G.B. Tiepolo 11, Trieste, Italy

[57] INAF/IASF Bologna, via Gobetti 101, Bologna, Italy

[58] INAF/IASF Milano, via E. Bassini 15, Milano, Italy

[59] INFN, Sezione di Bologna, viale Berti Pichat 6/2, 40127 Bologna, Italy

[60] INFN, Sezione di Ferrara, via Saragat 1, 44122 Ferrara, Italy

[61] INFN, Sezione di Roma 1, Università di Roma Sapienza, Piazzale Aldo Moro 2, 00185 Roma, Italy

[62] INFN, Sezione di Roma 2, Università di Roma Tor Vergata, via della Ricerca Scientifica, 1, 00185 Roma, Italy

[63] INFN/National Institute for Nuclear Physics, via Valerio 2, 34127 Trieste, Italy

[64] IPAG: Institut de Planétologie et d'Astrophysique de Grenoble, Université Grenoble Alpes, IPAG; CNRS, IPAG, 38000 Grenoble, France

[65] ISDC, Department of Astronomy, University of Geneva, ch. d'Ecogia 16, 1290 Versoix, Switzerland

[66] IUCAA, Post Bag 4, Ganeshkhind, Pune University Campus, 411 007 Pune, India

[67] Imperial College London, Astrophysics group, Blackett Laboratory, Prince Consort Road, London, SW7 2AZ, UK

[68] Infrared Processing and Analysis Center, California Institute of Technology, Pasadena, CA 91125, USA

[69] Institut Néel, CNRS, Université Joseph Fourier Grenoble I, 25 rue des Martyrs, 38042 Grenoble, France

[70] Institut Universitaire de France, 103, bd Saint-Michel, 75005 Paris, France

[71] Institut d'Astrophysique Spatiale, CNRS, Univ. Paris-Sud, Université Paris-Saclay, Bât. 121, 91405 Orsay Cedex, France

[72] Institut d'Astrophysique de Paris, CNRS (UMR 7095), 98bis boulevard Arago, 75014 Paris, France

[73] Institut für Theoretische Teilchenphysik und Kosmologie, RWTH Aachen University, 52056 Aachen, Germany

[74] Institute for Space Sciences, 077125 Bucharest-Magurale, Romania

[75] Institute of Astronomy, University of Cambridge, Madingley Road, Cambridge CB3 0HA, UK

[76] Institute of Theoretical Astrophysics, University of Oslo, Blindern, 0371 Oslo, Norway

[77] Instituto de Astrofísica de Canarias, C/Vía Láctea s/n, 38205 La Laguna, Tenerife, Spain

[78] Instituto de Física de Cantabria (CSIC-Universidad de Cantabria), Avda. de los Castros s/n, 39005 Santander, Spain

[79] Istituto Nazionale di Fisica Nucleare, Sezione di Padova, via Marzolo 8, 35131 Padova, Italy

[80] Jet Propulsion Laboratory, California Institute of Technology, 4800 Oak Grove Drive, Pasadena, California, USA

[81] Jodrell Bank Centre for Astrophysics, Alan Turing Building, School of Physics and Astronomy, The University of Manchester, Oxford Road, Manchester, M13 9PL, UK

[82] Kavli Institute for Cosmological Physics, University of Chicago, Chicago, IL 60637, USA

[83] Kavli Institute for Cosmology Cambridge, Madingley Road, Cambridge, CB3 0HA, UK

[84] Kazan Federal University, 18 Kremlyovskaya St., 420008 Kazan, Russia

[85] LAL, Université Paris-Sud, CNRS/IN2P3, 91898 Orsay, France

[86] LERMA, CNRS, Observatoire de Paris, 61 Avenue de l'Observatoire, Paris, France

[87] Laboratoire AIM, IRFU/Service d'Astrophysique – CEA/DSM – CNRS – Université Paris Diderot, Bât. 709, CEA-Saclay, 91191 Gif-sur-Yvette Cedex, France

[88] Laboratoire Traitement et Communication de l'Information, CNRS (UMR 5141) and Télécom ParisTech, 46 rue Barrault, 75634 Paris Cedex 13, France

[89] Laboratoire de Physique Subatomique et Cosmologie, Université Grenoble-Alpes, CNRS/IN2P3, 53 rue des Martyrs, 38026 Grenoble Cedex, France

[90] Laboratoire de Physique Théorique, Université Paris-Sud 11 & CNRS, Bâtiment 210, 91405 Orsay, France

[91] Lawrence Berkeley National Laboratory, Berkeley, California, USA

[92] Lebedev Physical Institute of the Russian Academy of Sciences, Astro Space Centre, 84/32 Profsoyuznaya st., 117997 Moscow, GSP-7, Russia

[93] Leung Center for Cosmology and Particle Astrophysics, National Taiwan University, 10617 Taipei, Taiwan

[94] Max-Planck-Institut für Astrophysik, Karl-Schwarzschild-Str. 1, 85741 Garching, Germany

[95] McGill Physics, Ernest Rutherford Physics Building, McGill University, 3600 rue University, Montréal, QC, H3A 2T8, Canada

[96] National University of Ireland, Department of Experimental Physics, Maynooth, Co. Kildare, Ireland

[97] Nicolaus Copernicus Astronomical Center, Bartycka 18, 00-716 Warsaw, Poland

[98] Niels Bohr Institute, Blegdamsvej 17, Copenhagen, Denmark

[99] Niels Bohr Institute, Copenhagen University, Blegdamsvej 17, 1165 Copenhagen, Denmark

[100] Nordita (Nordic Institute for Theoretical Physics), Roslagstullsbacken 23, 106 91 Stockholm, Sweden

[101] Optical Science Laboratory, University College London, Gower Street, London, UK

[102] Physics Department, Shahid Beheshti University, Tehran, Iran

[103] SISSA, Astrophysics Sector, via Bonomea 265, 34136 Trieste, Italy

[104] SMARTEST Research Centre, Università degli Studi e-Campus, via Isimbardi 10, Novedrate (CO), 22060, Italy

[105] School of Physics and Astronomy, Cardiff University, Queens Buildings, The Parade, Cardiff, CF24 3AA, UK

[106] School of Physics and Astronomy, University of Nottingham, Nottingham NG7 2RD, UK

[107] Sorbonne Université-UPMC, UMR7095, Institut d'Astrophysique de Paris, 98bis boulevard Arago, 75014 Paris, France

[108] Space Research Institute (IKI), Russian Academy of Sciences, Profsoyuznaya Str, 84/32, 117997 Moscow, Russia

[109] Space Sciences Laboratory, University of California, Berkeley, California, USA

[110] Special Astrophysical Observatory, Russian Academy of Sciences, Nizhnij Arkhyz, Zelenchukskiy region, 369167 Karachai-Cherkessian Republic, Russia

[111] Stanford University, Dept of Physics, Varian Physics Bldg, 382 via Pueblo Mall, Stanford, California, USA

[112] Sub-Department of Astrophysics, University of Oxford, Keble Road, Oxford OX1 3RH, UK

[113] Sydney Institute for Astronomy, School of Physics A28, University of Sydney, NSW 2006, Australia

[114] The Oskar Klein Centre for Cosmoparticle Physics, Department of Physics,Stockholm University, AlbaNova, 106 91 Stockholm, Sweden

[115] Theory Division, PH-TH, CERN, 1211 Geneva 23, Switzerland

[116] UPMC Univ Paris 06, UMR 7095, 98bis boulevard Arago, 75014 Paris, France

[117] Université de Toulouse, UPS-OMP, IRAP, 31028 Toulouse Cedex 4, France

[118] Universities Space Research Association, Stratospheric Observatory for Infrared Astronomy, MS 232-11, Moffett Field, CA 94035, USA

[119] University Observatory, Ludwig Maximilian University of Munich, Scheinerstrasse 1, 81679 Munich, Germany

[120] University of Granada, Departamento de Física Teórica y del Cosmos, Facultad de Ciencias, 11071 Granada, Spain

[121] University of Granada, Instituto Carlos I de Física Teórica y Computacional, 11071 Granada, Spain

[122] University of Heidelberg, Institute for Theoretical Physics, Philosophenweg 16, 69120 Heidelberg, Germany

[123] Warsaw University Observatory, Aleje Ujazdowskie 4, 00-478 Warszawa, Poland